ABSTRACT

Title of Dissertation:	INVESTIGATING THE INTERNAL STRUCTURE OF EARTH AND MARS WITH SEISMIC BODY WAVES
	Quancheng Huang, Doctor of Philosophy, 2020
Dissertation directed by:	Associate Professor Nicholas C. Schmerr, Department of Geology

Seismic waves propagating through the interior of planetary bodies are powerful imaging tools for revealing a high-resolution picture of their internal structures. Owing to the abundant seismic data on Earth, seismology has provided robust constraints on Earth's 1-D and 3-D internal structures. Deployments of seismometers on other terrestrial planets via spacecraft missions has opened the door to explore the interior of these planets through planetary seismology. My dissertation seeks to understand the mantle structures and dynamics of Earth and Mars using a joint approach of seismic data analysis and synthetic waveform modeling. I utilized a body wave approach, SS precursors, to investigate the topography and seismic anisotropy structures of Earth's mantle transition zone (MTZ). On Mars, I investigated the signatures of a seismic discontinuity associated with the olivine-to-wadsleyite phase transition in martian mantle using seismic data recorded by NASA's InSight Mission.

Global topography of MTZ discontinuities is characterized by regional thinning beneath hot spots and thickening beneath subduction zones, indicating mantle temperature plays a crucial role in the topography of MTZ discontinuities. I demonstrated with 3-D synthetic modeling that SS precursors can detect at least 3% azimuthal anisotropy in the MTZ as well as distinguish anisotropy from the shallow and deep upper mantle. I observed azimuthal anisotropy in the MTZ beneath subduction zones with SS precursors and the fast directions are predominantly trench-perpendicular, which is attributed to the lattice preferred orientation of wadsleyite. This is interpreted as the 3-D toroidal flow caused by trench migration.

On Mars, I investigated the detectability of the MTZ, and found that that triplicated waves are the most suitable phases for sensing the olivine phase changes. I combined a polarization filter and vespagram techniques to identify body waves in InSight data. I discovered the existence of multiple reflected waves in the near-field, and evidence for triplicated waves in the far-field after aligning Marsquakes on P- and S-arrivals. Preliminary depth estimate of olivine-to-wadsleyite phase transition from the triplications indicates a cold or hydrated martian mantle. A new seismology-based picture of the martian interior is emerging from my work on the InSight data.

INVESTIGATING THE INTERNAL STRUCTURE OF EARTH AND MARS WITH SEISMIC BODY WAVES

by

Quancheng Huang

Dissertation submitted to the Faculty of the Graduate School of the
University of Maryland, College Park, in partial fulfillment
of the requirements for the degree of
Doctor of Philosophy
2020

Advisory Committee:
Associate Professor Nicholas C. Schmerr, Chair
Associate Professor Vedran Lekić
Professor Wenlu Zhu
Assistant Professor Mong-Han Huang
Professor Jessica Sunshine, Dean's Representative

Preface

The research projects in this dissertation are formulated by the author under the supervision of Dr. Nicholas Schmerr, and contributed by the co-authors: Dr. Caroline Beghein, Dr. Lauren Waszek, Dr. Ross Maguire and InSight Science Team. Part of the dissertation has been published in scientific journals. Chapter 2 titled "Constraints on Seismic Anisotropy in the Mantle Transition Zone from Long-Period SS precursors" was published in Journal of Geophysical Research: Solid Earth in 2019 (DOI: http://doi.org/10.1029/2019JB017307). Chapter 3 titled "3-D Synthetic Modeling of Anisotropy Effects on SS Precursors: Implications for Mantle Flow in the Transition Zone" was submitted to Journal of Geophysical Research: Solid Earth and is currently under review (preprint available at https://doi.org/10.1002/essoar.10504351.1). Chapter 4 titled "Detecting Mantle Transition Zone of Mars from Triplicated and Reflected Seismic Waves" will be published at a later date. All coauthors have provided consent for using texts and figures in this dissertation.

Dedication

This dissertation is dedicated to my parents whose love and support have always motivated me to overcome challenges and pursue my career goals.

Acknowledgements

Sir Isaac Newton once said that “If I have seen further, it is by standing upon the shoulders of giants”. My PhD advisor, Dr. Nicholas C. Schmerr, is such a giant in my life who have inspired me to think deeper and see further during my research. I would like to thank Nick for always teaching me patiently when I asked naïve questions about seismology. During our meetings, his useful suggestions could always help me solve challenging problems in research as well as make important decisions in life, and his passion for science strongly motivates me to become a brilliant seismologist like him. I cannot be more grateful to Nick for introducing me to the InSight Science Team, which opens the door for me to study planetary seismology. I also want to thank him for sending me to various conferences to present my research and network with potential colleagues and advisors. None of my academic achievements would have been possible without his guidance so I want to thank him from the bottom of my heart.

I also appreciate the help from Dr. Vedran Lekić through my PhD studies. Ved could always point me to the right direction even when Nick couldn’t answer my questions. His classes such as observational geophysics, inverse theory and machine learning really have shaped my view of seismology and provided useful tools to my research. I would like to thank other dissertation committee members: Dr. Wenlu Zhu, Dr. Mong-Han Huang and Dr. Jessica Sunshine, for their helpful discussions and feedbacks on my dissertation.

My fellow graduate students and post-docs in the Planetary Geophysics Group and Seismology Group have offered me tremendous help these five years. I want to thank Angela Marusiak, Ernest Bell, Jonathan Guandique, Aisha Khatib, Brianna

Mellerson, Linden Wike, Lauren Waszek, Ross Maguire, Foivos Karakostas and Kira Olsen in our lab. I also thank Chao Gao, Erin Cunningham, Karen Pearson, Phillip Goodling, Pritwiraj Moulik, Doyeon Kim, Scott Burdick and Tolulope Olugboji in Ved's group. All of them have either helped me solve technical problems in my codes or provided feedbacks on my research projects. Special thanks to Chao for discussing potential career opportunities with me. I also thank other graduate students in our department especially for all the intramural sports we played together, which was a great fun beyond research!

I would like to thank all my friends at UMD especially the "international mafia". Thanks for hanging out with me and my life is more wonderful with your company! I miss the time when I was playing board games with Hailong Bai, Mark Larson and Tiange Xing in Mark's basement. I also really enjoyed all the werewolf parties and hiking trips with Meng Guo, Chao Gao, Xizheng Wang, Jiangyi Hou, Manyi Wang, Ming Tang, Huan Cui, Ziqin Ni, Goeun Ha, Weizhe Liu and Peizhi Du. Special thanks to Kristel Izquierdo and Israel Martinez for cooking delicious tacos, going skiing with me and teaching me Spanish!

I never felt alone even though I'm thousands of miles away from home. My family have always been incredibly supportive and closely connected to me since the moment I decided to come to USA. I want to thank my parents and grandma, my sister and brother for their love and inspirations which have shaped my independent and healthy personality. Great thanks to my fiancée, Qiaoya Zhang, for her selfless support, and she was always there with me whenever I felt frustrated. Thanks for traveling with

me all over the world! Each journey with her wrote a beautiful chapter in my life. I hope we will have more exciting adventures after the pandemic.

My work on Earth's MTZ was financially supported by National Science Foundation (NSF) under grant number EAR-1447041. The InSight project was supported by NASA under grant number 80NSSC18K1628. I was also supported by the teaching assistantships and Dean's Fellowship from Department of Geology at UMD. I would like to acknowledge the travel awards from Earth System Science Interdisciplinary Center (ESSIC), Jacob K. Goldhaber Travel Awards and International Student Support Award, which made it possible for me to travel to conferences.

Table of Contents

List of Tables

List of Figures

List of Abbreviations

APSE	Apollo Passive Seismic Experiments
BB	Broad Band
CMB	Core Mantle Boundary
HF	High Frequency
HP^3	Heat Flow and Physical Properties Package
InSight	Interior Exploration using Seismic Investigations, Geodesy and Heat Transport
IPGP	Université de Paris, Institut de physique du globe de Paris
IRIS	Incorporated Research Institutions for Seismology
ISAE	Institut Supérieur de l'Aéronautique et de l'Espace SUPAERO
LAB	Lithosphere Asthenosphere Boundary
LF	Low Frequency
LPO	Lattice Preferred Orientation
MLD	Mid-Lithospheric Discontinuity
MOLA	Mars Observer Laser Altimeter
MPS	Max-Planck-Institute for Solar System Research
MQS	Marsquake Service
MTZ	Mantle Transition Zone
NASA	National Aeronautics and Space Administration
NHNM	New High Noise Model
NLNM	New Low Noise Model
NSF	National Science Foundation
PDS	Planetary Data Service
PREM	Preliminary Reference Earth Model
RISE	Rotation and Interior Structure Experiment
RMS	Root Mean Square
SEIS	Seismic Experiment for Interior Structure
SNC	Shergottites, Nakhlites and Chassignites
SNR	Signal to Noise Ratio
SP	Short Period
SPO	Shape Preferred Orientation
UCLA	University of California, Los Angeles
UMD	University of Maryland
VBB	Very Broad Band
VHF	Very High Frequency
WTS	Wind and Thermal Shield
LVZ	Low Velocity Zone

Chapter 1: Introduction

1.1 Earth's Mantle Transition Zone

The Earth's mantle is a dynamic system actively interacting with Earth's surface and core through mantle convection (Morgan, 1971). The Earth's mantle can be subdivided into three distinct layers: (1) upper mantle, (2) mantle transition zone and (3) lower mantle (Birch, 1952; Ringwood, 1970). The mineralogy in these layers is determined by the temperature, pressure and composition of Earth's mantle (McDonough and Sun, 1995). The upper mantle is mainly composed of olivine (~60%), garnet and pyroxene (Figure 1.1a). The mantle transition zone (MTZ) is delineated by two seismic discontinuities at 410-km and 660-km depths, including a weaker discontinuity at 520-km depth (Figure 1.1b). The 410-km and 660-km discontinuities are manifested as sharp density and velocity jumps in Earth's 1-D seismic velocity and density models (e.g., Dziewonski and Anderson, 1981; Kennett et al., 1995). The formations of these discontinuities are associated with the pressure-induced phase transformations of upper mantle minerals: (1) olivine to wadsleyite at 410-km, (2) wadsleyite to ringwoodite at 520-km, and (3) the dissociation of ringwoodite to bridgmanite and ferropericlase at 660-km (Ringwood 1975; Ita and Stixrude, 1992). The lower mantle is dominantly composed of bridgmanite (~80%) and ferropericlase (Figure 1.1a).

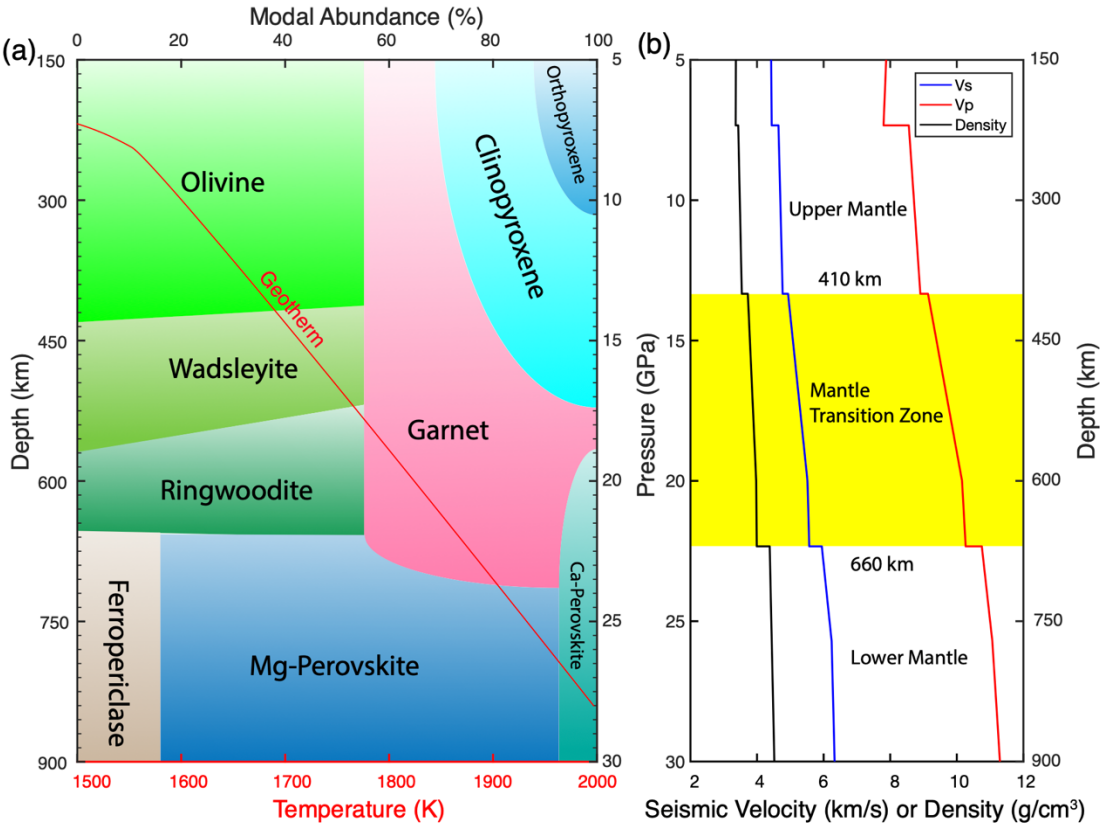

Figure 1.1 Phase diagram and seismic profiles of Earth's mantle between 150-900 km depth. (a) Phase diagram of mantle minerals. The red line denotes the temperature profile of mantle (geotherm). (b) Vertical profiles of Vp, Vs and density from the Preliminary Reference Earth Model (PREM, Dziewonski and Anderson, 1981). The mantle transition zone (MTZ) is highlighted in yellow color. The 410-km discontinuity is associated with olivine to wadsleyite phase transition; the 660-km discontinuity corresponds to the disproportion of ringwoodite to Mg-Perovskite and Ferropericlase. This figure is adapted from Bellini et al. (2013).

The depth of the MTZ discontinuities is controlled by the thermodynamic properties of the olivine phase transitions and local pressure (P), temperature (T), and composition of the mantle. In particular, the Clapeyron slope, or dP/dT slope of the coexistence curve between two phases, is the physical parameter that describes the relationship between the depth of a phase change and temperature. Mineral physics experiments with the olivine-wadsleyite phase transition measured the Clapeyron slope to be positive (+1.5 MPa/K in Akaogi et al., 1989; +2.9 MPa/K in Bina and Helffrich, 1994; +2.5 MPa/K in Katsura and Ito, 1989), whereas that of ringwoodite to

bridgmanite + ferropericlase is negative (-2.8 MPa/K in Ito and Takahashi, 1989; -1.9 MPa/K in Bina and Helffrich, 1994). The opposite signs of Clapeyron slopes indicates that the MTZ should be thinner in hotter mantle and become thicker in colder mantle. Although temperature plays a critical role, compositional heterogeneities, such as changes in water and magnesium content, also affect the depths of the olivine phase changes. For example, mantle hydration would lead to a shallower 410-km discontinuity (Smyth and Frost, 2002), and deeper 660-km discontinuity (Litasov et al., 2005), thereby thickening the MTZ. The enrichment of Mg content would stabilize the olivine to wadsleyite phase transition and increase the depth of 410-km discontinuity (Fei and Bertka, 1999). Thus, seismological constraints on topography of 410-km and 660-km discontinuities have been used to provide insights into the thermal and chemical heterogeneities of MTZ (Stixrude, 1997; Helffrich, 2000).

The topography of MTZ discontinuities is obtained through multiple seismological approaches: (1) triplicated waves (e.g., Grand & Helmberger, 1983); (2) SS and PP precursors (e.g., Flanagan & Shearer, 1998, 1999), (3) receiver functions (e.g., Lawrence & Shearer, 2006a), (4) ScS reverberations (e.g., Revenaugh & Jordan, 1991) , (5) P'P' precursors (e.g., Wu et al., 2019) and (6) topside reflections (e.g., Shearer & Buehler, 2019). Measurements of SS precursors, which are shear wave reflections occurring at the underside of MTZ discontinuities, revealed the first global topography map of 410-km and 660-km discontinuities (Chambers et al., 2005b; Deuss & Woodhouse, 2002; Flanagan & Shearer, 1998; Gu & Dziewonski, 2002; Houser et al., 2008; Huang et al., 2019; Lawrence & Shearer, 2008). Despite discrepancies in small-scale structures, the long wavelength structures generally agree well amongst the

different models: the cold circum-Pacific subduction zones are characterized by a thicker MTZ, whereas a thinner MTZ is observed near hot spots, especially in the Pacific Ocean (Deuss et al., 2009). The amplitudes of SS and PP precursors also provide constraints on the seismic impedance contrasts of MTZ discontinuities (Shearer et al., 1999; Rost & Weber, 2002). The sharpness of MTZ discontinuities was shown by Xu et al. (2008) to be predominantly controlled by mantle composition, and less affected by temperature. Therefore, measurements of impedance contrasts can shed light on the bulk composition of the mantle (e.g., pyrolite vs. piclogite model) and local compositional heterogeneities associated with subducting slabs or mantle plumes (Chambers et al., 2005a; Lawrence & Shearer, 2006b; Maguire et al, 2018; Yu et al., 2018).

The MTZ also plays a crucial role in global water circulation between Earth's surface and mantle. Subducting slabs have been argued to be potential pathways for transport of water on the surface into deep mantle (van Keken et al., 2011). Bercovici and Karato (2003) proposed that the MTZ could become a water reservoir in the mantle due to the large water solubility of wadsleyite and ringwoodite. In their model, water is trapped in the MTZ when ambient mantle materials ascend or descend through it (i.e., a water filter), producing dehydration melting either above 410-km (Song et al., 2014) or below 660-km discontinuities (Schmandt et al., 2014; Panero et al., 2020). However, constraints on water content in the MTZ remain controversial across different geophysical approaches. Pearson et al., (2014) discovered hydrous ringwoodite within inclusions of a diamond sample and inferred the water content to be ~1 wt.% in the MTZ. Magnetotelluric measurements of mantle electrical conductivity provide a direct

geophysical constraint on water content, but these studies either indicated a relatively hydrous MTZ with 0.1-0.2 wt.% water (Huang et al., 2005) or completely dry MTZ (Yoshino et al., 2008). Seismological observations with SS precursors have been interpreted to suggest a generally dry MTZ with << 1% water (Houser et al., 2016). Further observations of the effect of water on mantle fabric and slip systems, from electrical conductivity and seismology studies coupled with mineral physics experiments will provide a path forward to better interpret water content in the MTZ.

1.2 Seismic Anisotropy

Seismic velocity in a material is not always constant in all directions. Seismic anisotropy describes the dependence of seismic velocity on wave propagation or polarization direction. Seismic anisotropy is often linked to mantle deformation produced from two primary mechanisms: the lattice-preferred orientation (LPO) of intrinsically anisotropic minerals under a dislocation creep regime, or the shape-preferred orientation (SPO) of isotropic materials with distinct elastic properties (e.g., due to compositional layering or lenses of melt). Minerals that are intrinsically anisotropic can form LPO through the alignment of crystal lattices into a fabric via mantle flow and deformation (Figure 1.2). In the upper mantle, olivine is the most volumetrically abundant mineral with ~18% single-crystal Vs anisotropy (Mainprice et al., 2005; Webb 1989). Therefore, upper mantle anisotropy is often attributed to LPO of olivine caused by current mantle flow in the asthenosphere or paleo-flow directions frozen in the lithosphere. Wadsleyite can contribute to seismic anisotropy in the MTZ with ~14% Vs single-crystal anisotropy (Sawamoto et al., 1984; Sinogeikin et al., 1998; Zha et al., 1997), whereas ringwoodite is nearly isotropic because of the cubic mineral

structure (Kiefer et al., 1997; Li et al., 2006; Sinogeikin et al., 2003; Weidner et al., 1984). In the lower mantle, bridgmanite is the main candidate mineral to accommodate seismic anisotropy (e.g., Mainprice et al., 2008; Tsujino et al., 2016). The interpretation of seismic anisotropy in terms of mantle flow directions often requires interdisciplinary approaches including both mineral physics experiments (e.g., Karato et al., 2008) and geodynamic modeling (e.g., Faccenda, 2014).

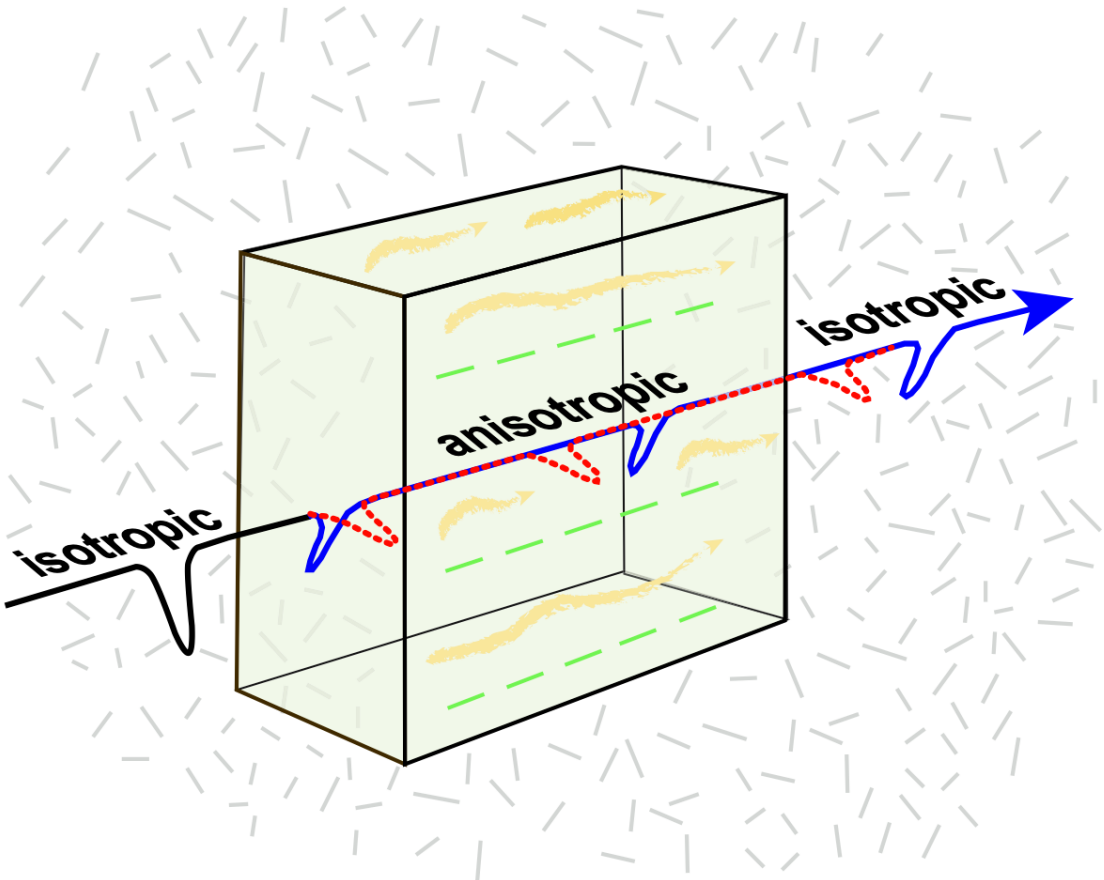

Figure 1.2 A schematic diagram illustrating shear wave splitting through anisotropic media. The minerals (green) in the box are aligned by mantle flow (yellow) to form lattice-preferred orientation (LPO) as opposed to random distributions of minerals (gray) outside the box. This figure is adapted from Edward Garnero's research website (http://garnero.asu.edu/research_images/images_anisotropy.html).

Seismic anisotropy is classified into two types: (1) radial anisotropy and (2) azimuthal anisotropy. Radial anisotropy is defined as the ratio of seismic velocities

between horizontally polarized shear wave (V_{SH}) and vertically polarized shear wave (V_{SV}). Radial anisotropy is often constrained from the discrepancies between the two types of surface waves, Rayleigh waves and Love waves, which are more sensitive to V_{SV} and V_{SH} respectively (e.g., Dziewonski and Anderson, 1981). Azimuthal anisotropy is defined as the dependence of seismic velocities (V_P or V_S) as a function of propagation directions on the horizontal plane. Azimuthal anisotropy can be deduced from variations of surface waves propagating at different source/receiver azimuths (e.g., Mongtagner and Nataf, 1986).

Seismological constrains on mantle anisotropy can provide insights into mantle dynamics associated with mantle plumes or subduction zones (e.g., Long 2013). The observations of seismic anisotropy are mainly obtained from three approaches: (1) shear wave splitting (e.g., Silver and Chan, 1988), (2) surface wave measurements (e.g., Anderson, 1962) and (3) normal mode splitting (e.g., Beghein and Trampert, 2003). Shear waves can split into two orthogonally polarized waves, parallel or perpendicular to the fast direction, when traveling through anisotropic media (Silver, 1996; Figure 1.2). Shear wave splitting is independent from lateral mantle heterogeneities and yields a high lateral resolution (~50 km), therefore this method has been widely applied to constrain mantle anisotropy (Long and Becker, 2010). However, the shear wave splitting method lacks vertical resolution because the measurements of splitting time and fast direction are results of integration of anisotropic effects along the raypath. Conversely, surface waves are sensitive to multiple depths of anisotropy through dispersion of waves in different frequencies but lack lateral resolution. The fundamental modes of surface waves are mainly sensitive to upper mantle anisotropy,

whereas the higher mode surface waves (overtones) have sensitivities as deep as the MTZ and uppermost lower mantle (e.g., Yuan and Beghein, 2013). However, the horizontal resolution of surface wave is poor (~6500 km in the MTZ from Visser et al, 2008, Yuan and Beghein, 2018) since this method averages raypath across a large range of distance.

Alternatively, a body wave approach using the SS precursors has been recently developed to constrain upper mantle and MTZ anisotropy (Huang et al., 2019; Rychert et al., 2012, 2014; Saki et al., 2018). This method is a complementary tool to investigate mantle anisotropy where data are underpopulated, or sensitivities are limited for shear wave splitting and surface wave analysis. Chapters 2 of my dissertation focuses on quantifying the observed azimuthal anisotropy with the SS precursors, both beneath subduction zones and hotspots, as well as globally. Chapter 3 studies the sensitivity of the SS precursors to MTZ azimuthal anisotropy and quantified the detectability and resolution of this seismic phase for constraining mantle anisotropy.

1.3 Interior Structure of Mars

Earth is one of several rocky interior planets of the solar system, including Mercury, Venus, and Mars. Like Earth, Mars was formed through accretion of planetesimals, into a rocky planet, and that further differentiated into three distinct layers: crust, mantle and core. However, there are key differences between the two planets. The martian planetary radius is about half of Earth's and it has a mass about $1/10^{th}$ of that of the Earth; therefore, the interior pressure at the base of the martian mantle (1500-1800 km depth; 20-23 GPa) is about equivalent to Earth's MTZ (520-660 km). However, until InSight landed in November of 2018, we did not have seismic

constraints on the martian interior. InSight and other future planetary missions to Mars will be essential for providing robust constraints on the physical and chemical states of Mars's interior. In Chapter 4 of my dissertation, I study seismic waves recorded by the seismometers on the NASA InSight mission to detect the MTZ in Mars.

The composition and interior structure of Mars is the key to understanding the formation and evolution of terrestrial planets, and the solar system. The bulk composition model of Mars is mainly derived from geochemical analysis of martian meteorites or geophysical observations from remote sensing and in-situ measurements (see review by Taylor, 2013). The geochemical approaches are based on the chemical composition of SNC (Shergottites, Nakhlites and Chassignites) meteorites that are pieces of the martian crust ejected by impacts onto the surface of Mars, and subsequently traveled to Earth and landed as meteorites. Derivations of martian composition from the SNC meteorites are divided into two approaches. The first uses a comochemical approach that assumes that the relative abundances of refractory elements are similar to that of CI chondrites (Dreibus and Wänke, 1985; Morgan and Anders, 1979; Taylor, 2013) and derives other components from martian meteorites. The second uses an approach that focuses on the analysis of oxygen isotopes of martian meteorites and chondrites (Burbine & O'Brien, 2004; Lodders and Fegley, 1997; Mohapatra & Murty, 2003; Sanloup et al, 1999; Warren, 2011). The model developed by Dreibus and Wänke (1985) has been considered as the standard bulk composition model of Mars. These composition models consistently reveal that the martian mantle is more enriched in Fe content than Earth's mantle. Geophysical predictions for the martian interior depend on the geochemical models and obtain new models through

numerical modeling (Longhi et al., 1992; Sohl & Spohn, 1997; Zharkov & Gudkova, 2005), mineral physics experiments (Bertka and Fei, 1997, 1998) or inversions of geophysical measurements such as moment of inertia or tidal love number (Khan & Connolly, 2008; Khan et al., 2018).

In addition to the geochemical constraints, orbital missions to Mars reveal structure about the crust and lithosphere. The Mars Observer Laser Altimeter (MOLA) provided accurate measurements on global topography of Mars (Zuber et al., 1992). Mars's surface topography is characterized by hemispheric dichotomy: northern lowland and southern highland (Smith et al., 1999). The elevation differences between lowland and highland can reach up to 5 km. The northern lowland appears younger and smoother with fewer craters, whereas the southern highland is older and heavily cratered, and characterized with large volcano systems (Tharsis region) and ancient impact craters (e.g., Hellas Planitia). The topography and gravity field of Mars measured from spacecraft (e.g., Genova et al., 2016) provide useful insights to the density and thickness of martian crust (e.g., Goossens et al., 2017; Neumann et al., 2004; Wieczorek and Zuber, 2004). The global crustal model suggests that the mean crustal thickness is 32 km and 58 km beneath the northern lowland and southern highland respectively (Neumann et al., 2004), although crustal thickness estimates are non-unique and assume a crustal density.

Current knowledge about the physical state and radius of martian core is based on the geophysical measurements of moment of inertia (e.g., Reasenberg, 1977) and solar tides (e.g., Van Hoolst et al., 2003) on Mars. The measurements of tidal k_2 Love numbers (Yoder et al., 2003) and high-pressure mineral physics experiments (Fei and

Bertka, 2005) revealed that at least the outer part of martian core is liquid. The tidal k_2 Love number is also sensitive to the core size. The most recent measurement of 0.01697 ± 0.0027 (Genova et al., 2016; Konopliv et al., 2016) indicates that the core radius is ~1,730-1,840 km (Khan et al., 2018). Seismological observations of core phases (e.g., ScS) on Mars can further reduce the uncertainties of martian core size and provide insights into core formation and evolution processes (e.g., Marusiak et al., 2020).

The geodetic and geochemical constraints on the martian interior allow for the construction of predictive models of the interior. Assuming a certain temperature profile (e.g., Plesa et al., 2016), Mars's mantle mineralogy and seismic profiles are deduced from the bulk composition models using an equation of state (e.g., Rivoldini et al., 2011). Here, we used a recent composition model by Yoshizaki and McDonough (2020), which is based on martian meteorites but avoids the assumption of CI chondrites as an analog to Mars, to illustrate the mantle structure of Mars (Figure 1.3). Similar to Earth, the upper mantle of Mars is dominated by olivine (~50%), pyroxene and garnet (Figure 1.3a). However, orthopyroxene (Opx) is more enriched in martian mantle (~20%) and transitions into high-pressure clinopyroxene (C2/C) at ~10 GPa, resulting in a seismic discontinuity at ~800 km (Figure 1.3b). The MTZ of Mars is also characterized by the phase transformations of olivine: olivine to wadsleyite at ~12 GPa, and wadsleyite to ringwoodite at ~15 GPa. Due to the smaller size of Mars, the olivine to wadsleyite phase transition produces a seismic discontinuity at ~1100-km (Figure 1.3b), much deeper than the 410-km discontinuity on Earth. The presence of a bridgmanite-ferropericlase layer in Mars is dependent on the core size and mantle

temperature since these two minerals are not stable under a low pressure and temperature regime (Bertka and Fei, 1997). The models with small core size and hot temperature favor the existence of a thin bridgmanite-ferropericlase basal layer, although most models predict the absence of this layer in Mars (Khan et al., 2018), consistent with the Yoshizaki and McDonough (2020) model.

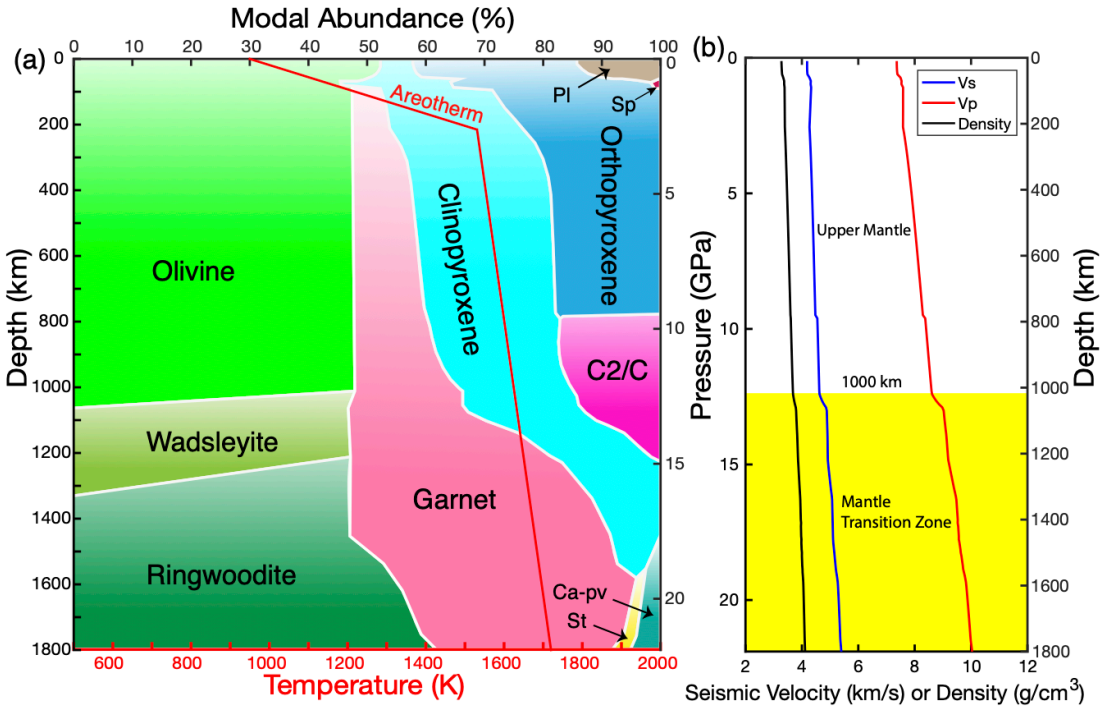

Figure 1.3 The composition and physical properties of martian mantle. (a) Phase diagram and temperature profile of martian mantle. The red line highlights the temperature profile (areotherm). Mineral abbreviations are: C2/C- high-pressure clinopyroxene; Pl-plagioclase; Sp-spinel; Ca-pv- Ca-perovskite; St-stishovite; (b) Vertical profiles of seismic velocity (Vp and Vs) and density as a function of depth. The martian MTZ is highlighted in yellow color. This figure is adapted from Yoshizaki and McDonough (2020).

1.4 Planetary Seismology

Planetary seismology extends the study of seismic waves to other planets beyond Earth by deploying seismometers directly on their surfaces (Lognonné and Mosser, 1993). Over the past half century of planetary exploration, seismic data have been acquired on the Moon and Mars, and have provided invaluable insights into the

internal structure, formation and evolution of terrestrial planets. The first extraterrestrial seismometer was deployed on the Moon during Apollo 11 mission as part of the Apollo Passive Seismic Experiments (APSE) package, but the instrument only operated for 21 days (Latham et al., 1969, 1970). The subsequent Apollo missions (Apollo 12, 14, 15 and 16) deployed a network of four seismic stations on the nearside of Moon. The Apollo seismic network operated for nearly 8 years between 1969-1977 and detected ~12,500 seismic events on the Moon (Nakamura et al., 1982). These seismic events were categorized as (1) meteoroid impacts, (2) artificial impacts, (3) shallow moonquakes and (4) deep moonquakes.

Unlike the Earth, the Apollo seismic data exhibit strong scattering with long duration codas (~1 hour); the codas are associated with scattering in the impact-fractured bedrock, ejecta blankets, and surface regolith (Lognonné, 2005). Lunar seismic data provided initial constraints on the lunar interior structure and seismicity rate (Lammlein et al., 1974; Nakamura, 1983; Toksöz 1974). Nearly 30 years later, detailed seismic velocity profiles of the lunar crust and mantle were obtained from inversions of P and S wave travel-times (Gagnepain-Beyneix et al., 2006; Lognonné, 2003; Nakamura, 2005; Khan et al., 2000, 2004) and receiver functions (Vinnik et al., 2001). New analyses of the Apollo data detected the lunar core using core reflected waves, revealing a liquid outer core and solid inner core possibly overlain by a partial melt layer (Garcia et al., 2011; Weber et al., 2011). New efforts are underway to deploy a new seismic network on the Moon, called the Lunar Geophysical Network, that would establish a global and permanent network of seismic stations on the near and farside of the Moon, building upon the success of the Apollo missions (Neal et al., 2019).

Following the Apollo Missions, seismometers were sent to Mars with the Viking-1 and Viking-2 landers. The seismometer on Viking-1 lander failed to uncage and collected no data, and the Viking-2 seismometer successfully collected 89 days of data starting from September 1976 (Anderson et al., 1976, 1977; Lazarewicz et al., 1981). The Viking-2 seismometer did not definitively detect any seismic events due to the strong wind noise on deck and limited sensitivity of the seismometer (Anderson et al., 1977). A possible seismic event was detected on Sol 80, but the wind contamination of the signal could not be ruled out (Anderson et al, 1977). Although the Viking seismometers did not reveal the internal structure of Mars, they provided an estimate for the martian seismic noise background, and were essential for the development of requirements for any follow-on seismic missions; namely that the instrument be placed on the ground and shielded from the martian atmosphere. On 26 November 2018, NASA's InSight (Interior Exploration using Seismic Investigations, Geodesy and Heat Transport) Mission landed in Elysium Planitia on Mars (Banerdt et al., 2020). The primary scientific objectives of the InSight mission are to determine the structures, compositions and thermal states of martian crust, mantle and core, and measure the seismicity and impact rates on Mars (Daubar et al., 2018; Lognonné et al., 2019; Panning et al., 2016; Smrekar et al., 2019).

The InSight lander consists of three primary payloads (Figure 1.4): (1) Seismic Experiment for Interior Structure (SEIS; Lognonné et al., 2019), (2) Heat Flow and Physical Properties Package (HP^3; Folkner et al., 2018) and (3) Rotation and Interior Structure Experiment (RISE; Spohn et al., 2018). Unlike the Viking seismometers, SEIS is directly deployed on the surface of Mars by the robotic arm and covered by the

wind and thermal shield (WTS) to reduce noise. SEIS includes two seismic sensors: Very Broad Band (VBB) and Short Period (SP) seismometers, which cover the 0.01-5 Hz and 0.1-50 Hz frequency bands respectively. After nearly two Earth years of operation at Mars (1 martian year), SEIS has detected > 1,000 seismic events, establishing that Mars is seismically active. Among these events, S0235b and S0173a are the two largest events (~Mw 3.5) and are both located near a potentially active fault system 1500-2000 km to the east of the landing site, Cerberus Fossae (Giardini et al., 2020). The seismic events shed light on the shallow elastic structures beneath InSight landing site as well as scattering and attenuation characteristics of Mars (Lognonné et al., 2020). The initial results have also revealed that the seismic activity rate is similar to terrestrial intraplate seismicity rate but higher than that of the Moon (Banerdt et al., 2020). Although a new impact crater was discovered near InSight lander from Mars Reconnaissance Obiter, no seismic event was definitively identified to originate from this impact event (Daubar et al., 2020). InSight will continue to record seismic events on Mars and bring more exciting science about martian interior structures. Chapter 4 of my dissertation uses InSight data to study marsquakes and detect the internal structure of the martian upper mantle and transition zone.

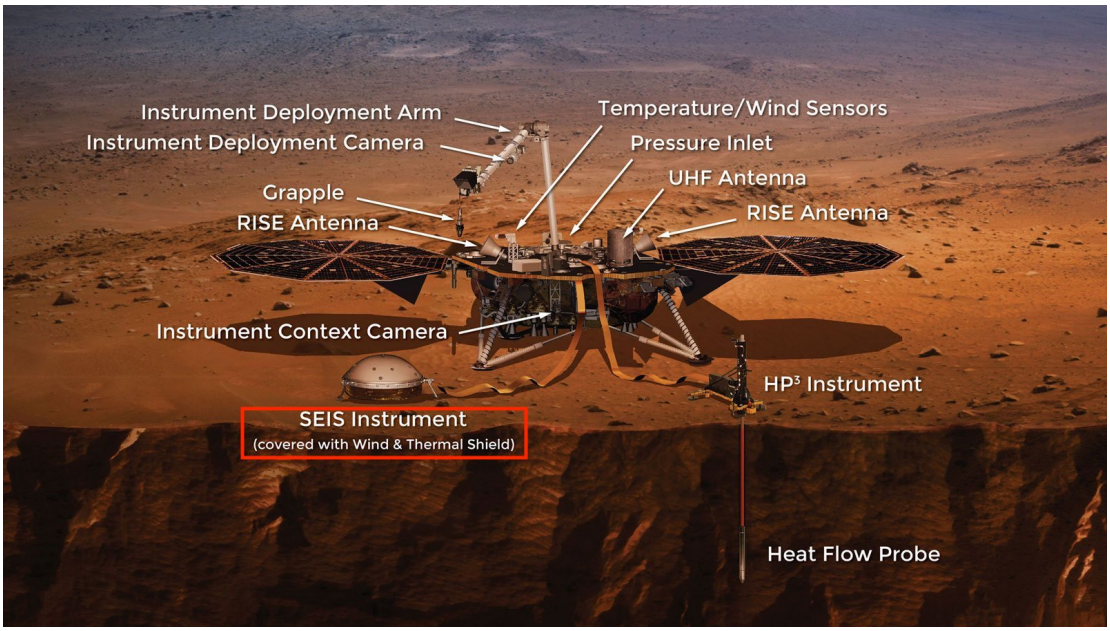

Figure 1.4 A conceptual diagram illustrating InSight lander on Mars. Three primary payloads are included on InSight lander: Seismic Experiment for Interior Structure (SEIS), Heat Flow and Physical Properties Package (HP^3) and Rotation and Interior Structure Experiment (RISE). SEIS is the first seismometer deployed on the surface of Mars (highlighted in red box). Image credit: NASA JPL (http://mars.nasa.gov/insight).

1.5 Project Overview

My dissertation aims to constrain the structures of Earth's MTZ and martian deep interior with seismic body waves. In Chapter 2, Huang et al., (2019), I developed a novel approach that used the SS precursors to investigate the topography and seismic anisotropy structures of Earth's MTZ. My observations indicated that seismic anisotropy is weak in the MTZ globally (<1%) but can be locally enhanced by mantle flow near subduction zones. In Chapter 3, (Huang et al., submitted to JGR-Solid Earth) I quantified the sensitivity of SS precursors to seismic anisotropy with 3-D synthetic waveforms. My modeling results demonstrated that SS precursors are capable of distinguishing multiple depths of anisotropy as well as detecting weak anisotropy in the MTZ, thus my method can complement other approaches such as shear wave

splitting and surface wave measurements. In Chapter 4, I first investigated the detectability of martian MTZ with three candidate body waves and identified triplicated waves as the most suitable approach. Then, I applied a polarization filter and vespagram analysis to detect body waves from InSight data. I found evidence for multiple reflected waves (e.g., PP and SS) in the upper mantle and triplicated waves from martian MTZ. The preliminary inversions shed light on the crust and upper mantle structures as well as the depth of olivine-to-wadsleyite phase transition on Mars. Chapter 5 summarizes all the observations and modeling results and discusses my future research directions to decipher interior structures of Earth and Mars.

Chapter 2: Constraints on Seismic Anisotropy in the Mantle Transition Zone From Long-Period SS Precursors

Huang, Q., Schmerr, N., Waszek, L., & Beghein, C. (2019). Constraints on Seismic Anisotropy in the Mantle Transition Zone From Long-Period SS Precursors. *Journal of Geophysical Research: Solid Earth*, *124*(7), 6779–6800. http://doi.org/10.1029/2019JB017307

Abstract

The mantle transition zone (MTZ) of Earth is demarcated by solid-to-solid phase changes of the mineral olivine that produce seismic discontinuities at 410 and 660 km depths. Mineral physics experiments predict that wadsleyite can have strong single-crystal anisotropy at the pressure and temperature conditions of the MTZ. Thus, significant seismic anisotropy is possible in the upper MTZ where lattice preferred orientation (LPO) of wadsleyite is produced by mantle flow. Here, we use a body wave method, SS precursors, to study the topography change and seismic anisotropy near the MTZ discontinuities. We stack the data to explore the azimuthal dependence of travel times and amplitudes of SS precursors, and constrain the azimuthal anisotropy in the MTZ. Beneath the central Pacific, we find evidence for ~4% anisotropy with a SE fast direction in the upper mantle, and no significant anisotropy in the MTZ. In subduction zones, we observe ~4% anisotropy with a trench-parallel fast direction in the upper mantle, and ~3% anisotropy with a trench-perpendicular fast direction in the MTZ. The transition of fast directions indicates that the LPO of wadsleyite induced by MTZ flow is organized separately from the flow in the upper mantle. Global azimuthal stacking reveals ~1% azimuthal anisotropy in the upper mantle, but negligible anisotropy (< 1%) in the MTZ. Finally, we correct for the upper mantle and MTZ anisotropy structures to

obtain a new MTZ topography model. The anisotropy correction produces ± 3 km difference, and therefore has minor overall effects on global MTZ topography.

2.1 Introduction

The mantle transition zone (MTZ) is bounded by the 410 and 660 km discontinuities and plays an important role in mantle convection and global water circulation between upper and lower mantle (e.g., Bercovici and Karato, 2003). These major MTZ discontinuities are characterized by sharp seismic velocity and density jumps as a primary 1-D feature of the Earth (e.g., Dziewonski and Anderson, 1981). The boundaries are attributed to the pressure-induced phase changes of olivine with increasing pressure and temperature: olivine to wadsleyite at 410 km, wadsleyite to ringwoodite at 520 km, and ringwoodite to ferropericlase + bridgmanite at 660 km (Ringwood, 1975; Ita and Stixrude, 1992). The phase changes at 410 and 660 km have opposite Clapeyron slopes (Katsura and Ito, 1989; Ito and Takahashi, 1989); this results in a thinner MTZ in hot regions, and thicker MTZ in cold regions, assuming pressure and temperature effects are dominant. The topography of MTZ discontinuities has previously been used successfully as a mantle thermometer to study thermal heterogeneities and map flow patterns (Bina and Helffrich, 1994; Stixrude, 1997; Gu et al., 1998; Helffrich, 2000).

Over the last two decades, the topography of MTZ discontinuities has been systematically mapped using various seismic methods, including SS and PP precursors (e.g., Flanagan and Shearer, 1998, 1999), ScS reverberations (e.g., Revenaugh and Jordan, 1991) and receiver functions (e.g., Lawrence and Shearer, 2006a). SS precursors are the underside reflections of shear waves at the 410 and 660 km

discontinuities (Figure 2.1). Measurements of SS precursors provided the first global-scale topography maps of the 410 and 660 km discontinuities (Shearer, 1991, 1993; Flanagan and Shearer, 1998; Deuss and Woodhouse, 2002; Gu and Dziewonski, 2002; Chambers et al., 2005b; Lawrence and Shearer, 2008; Houser et al., 2008). Regional-scale SS precursor studies were performed for areas of high data density, including the Pacific Ocean (Schmerr et al., 2006, 2010; Thomas and Billen, 2009; Cao et al., 2011; Yu et al., 2017), South America (Schmerr and Garnero, 2007), as well as central and eastern Asia (Heit et al., 2010; Lessing et al., 2014). Despite the discrepancies between topography models, deep 410 and shallow 660 km discontinuities (thin MTZ) are generally observed beneath hot mantle plume regions. Conversely, shallow 410 and deep 660 km discontinuities (thick MTZ) are typically detected beneath cold subduction zones. This is consistent with the mineralogical properties of the phase changes. However, seismic anisotropy in the upper mantle and transition zone has not been previously taken into account when mapping the 410 and 660 depths, which may cause significant biases for MTZ topography measurements in a region with limited azimuthal coverage.

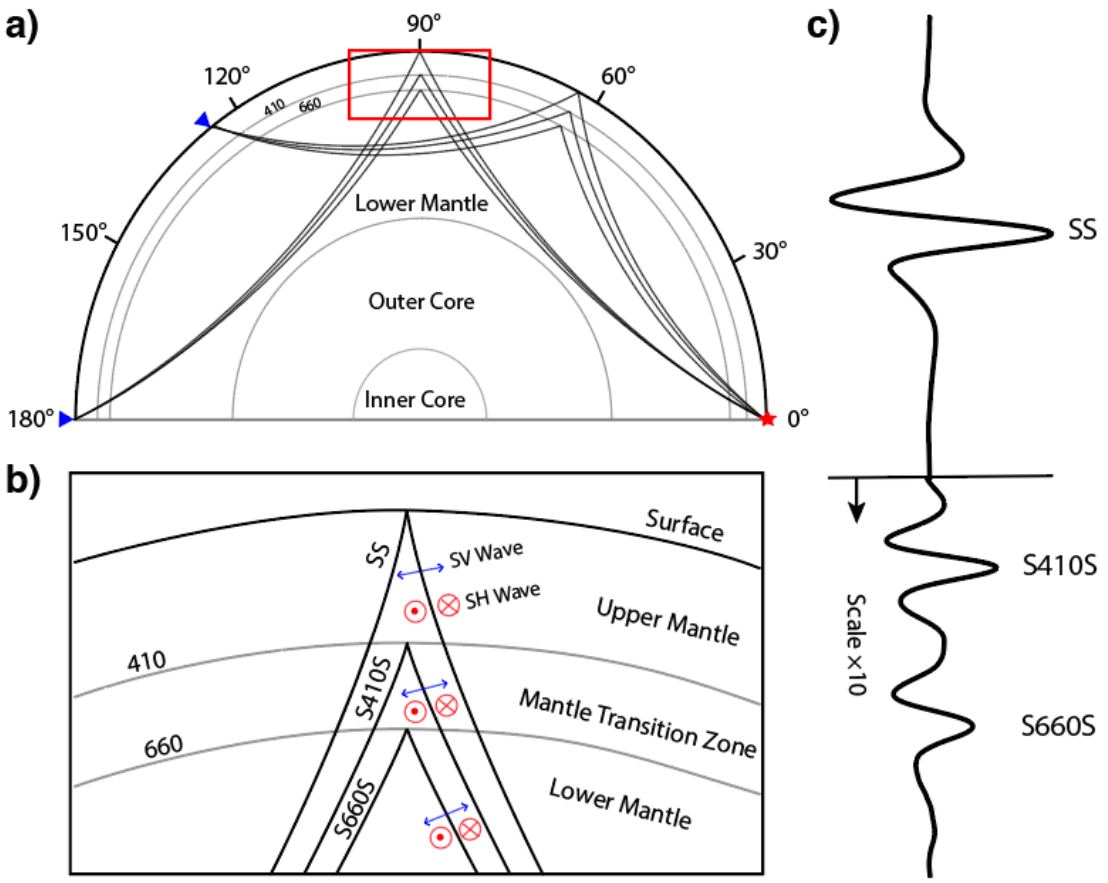

Figure 2.1 Example ray paths and seismograms of the SS precursors. a) The ray paths of SS precursors at the epicentral distances of 125° and 180°. The red star represents the source and blue triangles denote the stations. The reflections at the 410 and 660 km discontinuities are highlighted by the red box. b) Expanded view of SS precursor ray paths beneath the bounce point region. The SS precursors reflected off 410 and 660 km discontinuities are named as S410S and S660S respectively. The polarizations of SH and SV waves are plotted as red and blue arrows respectively. This study focuses on using the SH waves to detect azimuthal anisotropy. c) An example stacked seismogram of SS phase and the precursors.

Seismic anisotropy describes the dependence of seismic velocity on the propagation or polarization directions of seismic waves. It is produced by two primary deformation mechanisms within the Earth: the lattice preferred orientation (LPO) of anisotropic minerals, or the shape preferred orientations (SPO) of distinct isotropic materials. In the upper mantle, the LPO of olivine explains most observations of seismic anisotropy as olivine is the most volumetrically abundant mineral with ~18% of single crystal shear wave anisotropy (Webb, 1989; Mainprice et al., 2005, 2007). In

the transition zone, the orthorhombic wadsleyite has up to 14% single crystal shear wave anisotropy (Sawamoto et al., 1984; Zha et al., 1997; Sinogeikin et al., 1998). Ringwoodite, present in the deeper MTZ, has a cubic structure and is nearly isotropic with only ~2% shear wave anisotropy (Weidner et al., 1984; Kiefer et al., 1997; Sinogeikin et al., 2003; Li et al., 2006). The abundant majorite garnet is also nearly isotropic in the transition zone (Bass and Kanzaki, 1990; Pamato et al., 2016). Clinopyroxene would not produce significant seismic anisotropy due to its low volume fraction in the MTZ (Sang and Bass, 2014). As a result, wadsleyite is the main candidate to generate seismic anisotropy in the upper part of the MTZ. Thus, we hypothesize that the LPO of wadsleyite caused by the deformation from mantle flow (e.g., upwelling plume or subducting slab) will produce seismic anisotropy in the MTZ. It should be noted that magnesite, with ~40% shear wave anisotropy, in the regionally carbonated mantle (e.g., subducted slabs) might be a candidate as well (Yang et al., 2014).

Seismic evidence of upper mantle anisotropy (< 220 km) is widely reported in global tomography models (e.g., Beghein and Trampert, 2004; Lekić and Romanowicz, 2011; Moulik and Ekstrom, 2014; French and Romanowicz, 2014; Chang et al., 2015). However, observations of MTZ anisotropy are challenging due to the lower resolution and decrease in the strength of anisotropy at greater depths. Despite these difficulties, evidence for MTZ azimuthal anisotropy is provided by shear wave splitting measurements (Tong et al., 1994; Fouch and Fisher, 1996; Wookey et al., 2002; Chen and Brudzinski, 2003; Foley and Long, 2011), normal modes (Beghein et al., 2008), surface wave tomography (Trampert and van Heijst, 2002; Yuan and Beghein, 2013,

2014, 2018; Debayle et al., 2016), inversion of surface and S waveforms (Schaeffer et al., 2016), and the inversion of deep earthquake moment tensors (Li et al., 2018). For example, Trampert and van Heijst (2002) showed that Love wave overtones are compatible with the presence of azimuthal anisotropy in the MTZ. Wookey et al. (2002) found evidence for seismic anisotropy near the 660 km discontinuity beneath the Tonga-Kermadec subducting slabs using shear wave splitting, and this is interpreted as the mineral alignment by mid-mantle flow. Recently, Li et al. (2018) used the moment tensor of deep, non-double couple earthquakes to invert for in-situ seismic anisotropy assuming shear-dislocation faulting mechanism, and found 25% anisotropy in the MTZ, which was explained with the presence of magnesite or carbonate melt.

In Figure 2.2, we compare the root mean squares (RMS) of azimuthal anisotropy amplitudes from three recent surface wave tomography models which use higher modes of surface wave, and thus are sensitive to the azimuthal anisotropy in the MTZ. In all three models, the strongest azimuthal anisotropy (~2%) exists in the upper mantle above 220 km. The YB13SVani (Yuan and Beghein, 2013) and 3D2017_09Sv (Debayle et al., 2016) models found ~1.0% and ~0.8% azimuthal anisotropy in the whole transition zone respectively. However, the cross-model correlation of different surface wave tomography models in the MTZ is extremely low compared to their relatively good agreement in the upper mantle (Schaeffer et al., 2016). The coherence between surface wave tomography models and global SKS splitting measurements (Becker et al., 2012) is even lower in the MTZ. This implies that azimuthal anisotropy in the MTZ is not well constrained from either the surface wave or shear wave splitting methods.

In this study, we use a body wave method, SS precursors (SH wave), to constrain azimuthal anisotropy in the MTZ, via examining the azimuthal dependence of their travel times and amplitudes. The SS precursor method has excellent data coverage in oceanic regions, and a higher vertical resolution in the MTZ compared to shear wave splitting methods. This method has been previously applied to lithosphere-asthenosphere boundary (Rychert et al., 2012, 2014). Our study of MTZ anisotropy also provides corrections which contribute to a more precise MTZ topography model. These improved constraints on the MTZ anisotropy and topography structures illuminate the nature and style of mantle convection.

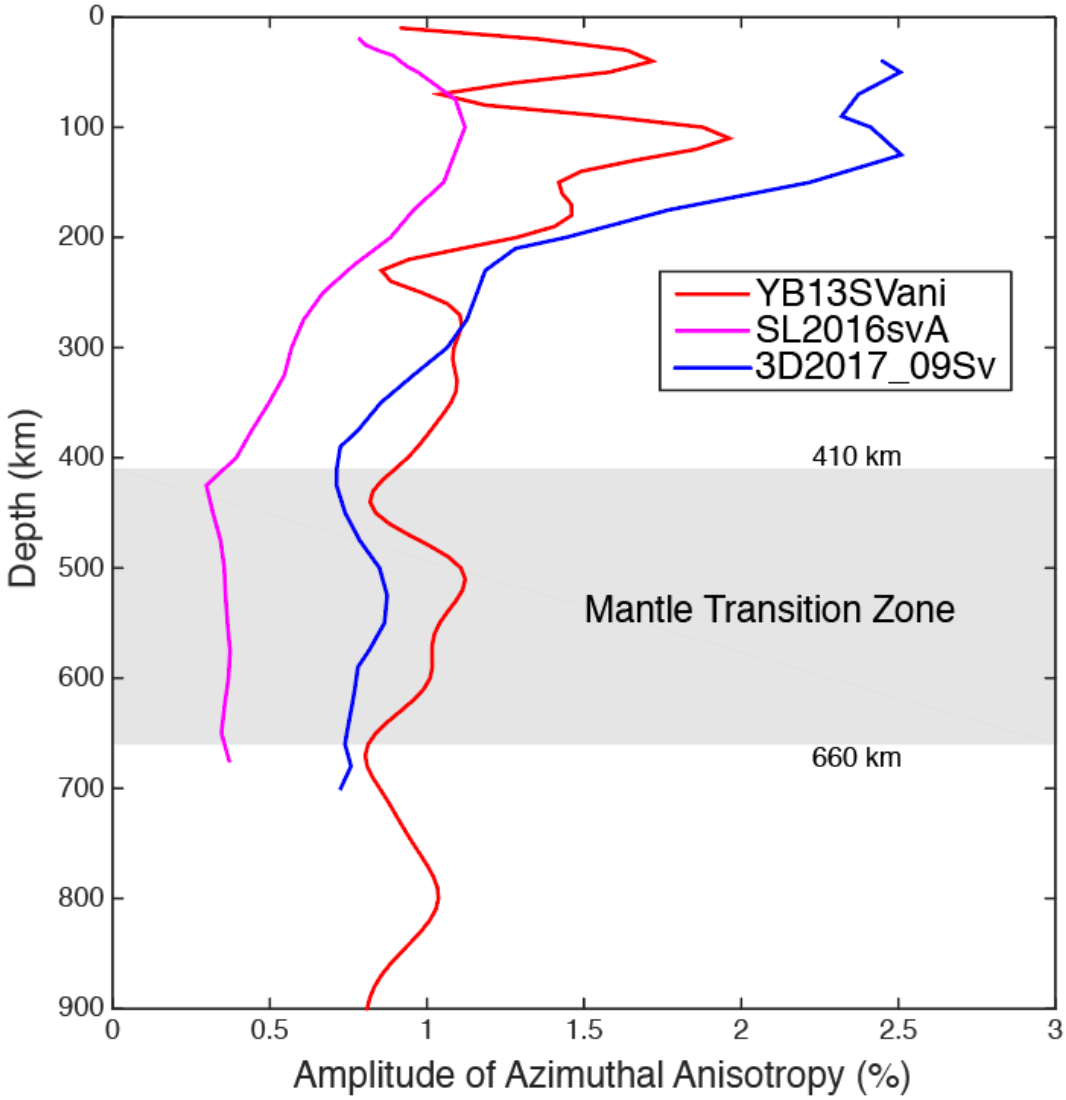

Figure 2.2 Root mean squares (RMS) of azimuthal anisotropy amplitudes from three surface wave anisotropy models: YB13SVani (Yuan and Beghein, 2013), SL2016svA (Schaeffer et al., 2016) and 3D2017_09Sv (Debayle et al., 2016) are plotted as a function of depth. The depth range of the MTZ (410 – 660 km) is highlighted in the gray box.

2.2 Methods

2.2.1 Data Set

Our study benefits from a global SS data set consisting of 45,624 seismograms (Waszek et al., 2018). The data set incorporates a global catalog of large earthquakes (6 <= Mw <=7) from 1988 and 2016, to ensure significant SS signals above the

background noise. The event depth criteria are shallower than 30 km to avoid interference with depth phases, with event-receiver epicentral distances between 100 and 180 degrees. The data are filtered using a Butterworth band-pass filter between 15 and 50 s to remove seismic noise, and records with signal to noise ratio (SNR) lower than 2.5 are discarded. Here, we use the transverse components (BHT) to study the SH waves for topography and azimuthal anisotropy in the MTZ. Predicted travel times from PREM (Dziewonski and Anderson, 1981) provide a time window to visually select the SS phase, which is handpicked. The polarities of SS phases are reversed to positive where necessary, and the seismograms are aligned to the peak maxima, then normalized.

The SS precursors are sensitive to the structure beneath the bounce points (Figure 2.1), and provide dense sampling coverage in oceanic regions such as the northwestern and central Pacific (Figure 2.3). Our goal is to map the azimuthal variations of SS precursor travel times and amplitudes as a function of bounce point azimuths. Thus, in addition to the number of records, we employ the azimuthal coverage criteria for selecting study regions to investigate azimuthal anisotropy in the MTZ. However, regions with high bounce point density tend to have uniform azimuthal distribution (e.g., South America and Indian Ocean) because most data are produced from similar event-receiver configurations. A global search for regions with both dense bounce points and sufficient azimuthal coverage identifies four suitable target locations to study azimuthal anisotropy: 1) the northwestern Pacific; 2) the central Pacific; 3) the central Atlantic and 4) Greenland (Figure 2.3).

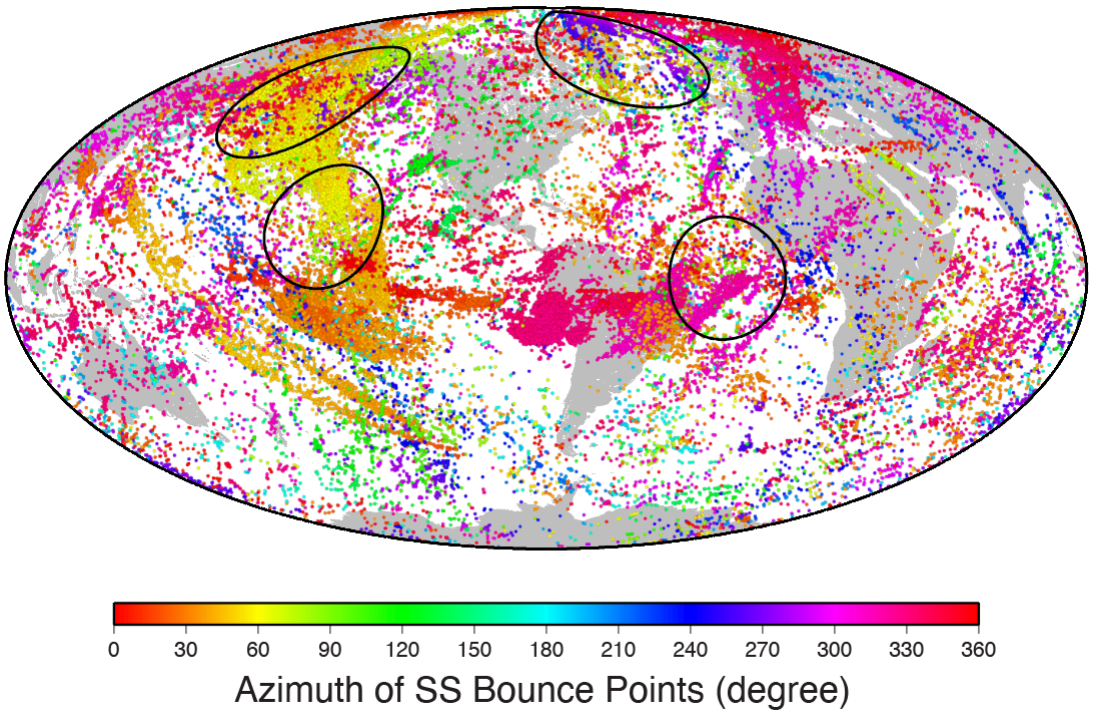

Figure 2.3 A map of SS bounce points in the SS data set. The colors represent the azimuths of SS bounce points which point from the sources to receivers. The black circles highlight the four regions with ample bounce points and azimuthal coverage.

2.2.2 Stacking Methods

The amplitudes of SS precursors are only ~5% of SS phase, which require stacking to suppress noise and improve the SNR. We follow the stacking method by Schmerr and Garnero (2006) to stack SS precursors along the predicted slowness curves, using 125° as the reference distance. We align the data to the predicted travel times of SS precursors at the reference distance from PREM in order for coherent stacking. We use distance exclusion windows to avoid the interference of other seismic arrivals that have similar amplitudes with SS precursors and could contaminate our results. These phases with similar amplitudes include topside reflections (e.g., s660sS) and ScS reverberations (e.g., ScS660ScS). The exclusion windows for S410S are 0-100° and 135-145°; S660S windows are 0-115° and 165-180° (Schmerr and Garnero,

2006). The travel times of SS precursors are then converted to depths using PREM. A bootstrap technique with 300 random resamples provides the 95% confidence level (2σ) of travel times and amplitudes of the stacking results (e.g., Efron and Tibshirani,1986).

We use different bin geometries to stack the data set: geographical bins and azimuthal bins. For the geographical bins, we place equally spaced 1000 km radius bins that are overlapping every 500 km to map the topography of 410 and 660 km discontinuities. For the azimuthal stacks, we place 2000 km radius geographical bins in the four target locations (Figure 2.3). We then further break down the records within the geographical bins to generate 30° azimuthal bins of the bounce point azimuths. The SS precursors traveling along one azimuth (e.g., α) are sensitive to the same velocity structure as those traveling in the opposite direction ($\alpha + \pi$). Consequently, we combine the two azimuthal bins with a π shift to improve the azimuthal sampling. This method provides regional estimates of MTZ anisotropy. A second technique for azimuthal stacking is used for data from subduction zones around the Pacific Ocean. Due to limited azimuthal coverage in each subduction zone, we combine all the subduction zones into one data set, and define a relative azimuth (Figure 2.7b). We then stack the subduction zone data according to the relative azimuths to explore MTZ anisotropy in the vicinity of subduction zones. Finally, we calculate the relative azimuths between bounce point azimuths and fast directions from global surface wave tomography models (e.g., Yuan and Beghein, 2013; Schaeffer et al., 2016; Debayle et al., 2016) for the entire data set. We stack the data into 15° bins of relative azimuths to study global azimuthal anisotropy patterns in the upper mantle and MTZ.

2.2.3 Crust and Tomography Corrections

The crustal thickness, surface topography, and upper mantle heterogeneities all affect the travel times of SS and its precursors, biasing the measurements of MTZ topography and anisotropy. Thus, we apply pre-stacking crust and tomography corrections for each record, to remove the effects from isotropic crustal and upper mantle structures. For the crust, we use CRUST 2.0 model (Bassin et al., 2000) to calculate travel time residuals beneath each bounce point with respect to PREM. Then, we use S40RTS tomography model (Ritsema et al., 2011) to correct for the lateral heterogeneities in the upper mantle. Using 1D ray tracing, we compute the travel time residuals for the SS phase and precursors (SdS) with respect to PREM. The SS – SdS differential travel time residuals are used as the tomography corrections. The 1D ray tracing approach does not account for the 3D effects of ray paths such as the sensitivity kernels of SS phase and precursors. As a result, the ray-theoretical corrections potentially underestimate the effect of 3D velocity structures, especially the small-scale structures, on the travel times of SS phase and precursors (e.g., Zhao and Chevrot, 2003; Bai et al., 2012; Koroni and Trampert, 2016). This may cause as much as 5 km errors (<3 km in a well-sampled region) in the depths of MTZ discontinuities (Bai et al., 2012). A recent study by Koroni et al. (2017) suggests that a full waveform approach, including both the 3D sensitivity kernels and boundary kernels, improves the accuracy of corrections for the mantle velocity structures and better constrains the MTZ topography. Here, we focus on the large-scale structures (> 1000 km) in the upper mantle and MTZ. Therefore, the ray-theoretical corrections can remove most of the large-scale heterogeneities and should be accurate enough for this study.

2.2.4 Inversion for Azimuthal Anisotropy

The azimuthal variations of SS precursor travel times arise from the seismic anisotropy in the upper mantle and MTZ. Here, we build 1D anisotropy models to quantify the strength and fast direction of azimuthal anisotropy from SS precursor travel times. In a transversely isotropic medium with a horizontal symmetry axis, the velocity of vertically propagating SH wave is expressed as the following equations (Crampin, 1984; Montagner et al., 2000):

$$\rho V_{qSH}^2 = L - G_c cos2\psi - G_s sin2\psi, \tag{2.1}$$

$$L = \rho V_{SV}^2 = \frac{1}{2}(C_{44} + C_{55}), \tag{2.2}$$

where V_{qSH} is the velocity of quasi-SH wave, ψ is the azimuth of wave propagation direction, L is a function of the isotropic SV wave velocity and can be expressed as elastic parameters C_{ij}, $Gc = \frac{1}{2}(C_{55} - C_{44})$ and $Gs = C_{54}$ are the 2ψ azimuthal terms of L (Montagner and Nataf, 1986).

We use equation (2.1) and (2.2) to perform an inversion for Gc and Gs values from the observed SdS travel times. To achieve this, we first build simple 1D anisotropy models with constant Gc and Gs values in the upper mantle (80 – 220 km) and MTZ (410 – 660 km) to predict SdS travel times. Then, we use a grid search method and chi-squared statistics to determine the best-fitting model and quantify the 2σ uncertainties:

$$\chi^2 = \sum_{i=1}^{N} \frac{(t_i^{obs} - t_i^{pre})^2}{\sigma_i^2}, \tag{2.3}$$

where t_i^{obs} is the observed SdS travel times, t_i^{pre} is the predicted SdS travel times, σ_i is the standard deviations of observed travel times, *N* is the number of measurements. The fast direction (Θ) and strength of anisotropy (G) are calculated from the best-fitting Gc and Gs values:

$$\Theta = \frac{1}{2}\arctan(G_s/G_c), \tag{2.4}$$

$$G = \sqrt{G_s^2 + G_c^2} \tag{2.5}$$

2.2.5 Amplitude Correction

The SS precursor amplitudes are sensitive to the impedance contrast at 410 and 660 km discontinuities, and thus can be used to detect seismic anisotropy near the discontinuities. However, five different factors contribute to the amplitudes: 1) reflection coefficient at the discontinuity; 2) attenuation along the ray path; 3) geometrical spreading; 4) focusing and defocusing effects from stacking; 5) radiation patterns from different focal mechanisms. Only the reflection coefficient is sensitive to seismic anisotropy near the MTZ discontinuities. Therefore, we apply a post-stacking amplitude correction based on synthetic data, to negate other influences. We generate a 1D synthetic data set using GEMINI (Friederich and Dalkolmo, 1995) for ak135 model (Kennett et al., 1995). The synthetics are matched with corresponding data by depth and epicentral distance, then processed and stacked following the same procedure as for the real data.

The radiation patterns for SS and SdS phases are similar, and cancelled out by taking the relative amplitude of SdS/SS. Subsequently, the stacked SdS/SS amplitudes can be expressed as a function of only four other factors:

$$A_{data}^{SdS/SS} = R_{SdS/SS}(\bar{\Delta}) * G * Q * F, \tag{2.6}$$

where $R_{SdS/SS}$ is the true reflection coefficient at the discontinuity, $\bar{\Delta}$ is the average epicentral distance of the bin, G is geometrical spreading factor, Q is attenuation factor, and F is the focusing and defocusing factor from stacking. The SdS/SS amplitude in synthetic stacking result can be expressed as:

$$A_{syn}^{SdS/SS} = R_{SdS/SS}^{mod}(\bar{\Delta}) * G * Q * \mathrm{F}\,, \tag{2.7}$$

where $R_{SdS/SS}^{mod}$ is the reflection coefficient in model ak135. We assume that the attenuation, geometrical spreading, and focusing and defocusing effects of data and synthetics are similar and thus can be removed. We also assume that the scaling factor of the reflection coefficient from the average epicentral distance ($\bar{\Delta}$) to the reference epicentral distance ($\Delta_{ref} = 125°$) is similar in data and synthetics. Based on equation (2.6) and (2.7), the true reflection coefficient at the discontinuity is then given as follows:

$$R_{SdS/SS}(\Delta_{ref}) = R_{SdS/SS}^{mod}(\Delta_{ref}) \cdot \frac{A_{data}^{SdS/SS}}{A_{syn}^{SdS/SS}}\,, \tag{2.8}$$

where Δ_{ref} is the reference epicentral distance $125°$, $A_{data}^{SdS/SS}$ is the SdS/SS amplitude of data stacking result and $A_{syn}^{SdS/SS}$ is the SdS/SS amplitude of synthetic stacking result. The reflection coefficient is recovered from the amplitude ratio of data over synthetic stacking results. After amplitude corrections, we use a similar method as the travel time inversion to invert for the azimuthal anisotropy near the 410 and 660 km discontinuities.

Saki et al. (2018) investigated the feasibility of using the reflection coefficients of PP and SS precursors, particularly the polarity change of amplitudes, to detect seismic anisotropy and constrain the type of deformation mechanisms near the 410 km

discontinuity. However, the polarity change of SS precursors only exists at short epicentral distance range (e.g., 30° - 40°), which is not applicable for SS precursor stacks due to the triplications and extremely low amplitudes in the range. Here, we focus on the azimuthal dependence of SS precursor amplitudes, which are all above zero, rather than detecting the polarity reversals.

2.3 Results

2.3.1 MTZ Topography

After stacking the data in 1000 km radius caps, we obtain global topography maps of 410 and 660 depths, and MTZ thickness (Figure 2.4), corrected for crustal and upper mantle velocity structures. The mean depths of 410 and 660 km discontinuities are 416.8 ($\pm$11.7) km and 661.1 ($\pm$11.9) km respectively. The MTZ thickness is calculated as the difference between the 410 and 660 depths, with a mean value of 244.4 ($\pm$13.1) km. This value is independent from the upper mantle velocity structures and thus more robust than the individual 410 and 660 depths.

The 410 depth shows a strong depression beneath most of the Pacific Ocean (Figure 2.4a). This result is consistent with the presence of hotspots here, including Hawaii, Bowie and Samoa, which can produce hot anomalies in the MTZ (e.g., Courtier et al., 2007). The 410 depth is slightly elevated beneath Sumatra and Philippine subduction zones, but no elevation is observed beneath Japan and South America subduction zones. A depression of the 660 depth is found beneath the subduction zones in the western Pacific (Japan, Izu-Bonin, Sumatra, Tonga), and South America (Figure 2.4b). This corresponds well with cold anomalies introduced by the subducting slabs.

The 660 depth is elevated beneath several hotspots such as Comoros, Iceland and Bowie. Conversely, the 660 depths beneath Hawaii and southern Pacific hotspots are close to the global average.

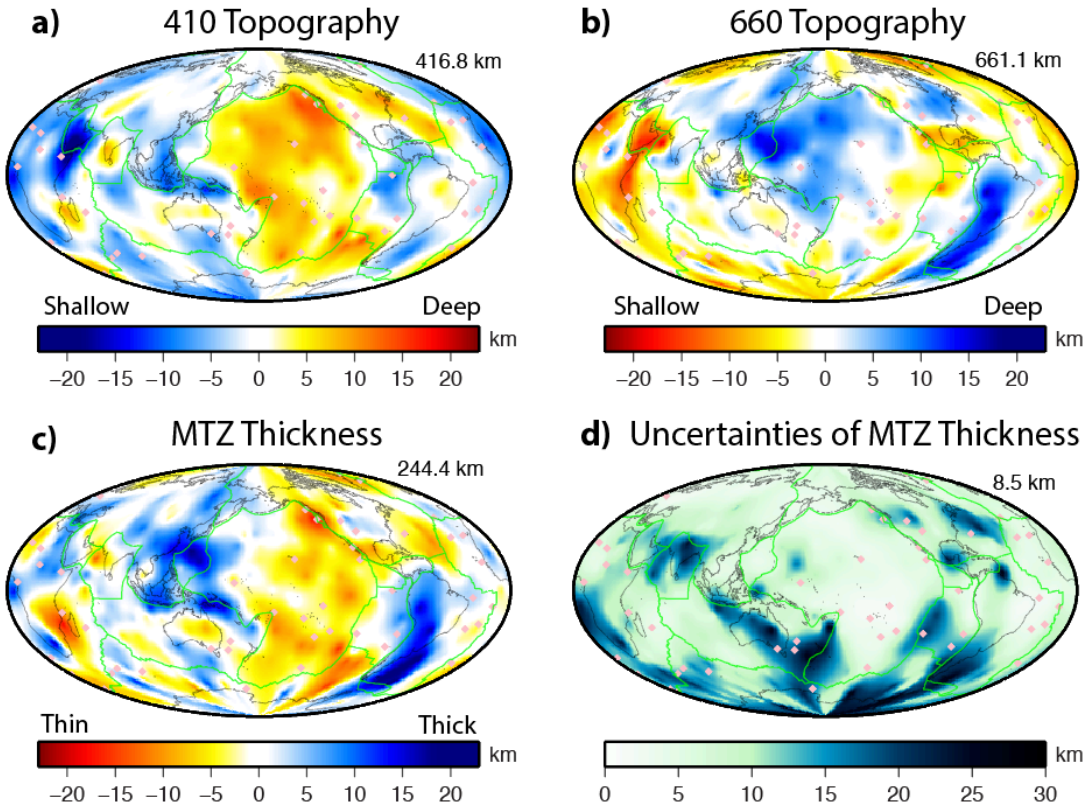

Figure 2.4 MTZ topography model corrected for crustal and upper mantle heterogeneities. The global map of a) 410 topography; b) 660 topography; c) MTZ thickness; d) uncertainty of MTZ thickness. The average depths, thickness and uncertainty are labeled on the top right corner of each panel. The pink dots denote the hot spots (Courtillot et al., 2003) and green lines are the plate boundaries (DeMets et al., 1990).

Correspondingly, the MTZ thickness is characterized by thinning in the Pacific and thickening beneath the western Pacific and South America subduction zones (Figure 2.4c). A thinned MTZ is observed beneath most hotspots in Pacific (e.g., Hawaii, Bowie, Cobb, Samoa, MacDonald), resulting mainly from the depressed 410 km discontinuity. In contrast, the thin MTZ beneath Iceland only arises from an elevation of the 660. The only thin MTZ region with both depressed 410 and elevated

660 km discontinuities is beneath the Comoros hotspot. A thickened MTZ beneath the western Pacific and South America subduction zones is primarily a consequence of the depression of 660 km discontinuity. The Sumatra subduction zone is the only thickened region to have both shallow 410 and deep 660 km discontinuities. The MTZ thickness is generally thinned in the hot mantle plume regions and thickened in the cold slab regions. The general correlation of thick (thin) MTZ to cold (hot) regions indicates that mantle temperature plays a dominant role in MTZ topography.

The errors on MTZ thickness are closely related to the data coverage (Figure 2.4d). The uncertainties in the southern hemisphere are larger than the northern hemisphere due to inhomogeneous station density. Most of the oceanic regions (e.g., Pacific and Indian Ocean) and the Eurasia continent have ample data sampling (number of records, NR > 500) that yield an uncertainty less than 5 km. On the contrary, the data coverage in Australia, India, South Africa, and Argentina is poor (NR < 100) so the uncertainties are above 10 km.

The 10 km variation in topography is equivalent to ~3s in travel time variation. In order to constrain azimuthal anisotropy from SdS travel times, we remove the effect of MTZ topography on the travel times by applying a pre-stacking topography correction to the entire data set. From the topography calculated for 1000 km radius bins, we compute the topography corrections from the difference between local 410, 660 depths and global mean values. We apply this correction prior to azimuthal stacking, ensuring the azimuthal variations of SdS travel times are independent from MTZ topography.

2.3.2 Regional Azimuthal Stacking

2.3.2.1 Central Pacific

The central Pacific bin is located near Hawaii and the radius is 2000 km (Figure 2.5a). Here, global stacks reveal that the MTZ thickness is thinned by ~10 km beneath Hawaii. The azimuths of bounce points are dominated by those oriented towards the USArray (30° - 60°), but the southeast direction (90° - 120°) is not well covered by the data. The data are stacked into 30° azimuthal bins (Figure 2.5b). The travel time variations of S410S and S660S have less than one second deviation from the mean values. The amplitude variations are highly correlated with the 1D synthetics (Figure 2.5c), indicating that most anomalies arise from attenuation and geometrical spreading, rather than azimuthal anisotropy at the discontinuities, and thus are removed by the amplitude corrections.

Considering the travel times and amplitudes of SS precursors as a function of bounce point azimuths (Figure 2.6), we find that the S410S travel time is sensitive to the upper mantle structure (0 – 410 km) and S660S travel time is sensitive to both the upper mantle and transition zone structure (0 – 660 km). The upper mantle anisotropy is mapped onto both SS precursors due to the SS reference phase. However, the differential S410S – S660S travel time is only affected by the transition zone structure (410 – 660 km), making it an independent indicator for MTZ anisotropy.

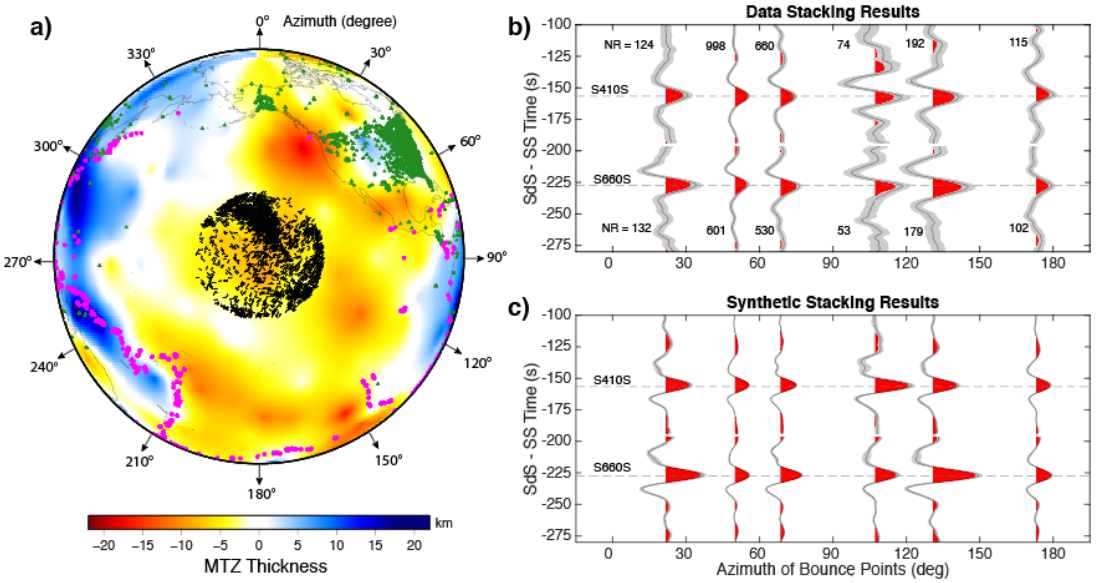

Figure 2.5 a) The bounce point map of the central Pacific bin is superimposed on the map of MTZ thickness. The radius of the bin is 2000 km. The black lines denote the bounce points and orientations of the SS ray paths. The pink circles and green triangles represent the earthquakes and stations respectively. b) The azimuthal stacking results of data in the central Pacific bin. The gray shaded region is the 95% confidence levels of amplitudes estimated from bootstraps. The positive amplitudes are indicated in red. A gap is produced near -190s because the S410S and S660S stacks are completed separately. The dash lines represent the average travel times of S410S and S660S. The number of records (NR) of each stack are labeled beside the seismograms. c) The azimuthal stacking results of corresponding synthetics.

We build 1D anisotropy models in both the upper mantle (80 – 220 km) and MTZ (410 – 660 km) to invert for the strength of anisotropy (dlnG = G/L) and fast direction (Θ) (Figure 2.6). The upper mantle model is applied to S410S and S660S travel times, and the MTZ model to the S410S – S660S travel time and amplitude inversions. The best-fitting model of S410S time is dlnG=4.0 ± 3.2% and Θ = 95° ± 21° (Figure 2.6a). We find the fast direction is oriented southeast; this result is consistent with surface wave anisotropy models at 150 km depth (e.g., dlnG=3.1%, Θ=102° in Yuan and Beghein, 2013) and APM models (e.g., Θ=155° in Becker et al., 2015) in the central Pacific region. The best-fitting model for S660S time is dlnG = 3.9 ± 2.7% and Θ = 117° ± 20° (Figure 2.6b). The strength of anisotropy is consistent with the S410S inversion, but the fast direction is more southeasterly due to the bias from

the MTZ structure. The 2σ error ellipses of S410S and S660S times do not include the zero-anisotropy point (Figure 2.6c); this means the strength of anisotropy in the upper mantle is significantly above zero.

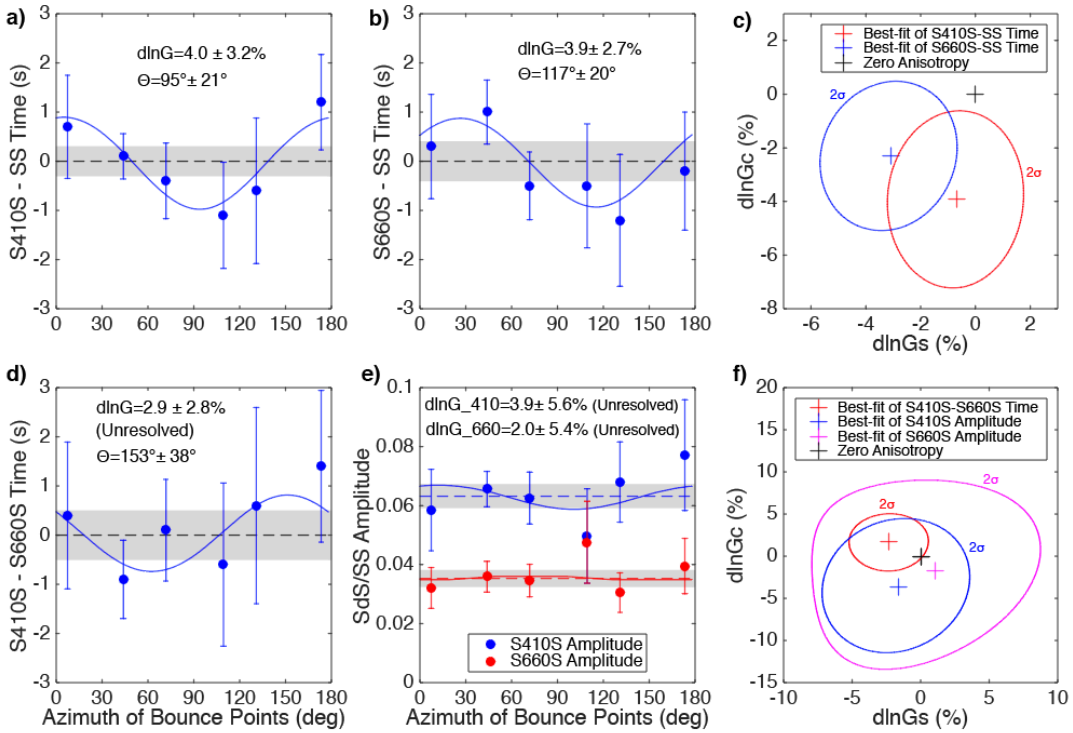

Figure 2.6 Measurements of relative travel times and amplitudes of SS precursors in the central Pacific bin are plotted as a function of bounce point azimuths. a) The S410S – SS travel time residuals. The dash line is average travel time measured from the stacking of all data in the central Pacific bin and the gray shaded box denotes the uncertainty. The blue curve is the best-fitting model inverted from the 1D anisotropy model. The dlnG and Θ values represent the strength of anisotropy and fast direction of the best-fitting model respectively. b) The S660S – SS travel time residuals. c) The 2σ error ellipses of the best-fitting models of S410S and S660S times estimated from the chi-squared statistics. The black cross denotes the zero-anisotropy point. d) The S410S – S660S travel time residuals. e) The S410S/SS (blue) and S660S/SS (red) amplitudes. f) The 2σ error ellipses of the best-fitting models of S410S - S660S time, S410S amplitude and S660S amplitude.

Our inversion result of S410S – S660S time beneath the central Pacific bin is dlnG = 2.9 $\pm$ 2.8% and Θ = 153° $\pm$ 38° (Figure 2.6d). This indicates ~3% anisotropy existing in the MTZ here, and the fast direction is again oriented southeast. However, this value is not significantly above zero (Figure 2.6f) indicating that the MTZ anisotropy is not well-resolved, in agreement with the uncertainty estimates of Yuan

and Beghein (2018). Future work with additional data and less noisy stacks can help reduce the uncertainties of travel time measurements, and perhaps resolve the structure. The inversion results of S410S and S660S amplitudes are also not significantly above zero, and the 2σ errors are quite large compared to the S410S – S660S time (Figure 2.6e-f). We also examine the stacking results in the northwestern Pacific, Greenland and central Atlantic, but do not find significant signals for MTZ anisotropy (Figure 2.S1-S3).

2.3.2.2 Subduction Zones

Subducting slabs can introduce strong mantle flow into the MTZ and cause azimuthal anisotropy (e.g., Billen, 2008). Unfortunately, the SS data set does not have sufficient azimuthal coverage in any individual subduction zone to perform single region studies. Thus, to explore the presence of azimuthal anisotropy near slabs, we select six subduction zones around the Pacific Ocean using the SLAB 1.0 model (Hayes et al., 2012): 1) Kamchatka/Japan/Izu-Bonin; 2) Aleutian; 3) Cascadia; 4) South America; 5) Kermadec-Tonga; 6) Sumatra (Figure 2.7). We select the SS bounce points that are located beneath the slab contours defined by SLAB 1.0 model. Then, we define a new coordinate system using the trench perpendicular and parallel directions to combine the six subduction zones into one data set (Figure 2.7b). We then calculate the relative azimuths between bounce point azimuths and trench perpendicular directions. We stack the whole subduction zone data set by relative azimuths into 30° bins. The stacking results are plotted as a function of relative azimuths (Figure 2.8); the 0° and 180° represent the trench perpendicular direction and 90° represents the trench parallel direction.

The S410S travel time (Figure 2.8a) has stronger variations than the S660S travel time (Figure 2.8b). We use the 1D anisotropy model (80 – 220 km) to invert for the upper mantle anisotropy, finding a best-fitting model of S410S time as dlnG = 4.3 ± 2.4% and Θ = 100° ± 17°. This suggests that ~4% azimuthal anisotropy exists in the upper mantle beneath subduction zones with a nearly trench-parallel fast direction. The dlnG value inverted from S410S time is significantly above zero while the one from S660S time is not significant (Figure 2.8c), which indicates that strong perturbations are caused by the MTZ structures beneath subduction zones.

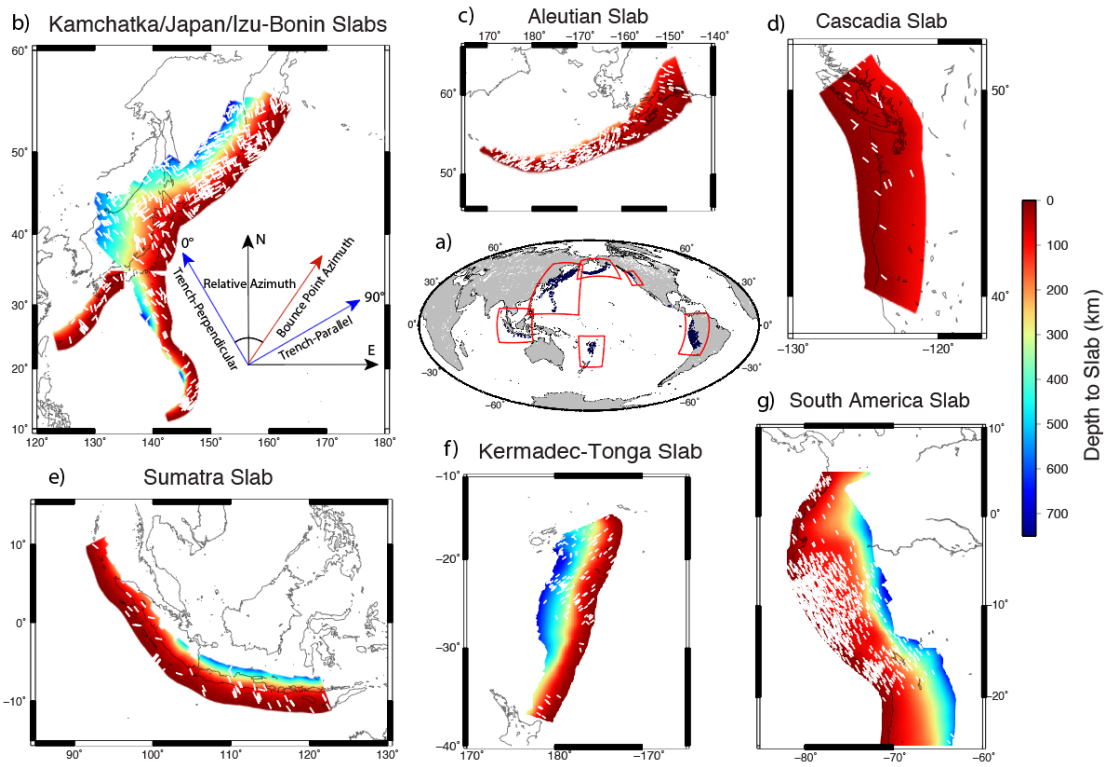

Figure 2.7 SS precursor azimuthal sampling in subduction zones. The geometries of slabs are from SLAB 1.0 model (Hayes et al., 2012). a) The global map of bounce points in subduction zones. The blue points denote the bounce points and the red boxes highlight the locations of six subduction zones. The six subduction zones are: b) Kamachatka/Japan/Izu-Bonin slabs and the illustration of the trench-perpendicular/parallel coordinate system; c) Aleutian slab; d) Cascadia slab; e) Sumatra slab; f) Kermadec-Tonga slab; g) South America slab. The color bar shows the depth to slab and the white vectors denote the azimuths of the bounce points.

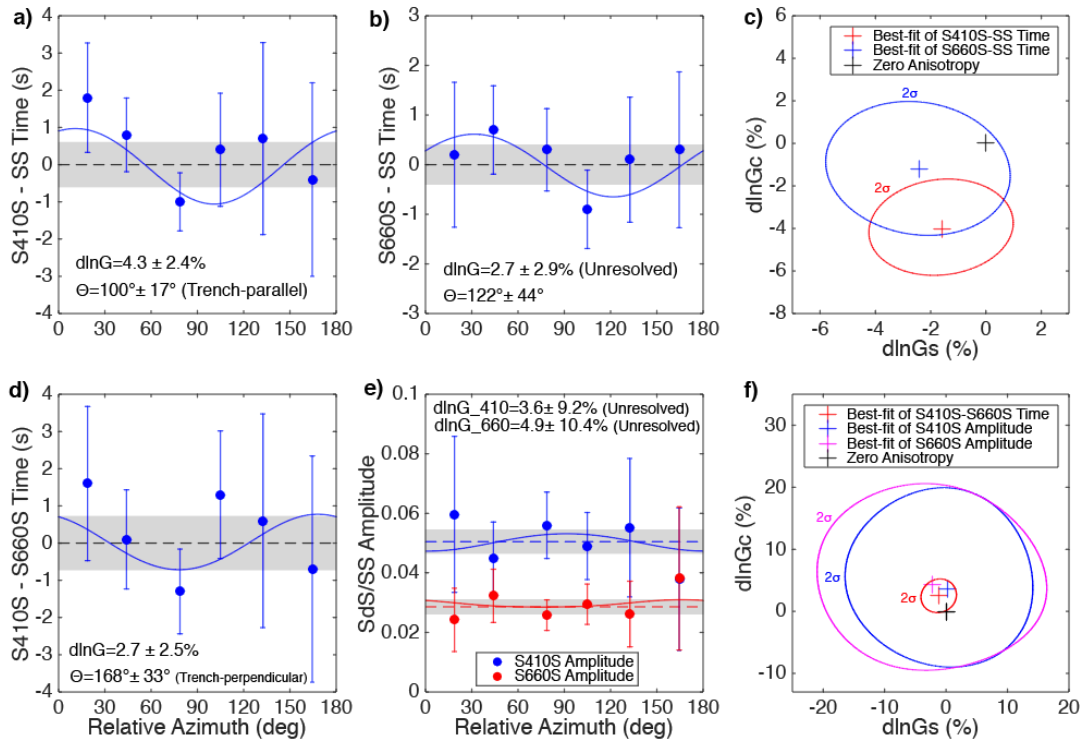

Figure 2.8 Azimuthal stacking results of subduction zones. a) S410S travel time residuals; b) S660S travel time residuals; c) The 2σ error ellipses of the best-fitting models of S410S and S660S times; d) S410S-S660S travel time residuals; e) S410S and S660S amplitudes; f) The 2σ error ellipses of the best-fitting models of S410S - S660S time, S410S amplitude and S660S amplitude. The legends are the same as Figure 2.6. The 0° and 180° represent the trench-perpendicular direction and 90° represents trench-parallel direction.

The best-fitting model of S410S – S660S time is dlnG = 2.7 $\pm$ 2.5% and Θ = 168° $\pm$ 33° (Figure 2.8d). It suggests that ~3% anisotropy exists in MTZ beneath subduction zones with a nearly trench-perpendicular fast direction. The strength of anisotropy is slightly weaker than the upper mantle, in agreement with the weaker elastic anisotropy of wadsleyite and ringwoodite compared to olivine. The fast direction transitions from trench-parallel in the upper mantle into trench-perpendicular in the MTZ, indicating that there could be a change of mantle flow direction with depth. The S410S and S660S amplitudes showed strong variations with relative azimuths, but they exhibited a higher correlation than other stacks ($r^2 = 0.67$). This may result from uncorrected 3D attenuation structures in the upper mantle, which map SS amplitude

variations onto S410S and S660S amplitudes. Thus, we further correct the correlated components between S410S and S660S amplitudes. After correction, neither of S410S and S660S shows significant variations with relative azimuths, which indicates no strong anisotropy exists near MTZ discontinuities (Figure 2.8e). The dlnG value inverted from S410S – S660S time is slightly above zero, while the amplitudes are not significant and have large uncertainties (Figure 2.8f).

2.3.3 Global Azimuthal Stacking

The regional azimuthal stacks are limited to locations with sufficient azimuthal coverage. Here, we also interrogate the upper mantle and MTZ anisotropy at a global scale. In surface wave anisotropy models, the fast directions change as a function of depth at any given location. We therefore compute an average anisotropy model across a certain range of depths (e.g., 410 – 660 km) for the global azimuthal stacking. We follow the methods of Montagner et al (2000) to compute the synthetic shear wave splitting models from surface wave models:

$$\delta t = \sqrt{\left(\int_{h_1}^{h_2} \frac{G_c(z)}{V_s(z)L(z)}\,dz\right)^2 + \left(\int_{h_1}^{h_2} \frac{G_s(z)}{V_s(z)L(z)}\,dz\right)^2}, \tag{2.9}$$

$$\phi = \frac{1}{2}\arctan\left(\frac{\int_{h_1}^{h_2} \frac{G_s(z)}{V_s(z)L(z)}\,dz}{\int_{h_1}^{h_2} \frac{G_c(z)}{V_s(z)L(z)}\,dz}\right), \tag{2.10}$$

where δt is the shear wave splitting time, ϕ is the fast direction, z is the depth, h_1 and h_2 are the lower and upper bounds of the depth range, V_s is the shear wave velocity. We select two depth ranges to calculate the synthetic shear wave splitting models: 1)

80 – 220 km (upper mantle); 2) 410 – 660 km (MTZ). We use the fast directions of the synthetic shear wave splitting model as an average model in these two depth ranges. The relative azimuths between the bounce point azimuths and averaged fast directions for the global azimuthal stacking allow us to examine the evidence of azimuthal anisotropy in the upper mantle and MTZ at a global scale.

The synthetic shear wave splitting models are computed from three surface wave anisotropy models using equations (2.9) and (2.10) (Figure 2.9). In the upper mantle, the fast directions are generally consistent in three models although 3D2017_09Sv model shows stronger anisotropy. In the MTZ, YB13SVani is the only model with relatively strong anisotropy compared to the upper mantle structure. Moreover, the fast directions from the three models are inconsistent, implying that the MTZ anisotropy is not well-resolved from surface waves. We compute the relative azimuths of SS bounce points from the fast directions, in a similar way to the subduction zone data subsets. Benefitting from sufficient azimuthal coverage, we stack the global data set into 15° bins according to relative azimuth.

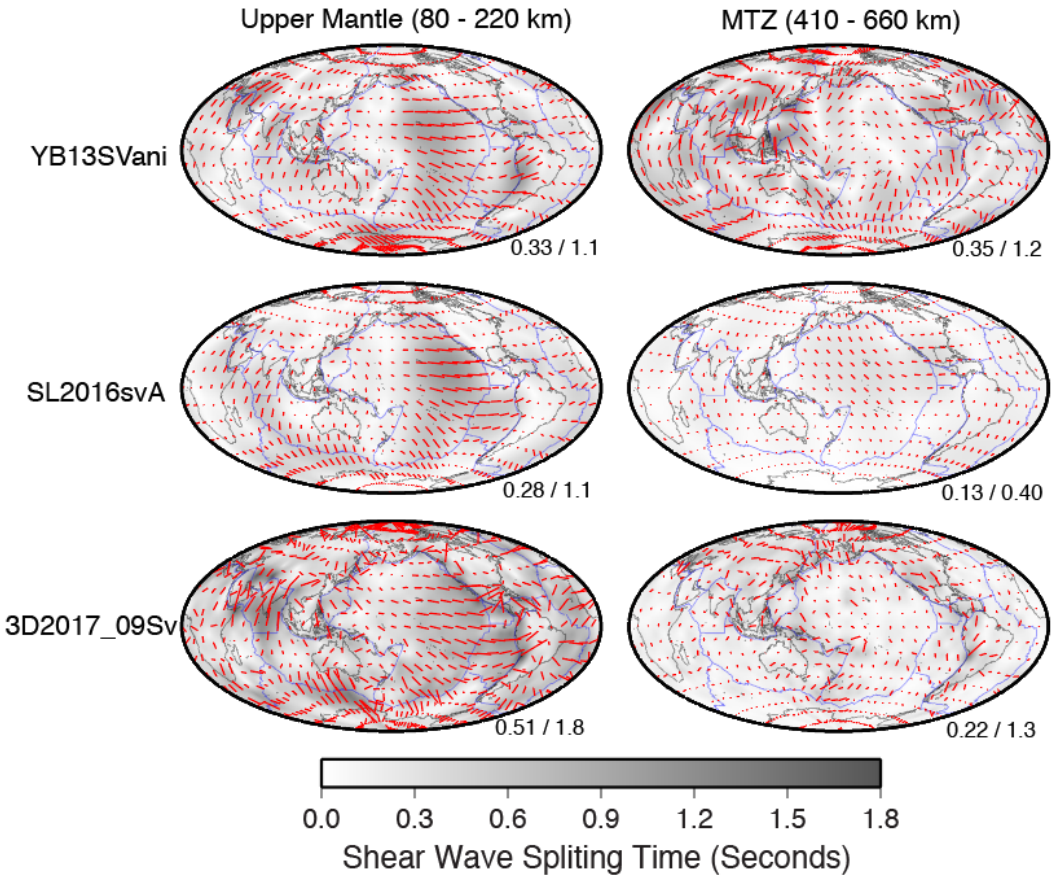

Figure 2.9 The depth averaged shear wave splitting models computed from the surface wave anisotropy models: YB13SVani (Yuan and Beghein, 2013), SL2016svA (Schaeffer et al., 2016) and 3D2017_09Sv (Debayle et al., 2016). The first and second column represent the models for the upper mantle (80 – 220 km) and MTZ (410 – 660 km) respectively. The red vectors denote the fast directions of azimuthal anisotropy and the length is scaled with the strength of anisotropy. The numbers on the bottom right of each panel denote the mean/maximum shear wave splitting time. The fast directions of shear wave splitting models are used for global azimuthal stacking. The blue lines are the plate boundaries (DeMets et al., 1990).

2.3.3.1 Upper Mantle

Upper mantle anisotropy affects the travel times of SS phase, which are mapped onto the S410S and S660S travel times. If the fast directions from the surface wave models are consistent with the Earth's anisotropy structures, we expect to observe a fast direction from SS precursors to be close to 0° or 180°. We inverted the observed travel times and amplitudes for the fast direction (Θ) and strength of anisotropy (dlnG)

in the upper mantle assuming a 1-D anisotropy model like we did in regional studies (Figure 2.10).

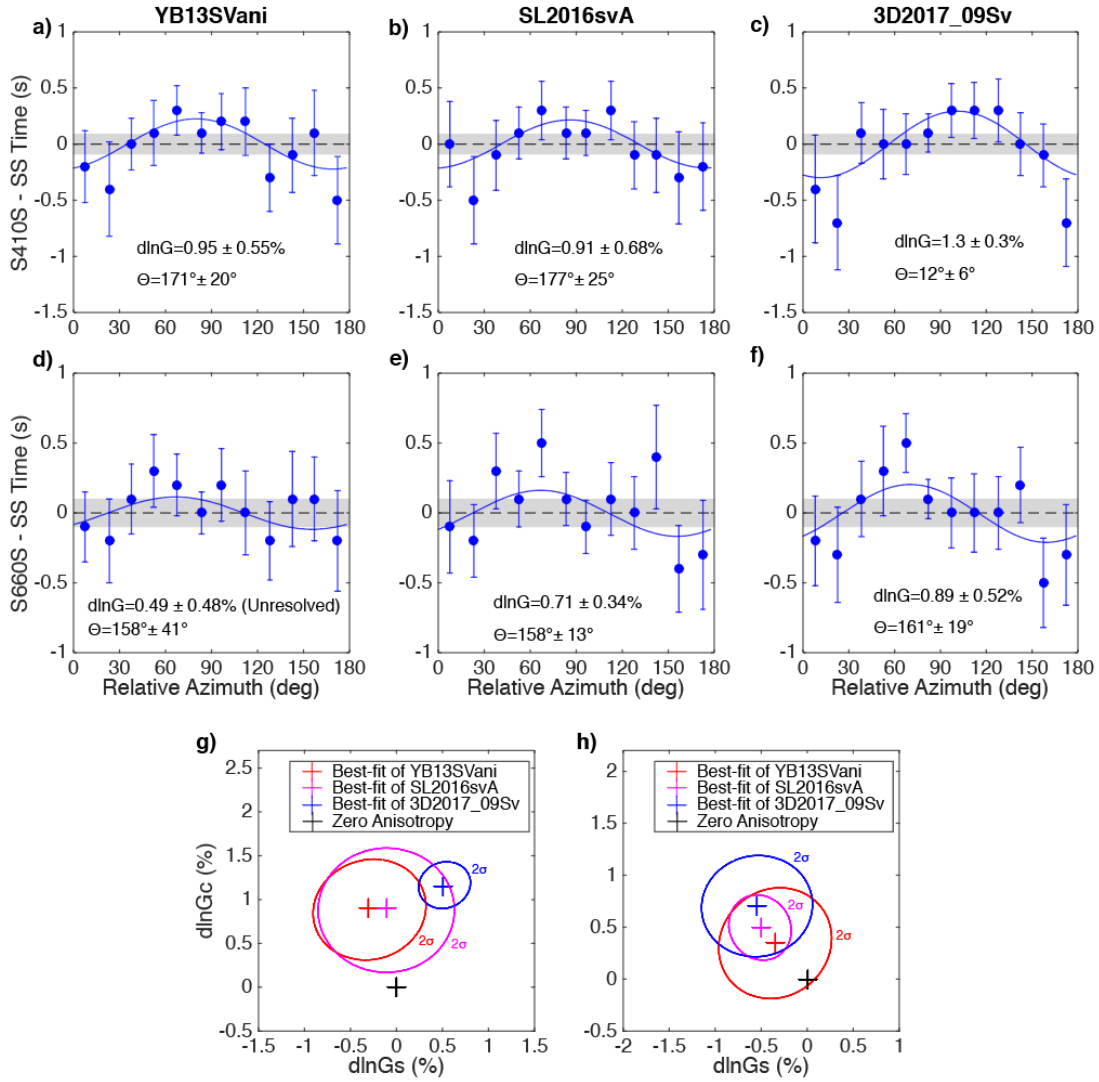

Figure 2.10 Global azimuthal stacking results for the upper mantle anisotropy. a-c) The S410S travel time residuals plotted as a function of relative azimuths which are computed from the fast directions of three surface wave models. d-f) The S660S travel time residuals plotted as a function of relative azimuths. The legends are the same as Figure 2.6. The strength of anisotropy (dlnG) and fast direction (Θ) of the best-fitting model is labeled in each panel. The 2σ error ellipses of the best-fitting models of g) S410S times and h) S660S times.

The S410S times show a clear 2ψ azimuthal variation, and the fast directions are close to 0° or 180° (Figure 2.10a-c). This supports the concept that the fast directions in the upper mantle are well constrained from three surface wave models.

The strengths of upper mantle anisotropy inverted from YB13SVani, SL2016svA and 3D2017_09Sv models are dlnG=0.95±0.55%, dlnG=0.91±0.68% and dlnG=1.3±0.3% respectively. The dlnG values from three models are all significantly above zero (Figure 2.10g), suggesting that ~1% azimuthal anisotropy exists between 80 – 220 km in the upper mantle. This is weaker than the RMS amplitudes of azimuthal anisotropy in YB13SVani and 3D2017_09Sv model but stronger than SL2016svA model (Figure 2.2).

The S660S times produce more outliers than S410S times; these outliers are excluded from the inversions because they may be contaminated by MTZ structures (Figure 2.10d-f). The best-fitting S660S fast directions are close to 160° in all three surface wave models, which is ~20° from the predicted 180° fast direction. The dlnG values for YB13SVani, SL2016svA and 3D2017_09Sv models are dlnG=0.49±0.48%, dlnG=0.71 ± 0.34% and dlnG=0.89 ± 0.52% respectively. The dlnG value from YB13SVani is not significantly above zero but the other two models are both significant (Figure 2.10h). The S660S times also support ~1% azimuthal anisotropy exists in the upper mantle although the Θ and dlnG values may be inaccurate due to the contamination of uncorrected MTZ heterogeneities.

In summary, the upper mantle anisotropy is resolvable from S410S and S660S times for global azimuthal stacking. We find that the average strength of anisotropy is ~1% in the upper mantle (80 - 220 km), which is weaker than the estimates from surface waves. However, the strength of anisotropy is dependent on the thickness of the upper mantle model used for inversion, and the body wave method is intrinsically different from surface waves. To the first order, the upper mantle anisotropy from SS precursors

is consistent with the surface wave models. However, our result suggests that the S410S and S660S travel times can be biased by ~0.5s from upper mantle anisotropy, motivating an anisotropy correction to obtain more accurate 410 and 660 depths.

2.3.3.2 Mantle Transition Zone

We continue our experiments using global anisotropy models to stack for the structures in the MTZ. The S410S–S660S times and S410S, S660S amplitudes are the measurements sensitive to MTZ anisotropy. Considering these parameters as a function of relative azimuths (Figure 2.11), we find that the S410S – S660S times have weaker variations (Figure 2.11a-c) than the upper mantle stacks. The dlnG values for YB13SVani, SL2016svA and 3D2017_09Sv models are dlnG=0.43 $\pm$ 0.48%, dlnG=0.75$\pm$0.84% and dlnG=0.98$\pm$1.2% respectively. None of the three models shows significant anisotropy signals above zero (Figure 2.11a-c, 11g), which can be attributed to the poorly constrained anisotropy in the surface wave models. Alternatively, extremely weak anisotropy in the MTZ caused by the weak single-crystal anisotropy of wadsleyite and ringwoodite can explain this as well.

Figure 2.11d-f reveal that the S410S and S660S amplitudes are close to the mean values and do not show a clear 2ψ variation after the amplitude corrections, except several outliers which are excluded from the inversions. The S410S and S660S amplitudes are correlated with each other in the SL2016svA model (r^2=0.65) indicating that the variations could result from the SS amplitude changes. We correct for the correlated component between S410S and S660S amplitudes. Only the dlnG value of S410S amplitude from YB13SVani model, dlnG= 3.9$\pm$3.3%, is significantly above zero (Figure 2.11d). However, the fast direction, $\Theta = 119° \pm 25°$, is nearly

perpendicular to the predicted 180° fast direction, which suggests this signal is not well-constrained. None of the other dlnG values is significantly above zero from the three surface wave models (Figure 2.11h-i). This result indicates that no strong anisotropy exists at 410 and 660 km discontinuities at the global scale.

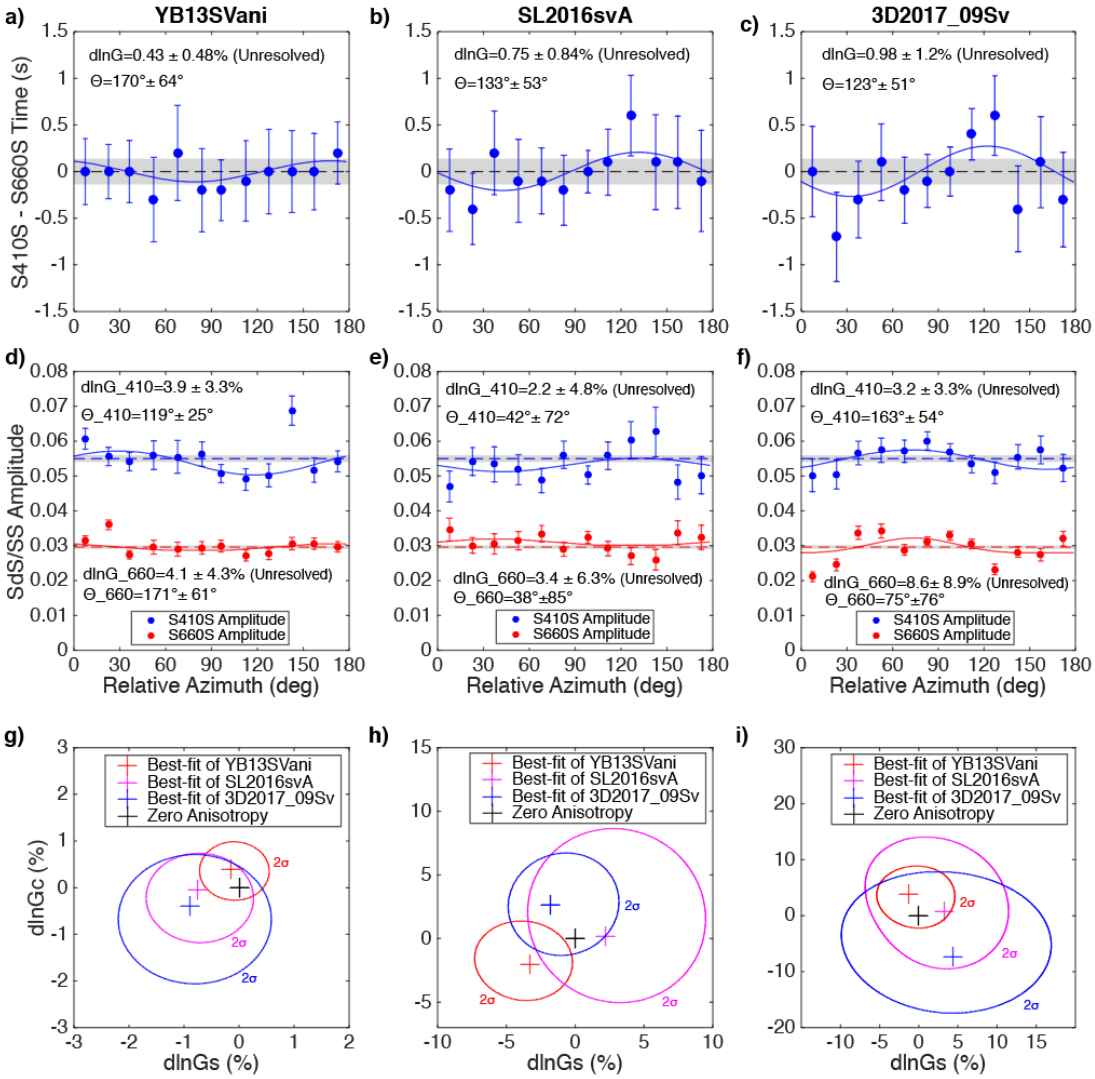

Figure 2.11 Global azimuthal stacking results for the MTZ anisotropy. a-c) The S410S – S660S travel time residuals plotted as a function of relative azimuths. d-f) The S410S/SS (blue) and S660S/SS amplitudes (red) plotted as a function of relative azimuths. The 2σ error ellipses of the best-fitting models of g) S410S – S660S time, h) S410S amplitude, and i) S660S amplitude in the MTZ. The legends are the same as Figure 2.6.

Overall, we find that the MTZ anisotropy inverted from the global stacking approach is relatively weak; if it exists, it is less than 1%. It is difficult to quantify a

small amount of anisotropy from S410S – S660S travel times alone. Furthermore, the S410S and S660S amplitudes cannot resolve the anisotropy near 410 and 660 km discontinuities at the global scale, suggesting signals are isolated to regional structures.

2.4 Discussion

2.4.1 Weak MTZ Anisotropy

In the global azimuthal stacking, we find evidence for ~1% azimuthal anisotropy in the upper mantle (80 – 220 km). We stack the global data set using the patterns of surface wave anisotropy at the depth range of crust (0 – 40 km) and deep upper mantle (220 – 410 km), but do not find a coherent anisotropy signal from the stacks. This indicates that the anisotropy arises from the shallow upper mantle (80 – 220 km). The LPO of olivine induced by the shear deformations is the most likely contribution to ~1% anisotropy in the asthenosphere (e.g., Karato et al., 2008). We divide the global data set into oceanic and continental sub-datasets to study the heterogeneities of anisotropy structures beneath oceans and continents in the asthenosphere. Our observations reveal that oceanic regions are consistent with the global average of ~1% anisotropy (Figure 2.S4). However, the continental regions do not display a significant signal of anisotropy in the asthenosphere (Figure 2.S5). Consequently, the global average is likely dominated by oceanic regions. We also test the SL2016svAr model by Schaeffer et al. (2016), which has smaller scale variations and larger amplitudes, and we find similar results compared to the SL2016svA model.

We find that azimuthal anisotropy in the MTZ is weaker than 1% at the global scale. It is still uncertain that the non-detection of global MTZ anisotropy arises from

using unconstrained surface wave anisotropy models as a reference, or simply by weak anisotropy in the MTZ. The global azimuthal stacking is dependent on the fast directions of surface wave models; hence, the anisotropy signal is cancelled if the fast directions are not accurate. On the other hand, the extremely weak anisotropy in the MTZ could be responsible for the non-detection. From a mineral physics perspective, it is debated that the LPO of wadsleyite is strong enough to produce detectable seismic anisotropy, even if it has relatively strong single crystal anisotropy (~14%). For example, the mineral physics modeling predicts that a polycrystal of pyrolitic composition (60% wadsleyite, 40% garnet) under the shear strain of mantle flow can produce ~1% seismic anisotropy in the MTZ (Tommasi et al., 2004; Kawazoe et al., 2013). However, a recent mineral physics study by Zhang et al. (2018) suggests that 1% or more anisotropy in the MTZ cannot be explained by the LPO of wadsleyite as a primary source. They propose other mechanisms such as metastable olivine or SPO to explain observations of more than 1% anisotropy in the MTZ. Moreover, the mineral recrystallization of olivine at 410 km during the phase change to wadsleyite would also cause the loss of seismic anisotropy in the MTZ (Karato, 1988). Our observations with SS precursors are consistent with Zhang et al. (2018), which do not support more than 1% azimuthal anisotropy in the MTZ. This result contrasts with observations from surface waves that found more than 1% azimuthal anisotropy could exist in the MTZ (e.g., Yuan and Beghein, 2013). However, given that uncertainties in global surface wave tomography can be quite large (Yuan and Beghein, 2018), and intrinsic discrepancies between body waves and surface waves, it would be difficult to compare them directly.

2.4.2 Mantle Flow in the MTZ

The MTZ anisotropy is weak at a global scale, but could be regionally enhanced near strong mantle flow such as hotspots or subduction zones. In regional stacks of the central Pacific, we find evidence for ~4% azimuthal anisotropy in the upper mantle but no significant anisotropy in the MTZ. Surface wave studies reported upper mantle anisotropy in the central Pacific region (e.g., Nishimura and Forsyth, 1989; Ekström and Dziewonski, 1998; Montagner, 2002), including the three surface wave anisotropy models used in this study. Our observation of upper mantle anisotropy is consistent with the LPO fabrics of olivine induced by the horizontal mantle flow beneath Hawaii. However, the mantle plume mainly produces vertical flow in the MTZ, which cannot result in strong azimuthal anisotropy of SH wave (e.g., Tommasi et al., 2004). Thus, we would not expect a strong azimuthal anisotropy signature in the MTZ beneath plume regions.

Subducting slabs can introduce horizontal flow into the MTZ, and may be a source of stronger azimuthal anisotropy. Beneath the subduction zones in this study, we find evidence for ~4% anisotropy in the upper mantle with a trench-parallel fast direction, and ~3% anisotropy in the MTZ with a trench-perpendicular fast direction. The trench-parallel fast direction in the upper mantle is consistent with the observations by shear wave splitting measurements, e.g., Long and Silver (2008, 2009) found that trench migration induced dominantly trench-parallel flow and anisotropic directions in the sub-slab mantle. However, other studies show that the fast directions in the mantle wedge are complicated in some areas, with a transition from trench-parallel in the fore-arc to trench-perpendicular in the back-arc (Long and Wirth, 2013). This may be caused

by a combination of trench-perpendicular corner flow and B-type olivine or serpentinite minerals in the mantle wedge. However, the trench-parallel fast direction observed by our study of SS precursors is an average summation of the mantle wedge and sub-slab mantle structure, and may not be sensitive to a smaller scale transition of fast direction in the mantle wedge. Our result indicates that trench-parallel mantle flow is dominant in the upper mantle at the vicinity of subducting slabs.

A complication in interpreting our observations is that stacking produces an average result combining six subducting slabs with various velocity anomalies, thickness, dipping angles and convergence directions at the trench. The stacking of data across multiple subduction zones would average out any local anisotropic structures that may dominate in a particular slab configuration. For example, the slabs with shallower dipping angles may cause stronger horizontal flow in the MTZ or have larger effects of SPO, thus contribute more to our anisotropy measurements over more vertically oriented slabs. Furthermore, the plate motion convergence directions are not always trench-perpendicular (e.g., Becker et al., 2015), which increases the uncertainties of measured fast directions and strength of anisotropy. Since we focus on the coherent mantle flow pattern across different subduction zones, these incoherent structures would cancel out or contribute to the uncertainties in the stacks.

Despite these uncertainties, it is intriguing to find that the fast direction transitions from trench-parallel in the upper mantle into trench-perpendicular in the MTZ. Very few shear wave splitting studies have found evidence for the MTZ anisotropy (e.g., Fouch and Fisher, 1996; Wookey et al., 2002; Chen and Brudzinski, 2003), although one study detected a trench-parallel fast direction beneath the Tonga

slab (Foley and Long, 2011). The surface wave models reveal a complicated pattern for the MTZ anisotropy beneath subduction zones. For example, the YB13SVani model (Yuan and Beghein, 2013) reports a trench-perpendicular fast axis beneath the Japan and Aleutian slabs, but a trench-parallel fast axis beneath the South America slab (Figure 2.9). We note, however, that the lateral resolution of such models is lower than that necessary to resolve a subducting slab. Our results suggest that the trench-perpendicular mantle flow becomes dominant in the MTZ beneath subduction zones. As subducting slabs descend into the mid-mantle, they can either penetrate through the MTZ or stagnate at the bottom of the MTZ (e.g., Fukao et al., 2001). The trench-perpendicular fast axis better agrees with the mantle flow field caused by stagnant slabs in the MTZ (e.g., Billen, 2010), thus our signals may be dominated by stagnant slabs (e.g., Japan). However, because of uncertainties on the effect of pressure, water, or recrystallization across the MTZ boundaries on seismic anisotropy, we cannot rule out that mantle flow direction remains constant with depth and that we are seeing the signature of these other factors on the anisotropy (Yuan and Beghein, 2013). Additionally, other mechanisms such as the SPO produced within slabs and different slip systems of wadsleyite (e.g., Kawazoe et al., 2013) can also explain our observations of the MTZ anisotropy beneath the subduction zones.

2.4.3 The Effect of Anisotropy on MTZ Topography

We next explore how upper mantle and MTZ anisotropy affect the travel times of SS precursors, an effect that has been neglected in previous MTZ topography studies. The MTZ topography can be biased by strong seismic anisotropy if the azimuthal distribution of SS bounce points is uniform in the region, a common scenario in many

bins from our data set. Here, we apply an anisotropy correction based on surface wave anisotropy models to obtain a more precise MTZ topography model. First, we collect Gc and Gs values from the YB13SVani surface wave model (Yuan and Beghein, 2013) to compute velocity perturbations along each raypath using equation (2.1) and (2.2). Then, we use the same 1D ray tracing technique as in section 2.2.3 to compute the travel time residuals from PREM as a reference for the anisotropy corrections. After the anisotropy correction, we obtain a new MTZ topography model independent from upper mantle and MTZ anisotropy structures (Figure 2.12). The mean values of the 410, 660 depths and MTZ thickness remain almost the same after anisotropy correction (Figure 2.13). The mean values of the topography difference are all close to zero (Figure 2.13bdf); the anisotropy correction results in only ± 3 km topography difference, even smaller than the topography uncertainties.

The amplitude of 410 topography (Figure 2.13a) and MTZ thickness difference (Figure 2.13e) are smaller than that of 660 topography (Figure 2.13c), as S660S is affected by both the upper mantle and MTZ anisotropy structures. The Pacific and South America represent the areas with multiple MTZ topography studies. If we account for mantle anisotropy structures, the 410 and 660 depths would be ~2 km deeper in the western and southern Pacific, and ~4 km deeper in South America. The MTZ thickness would be thickened by ~3 km in southern East Pacific Rise and Izu-Bonin subduction zones, and thickened by ~6 km in the Middle East. Regional studies of MTZ topography in the western and southern Pacific, and South America should therefore incorporate an anisotropy correction to obtain a more precise topography model that is unbiased by anisotropy. Conversely, the difference in the central and

northwestern Pacific is less than 1 km, which is negligible considering the uncertainties of topography.

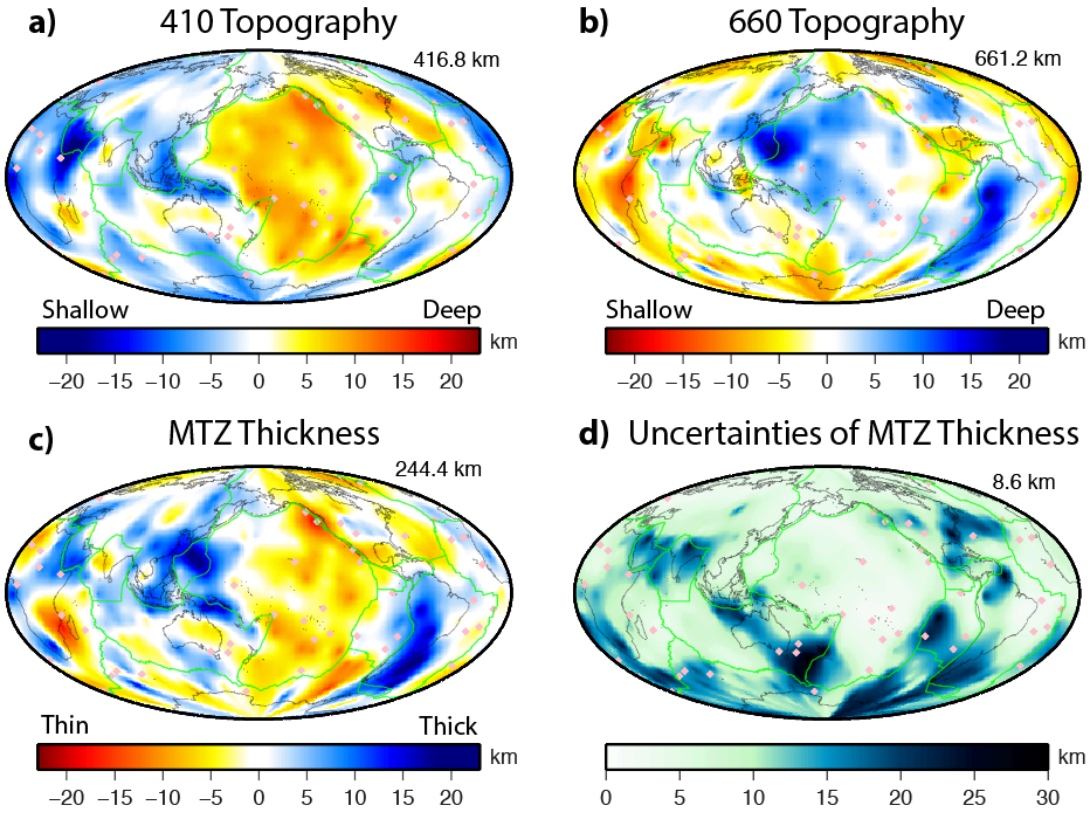

Figure 2.12 MTZ topography model corrected for the upper mantle and MTZ anisotropy structures using YB13SVani model (Yuan and Beghein, 2013). The global map of a) 410 topography; b) 660 topography; c) MTZ thickness; d) uncertainty of MTZ thickness. The legend is the same as Figure 2.4.

We apply a spherical harmonic analysis to our MTZ topography model using a hierarchical Bayesian approach (Muir and Tkalčić, 2015). We find that the 410 topography has strong degree-1 power, while the 660 topography and MTZ thickness are both dominated by degree-2 power. This is consistent with previous global SS precursor studies (e.g., Gu et al., 2003; Houser et al., 2008). This also suggests that our MTZ topography model is characterized by long wavelength structures such as the subduction zones in the western Pacific and south America, and hotspots in the Pacific.

These large-scale structures are in good agreement with previous global MTZ topography models, despite different stacking and inversion techniques are applied (Flanagan and Shearer, 1998; Gu et al., 2003; Lawrence and Shearer, 2006a, 2008; Houser and Shearer 2008; Deuss, 2009). Although long wavelength structures agree, the small-scale structures have poor consistency among the models, especially in the Pacific. Some of these discrepancies have been noted before (e.g., Deuss, 2009; Lessing et al., 2015) as a result of using different bin sizes, filter selection and data regularization, and choice of tomography models for the corrections. Full 3-D waveform modeling (e.g., Chaljub and Tarantola, 1997; Bai et al., 2010; Koroni et al, 2017) coupled with large and carefully selected SS waveform datasets will provide a way forward to both benchmark across methods, and assist in interpreting smaller scale structures associated with mantle heterogeneities.

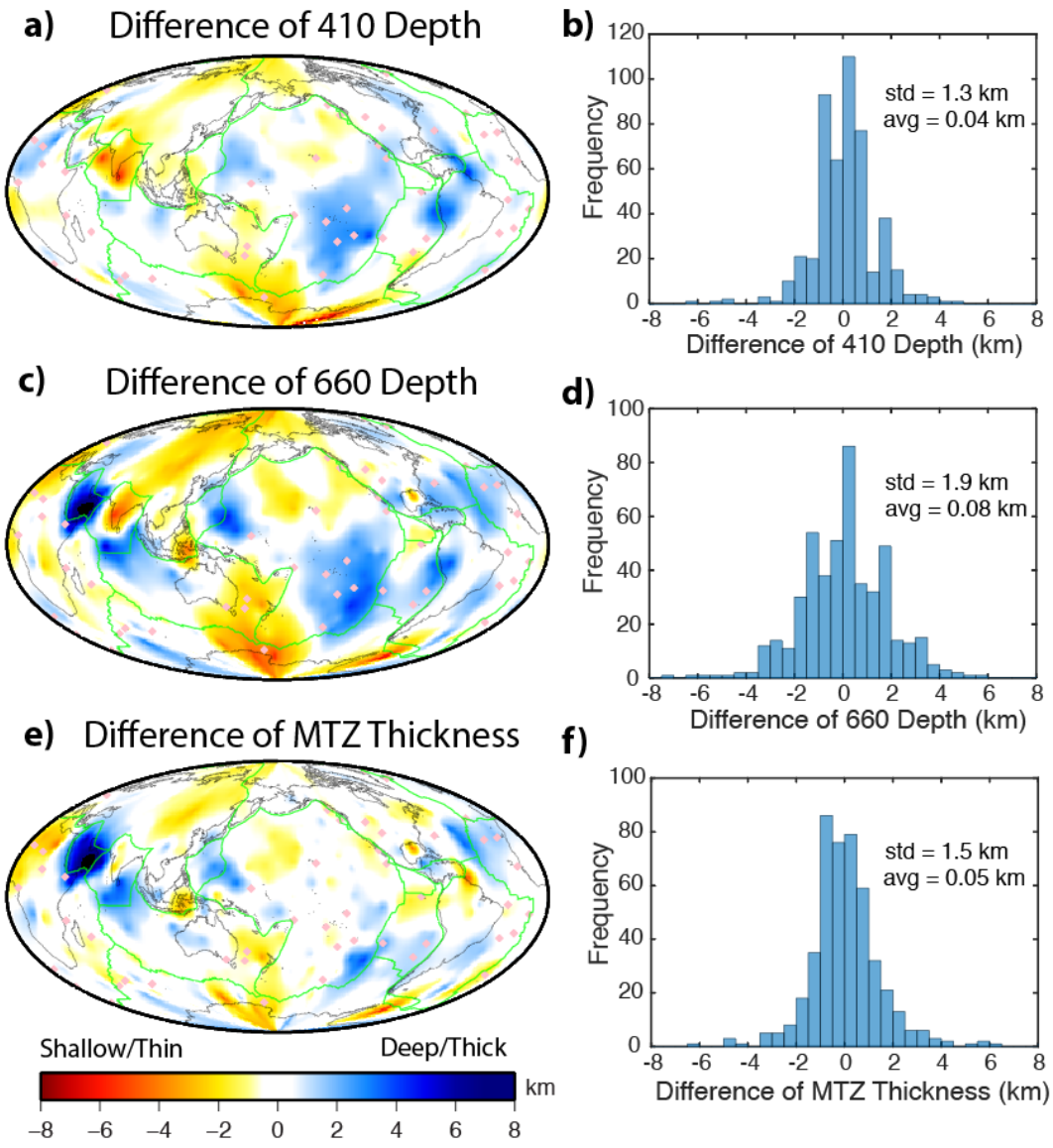

Figure 2.13 The difference of MTZ topography after the anisotropy correction. The map of the difference of a) 410 topography, c) 660 topography and e) MTZ thickness. The legend is the same as Figure 2.4. b, d, f) The histograms of the topography difference. The mean values (avg) and the standard deviations (std) are labeled in each panel.

2.5 Conclusions

Using a large global data set of SS precursors, we have mapped the global MTZ structure for 410 and 660 km depths, MTZ thickness, and MTZ anisotropy. We find that the MTZ is thickened beneath subduction zones, and thinned beneath hotspots; this is consistent with many previous studies, and confirms that temperature plays a key

role in the MTZ topography. We interrogate the azimuthal anisotropy in the upper mantle and transition zone at regional and global scales. In the central Pacific, we determine ~4% azimuthal anisotropy, with a SE fast direction in the upper mantle. We observe no significant azimuthal anisotropy within the MTZ beneath the central Pacific, consistent with a pattern of vertically dominated mantle flow in the MTZ. In the subduction zones, we detect ~4% anisotropy with a trench-parallel fast direction in the upper mantle. In the MTZ, we find ~3% anisotropy with a trench-perpendicular fast direction near slabs, which we attribute to the LPO of wadsleyite induced by the strong mantle flow near subduction zones. Globally, we observe ~1% azimuthal anisotropy in the upper mantle but no significant anisotropy in the MTZ. Thus, SS precursors suggest that the strength of azimuthal anisotropy in the MTZ is weaker than 1% at a global scale. We correct for upper mantle and MTZ anisotropy structures using surface wave anisotropy models, to obtain a more accurate MTZ topography model. The anisotropy correction corresponds to only $\pm$3 km difference in the MTZ topography, within the range of the uncertainties. However, the regional studies of MTZ topography in the western Pacific, southern Pacific and South America require corrections for the upper mantle and MTZ anisotropy structures.

Acknowledgements

The SS data set was downloaded from Incorporated Research Institutions for Seismology, Data Management Center (IRIS DMC). The SS data set and MTZ topography model are available at http://hdl.handle.net/1903/21819 (DOI: https://doi.org/10.13016/3ecr-1hsu). We thank the editors and two anonymous reviewers for constructive comments and suggestions. We also thank Vedran Lekić for

helpful discussions about spherical harmonic analysis and anisotropy inversions. QH, LW and NS were supported by National Science Foundation (NSF) grant EAR-1447041. LW is the recipient of a Discovery Early Career Research Award (DE170100329) funded by the Australian Government. CB was supported by NSF grant EAR-1446978.

Supporting Information

The supporting information includes the regional azimuthal stacking results in the northwestern Pacific, Greenland, and central Atlantic; global azimuthal stacking results in the oceanic and continental regions.

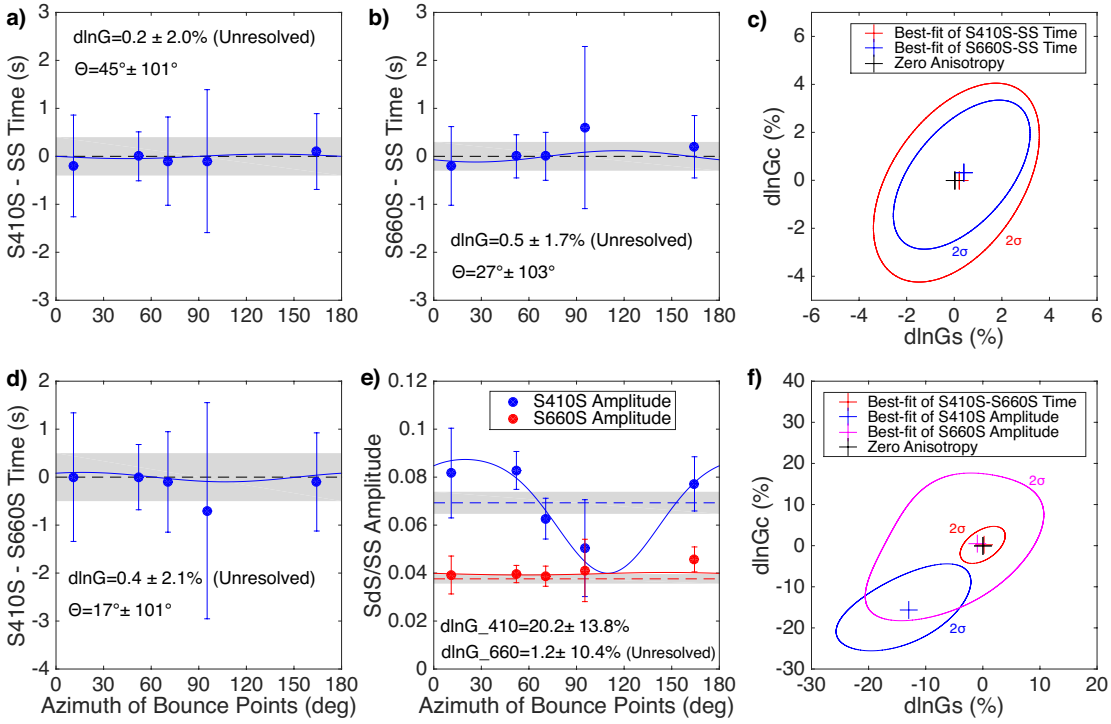

Figure 2.S1 Same as Figure 2.6 but for the northwestern Pacific region. The azimuthal bin between 120° and 150° is discarded due to the large uncertainties.

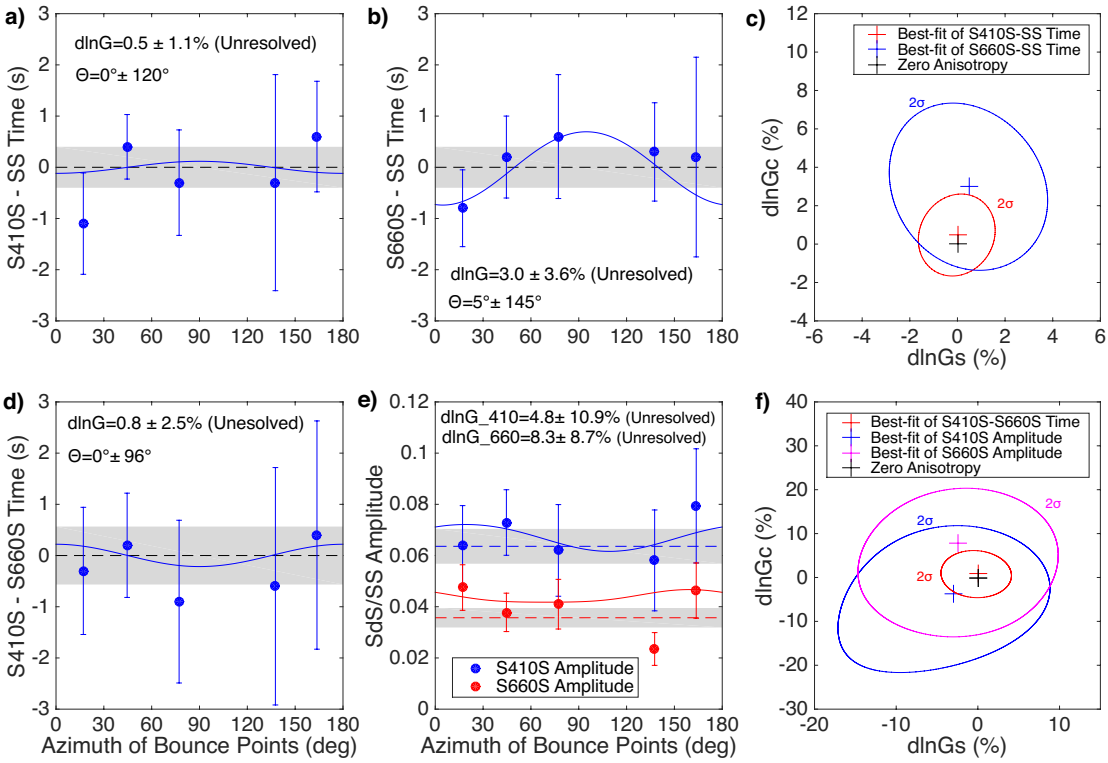

Figure 2.S2 Same as Figure 2.6 but for the Greenland region. The azimuthal bin between 90° and 120° is discarded due to the large uncertainties.

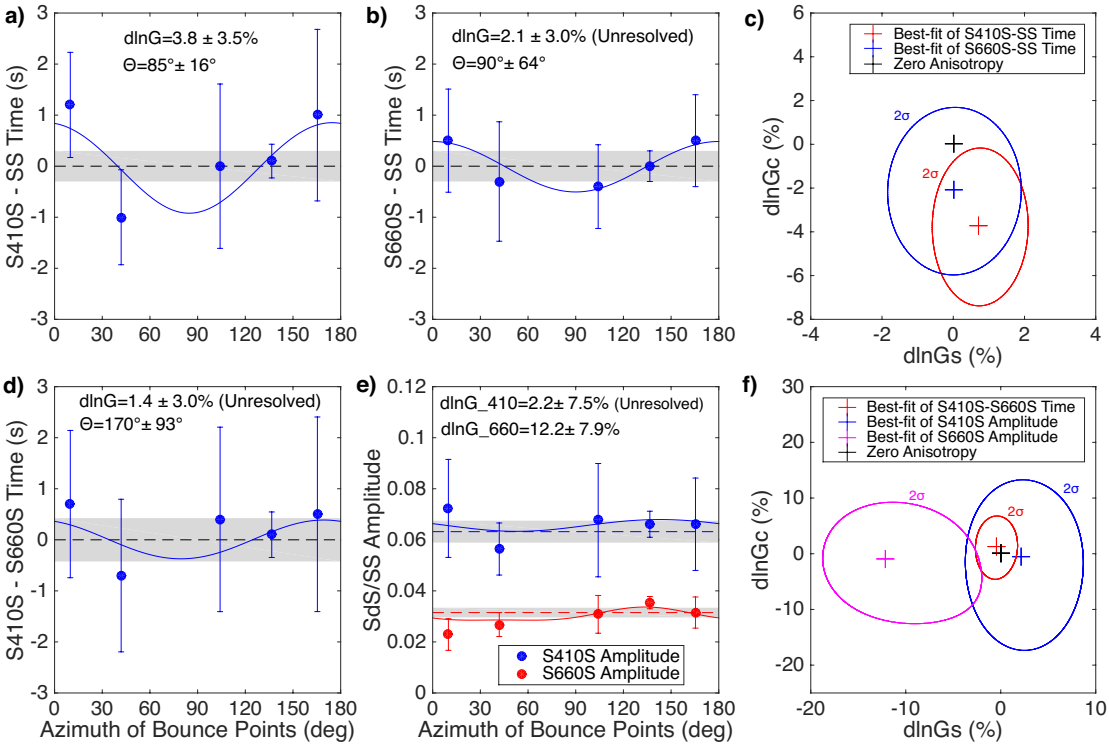

Figure 2.S3 Same as Figure 2.6 but for the central Atlantic region. The azimuthal bin between 60° and 90° is discarded due to the large uncertainties.

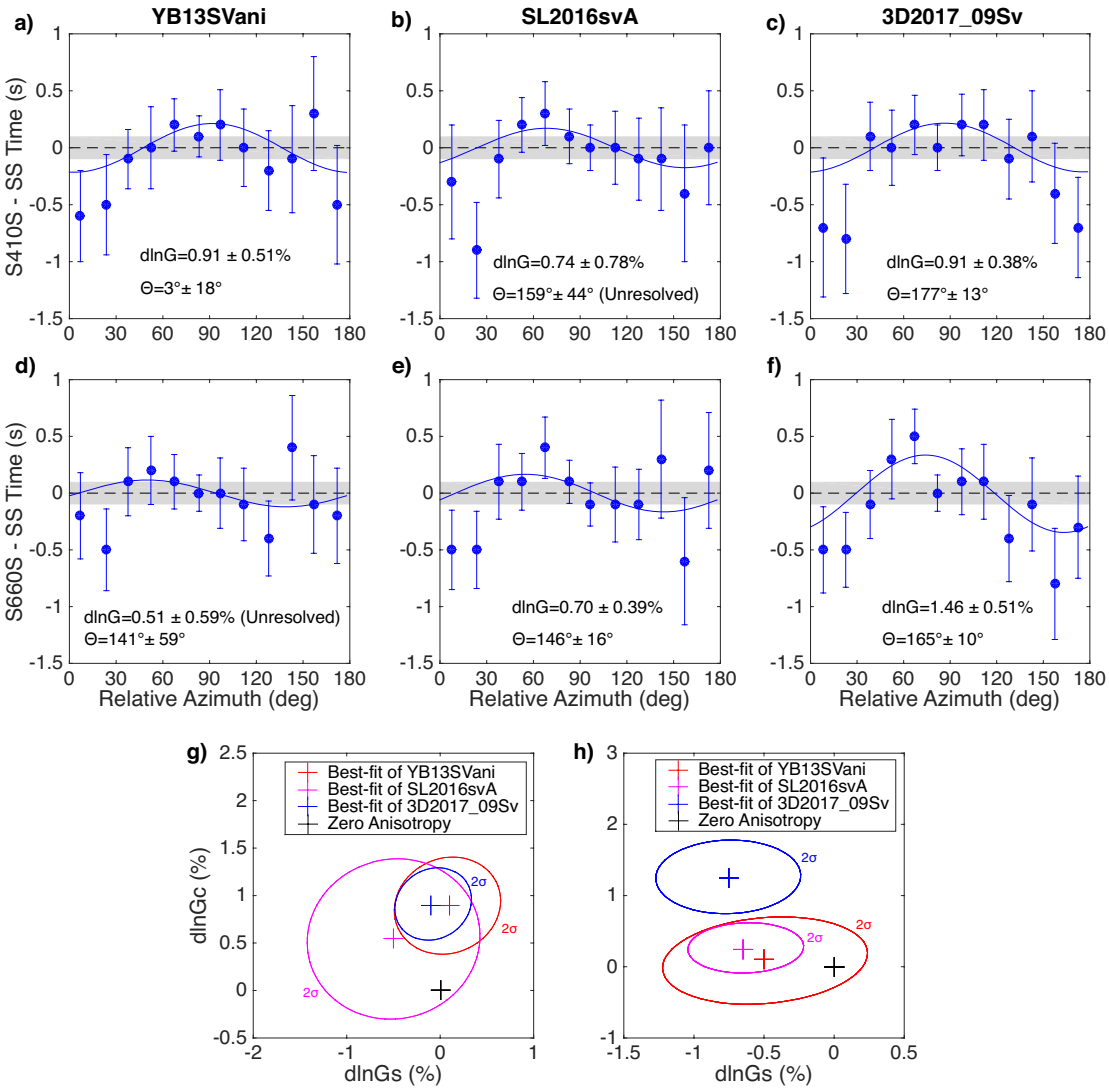

Figure 2.S4 Same as Figure 2.10 but for oceanic regions.

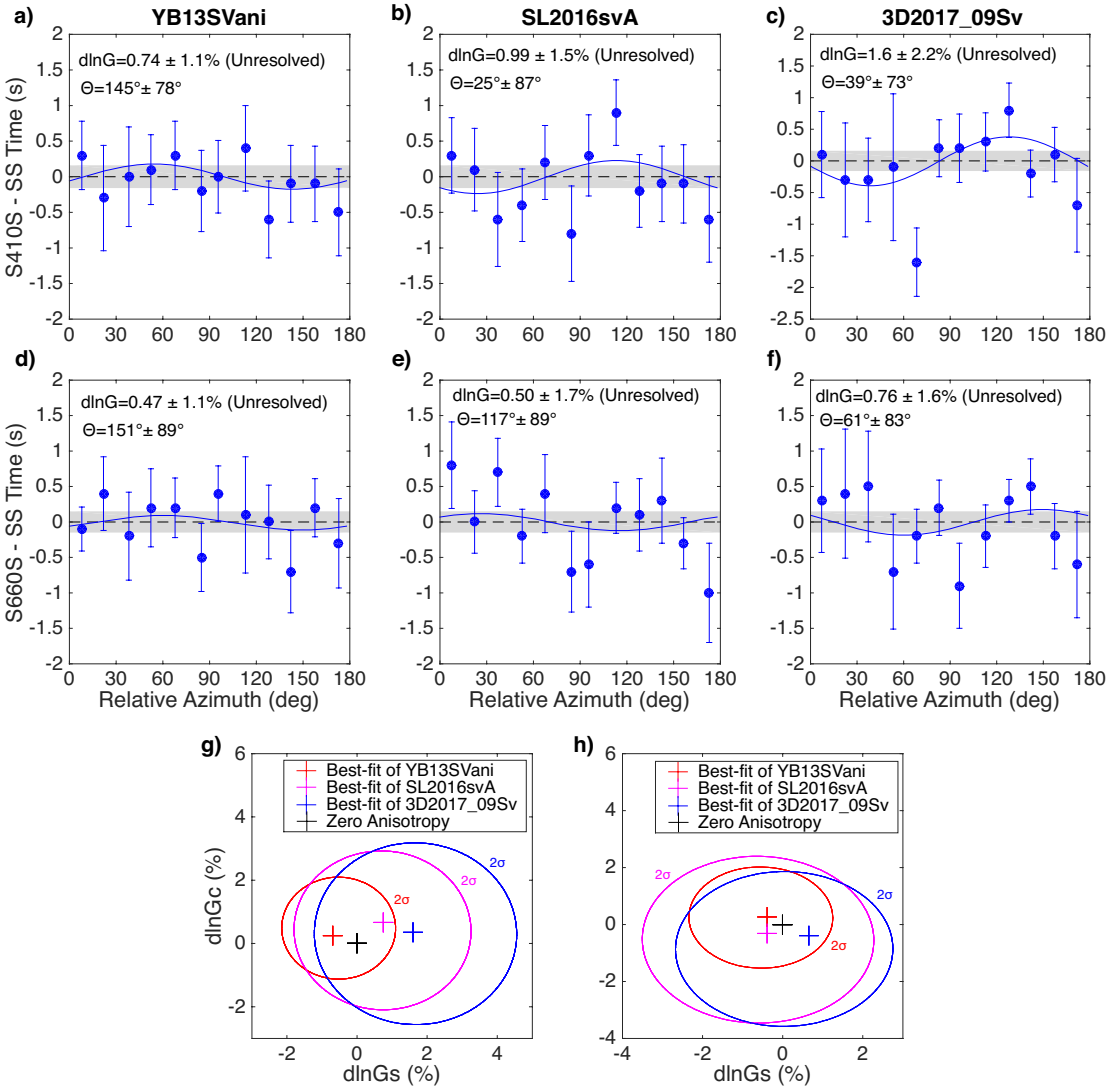

Figure 2.S5 Same as Figure 2.10 but for continental regions.

Chapter 3: 3-D Synthetic Modeling of Anisotropy Effects on SS Precursors: Implications for Mantle Flow in the Transition Zone

Abstract

The Earth's mantle transition zone (MTZ) plays a key role in the thermal and compositional interactions between the upper and lower mantle. Seismic anisotropy provides useful information about mantle deformation and dynamics across the MTZ. However, seismic anisotropy in the MTZ is difficult to obtain from surface wave or shear wave splitting measurements. Here, we investigate the sensitivity to anisotropy of a body wave method, SS precursors, through 3-D synthetic modeling. Our study shows that the SS precursors can distinguish the anisotropy originating from three depths: shallow upper mantle (80-220 km), deep upper mantle above 410-km, and MTZ (410-660 km). Synthetic resolution tests indicate that SS precursors can resolve ≥3% azimuthal anisotropy where data have an average signal to noise ratio (SNR=7) and azimuthal coverage is sufficient. To investigate regional sensitivity, we apply the stacking and inversion methods to two densely sampled areas: Japan subduction zone and a central Pacific region around the Hawaiian hotspot. We find evidence for a trench-perpendicular fast direction (Θ=87°) of MTZ anisotropy in Japan, but the strength of anisotropy is poorly constrained due to limited azimuthal coverage. We attribute the azimuthal anisotropy to lattice-preferred orientation of wadsleyite induced by trench-parallel mantle flow near the stagnant slab. In the central Pacific study region, there is a non-detection of MTZ anisotropy, although modeling suggests the data

coverage should allow us to resolve up to 3% anisotropy. Therefore, the Hawaiian mantle plume does not produce detectable azimuthal anisotropy in the MTZ.

3.1 Introduction

The Earth's mantle convection is strongly influenced by the properties of the mantle transition zone (MTZ), a distinct layer that controls the thermal and compositional exchange between the upper and lower mantle (e.g., Bercovici & Karato, 2003; Morgan & Shearer, 1993). The boundary of the MTZ is defined by two sharp seismic discontinuities at 410-km and 660-km depths. The formation of these discontinuities is a consequence of the pressure-induced phase changes of upper mantle mineral olivine. Mineral physics experiments show that the phase change of olivine to wadsleyite occurs at 410 km depth, and the dissociation of ringwoodite to bridgmanite + ferropericlase occurs at 660 km depth (Ita & Stixrude, 1992; Ringwood, 1975). The opposite Clapeyron slopes of the olivine phase changes (Ito & Takahashi, 1989; Katsura & Ito, 1989) make them useful for studying the mantle thermal and compositional heterogeneities (Bina & Helffrich, 1994; Helffrich, 2000; Stixrude, 1997) via mapping of MTZ topography (e.g., Flanagan & Shearer 1998).

The SS precursors are seismic body waves that manifest as shear wave reflections occurring at the underside of the 410-km and 660-km discontinuities (Figure 3.1). The SS precursors have served as a primary tool to investigate topography on these discontinuities at both regional (e.g., Schmerr et al., 2010; Thomas & Billen 2009; Yu et al., 2017) and global scales (e.g., Deuss & Woodhouse, 2002; Flanagan & Shearer, 1998; Gu & Dziewonski, 2002; Houser et al, 2008; Huang et al., 2019; Lawrence & Shearer, 2008). The SS precursors that reflect from the 410-km and 660-

km discontinuities are named as S410S and S660S respectively, or generally referred as SdS where d is the depth of discontinuity within the Earth. Several studies of the SS precursors have detected seismic anisotropy in the upper mantle and MTZ (Huang et al., 2019; Rychert et al., 2012, 2014). Seismic anisotropy, the dependence of seismic velocity on direction and polarization, is a useful tool to constrain mantle deformation and dynamics, and it is primarily produced by two key mechanisms: the lattice-preferred orientation (LPO) of intrinsically anisotropic minerals under a dislocation creep regime, or the shape-preferred orientation (SPO) of isotropic materials with distinct elastic properties (e.g., due to compositional layering or lenses of melt). Here we further evaluate the sensitivity of the SS precursors to mantle anisotropy, to assess the extent to which these seismic phases can provide insights into mantle deformation and dynamics in the MTZ.

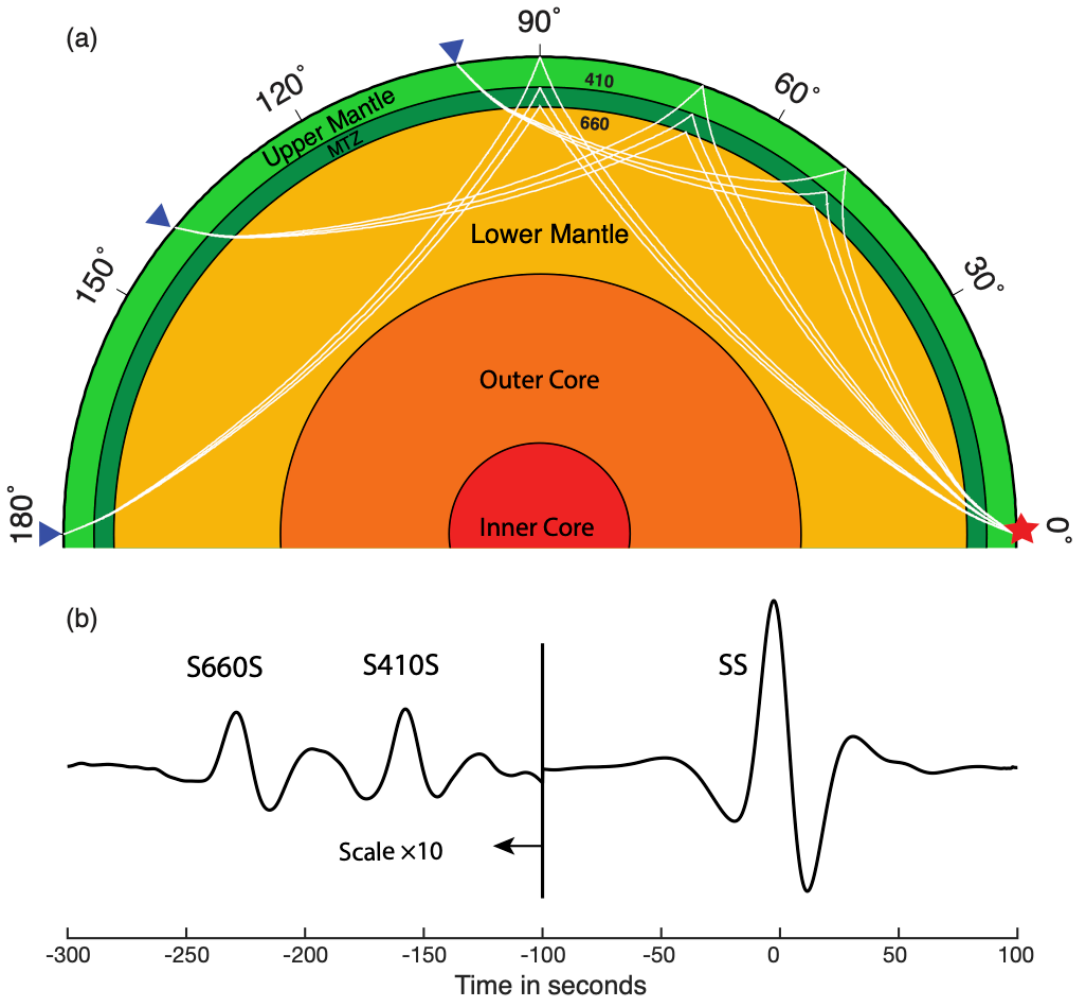

Figure 3.1 (a) Ray paths of SS phase and SS precursors at the epicentral distances of 100, 140 and 180 degrees. The red star and blue triangles represent the source and receivers respectively. (b) An example of stacked waveform of SS phase and SS precursors. The amplitudes of S410S and S660S are amplified by 10 times to facilitate comparisons with the SS phase.

Observations of upper mantle anisotropy are traditionally obtained from shear wave splitting (e.g., Long & van der Hilst, 2005; Marone & Romanowicz, 2007; Silver & Chan, 1988), surface wave dispersion (e.g., Anderson, 1962; Montagner & Nataf, 1986; Nettles & Dziewonski, 2008) and global tomography models (e.g., Chang et al., 2015; Gung et al., 2003; Moulik & Ekström, 2014). Upper mantle anisotropy is typically interpreted as the LPO of olivine (e.g., Karato et al., 2008) caused by current pattern of mantle flow in the asthenosphere or the preservation of paleo-flow directions

in the lithosphere (i.e., “fossil anisotropy”). At MTZ depths, evidence for seismic anisotropy is more limited, but consistently reported from multiple methods: shear wave splitting (Chen & Brudzinski, 2003; Foley & Long, 2011; Fouch & Fischer, 1996; Tong et al., 1994), surface wave measurements (Debayle et al., 2016; Trampert & van Heijst, 2002; Yuan and Beghein 2013, 2014, 2018), coupling of normal modes (Beghein et al., 2008), and inversion of deep earthquake focal mechanisms (Li et al., 2018). The surface wave models that incorporate higher mode surface waves (Debayle et al., 2016; Schaeffer et al., 2016; Yuan and Beghein, 2013, 2014) suggest that ~1% azimuthal anisotropy exists in the MTZ globally, despite regional discrepancies amongst these models. Recently, Ferreira et al. (2019) discovered ubiquitous radial anisotropy in the MTZ and uppermost lower mantle in the vicinity of western Pacific subduction zones. Our previous study using SS precursors (Huang et al., 2019) also found regional evidence for 3% azimuthal anisotropy in the MTZ beneath subduction zones but detected negligible anisotropy (< 1%) at a global scale.

Unlike the upper mantle, where deformation is expressed in the LPO of the mineral olivine, the MTZ may have several mechanisms for accommodating seismic anisotropy. For example, the MTZ anisotropy in subduction zones has primarily been attributed to the LPO of wadsleyite (Kawazoe et al., 2013), although the SPO of subducting slabs has also been proposed (Faccenda et al., 2019). In the upper transition zone (410-520 km), wadsleyite has up to ~14% single-crystal Vs anisotropy (Sawamoto et al., 1984; Sinogeikin et al., 1998; Zha et al., 1997), making wadsleyite the main candidate mineral for accommodating anisotropy at these depths. Below 520 km, ringwoodite is nearly isotropic with a cubic structure (Kiefer et al., 1997; Li et al.,

2006; Sinogeikin et al., 2003; Weidner et al., 1984). Other minerals such as majorite garnet and clinopyroxene have either weak single-crystal anisotropy, or not enough mineral fraction abundance to accommodate the seismic observations of MTZ anisotropy (Bass and Kanzaki, 1990; Pamato et al., 2016; Sang and Bass, 2014). Slab mineralogy and layering may provide an alternative mechanism for accommodating anisotropy in the deep transition zone (Faccenda et al., 2019). Although wadsleyite can accommodate up to 14% anisotropy, it must be aligned by mantle dynamics into a fabric detectable by seismic waves. Numerical simulations of strain-induced fabric of mantle mineral aggregates are therefore key to understanding the relationship between mantle flow direction (or strength) and fast direction (or strength) of seismic anisotropy in the MTZ. Previous modeling has focused primarily on the upper mantle anisotropy (e.g., Becker et al., 2006), whereas few studies explore deeper anisotropy in the MTZ and uppermost lower mantle (Faccenda, 2014; Sturgeon et al., 2019). For example, Sturgeon et al. (2019) predicts that up to ~2% Vs radial anisotropy may form in the MTZ beneath subduction zones. Mineral physics modeling by Tommasi et al. (2004) predicts that ~1% Vs azimuthal anisotropy can exist within the MTZ.

Although the sensitivities of SS precursors to the topography of 410-km and 660-km discontinuities have been investigated (Bai et al., 2012; Koroni & Trampert, 2016; Zhao & Chevrot, 2003), their sensitivity to azimuthal anisotropy at MTZ depths remains unexplored. Motivated by both geodynamic and mineral physics predictions, we use SS precursors to better constrain anisotropy at MTZ depths, thereby illuminating the dynamics of the upper mantle. In this study, we construct 3-D models of anisotropy and propagate synthetic seismic waves through the model to test the

sensitivity of SS precursors to azimuthal anisotropy. We next compare the results of our modeling to observations in the central Pacific region and Japan subduction zone to determine the detectability and sensitivity of the SS precursory phases to MTZ anisotropy. Finally, we interpret the mantle flow pattern in the MTZ in the context of our observations.

3.2 Methods

3.2.1 SS Dataset

We expanded a global hand-picked SS dataset described in Huang et al. (2019) and Waszek et al. (2018) to include earthquakes in the depth range 0-75 km (previously only 0-30 km) and broadband stations from 1988 to 2017. Any records with signal-to-noise ratio (SNR), which was computed from the amplitude of SS phase over the maximum amplitude in a noise window (65 to 275 seconds before SS phase), lower than 2.5 were removed from the dataset. The final SS dataset consists of 58,566 seismograms. We used the transverse component of the data to study the azimuthal anisotropy. To remove seismic noise, we filtered the data between 15 and 50 s using a Butterworth band-pass filter and aligned the waveform at the peak amplitude of SS phase. Each SS seismogram was normalized to unity to equalize the SS arrivals across events and stations.

3.2.2 3-D Synthetics

We used the spectral element code SPECFEM3D_GLOBE (Komatitsch & Tromp, 2002 a, b) to compute 3-D synthetic SS precursor waveforms. The mesh consisted of 6 chunks with 320 spectral elements on each side. Therefore, the minimum

period of the synthetics was 13.6 seconds. We created 13 earthquakes around the target region to provide ideal azimuthal coverage (Figure 3.2 & 3.3). The focal mechanism of each earthquake was set to maximize the SH energy in the receiver direction. We chose a dense array to guarantee ideal azimuthal coverage as well. After computing the synthetics, we generated random noise based on the realistic power spectrum of Earth's noise (Peterson 1993) and added it to the synthetics. The synthetics were then processed in the same way as the data in section 3.2.1.

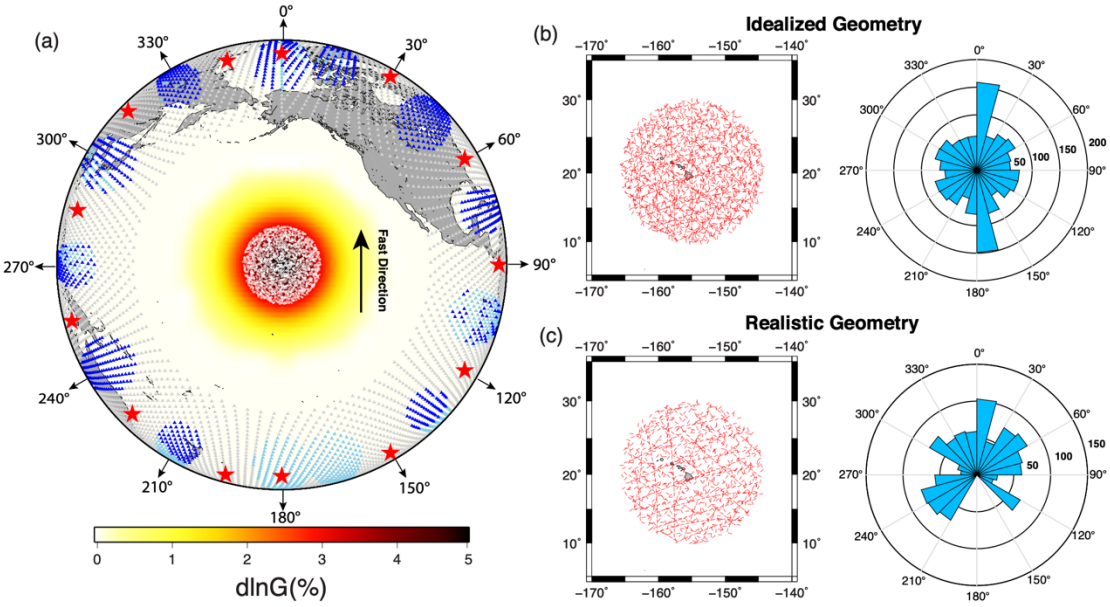

Figure 3.2 (a) Source-receiver geometry for the model in the central Pacific region. The red stars denote the earthquake sources. The input fast direction is due north (0°). The triangles represent all the stations: the light blue + dark blue stations are the ones used for the idealized geometry; the dark blue stations only are the ones used for the realistic geometry; the grey stations are the unused ones. The white points in the center are the SS bounce points with a bin radius of 10 degrees (~1100 km). (b) The SS bounce points in the idealized geometry (left) and their azimuthal distribution (right). (c) The SS bounce points in the realistic geometry (left) and the azimuthal distribution of the bounce points (right) which mimics the azimuthal coverage of data in this region.

We chose two study regions that are densely sampled by the SS phase: (1) the central Pacific region near Hawaii (Figure 3.2) and (2) Japan subduction zone (Figure 3.3). The goal was to simulate the azimuthal anisotropy generated by a mantle plume versus a subducting slab. In each region, we created two types of source-receiver

geometries: idealized, and realistic geometry. The idealized geometry provided at least 100 records in each 15° azimuthal bin to ensure enough data for the stacking of SS precursors. The realistic geometry was a subset of the idealized geometry to mimic the actual azimuthal coverage of the data that sample each region. This anisotropic structure was introduced over the Preliminary Reference Earth Model (PREM, Dziewonski & Anderson, 1981) at three depth ranges: (1) the shallow upper mantle (80 – 220 km); (2) the deep upper mantle (250 – 400 km); (3) the MTZ (400 – 670 km). The boundaries of these layers coincide with the discontinuities in PREM such as 220-, 400- and 670-km discontinuities. The models at each depth included three strengths of anisotropy: 1%, 3% and 5%. The input fast directions were due north (0°) in the central Pacific bin and trench perpendicular (270°) in the Japan bin. We set the radius of the central Pacific bin to 10 degrees (~1100 km) and the size of Japan bin was 1500 × 1000 km. The choice in size of the central Pacific structure was controlled by the standard deviation of normal distribution, and we explored the effects of lateral size of anisotropic structures on resolution using 5- and 2.5-degrees radius.

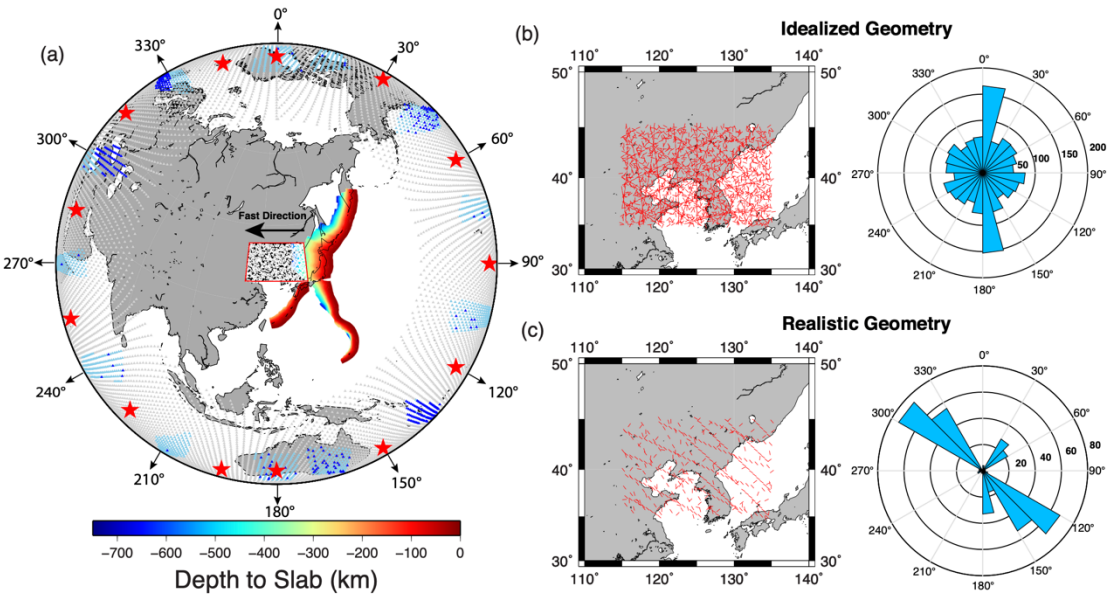

Figure 3.3 (a) Source-receiver geometry for the model in Japan subduction zone. The source, receiver and bounce point legends are the same as Figure 3.2. The study region is highlighted by the red box and the size is 1500 km×1000 km. The strength of anisotropy is a uniform value thus represented in black color and the fast direction is trench-perpendicular (270°). The values of slab depths are from Slab 1.0 model (Hayes et al., 2012). (b) The SS bounce points in the idealized geometry (left) and their azimuthal distribution (right). (c) The SS bounce points in the realistic geometry (left) and their azimuthal distribution (right).

3.2.3 Stacking and Corrections

SS precursors are typically similar in amplitude to background noise or less, thus their retrieval requires stacking when noise is present. Here, we followed the stacking methods of Schmerr and Garnero (2006) to stack the precursors along the predicted travel-time curves from PREM. We chose 125 degrees as our reference distance and applied distance exclusion windows (0°-100° and 135°-145° for S410S; 0°-115° and 165°-180° for S660S) to avoid interferences of other seismic phases. We stacked the data by azimuth of the ray-path at the central bounce-point of SS to study the azimuthal variations of SS precursor travel-times and amplitudes. The 2σ uncertainties of travel-time and amplitude measurements were estimated from a

bootstrapping technique that implemented 300 resamples, allowing replacements within each bin (Efron & Tibshirani, 1986).

We applied a series of travel-time and amplitude corrections to ensure that precursor travel-times and amplitudes were not contaminated by factors other than anisotropy, and then inverted for azimuthal anisotropy. Full details regarding travel-time and amplitude correction methods are contained in Huang et al. (2019). (1) The travel-times of SS precursors are affected by the lateral heterogeneities of crustal and upper mantle structures. We used CRUST 2.0 model (Bassin et al., 2000) for the crustal corrections and S40RTS model (Ritsema et al., 2011) for the tomography corrections. We computed travel-time residuals with respect to PREM based on 1-D ray tracing as pre-stacking travel-time corrections for each individual record. (2) We also corrected for the travel-time perturbations caused by topography of 410-km and 660-km discontinuities using the MTZ topography measurements by Huang et al. (2019). We computed the topography corrections from the differences between the local 410-km, 660-km depths and their global mean depths. (3) The amplitudes of SS precursors were corrected for attenuation, geometrical spreading, and focusing and defocusing effect using the 1-D synthetics generated by GEMINI code (Friederich and Dalkolmo, 1995). We calculated the amplitude ratios between the stacking results of data and corresponding 1-D synthetics and multiplied by the amplitudes at reference distance (125°) to remove these effects on amplitudes. The observed data were corrected for both travel-time and amplitude, but the 3-D SPECFEM synthetics were only corrected for amplitude.

3.2.4 Inversion for Azimuthal Anisotropy

After applying the amplitude and travel time corrections, we inverted for the strength and fast direction of azimuthal anisotropy from SdS travel-times and amplitudes. In a transversely isotropic medium with a horizontal symmetry axis, the velocity of vertically propagating SH wave is expressed as the following equations (Crampin, 1984; Montagner and Nataf, 1986):

$$\rho V_{qSH}^2 = L - G_c cos2\psi - G_s sin2\psi \tag{3.1}$$

$$L = \rho V_{SV}^2 = \frac{1}{2}(C_{44} + C_{55}) \tag{3.2}$$

where ρ is density, V_{qSH} is the velocity of quasi-SH wave, ψ is the azimuth of wave propagation direction, L is a function of the isotropic SV wave velocity and can be expressed as elastic parameters C_{ij}, $Gc = \frac{1}{2}(C_{55} - C_{44})$ and $Gs = C_{54}$ are the 2ψ azimuthal terms of L (Montagner et al., 2000). The strength of anisotropy (G) and fast direction (Θ) are derived from the G_c and G_s parameters:

$$G = \sqrt{G_s^2 + G_c^2} \tag{3.3}$$

$$\Theta = \frac{1}{2} arctan\left(\frac{G_s}{G_c}\right) \tag{3.4}$$

First, we built simple 1-D anisotropy models with constant G_c and G_s values at the three depth ranges mentioned in section 3.2.2. Then, we computed the predicted travel-times and amplitudes based on equation (3.1) and (3.2). Finally, we used a grid-search method to find the best-fitting G_c and G_s values and used equation (3.3) and (3.4) to compute the best-fitting fast direction and strength of anisotropy. The uncertainties of the anisotropy fit are estimated from the chi-squared statistics using p-values for 2 standard deviations.

3.3 Results

In this section, we first investigated the effect of depth, strength, and size of anisotropy on measurement resolution using clean synthetics in the central Pacific region. Next, we examined the data in the central Pacific region and Japan subduction zone from which we inverted azimuthal anisotropy and quantified the uncertainties. Finally, we added realistic noise to the 3-D synthetics for direct comparison to the data, and we also explored the effect of source-receiver geometry on the resolution.

3.3.1 Effects of Depth, Strength and Size of Anisotropy

Unlike shear wave splitting measurements, SS precursors can distinguish the depths of anisotropy structures based on the combinations of five differential travel-time and amplitude ratio measurements: S410S-SS time, S660S-SS time, S660S-S410S time, S410S/SS and S660S/SS amplitudes. In order to understand the effect of depth, we fixed the size of anisotropic region to be 10-degrees in radius and varied in depth extent. We then performed the following synthetic tests.

Test (1): Shallow Upper Mantle, Fixed Size. The first experiment simulates anisotropy in the asthenosphere (80-220 km), which is often attributed to the LPO of olivine (Figure 3.4a). The SS travel-times are sensitive to the asthenosphere anisotropy and their variations are mapped to S410S-SS (Figure 3.4b) and S660S-SS travel-times (Figure 3.4c) since SS is our reference phase. The S660S-S410S time (Figure 3.4d) and amplitudes (Figure 3.4e) remain constant because their ray paths do not encounter the anisotropic layer.

Test (2): Deep Upper Mantle, Fixed Size. The second case creates the scenario where anisotropy is present in the deep upper mantle (250-400 km, Figure 3.5a), which

can still be caused by the fabric of olivine (e.g., Mondal and Long, 2020). In this model, the S410S/SS amplitude starts to vary with azimuth due to the change of reflection coefficients at 410-km (Figure 3.5e), whereas the S660S-S410S time (Figure 3.5d) and S660S/SS amplitudes (Figure 3.5e) still remain constant.

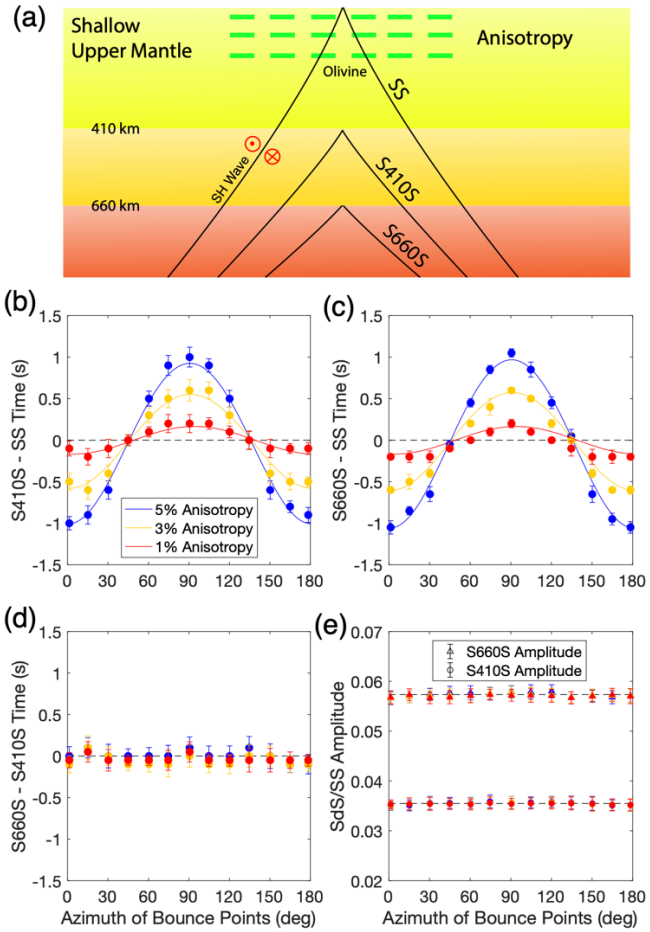

Figure 3.4 (a) The anisotropy model in the shallow upper mantle (80-220 km). The green bars represent the LPO of olivine. The black curves are the ray paths of SS precursors beneath the bounce point region. The measurements of (b) S410S – SS time, (c) S660S – SS time, (d) S660S – S410S time, (e) S410S/SS and S660S/SS amplitudes from the azimuthal stacking of SPECFEM3D synthetics as a function of bounce point azimuths. The solid lines are the best-fitting models for 1%, 3% and 5% input anisotropy. The dashed lines denote the mean values of each measurement.

Test (3): MTZ anisotropy, Fixed Size. The final scenario models an anisotropic layer in the MTZ where the LPO of wadsleyite and ringwoodite are formed (Figure 3.6a). The S660S-S410S time becomes an independent measurement for MTZ anisotropy (Figure 3.6d) which is not affected by the upper mantle anisotropy. This model includes anisotropy throughout the whole MTZ so both S410S/SS and S660S/SS amplitudes (Figure 3.6e) display variations with azimuth. These two amplitudes have

opposite trends because the MTZ anisotropy is below the 410-km but above the 660-km discontinuities, therefore changing the signs of reflection coefficients.

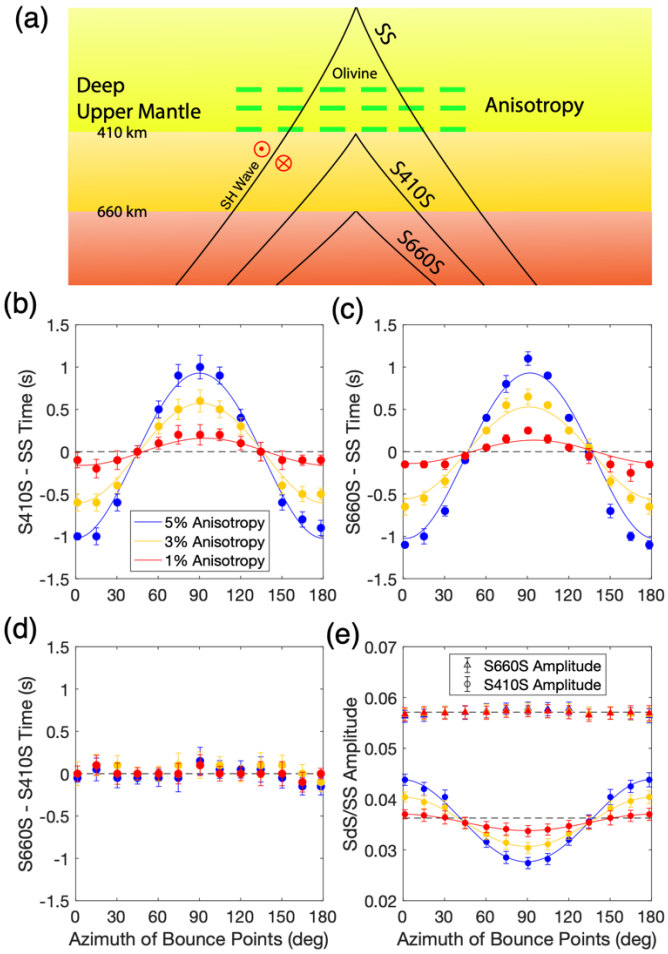

Figure 3.5 (a) Same as Figure 3.4 but for anisotropy model in the deep upper mantle (250 – 400 km). The measurements of (b) S410S – SS time, (c) S660S – SS time, (d) S660S – S410S time, (e) S410S/SS and S660S/SS amplitudes from the azimuthal stacking of SPECFEM3D synthetics as a function of bounce point azimuths.

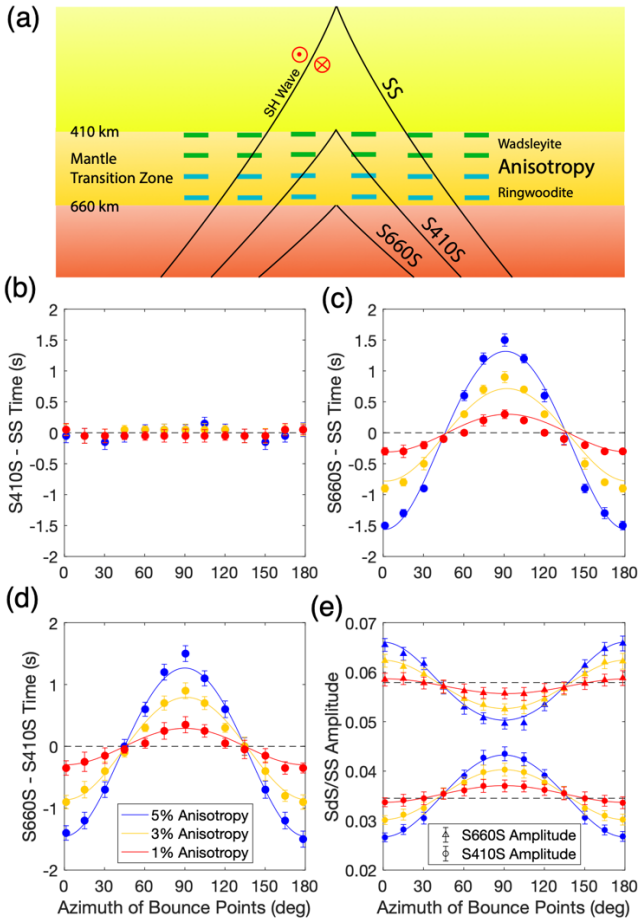

Figure 3.6 (a) Same as Figure 3.4 but for anisotropy model in the MTZ (400 – 670 km). The green and blue bars represent the LPO of wadsleyite and ringwoodite respectively. The measurements of (b) S410S – SS time, (c) S660S – SS time, (d) S660S – S410S time, (e) S410S/SS and S660S/SS amplitudes from the azimuthal stacking of SPECFEM3D synthetics as a function of bounce point azimuths.

Test (4): Fixed Depth in the MTZ, Varied Size: The strength and size of anisotropy control the peak-to-peak amplitudes of SdS travel-time and amplitude variations. In this test, the bin radius was fixed at 10 degrees and the anisotropy layer was in the MTZ. Then, we varied the strength and size of anisotropy and identified four measurements that were sensitive to MTZ anisotropy: S660S-SS time (Figure 3.7a), S660S-S410S time (Figure 3.7b), S410S/SS and S660S/SS amplitude (Figure 3.7c).

The first column of Figure 3.7 shows that 3-5% MTZ anisotropy with 10-degree radius can translate into 0.9-1.5 seconds travel-time variations respectively. Generally, the variations caused by anisotropy need to be greater than the corresponding uncertainties of SdS travel-times or amplitudes to become detectable. The amplitudes

of uncertainties are directly related to the noise level in the data or synthetics. We estimated the average 2σ uncertainties by adding random noise (SNR=7, average noise level of our SS dataset) to synthetics before stacking (see section 2.2). The average uncertainties, which are shown as gray shaded regions in Figure 3.7, can be used as detection thresholds for SdS travel-times and amplitudes. When the radius is 10 degrees, Figure 3.7 illustrates that the S660S-SS and S660S-S410S times can both detect $\geq$3% anisotropy. The uncertainties of SdS amplitudes are generally larger in terms of percentage so anisotropy is more difficult to detect, requiring over 5% anisotropy to be detectable. Moving from left to right in Figure 3.7, the peak-to-peak amplitudes of SdS travel-times and amplitudes both decrease as the size of the structure is reduced. When the radius is decreased to 5 degrees, the S660S-SS and S660S-S410S times can only detect $\geq$5% anisotropy, whereas the variations of SdS amplitudes are below the detection thresholds. The 2.5-degrees radius structures are too small to be detectable because all the variations become much lower than the detection thresholds.

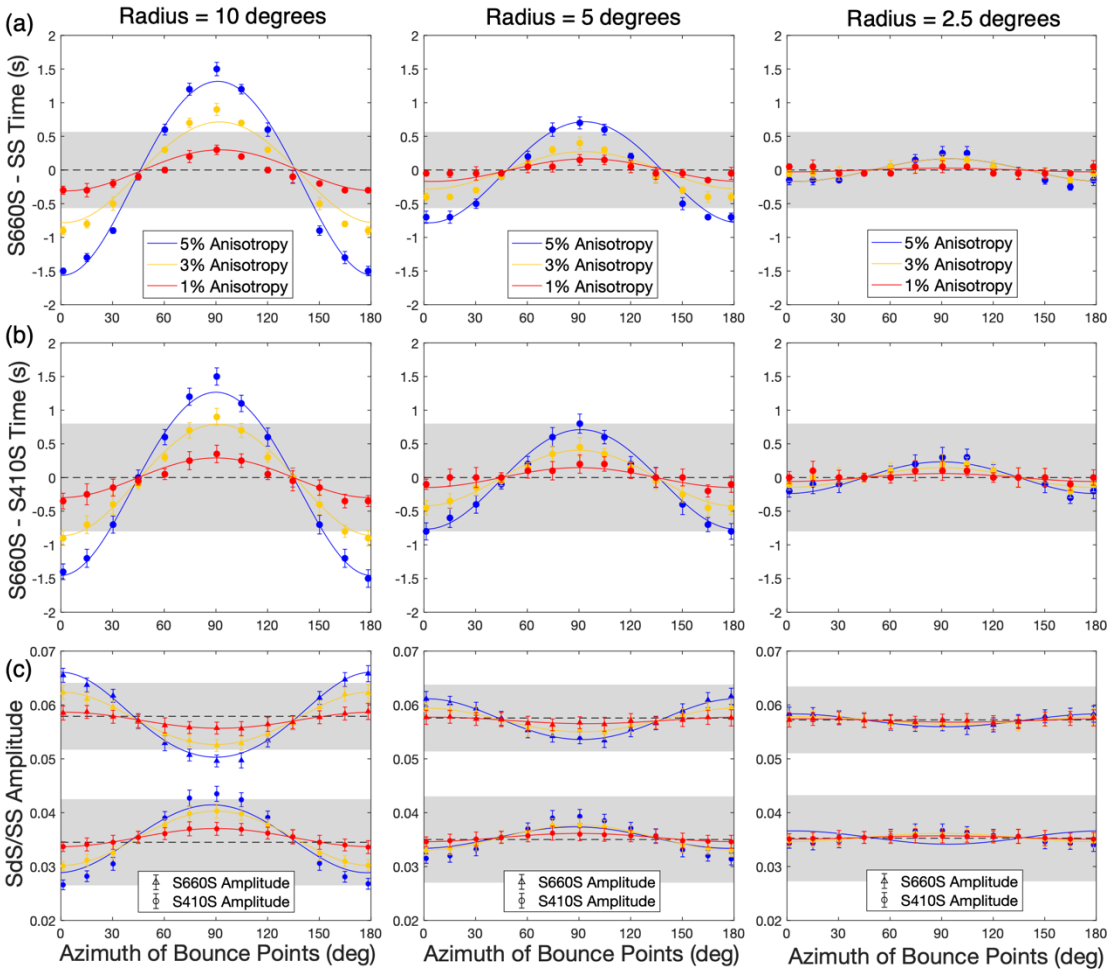

Figure 3.7 Effects of anisotropy size and strength on SS precursors. The measurements of (a) S660S – SS time, (b) S660S – S410S time, (c) S410S/SS and S660S/SS amplitudes as a function of bounce point azimuths. The radius of anisotropy decreases from 10 degrees to 5 degrees and 2.5 degrees from left to right, whereas the bin radius remains 10 degrees. The depth of anisotropy is in the MTZ (400 – 670 km). The solid lines represent the best-fitting models for 1%, 3% and 5% input anisotropy. The dashed lines denote the mean values of each measurement. The gray shaded regions represent the detection thresholds for SdS travel-times and amplitudes estimated from the stacking of synthetics with average noise level (SNR=7).

3.3.2 Central Pacific Data and Resolution Test

Following the depth, strength, and size 3-D synthetic tests, we used our modeling to study the detectability of anisotropy for an SS precursor dataset sampling the central Pacific region. In Figure 3.8a, the MTZ thickness beneath the central Pacific bin is thinner than average predominantly due to the hot thermal anomalies caused by the Hawaiian hot spot (e.g., Schmerr et al., 2010). This bin has sufficient azimuthal

coverage and number of records (NR > 100) in five azimuthal bins (Figure 3.8c), therefore both S410S and S660S were observed in data and synthetics from azimuthal stacking (Figure 3.8b). We measured the S660S-S410S times from the azimuthally stacked data results and inverted for azimuthal anisotropy after removing topography variations. As shown in Figure 3.8d, the recovered strength of anisotropy (dlnG=2.9±2.8%) is not significantly above zero based on the chi-squared statistics, which suggests that the central Pacific region has very weak MTZ anisotropy.

To further test the weak anisotropy hypothesis, we added noise to the 3-D synthetics (see Section 3.2.2) with different SNR values, using both idealized and realistic geometries to explore the effect of data coverage in the central Pacific region (Figure 3.2). The goal was to test the resolution of the SS precursors in the central Pacific region and determine the minimum strength of anisotropy that would provide a detectable signal in the data. To quantify detectability of anisotropy, we define a parameter ε as the total misfit of the best-fitting model compared to the input anisotropy model:

$$\varepsilon_G = \sqrt{\left(\frac{dlnG_{out} - dlnG_{in}}{dlnG_{in}}\right)^2 + \left(\frac{2\sigma_G}{dlnG_{out}}\right)^2} \tag{3.5}$$

$$\varepsilon_\Theta = \sqrt{\left(\frac{\Theta_{out} - \Theta_{in}}{\pi/2}\right)^2 + \left(\frac{2\sigma_\Theta}{\pi/2}\right)^2} \tag{3.6}$$

where ε_G and ε_Θ are the total misfit for strength of anisotropy and fast direction respectively, $dlnG_{in}$ and Θ_{in} are the input strength of anisotropy and input fast direction respectively, $dlnG_{out}$ and σ_G are the best-fitting strength of anisotropy and

1σ error from inversions respectively, Θ_{out} and σ_{Θ} are the best-fitting fast direction and 1σ error respectively. ε can quantify detectability of anisotropy as it takes into account the misfit between the input and best-fitting anisotropy parameters, and the uncertainties of the best-fitting model as well. ε is a positive value, and if $\varepsilon < 1$, we define this scenario as a detectable case. Conversely, if $\varepsilon \geq 1$, we define this scenario as a non-detectable case. Since ε represents the misfit of the best-fitting model, the larger this value is, the lower the detectability.

For the idealized geometry models, the detectability of anisotropic variations from SdS travel times and amplitudes are shown in Figure 3.9. Generally, the detectability of anisotropy increases as the input anisotropy increases or the noise level decreases. Figure 3.9a illustrates that the S660S-S410S time can detect 3% anisotropy with intermediate level of noise (SNR=7). Figure 3.9b suggests that the S660S-SS time has better resolution and can detect 3% anisotropy even with higher levels of noise (SNR=4). However, our tests with shallow anisotropy demonstrates that S660S-SS time is also potentially affected by the upper mantle structure (Figure 3.4c), so it is not a unique indicator for MTZ anisotropy. The test also indicates that S410S and S660S amplitudes have lowered resolutions compared to the travel-time metrics. The S410S amplitude can only resolve 5% anisotropy with intermediate level of noise (Figure 3.9c), and the detectability of anisotropy with the S660S amplitude is always low even when noise is absent (Figure 3.9d). When using a more realistic geometry model, detectability is further degraded due to the lack of stations in the southern Pacific (Figure 3.10). However, despite the incomplete azimuthal coverage, our tests prove that the S660S-S410S time should present a detectable travel-time anomaly where there

is 3% anisotropy in the central Pacific region (Figure 3.10a). The conclusion is that the central Pacific data have the potential to resolve 3% or greater anisotropy but the data failed to detect an anomaly of this magnitude, and as a result, the azimuthal anisotropy in this region is likely to be smaller than 3%.

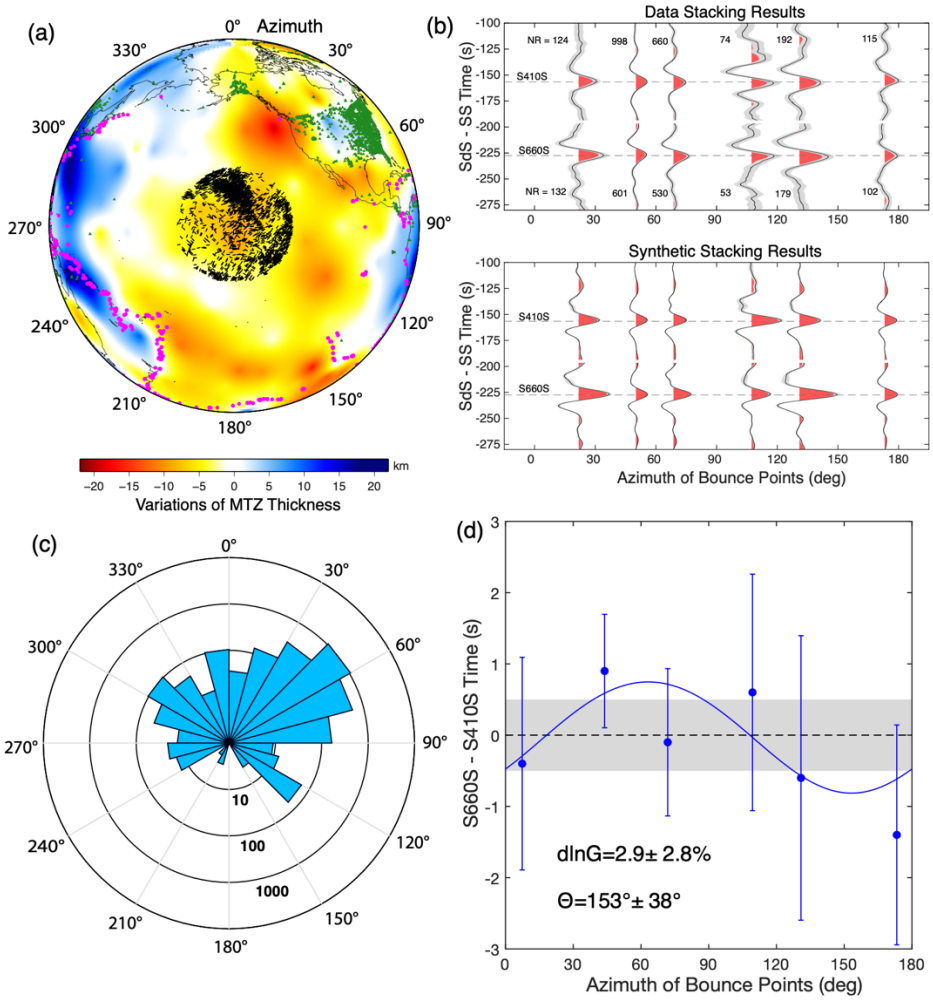

Figure 3.8 (a) Central Pacific bin of SS precursor data superimposed on the MTZ topography map. The MTZ thickness from Huang et al. (2019) is expressed as the variations with respect to the mean value 244.4 km. The black bars represent the SS bounce points and the azimuths of SS ray paths. The radius of the bin is 2000 km. The pink circles denote the earthquakes and the green triangles represent the stations. (b) The azimuthal stacking results of the data (top) and synthetics (bottom) in the central Pacific bin. The number of records (NR) of each azimuthal bin is labelled beside the waveform. The dashed lines highlight the average SdS travel times. (c) Rose diagram showing the azimuthal coverage of SS bounce points in log scale. (d) The S660S – S410S times and 2σ errors shown as a function of azimuth. The solid line is the best-fitting model. The dlnG and Θ values are the best-fitting strength of anisotropy and fast direction respectively. The dashed line is the average S660S-S410S time from the stacking of all azimuthal bins, and gray shaded box is the corresponding 2σ errors.

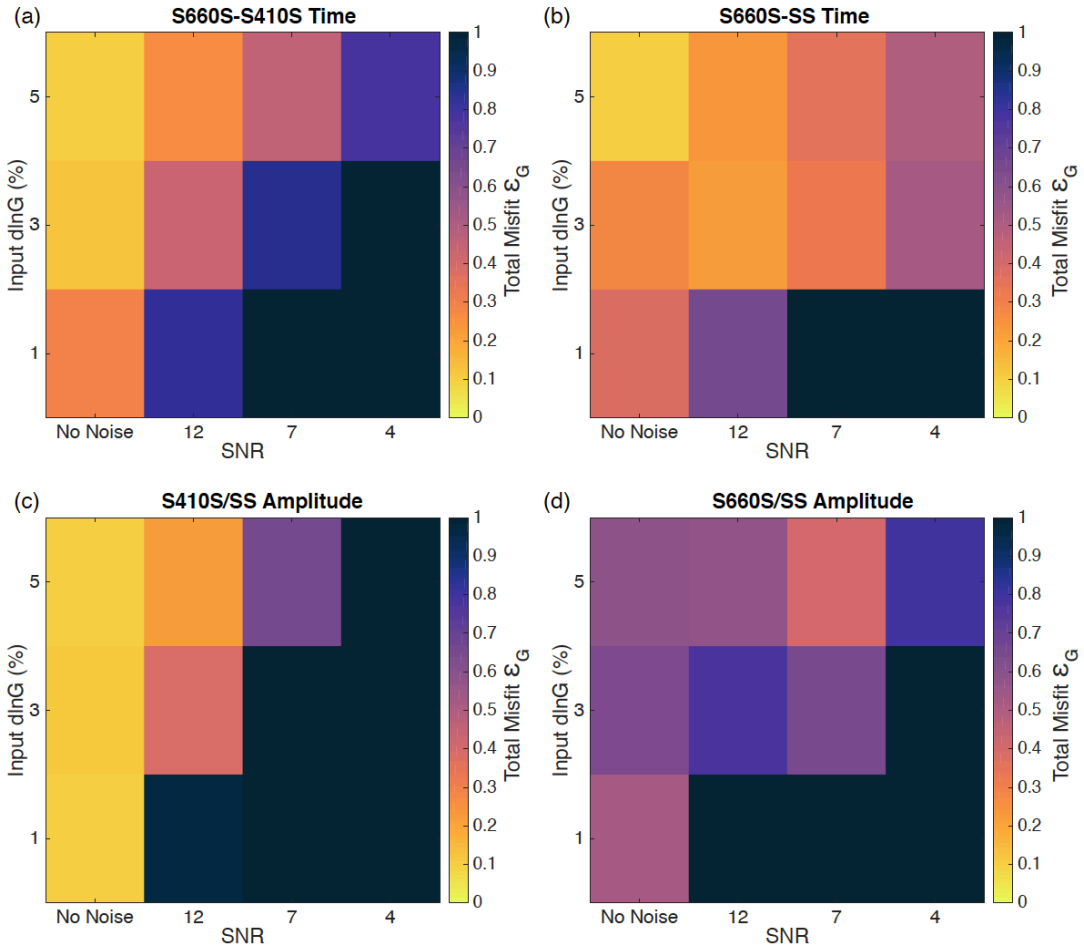

Figure 3.9 Detectability matrix for the central Pacific bin using an idealized source-receiver geometry. The dlnG detectability matrix for (a) S660S-S410S time, (b) S660S-SS time, (c) S410S/SS amplitude, and (d) S660S/SS amplitude. SNR=7 is the average noise level of our SS dataset. The total misfit ε_G of dlnG is inversely correlated with the detectability. When ε_G is greater than 1 (saturated in the plot), the model is considered as non-detectable.

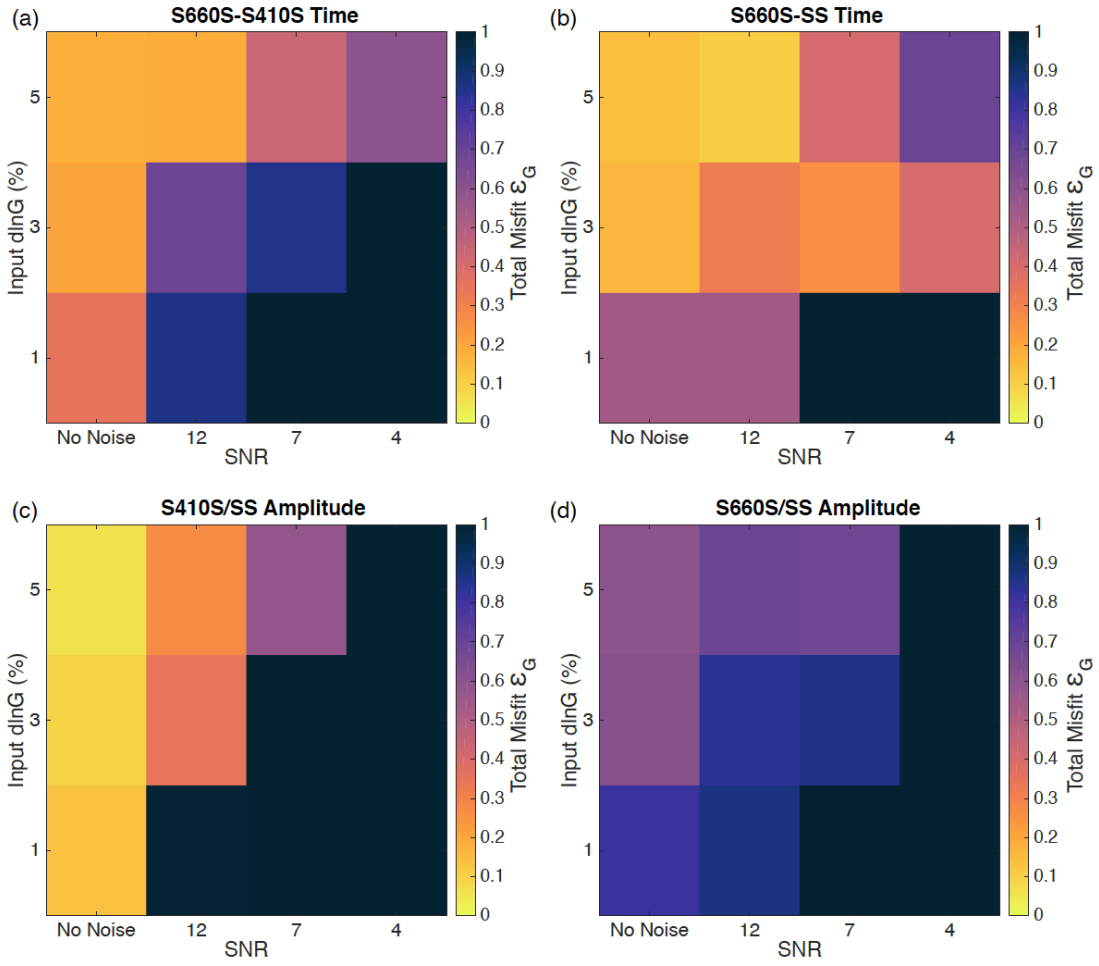

Figure 3.10 Same as Figure 3.9 but using a realistic source-receiver geometry. The dlnG detectability matrix for (a) S660S-S410S time, (b) S660S-SS time, (c) S410S/SS amplitude, and (d) S660S/SS amplitude.

3.3.3 Japan Subduction Zone

In Huang et al. (2019), we found evidence for ~3% MTZ anisotropy beneath the circum-Pacific subduction zones. However, the results were based on the stacking of multiple subduction zones, so there was ambiguity about where the signal originated, or if it was ubiquitous amongst all subduction zones. Due to the relatively high density of data, we identified the Honshu subduction zone near Japan as a study region to uniquely determine the character of MTZ anisotropy. Honshu subduction zone is located in a region where the MTZ is thickened primarily due to the cold slab (e.g.,

Helffrich, 2000; Figure 3.11a). The tomography models also suggest that the Japan slab is stagnant above the 660 km discontinuity beneath eastern China and Korea (e.g., Fukao and Obayashi, 2013). We chose this region to study the mantle flow associated with the stagnant slab, and it is the best-sampled subduction zone in our SS dataset. However, the azimuthal coverage is relatively poor, with only four usable azimuthal bins for stacking and especially lacking the data with east-west orientations (Figure 3.11c). The data and synthetic stacking results are shown in Figure 3.11b. Despite limited data coverage, the S410S and S660S are recovered from stacking in all these four bins, noting that the S410S in 90 degrees bin (NR=2) is very noisy. We inverted the strength of anisotropy and fast direction from the S660S-S410S time (Figure 3.11d). The strength of anisotropy (dlnG=4.5±9.5%) is not significantly above zero due to the large uncertainties of travel-time measurement in 90° bin. The fast direction (Θ=87°±50°) is trench-perpendicular and shows relatively smaller uncertainties compared to dlnG. The fast direction is consistent with our observations in Huang et al. (2019), which suggests that the structure beneath Japan is representative of the structure found in the circum-Pacific subduction zones.

Following the Central Pacific study region methodology, we ran a similar resolution test for Japan subduction zone using both idealized and realistic source and receiver geometries (Figure 3.3). The resolution of the idealized geometry model is very similar to that of the central Pacific region although the bin size is smaller. However, the realistic geometry model using the actual azimuthal coverage of Japan displays poorer detectability in Figure 3.12. The SS precursors generally require tens of data points to obtain a stable stacking which is not the case here. Figure 3.12a

illustrates that the S660S-S410S time can only resolve 5% anisotropy when noise level is very low (SNR=12) which is hardly observed in real data. Surprisingly, Figure 3.12b reveals that the resolution of fast directions is relatively higher, and S660S-S410S time can reconstruct the input fast direction of 3% anisotropy even when noise level is high (SNR=4). This suggests that SS precursors can still recover the input fast directions even if they cannot resolve the strength of anisotropy. This also indicates that the trench-perpendicular fast direction in Japan subduction zone is robust, thus can be used to infer mantle flow directions in the MTZ. The S660S-SS time has slightly better resolution (Figure 3.12c), whereas the S410S amplitude has similar resolution to S660S-S410S time (Figure 3.12d).

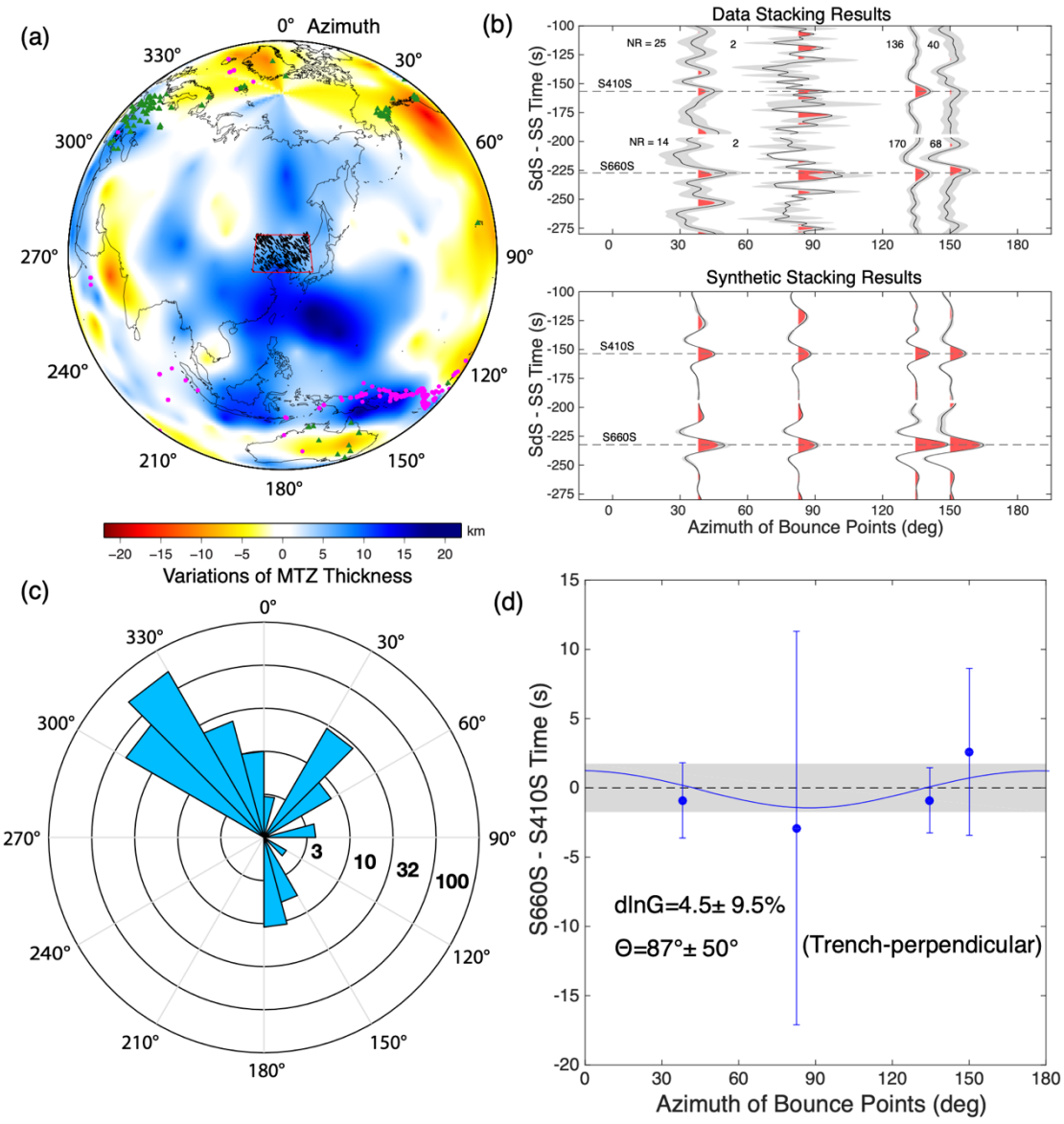

Figure 3.11 (a) SS precursor data in Japan subduction zone superimposed on the MTZ topography map. The legends are the same as Figure 3.8. The study region is highlighted by the red box, and the size is 1500 km × 1000 km. (b) The azimuthal stacking results of the data (top) and synthetics (bottom) in Japan subduction zone. The number of records (NR) of each azimuthal bin is labelled beside the waveforms. The dashed lines highlight the average SdS travel times. (c) The rose diagram showing the azimuthal coverage of SS bounce points in log scale. (d) The S660S – S410S times and 2σ errors shown as a function of azimuths. The best-fitting fast direction is trench-perpendicular. The dashed line is the average S660S-S410S time from the stacking of all azimuthal bins, and gray shaded box is the corresponding 2σ errors.

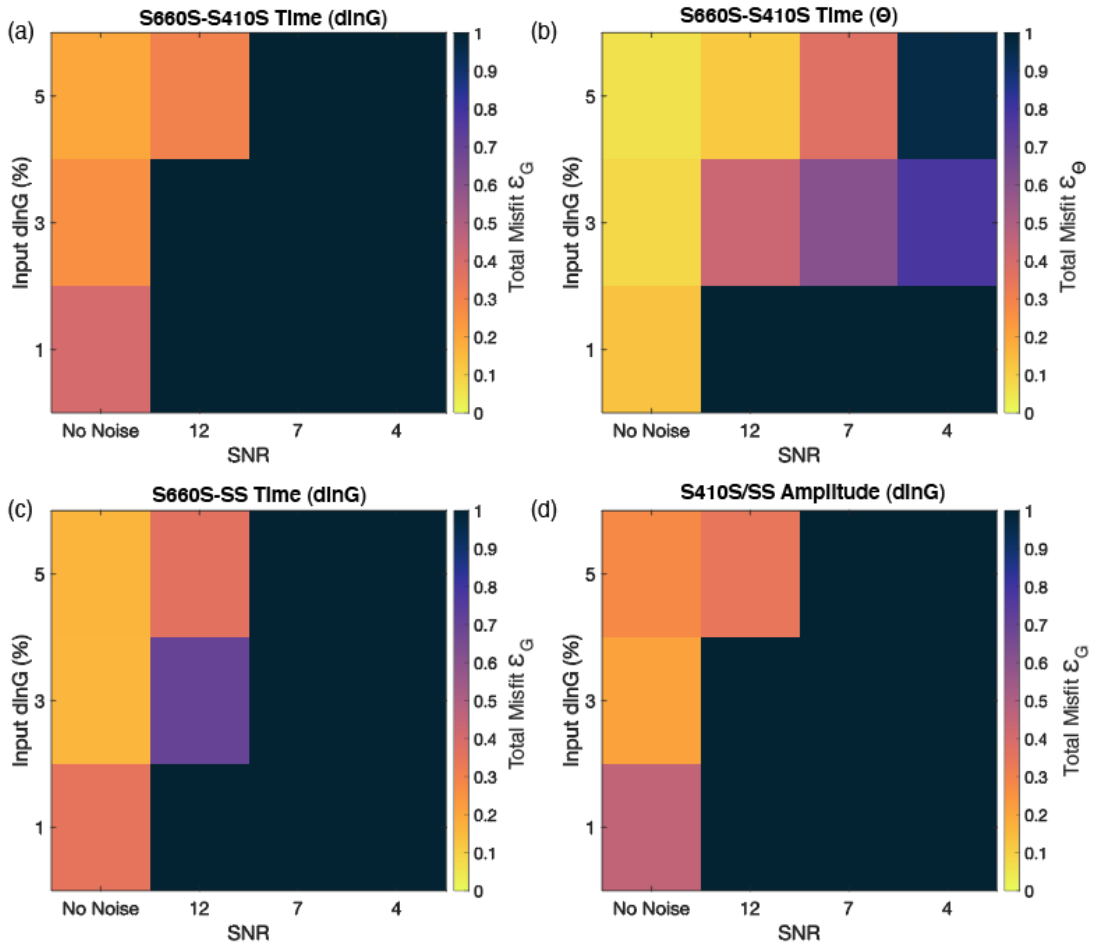

Figure 3.12 Detectability matrix for Japan subduction zone using a realistic source-receiver geometry. The (a) dlnG and (b) Θ detectability matrix for S660S-S410S time. The dlnG detectability matrix for (c) S660S-SS time and (d) S410S/SS amplitude.

3.4 Discussion

3.4.1 Proof of concept: the resolution and limitation of SS precursors

Currently, the two major tools to constrain deep mantle anisotropy are shear wave splitting and higher mode surface waves. However, the shear wave splitting method has limited vertical resolution to distinguish the depth-distribution of anisotropy, while surface waves have low horizontal resolution (~6500 km in the MTZ from Visser et al, 2008, Yuan and Beghein, 2018) and cannot detect small-scale anisotropy such as the structures near subduction zones. For comparison, the horizontal

resolutions of long-period SS precursors (i.e. Fresnel zone) are ~1,000 km in radius (e.g., Dalhen 2005; Lawrence & Shearer, 2008). We have demonstrated that stacks of the SS precursors have sensitivity to azimuthal anisotropy in the upper mantle and MTZ through 3-D synthetic modeling. The travel-times of SS precursors can detect ≥3% azimuthal anisotropy in the MTZ with intermediate level of noise (SNR=7). The amplitudes of SS precursors shed light on the anisotropy change across a seismic discontinuity such as 410-km discontinuity (Saki et al., 2018). Due to the effect of stacking, the uncertainties of SdS amplitudes are often larger than travel-time measurements so they can only detect ≥5% azimuthal anisotropy in the MTZ. However, we can apply this method to a shallower upper mantle discontinuity with stronger anisotropy such as the lithosphere-asthenosphere boundary (LAB) or mid-lithosphere discontinuity (MLD) where the polarity change of the amplitudes can take place (e.g., Rychert et al., 2014; Wirth and Long, 2014).

Sufficient azimuthal coverage is key to successfully applying SS precursors to anisotropy studies. This method requires at least 4 to 5 different azimuths with NR>100 in each azimuthal bin to obtain a robust estimate of strength and fast direction of anisotropy. However, insufficient azimuthal coverage is common in our SS dataset, and we only identify four candidate locations suitable for constraining azimuthal anisotropy: (1) the northwestern Pacific, (2) the central Pacific, (3) the central Atlantic, and (4) Greenland (Huang et al., 2019). This is primarily due to the uneven distributions of large earthquakes concentrated near plate boundaries and dense stations mostly in North America (e.g., USArray). This means that although the western Pacific subduction zones have large numbers of records sampling the region, azimuthal

coverage is actually quite limited. The data could be augmented by future ocean bottom seismometers (OBS) deployed across the Pacific Ocean (e.g., Kawakatsu et al., 2009).

A second challenge presented by this approach is the determination of the depth and thickness of the anisotropic layer. Our tests show that the SS precursors cannot resolve multiple sub-layers of anisotropy structures in the target depth range. For example, the SS precursors cannot distinguish whether MTZ anisotropy is located in the upper or lower MTZ, or the whole MTZ. Thus, in our modeling and data analysis, we only assume uniform anisotropy across the whole MTZ, which may underestimate the strength of anisotropy if it is only localized in a sub-layer. The final challenge is that we focus only on the SH waves to constrain azimuthal anisotropy, but SV waves can also provide useful information about anisotropy, via the splitting of the SS phase and its precursors (e.g., Wolfe & Silver, 1998). Despite these limitations, SS precursors can serve as a new method to constrain seismic anisotropy in the upper and mid-mantle, especially beneath oceanic regions where seismic stations are underpopulated for shear wave splitting measurements.

3.4.2 Interpretation of mantle flow in the transition zone

In the central Pacific region, we have not found any definitive evidence for MTZ anisotropy near the Hawaiian hot spot. Few shear wave splitting studies have reported evidence for MTZ anisotropy in this region, either due to the interference of strong lithosphere and asthenosphere anisotropy (e.g. Collins et al., 2012) or simply lack of data. Therefore, we compare our results to three higher mode surface wave models at 500-km depth: YB13SVani (Yuan and Beghein, 2013), SL2016SvA (Schaeffer et al., 2016), and 3D2017_09Sv (Debayle et al., 2016). These three models

only show 0.5–1.0% azimuthal anisotropy near Hawaiian hot spot. Ideally, the SS precursors can only detect 1% azimuthal anisotropy with very clean data (SNR > 12, Figure 3.9). In this case, the strength of MTZ anisotropy beneath Hawaiian hot spot is likely below our resolution. This suggests the mantle flow associated with the Hawaiian plume does not produce significant MTZ azimuthal anisotropy (Figure 3.13).

We find that the fast direction of MTZ anisotropy is trench-perpendicular (parallel to the Pacific plate motion direction) beneath the Japan subduction zone. The strength of anisotropy is well constrained than the fast direction because inversion of fast direction only requires azimuthal coverage in the fast and slow directions. The mantle flow direction can be inferred from the fast direction of azimuthal anisotropy. Our results are consistent with previous observations using source-side shear wave splitting measurements of deep earthquakes (e.g., Lynner and Long, 2015; Nowacki et al., 2015). Lynner and Long (2015) found evidence for azimuthal anisotropy originating from the MTZ and uppermost lower mantle beneath Japan, and the fast splitting direction is also trench-perpendicular. The higher mode surface wave model (Yuan and Beghein, 2018) shows trench-perpendicular fast direction as well at 450 km depth beneath Japan. The consistency among these three different methods combined with our 3-D synthetic modeling suggest that trench-perpendicular is a definitive feature of the MTZ beneath the Japan subduction zone. However, the fast splitting directions in the MTZ display a heterogeneous pattern across different subduction zones around the Pacific Ocean. Beneath Tonga subduction zone, the dominant fast direction is trench-parallel (Foley and Long, 2011; Mohiuddin et al., 2015); whereas the Sumatra and South America subduction zones show both trench-parallel and trench-

perpendicular fast directions (Nowacki et al, 2015; Di Leo et al., 2012; Lynner and Long, 2015). Our previous study (Huang et al., 2019) combined all the data in the circum-Pacific subduction zones for stacking and concluded that trench-perpendicular fast direction is the most coherent pattern, however our data could be biased by Japan and South America where the data coverage is densest. The variability of fast directions also suggests heterogeneous flow patterns associated with different subducting slabs (penetrating or stagnant) in the mid-mantle.

The observed trench-perpendicular fast direction of MTZ anisotropy could be attributed either to the SPO of subducting slab, or the LPO of wadsleyite. Geodynamic modeling suggests that the strain induced LPO under a dislocation creep regime can better fit the global tomography model than SPO in the mid-mantle (Ferreira et al., 2019; Sturgeon et al., 2019). Therefore, we assume that LPO of wadsleyite is the primarily contributor to the MTZ anisotropy beneath the Japan subduction zone. This interpretation of mantle flow direction from the fast direction of mantle anisotropy requires the experimental data of wadsleyite's dominant slip systems (Sharp et al., 1994; Thurel et al., 2003; Demouchy et al, 2011; Kawazoe et al, 2013; Ohuchi et al., 2014). Kawazoe et al. (2013) reported that the dominant slip system of wadsleyite is [001] (010), therefore the mantle flow direction is perpendicular to the fast polarization direction of shear wave, which is the same as B-type olivine (e.g., Jung and Karato, 2001). Under the assumption of a [001] (010) slip system for wadsleyite, the seismic trench-perpendicular fast direction then infers trench-parallel flow near the stagnant Japan slab in the MTZ (Figure 3.13). The inferred flow also agrees with the trench-parallel flow directions in the sub-slab MTZ predicted by 3-D geodynamic modeling

(Faccenda, 2014). Our previous study (Huang et al., 2019) reported that trench-parallel fast direction is dominant in the upper mantle beneath the slab, which is also consistent with trench-parallel flow assuming A-type olivine fabric (e.g., Karato et al., 2008). The trench-parallel flow around slabs is consistent with the toroidal flow induced by trench migration (Faccenda and Capitanio, 2012). Consequently, our results suggest the mantle flow direction remains consistently trench-parallel throughout the entire sub-slab upper mantle and transition zone in Japan (Figure 3.13). Alternatively, the flow direction in the transition zone can rotate by 90 degrees and become trench-perpendicular if we assume the dominant slip system of wadsleyite is [100] (0kl) (Demouchy et al., 2011). Other complexities such as the water and iron content in the MTZ (e.g. Zhang et al., 2018), mineral recrystallization through phase changes (e.g. Karato, 1988), and LPO of slabs would alter our interpretations.

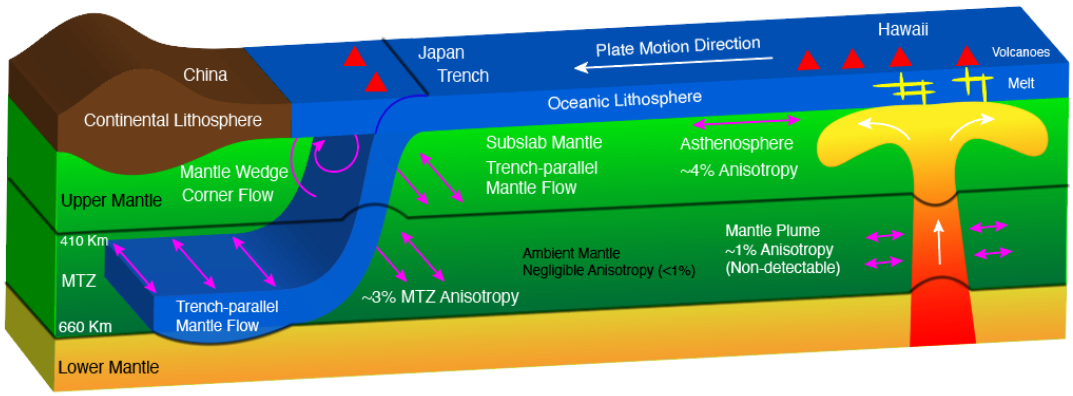

Figure 3.13 A schematic diagram depicting the mantle flow patterns in the upper mantle and transition zone observed from SS precursors. The pink arrows denote the inferred mantle flow direction from azimuthal anisotropy assuming A-type olivine in the upper mantle and [001] (010) slip system of wadsleyite in the MTZ (Kawazoe et al., 2013). On the left, the trench-parallel flow consistently exists in the sub-slab upper mantle and MTZ beneath Japan subduction zone (Huang et al., 2019). The trench-perpendicular fast direction near the stagnant slab is interpreted as trench-parallel flow in the MTZ as well. The mantle wedge is likely dominated by the trench-perpendicular corner flow which is not observed in our study. On the right, the Hawaiian mantle plume can only produce very weak azimuthal anisotropy (~1%) which is not detectable from SS precursors. The asthenosphere beneath Hawaii show strong azimuthal anisotropy (~4%) with a fast direction parallel to the plate motion direction (Huang et al., 2019). The azimuthal anisotropy is negligible (<1%) in the ambient mantle.

3.5 Conclusions

We have investigated the sensitivity of SS precursors to azimuthal anisotropy using 3-D synthetics computed from SPECFEM3D_GLOBE. We tested the following factors that affect the sensitivity of SS precursors: the depth of anisotropy, size and strength of anisotropy, source and receiver geometry, and noise level. We demonstrate that the SS precursors can distinguish between anisotropy in the upper mantle versus the MTZ via the azimuthal variations of SdS amplitudes and travel-times. The source and receiver geometry and azimuthal coverage all play key roles in constraining the strength of anisotropy and fast direction. When data coverage is sufficient (i.e., NR>100 in each azimuthal bin), the SS precursors can resolve $\geq 3\%$ azimuthal anisotropy in the MTZ with average level of noise (SNR=7). In case of biased or limited azimuthal coverage (e.g., Japan), the fast direction can still be inferred from S660S-S410S time even if the strength of anisotropy is poorly constrained.

We searched for evidence for mantle flow associated with a mantle plume or subducting slab in the MTZ beneath the central Pacific region and Japan subduction zone. In the Japan subduction zone, we find evidence for trench-perpendicular fast direction ($\Theta=87°\pm50°$) in the MTZ, which is consistent with previous shear-wave splitting and surface wave measurements. We attribute this MTZ anisotropy to the LPO of wadsleyite such that the trench-perpendicular fast direction in Japan is interpreted as trench-parallel mantle flow based on the dominant slip system of wadsleyite. We infer that the mantle flow direction beneath Japan is likely to remain consistently trench-parallel throughout the entire sub-slab upper mantle and transition zone. In the central Pacific region, the resolution test suggests that our data can resolve 3% anisotropy, but

no anisotropy is detected. The MTZ anisotropy is probably << 3% beneath central Pacific, which is consistent with ~1% anisotropy from the surface wave models, and therefore below the detection threshold of SS precursors. This suggests that the vertical flow caused by the mantle plume beneath Hawaiian hotspot cannot produce strong azimuthal anisotropy in the MTZ.

Acknowledgements

The SS dataset was downloaded from Incorporated Research Institutions for Seismology, Data Management Center (IRIS DMC). The SS dataset and MTZ topography model are available at http://hdl.handle.net/1903/21819 (DOI: https://doi.org/10.13016/3ecr-1hsu). We also thank the developers of SPECFEM3D for distributing the codes freely online. QH and NS were supported by the National Science Foundation (NSF) under grant NO. EAR-1447041. CB was supported by NSF under grant NO. EAR-1446978. LW is the recipient of a Discovery Early Career Research Award (project number DE170100329) funded by the Australian Government and supported by NSF under grant NO. EAR-1661985 and EAR-1853662. RM was supported by NSF EAR Postdoctoral Fellowship 1806412.

Chapter 4: Detecting the Mantle Transition Zone of Mars with Triplicated and Reflected Seismic Waves

Abstract

The mantle transition zone (MTZ) of Mars is associated with the phase transition from olivine to wadsleyite that is expected to produce a seismic discontinuity at ~1,000-km depth. Constraints on the depth of the 1,000-km discontinuity will shed light on the composition and temperature of the martian interior. NASA's InSight Mission to Mars provides a unique opportunity to detect the martian MTZ with a single station approach. Here, we investigated the triplicated and reflected waves (topside + underside) as candidate body waves to investigate the martian MTZ. We used AxiSEM to compute high frequency synthetics (1 Hz) based upon a priori radial model for Mars (EH45TcoldCrust1, Rivoldini et al., 2011). We quantified the detectability of candidate phases by calculating the signal-to-noise ratios (SNR) given the typical SEIS VBB noise levels. We found that the triplications can be detectable, whereas the reflections required at least Mw 5 events; however, events of this size have not been observed yet on Mars. We also characterized how the regolith layer and crustal scattering affect the detectability of martian MTZ. While the presence of a regolith layer has negligible effects on triplicated waves, interference from crustal scattering affects P triplications more strongly than S triplications. To search for triplications in InSight data, we applied a polarization filter to enhance the SNR of body waves and align the low-frequency (LF) and broadband (BB) events on P and S waves. We constrained the back-azimuths of these events from the polarization analysis of P waves. Multiple reflected waves

(e.g., PP and SS) were identified from the vespagram analysis of polarization filtered envelopes. We picked the travel-times of these phases based on the slowness and arrival-time measurements from vespagrams. We inverted the velocity and density structures of martian crust and upper mantle using the travel-time measurements. Furthermore, we discovered 12 candidate events in the target distance range (60-85 degrees) for triplicated waves. The alignments of these triplication events reveal seismic phases after P and S waves with a "bow-tie" travel-time curve. These phases are identified as P and S triplications from the martian MTZ based on synthetic waveform modeling. Preliminary estimate on the depth of olivine-to-wadsleyite phase transition is 1,016±32 km based on the S triplication. Our results indicate a cold martian mantle with mantle potential temperature of 1,600±100 K.

4.1 Introduction

The composition and internal structures of terrestrial planets are the key to understanding the formation and evolution of the solar system. Earth is one of several rocky interior planets of the solar system, including Mercury, Venus and Mars. Like Earth, Mars was formed through accretion of planetesimals, into a rocky planet, and then further differentiated into three distinct layers: crust, mantle and core. Planetary seismology extends the study of seismic waves to other planets beyond Earth by deploying seismometers directly on their surfaces (Lognonné and Mosser, 1993). Over the past half century of planetary exploration, seismic data have been acquired on the Moon and Mars, and have provided invaluable insights into the internal structure, formation and evolution of terrestrial planets (e.g., Nakamura, 1983; Anderson et al., 1976). On 26 November 2018, NASA's InSight (Interior Exploration using Seismic

Investigations, Geodesy and Heat Transport) Mission landed in Elysium Planitia on Mars (Banerdt et al., 2020). The primary scientific objectives of InSight mission are to determine the structures, compositions and thermal states of martian crust, mantle and core, and measure the seismicity and impact rates on Mars (Daubar et al., 2018; Lognonné et al., 2019; Panning et al., 2016; Smrekar et al., 2019).

The InSight lander deployed the first seismometer SEIS (Seismic Experiment for Interior Structure) on the surface of Mars and covered it with wind and thermal shield (WTS), which significantly reduced the noise level compared to the on-deck Viking seismometer (Anderson et al., 1977). SEIS includes two seismic sensors: Very Broad Band (VBB) and Short Period (SP) sensors, which cover the 0.01-5 Hz and 0.1-50 Hz frequency band respectively (Lognonné et al, 2019). After nearly two Earth years of operation on Mars (1 martian year), SEIS has detected $>$ 1000 seismic events (Clinton et al., 2020), establishing that Mars is seismically active. Initial results from these marsquakes revealed invaluable information about the seismicity rate of Mars (Banerdt et al., 2020; Giardini et al., 2020), shallow structures of Mars (Lognonné et al, 2020) and a new impact crater near InSight landing site (Daubar et al., 2020).

During the 40 years before the InSight Mission, scientists have attempted to construct composition models of Mars using geochemical data from martian meteorites and chondrites, as well as geophysical data from remote sensing or in situ measurements (see review by Taylor, 2013). The geochemical approaches are based on the chemical composition of SNC (Shergottites, Nakhlites and Chassignites) meteorites that are pieces of the martian crust ejected by impacts onto the surface of Mars, and subsequently traveled to Earth and landed as meteorites. Derivations of martian

composition from the SNC meteorites are divided into two approaches. The first uses a comochemical approach that assumes that the relative abundances of refractory elements are similar to that of CI chondrites (Dreibus and Wänke, 1985; Morgan and Anders, 1979; Taylor, 2013) and derives other components from martian meteorites. Recently, Yoshizaki & McDonough (2020) presented a new composition model from martian meteorite and spacecraft data avoiding the assumption of CI chondrite as an analog to Mars. The second is based on the analysis of oxygen isotopes of martian meteorites and chondrites (Burbine & O'Brien, 2004; Lodders and Fegley, 1997; Mohapatra & Murty, 2003; Sanloup et al, 1999; Warren, 2011). Geophysical predictions for the martian interior depend on the geochemical models and derive models through numerical modeling (Longhi et al., 1992; Sohl & Spohn, 1997; Zharkov & Gudkova, 2005) and mineral physics experiments (Bertka and Fei, 1997, 1998). Unlike other models, Khan & Connolly (2008) inverted the composition model of Mars from geophysical data such as moment of inertia, tidal love number and tidal dissipation without a priori assumption on the composition. Among these geochemical and geophysical models, the Dreibus and Wänke (1985) model has been considered as the standard model of Mars. We summarize 9 representative bulk composition models of silicate Mars in Table 4.1. Despite different approaches, these composition models are generally consistent, and indicate that Mars is more enriched in FeO (~17%) compared to Earth (e.g, ~8% in McDonough and Sun, 1995).

Table 4.1 Major element compositions of bulk silicate Mars (crust + mantle).

Composition Models (wt%)	*SiO_2*	*Al_2O_3*	*MgO*	*CaO*	*Na_2O*	*FeO*	*Total*
Morgan and Anders (1979)	41.60	6.39	29.78	5.16	0.10	15.85	98.88
Dreibus and Wänke (1985)	44.40	3.02	30.20	2.45	0.50	17.90	98.47
Lodders and Fegley (1997)	45.49	2.89	29.71	2.35	0.98	17.22	98.64
Bertka and Fei (1997)	43.68	3.13	31.50	2.49	0.50	18.71	100.01
Sanloup et al. (1999) (EH45:H55 model)	47.50	2.50	27.30	2.00	1.20	17.70	98.20
Mohapatra and Murty (2003)	47.10	2.50	29.10	1.90	1.20	16.90	98.7
Khan and Connolly (2008)	44.00	2.50	33.00	2.20	-	17.00	98.70
Taylor (2013)	43.70	3.04	30.50	2.43	0.53	18.10	98.30
Yoshizaki and McDonough (2020)	45.50	3.59	31.00	2.88	0.59	14.70	98.26

The geodetic and geochemical constraints on the martian interior allow for the construction of predictive models of the interior. The density and seismic velocities of martian interior can be derived from the composition models and temperature profiles of Mars (e.g., Plesa et al., 2016) using equations of state (Khan et al., 2018; Rivoldini et al., 2011). The martian planetary radius is about half of Earth's and it has a mass about $1/10^{th}$ of that of the Earth; therefore, the interior pressure at the base of the martian mantle (1500-1800 km depth; 20-23 GPa) is about equivalent to Earth's MTZ (520-660 km). In Figure 4.1, we show the reference 1-D models from the Marsquake Service (MQS) blind tests performed before the landing of InSight Mission (Clinton et al., 2017). Three prominent boundaries are predicted to exist in the martian interior: (1) crust-mantle boundary, (2) olivine-to-wadsleyite phase transition, (3) core-mantle boundary (CMB). The olivine-to-wadsleyite phase transition marks the boundary between upper mantle and mantle transition zone (MTZ), which is equivalent to the 410-km discontinuity on Earth (e.g., Dziewonski & Anderson, 1981). Unlike the core-mantle boundary, the depths of olivine-to-wadsleyite phase transition are fairly consistent among these models at ~1,000 km, hereafter named as 1,000-km discontinuity. The orthopyroxene (Opx) to high-pressure clinopyroxene (HP-Cpx)

produces a smaller discontinuity at ~800 km depth. The absence of a bridgmanite-ferropericlase layer is ubiquitous among these models because the stabilities of these two minerals are sensitive to the core size and mantle temperature (Bertka and Fei, 1997). The models with small core size and hot temperature favor the existence of a thin bridgmanite-ferropericlase basal layer. The radius of martian core is inferred to be ~1,730-1,840 km based on the measurements of tidal k2 Love number, thus incompatible with the existence of a bridgmanite-ferropericlase layer (Khan et al., 2018). The measurements of tidal k2 Love number (Yoder et al., 2003) and high-pressure mineral physics experiments (Fei and Bertka, 2005) both indicate that at least the outer part of martian core is liquid.

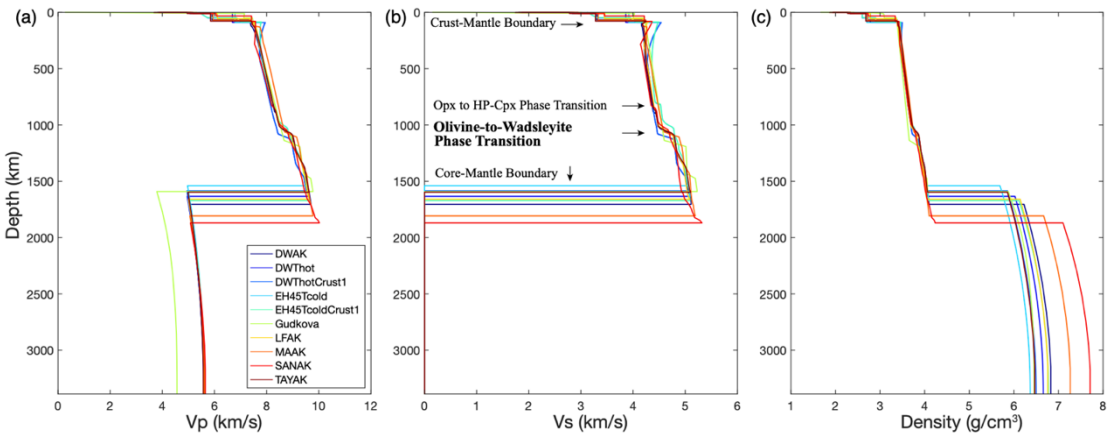

Figure 4.1 Vertical profiles of (a) Vp, (b) Vs, (c) density in the 1-D reference models of Mars (Clinton et al., 2017). The major seismic discontinuities of martian interior are highlighted with black arrows. Opx and HP-Cpx are the abbreviations for orthopyroxene and high-pressure clinopyroxene respectively. The model names starting with "DWT" and "EH45T" are from Rivoldini et al. (2011); the model names ending with "AK" are from Khan et al. (2016); Gudkova model is from Zharkov & Gudkova (2005).

Earth's MTZ is demarcated by two seismic discontinuities at 410-km and 660-km depths, manifested as sharp velocity and density jumps in Earth's 1-D models (e.g., Dziewonski and Anderson, 1981). The formations of these discontinuities are associated with the pressure-induced phase transformations of upper mantle minerals:

(1) olivine to wadsleyite at 410-km, (2) wadsleyite to ringwoodite at 520-km, and (3) the dissociation of ringwoodite to bridgmanite and ferropericlase at 660-km (Ringwood 1975; Ita and Stixrude, 1992). Early studies on MTZ structures utilized the refracted waves bottoming at the depths of MTZ discontinuities, also known as triplications, together with waveform modeling to invert 1-D velocity structures of upper mantle (e.g., Grand & Helmberger, 1984; Walck, 1984). The triplicated waves (e.g., P and S wave) display three branches of travel-time curves with robust amplitudes and sample the MTZ extensively, thus providing useful insights into mantle heterogeneities such as partial melt associated with the subducting slabs (e.g., Song et al., 2004; Tajima & Grand, 1998; Ye et al., 2011). Recent studies have employed secondary phases with smaller signal-to-noise ratios (SNR) that reflect or convert at the MTZ discontinuities: (1) SS and PP precursors (e.g., Flanagan & Shearer, 1998, 1999), (2) receiver functions (e.g., Lawrence & Shearer, 2006), (3) ScS reverberations (e.g., Revenaugh & Jordan, 1991) , (4) P'P' precursors (e.g., Wu et al., 2019) and (5) topside reflections (e.g., Shearer & Buehler, 2019). Measurements of SS precursors, which are shear wave reflections occurring at the underside of MTZ discontinuities, revealed the first global topography map of 410-km and 660-km discontinuities on Earth (Chambers et al., 2005; Deuss & Woodhouse, 2002; Flanagan & Shearer, 1998; Gu & Dziewonski, 2002; Houser et al., 2008; Huang et al., 2019; Lawrence & Shearer, 2008). However, these approaches require stacking of hundreds of seismograms recorded by station arrays in order to bring the secondary phases out of noise. This will become a challenge for InSight Mission that only focuses on single station approach on Mars.

Here, we use synthetic seismograms to determine the detectability of seismic phases that interact with the martian MTZ and constrain the mantle velocity as well as depth of mantle discontinuities from InSight data. Both are needed to determine the exact depth of the 1,000-km discontinuity and compare to the mineral physical model to infer the temperature and composition of the martian mantle. As the Clapeyron slope of olivine-to-wadsleyite phase change is positive (Ita & Stixtrude, 1992; Katsura & Ito, 1989), the 1,000-km discontinuity is expected to become shallower in cold mantle, and deeper in hot mantle. Therefore, constraints on the depth of 1,000-km discontinuity from seismic observations can provide a way of measuring the mantle temperature of Mars. We first computed synthetic seismograms to study the detectability of 1,000-km discontinuity from two candidate body waves: triplicated and reflected waves. Then, we investigated how regolith layer and crustal scattering affect the detectability. We then used body wave arrival times for multiple reflected waves to derive a 1-D velocity model of the martian upper mantle. Finally, we examined the InSight data to search for seismic waves interacting with the martian MTZ and used their arrival times and inferred discontinuity depth to constrain the composition and temperature of the martian mantle.

4.2 Methods

4.2.1 Detectability Study Approach

4.2.1.1 Candidate Body Waves

The first type of candidate phases interacting with the martian MTZ is the reflected waves. They can be further divided into two categories: the topside reflections

and underside reflections (Figure 4.2). The topside reflections include Pv1000P and Sv1000S, which are named as PcP and ScS precursors respectively. Similarly, Sv1000P and Pv1000P are defined as ScP and PcP precursors, but they are not considered for this study because they arrive too close to the surface waves. Other topside reflections are the continuations of the precursors such as topside P or S waves (Pv1000pP and Sv1000sS) and topside PcP or ScS waves (Pv1000pPcP and Sv1000sScS). The underside reflections include the PP or SS precursors (P1000P and S1000S), and PcP or ScS reverberations (PcP1000PcP and ScS1000ScS). We computed the travel-time curves of these reflections (Figure 4.2a) based on EH45TcoldCrust1 model (Rivoldini et al., 2011) using TauP software (Crotwell et al., 1999). We selected the candidate reflected waves based on the following criteria: (1) large amplitude; (2) little interference with other phases. Therefore, the ScS precursor (Sv1000S) and PP precursor (P1000P) were chosen as candidate reflected waves in the near-field and far-field respectively. Figure 4.2b displays the ray-paths of these two waves.

The second type of candidate phases is the triplicated waves including P and S triplications. The 1,000-km discontinuity is a steep velocity gradient, thus would change the P and S waves from prograde to retrograde and back to prograde again as epicentral distance increases (ray-path in Figure 4.2b). These changes in slowness form three branches of travel-time curves referred as triplications. The triplicated waves have been widely used to constrain the structures of 410-km and 660-km discontinuities on Earth, mainly through ray-theoretical or finite frequency waveform modelling approaches (e.g., Song et al., 2004; Stahler et al., 2012). Here, we focus on the travel-

time measurements of triplications as a function of distance and then determine the depth of 1,000-km from the move-out of the triplications.

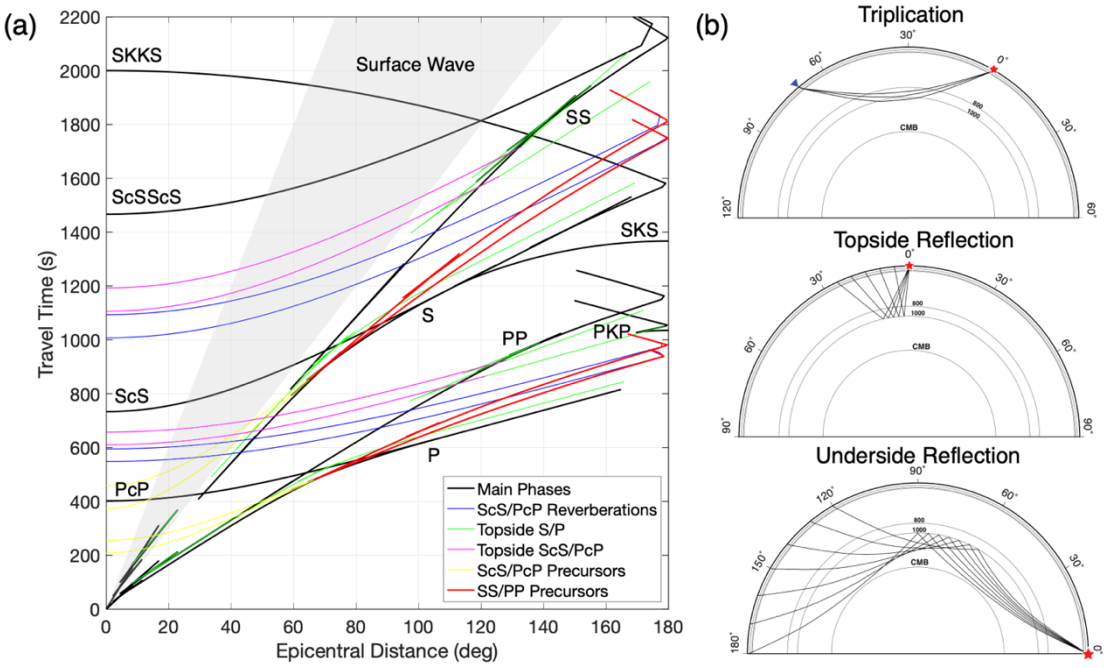

Figure 4.2 (a) Predicted travel-time curves using EH45TcoldCrust1 model (Rivoldini et al., 2011) from TauP (Crotwell et al., 1999). The black curves are the travel-times of main body waves. The colored curves are the MTZ associated phases such as topside and underside reflections. The gray shaded region represents the surface waves. (b) Ray paths of candidate body waves. We identify P and S triplications, topside S reflection (ScS precursor) and underside P reflection (PP precursor) as the body waves to detect the MTZ of Mars. The candidate waves should have strong amplitudes and no interference with other waves.

4.2.1.2 Estimating SEIS VBB Noise Level

The detectability study of candidate body waves requires the knowledge of noise levels on martian surface. SEIS is covered by the Wind and Thermal Shield (WTS) to provide protection from wind and thermal variations on Mars (Lognonné et al, 2019). However, due to the ground coupling between atmosphere and InSight Lander/WTS, multiple sources of noise can still contribute to SEIS data such as the environmental noise from atmospheric pressure change or wind, and instrument self-noise (Mimoun

et al., 2017). We obtained the mean noise amplitude spectra from the VBB data in July 2019 (Panning et al., 2020) to study the characteristics of martian noise. Figure 4.3 illustrates the comparison between martian and terrestrial noise (Peterson, 1993) in both acceleration and displacement. The martian noise level is significantly lower than Earth, especially between 1-10 s period. On Earth, part of the micro-seismic noise originated from the ocean waves dominate the 1-10 s period range (Friedrich et al., 1998). However, martian noise is even lower than the New Low Noise Model (NLNM) on Earth due to the lack of oceans on the surface. The extremely quiet environment on Mars provides an ideal condition to detect subtle seismic signals.

Martian noise shows strong diurnal variations: the day noise level is ~10 times stronger than the night noise level (Figure 4.3). The more turbulent atmospheric activities during the day cause the noisier environment compared to the night (Lognonné et al, 2020; Murdoch et al., 2017). The nighttime was once the ideal time to detect seismic events due to the low noise level. However, after one-year of noise evolutions, the night noise level increased and converged with day noise in June 2020, which reduced the number of detectable seismic events. The second feature is that the horizontal components (BHN and BHE) are noisier than the vertical component (BHZ) in long period range (> 5s). We used the night noise level as the noise floor to determine the detectability of candidate phases. We computed the average amplitude spectrum between BHE and BHN components as horizontal noise level for S wave detections. The vertical (BHZ) amplitude spectrum was used for P wave detections.

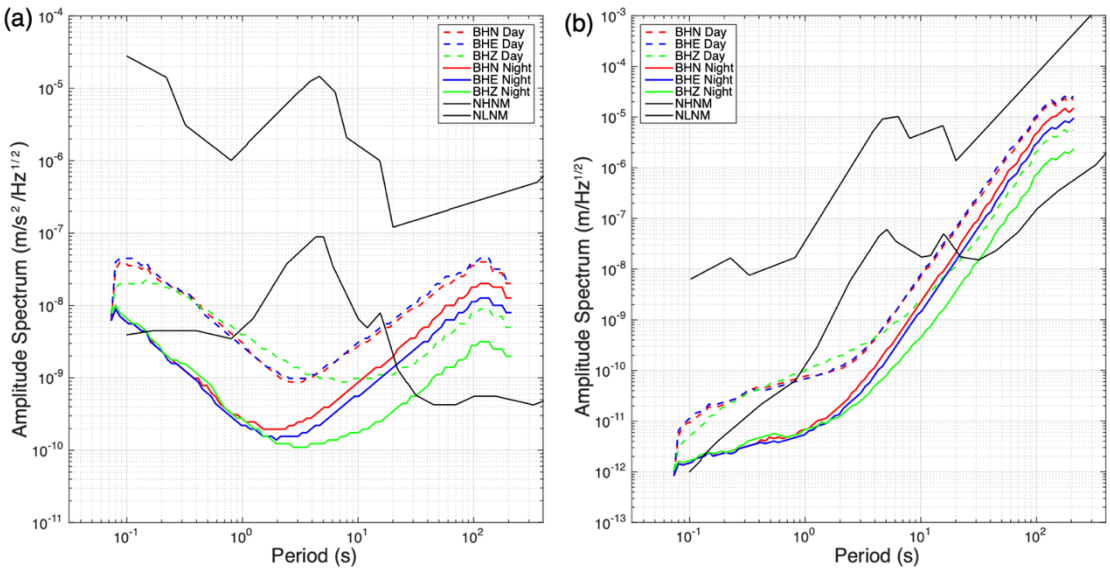

Figure 4.3 Amplitude spectra of martian noise in (a) acceleration and (b) displacement. The amplitude spectra are computed from the VBB data in July 2019 (Panning et al., 2020). The dashed lines denote the day noise level and the solid lines represent the night noise level. The Earth's noise spectra including New Low Noise Model (NLNM) and New High Noise Model (NHNM) are shown in black lines for comparison (Peterson, 1993). The night noise level is used to calculate the magnitude thresholds for detecting candidate body waves.

4.2.1.3 AxiSEM Synthetics

We propagated synthetic seismic waves through predicted martian models to quantify the detectability of our candidate body waves. We computed high frequency synthetics using a spectral element code AxiSEM (Nissen-Meyer et al., 2014). AxiSEM can simulate 3-D seismic wave propagations at a cheaper computational cost by reducing the dimensionality from 3-D to quasi 2-D in axi-symmetric media. This allows us to compute high frequency synthetics up to 1 Hz. We focused on two 1-D Mars models: EH45TcoldCrust1 (Rivoldini et al., 2011) and EH45TcoldCrust1rq (Daubar et al., 2018). These two models are almost identical except for EH45TcoldCrust1rq model has a very low velocity layer right below the surface representing the regolith layer on Mars. The goal was to understand the role of regolith layers in the detectability of candidate phases. The dominant period was 1s for EH45TcoldCrust1 model but

increased to 3s for EH45TcoldCrust1rq model because the simulations of regolith layer were more computationally expensive. We used a Mw 5 source on the surface with a moment tensor shown in Figure 4.4. We chose this moment tensor to allow for seismic energy in the receiver direction from all three types of waves: P wave, SH wave and SV wave. The receivers were placed on the equator from 0 to 180 degrees with a 0.2 degree spacing (11.8 km). The source depth was initially set to zero and subsequently moved deeper in the crust (e.g., 40 km) in some models.

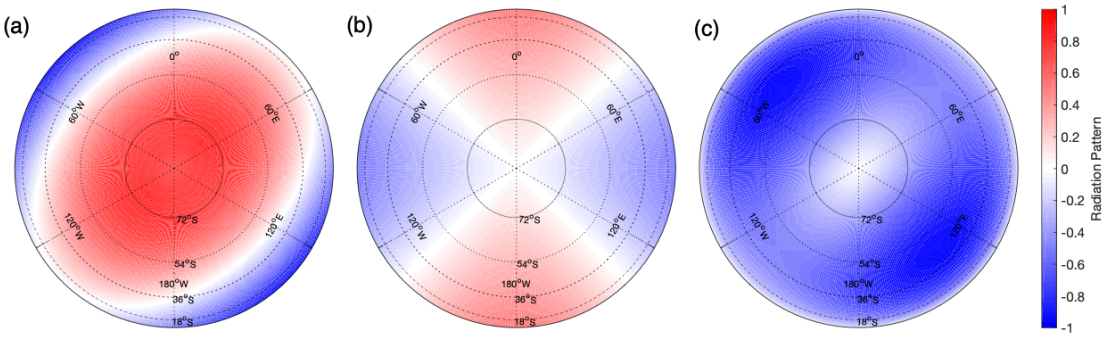

Figure 4.4 Radiation patterns for (a) P wave, (b) SH wave and (c) SV wave used as the seismic source for AxiSEM synthetics. This moment tensor was chosen to allow for energy from all three types of waves in the receiver direction.

Similar to the Moonquakes, the seismic events on Mars are also dominated by strong scattering (Lognonné et al, 2020). We used AxiSEM3D (Leng et al., 2016, 2019) to model the scattered waves in the martian crust and understand how scattering can affect the detection of 1,000-km discontinuity. AxiSEM3D is a hybrid code of 3-D spectral element and pseudo-spectral element method, which takes advantage of the smoothness of azimuthal dimension. AxiSEM3D can model the out-of-plane scattering and are significantly faster than a full spectral-element code such as SPECFEM3D (Komatitsch & Tromp, 2002a, 2002b). We used EH45coldCrust1 model as our reference model and added spherical heterogeneities to the crust as scatterers (Figure

4.5). We controlled the physical properties of the scatterers by changing the following parameters: velocity (dVp, dVs) and density (dRho) perturbations, radius of scatterers (R), spacing between scatterers (L) and the number of layers (N). Here is one example of our end-member scattering model: dVp=dVs=-30%, dRho=-6%, R=5 km, L=10 km, N=3. The whole martian crust was saturated with scatterers in this model to simulate the strongest scattering effect. The dominant period was 5 s for all the scattering models. The source and receivers were the same as AxiSEM synthetics described above.

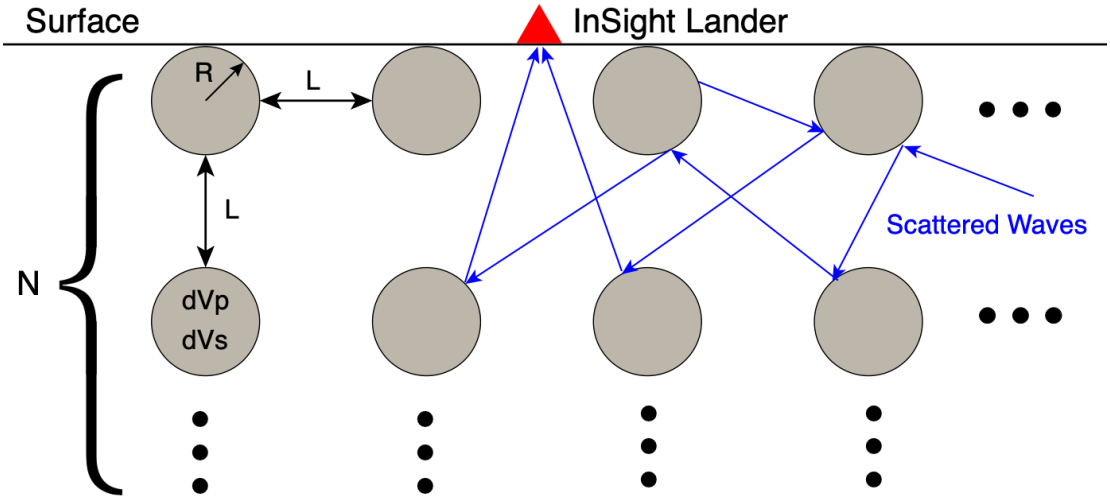

Figure 4.5 A schematic diagram showing the scattering model used in AxiSEM3D. The gray circles represent the scatterers in the crust and the blue arrows denote the scattered waves. L is the spacing between scatterers; R is the radius of scatterer; dVp and dVs are the velocity perturbations; and N is the number of layers.

4.2.2 Data Processing Approach

We analyzed the waveforms recorded by the InSight SEIS-VBB instrument to search for evidence of martian MTZ as well as other types of body waves. We applied polarization filtering techniques to improve the SNR for body waves. We also computed the back-azimuths of the events based on P wave polarizations and rotated the events to radial and transverse components. The goal is to align the seismic events on P- and S- arrivals and identify consistent moveout of body waves.

4.2.2.1 InSight Dataset

The seismic events on Mars are broadly classified as two types: (1) low-frequency (LF) and (2) high-frequency (HF) events based on their frequency content (Giardini et al., 2020). The dominant energy of LF events is below 1 Hz, while some events have more broadband energy extended above 1 Hz which are classified as a subgroup: broadband (BB) events. The HF events have energy mostly above 1 Hz and can extend up to 6-12 Hz. The Very High Frequency (VHF) events are special type of HF events that show higher frequency energy in the horizontal components. Another type of HF events, which is named as 2.4 Hz events, only have narrow banded energy around 2.4 Hz resonance. MQS ranks these events from Quality A to D (A is the best) based on the clarity and polarization of the phases (Clinton et al., 2020). We selected 14 high-quality LF and BB events (Quality A and B) where P- and S- arrivals can be clearly identified (Table 4.2). We picked the P and S arrival times of these events and align them based on the S-P time, which is equivalent to epicentral distance. However, these high-quality events are mostly located about 25-40 degrees away from the InSight lander. Therefore, we also searched the low-quality LF and BB events (Quality C and D) and HF events for distant events (> 50 degrees). These lower quality events have lower SNR so the P- and S- arrivals are more difficult to identify.

4.2.2.2 Polarization Filter and Event Rotation

The waveforms of marsquakes are often characterized by strong coda due to scattering (Lognonné et al., 2020), thereby complicating the identifications of body waves. Polarization filtering is a method used to enhance linearly polarized waves such as body waves while suppressing other non-polarized waves including background

noise or scattered waves. A polarization filter was used to detect core-reflected body waves in the Apollo seismic data (Weber et al., 2011). Here we followed the method by Montalbetti & Knasewich (1970) to design a polarization filter for improving the signal-to-noise ratio (SNR) of martian body waves. First, we computed the covariance matrix of the three-component data (R, T, Z) in a given time window (e.g., 5 s) around t_0, and the eigenvectors and eigenvalues of this matrix. The rectilinearity at time t_0 is defined as the following equation:

$$RL(t_0) = \left[1 - \left(\frac{\lambda_2}{\lambda_1}\right)^n\right]^J \tag{4.1}$$

where λ_1 and λ_2 are the largest and second largest eigenvalues respectively, n and J are the empirical exponents. The eigenvector associated with the principal axis is $\vec{E}$ = (e_1, e_2, e_3) with respect to the R, T, Z coordinate system. The weights on each direction at time t_0 is given by:

$$D_i(t_0) = e_i^K \tag{4.2}$$

where i = 1, 2, 3 (R, T, Z), K is the empirical exponent. We chose these empirical values for the exponents: n=0.5, J=1, and K=2. The polarization filter for each component is defined as the product of rectilinearity and the corresponding direction weight. The filtered three-component seismograms at any time t are given by:

$$R_f(t) = R(t) \cdot RL(t) \cdot D_R(t) \tag{4.3}$$

$$T_f(t) = T(t) \cdot RL(t) \cdot D_T(t) \tag{4.4}$$

$$Z_f(t) = Z(t) \cdot RL(t) \cdot D_Z(t) \tag{4.5}$$

In practice, the InSight data were only provided as N, E, Z three components instead of R, T, Z due to the unconstrained back-azimuths of the source locations.

Fortunately, the polarization filter can also serve as a polarization analysis tool to determine the polarizations of P waves, thus provide constraints on the back-azimuths. We computed the average principal axis of P-wave particle motions, which is expressed as $\vec{P} = (P_E,\ P_N,\ P_Z)$, using a 5 s time window centered around the P wave. The back-azimuth of the event is then calculated using the following equation:

$$BAZ = \arctan\left(\frac{P_E}{P_N}\right) + \pi \tag{4.6}$$

Once we obtained the back-azimuths, we rotated the seismograms to radial and transverse components and then applied the polarization filter in the ZTR coordinate frame. We also computed the incidence angle of P wave using the following equation:

$$INC = \arctan\left(\frac{\sqrt{P_E^2 + P_N^2}}{|P_Z|}\right) \tag{4.7}$$

4.2.2.3 Data Processing Steps

Here we use the broadband S0235b event, which is the best-quality event recorded by InSight, as an example to illustrate how we pick P- and S- arrivals and obtain the back-azimuths and incidence angles of the LF and BB events. First, instrument response was removed from the data to obtain seismograms in velocity, and the 3 SEIS-VBB components were rotated to the BHZ, BHN, and BHE coordinate frame. Then, we bandpass filtered the seismogram between 0.3-0.9 Hz to remove long-period noise and tick-noise from crosstalk between the seismometer and the temperature sensors in the SEIS instrument package (Compaire et al, 2020; Daubar et al., 2020). Figure 4.6a shows the bandpass filtered seismograms and envelopes on vertical component (BHZ). This event lasted for ~10 min, and the P and S waves can be clearly identified. The time-series and spectral envelopes both show clear coda

decays of P and S waves due to the intrinsic and scattering attenuations. Then, we applied polarization filter to the band-pass filtered data on all three components (ZNE). As shown in Figure 4.6b, the P and S coda are suppressed by the polarization filter due to the lack of linear polarization, whereas the P waves are enhanced on the vertical component. The spectrogram of S0235b event (Figure 4.6c) illustrates that this event is dominated by low-frequency energy, but the broadband energy is also extended up to ~3 Hz. We can determine the onsets of P and S waves from the spectrogram. We picked the P-arrival at the maximum amplitude of time-series envelope based upon the MQS reported P arrival time (Clinton et al., 2020).

To obtain event back-azimuth, we cut a ±5-s time window centered around the selected P-arrival and used the P-wave energy partitioning amongst the horizontal components to determine the back-azimuth and incidence angle of each event (e.g., Scholz et al., 2017). The back-azimuth and incidence angle of P wave were calculated using equation (4.6) and (4.7). The histogram (Figure 4.6d) demonstrates that the back-azimuth ($81.8 \pm 3.1°$) is well-constrained and consistent with the estimate from MQS (Giardini et al., 2020). The incidence angle shows relatively larger uncertainties on the histogram (Figure 4.6e). We rotated the horizontal components (BHN and BHE) of the event to radial (BHR) and transverse (BHT) components based on the P-wave derived back-azimuth. Then, we applied polarization filtering again in the ZTR coordinate frame and picked S-arrivals on the transverse component with guidance from the MQS picks (Clinton et al., 2020). The joint information of S-P times and back-azimuths can reveal the event locations assuming certain Mars velocity models. S0235b event is located near Cerberus Fossae, which is a potentially active fault system associated with

possible volcanic activities (Taylor et al., 2013; Vaucher et al., 2009). Finally, we repeated the procedures described above and picked the P- and S-arrivals of 14 high-quality LF and BB events (e.g., Quality A and B) and summarize the distances and back-azimuths of these events in Table 4.2. Note that these three events: S0105a, S0133a and S0154a were relegated to Quality C recently after we finished our data analysis. However, we continue to use these events because our analyses are not directly related to MQS's evaluations of the events.

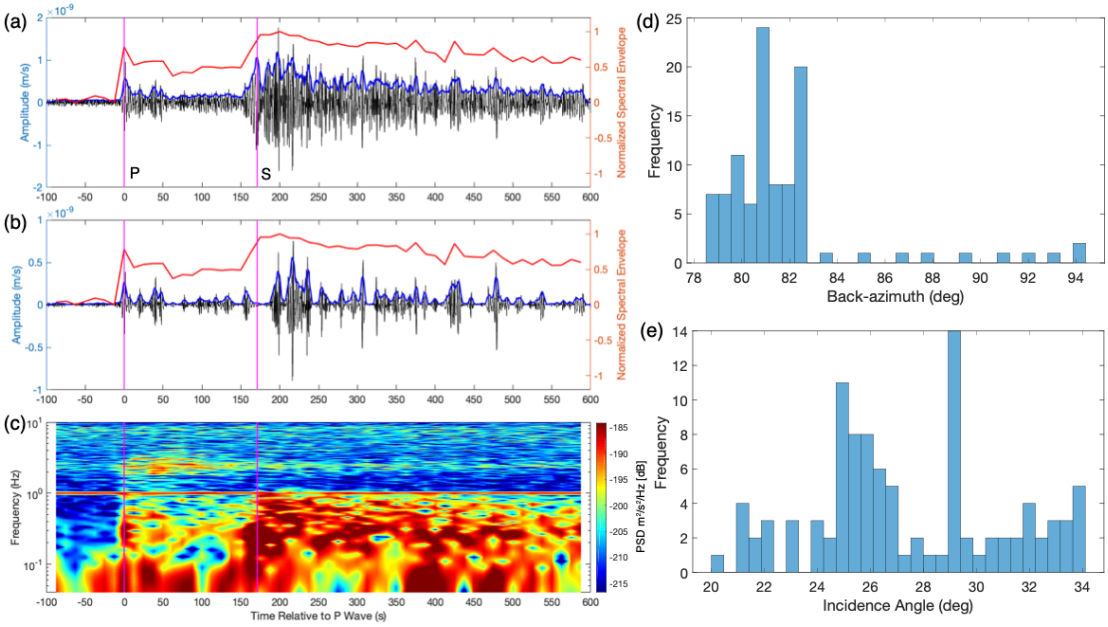

Figure 4.6 Data analysis of S0235b event based on polarization filter. (a) The waveform (black) of S0235b event on vertical component (BHZ) bandpass filtered between 0.3-0.9 Hz. (b) The polarization filtered waveform (black) of S0235b event. The blue curves represent the envelopes of time-series waveforms, and red lines denote the normalized spectral envelopes from spectrograms. (c) The spectrogram of S0235b event. The magenta lines highlight the travel-time picks of P and S waves based upon polarization filter. (d) The histogram of S0235b back-azimuths derived from P wave polarization. (e) The histogram of P wave incidence angle.

Table 4.2 Summary of distances, back-azimuths and incidence angles of high-quality LF and BB events.

Event	Type	Quality	S-P time (s)	Distance (degree)	Back-azimuth (degree)	Incidence Angle (degree)
S0105a	LF	B -> C	180.1±5.0	30.6±0.9	121.2±3.4	47.7±2.2
S0133a	BB	B -> C	195.5±5.0	33.4±0.9	307.1±6.3	50.4±2.7
S0154a	BB	B -> C	260.8±5.0	45.3±0.9	268.7±8.6	47.6±3.5
S0173a	LF	A	172.8±5.0	29.3±0.9	87.3±1.3	36.5±5.9
S0183a	LF	B	305.6±5.0	53.4±0.9	99.8±2.8	17.8±1.3
S0185a	LF	B	360.4±5.0	63.1±0.9	161.0±4.1	37.6±4.5
S0189a	LF	B	195.1±5.0	33.3±0.9	200.8±13.4	30.7±10.1
S0235b	BB	A	171.1±5.0	29.0±0.9	81.8±3.1	27.4±3.6
S0290b	LF	B	225.2±5.0	38.8±0.9	277.4±5.4	14.7±1.4
S0325a	LF	B	230.2±5.0	39.7±0.9	107.7±7.6	13.6±3.0
S0395a	BB	B	209.2±5.0	35.9±0.9	109.3±16.6	38.7±5.6
S0407a	LF	B	171.0±5.0	28.9±0.9	118.9±29.5	14.2±3.1
S0409d	LF	B	164.1±5.0	27.7±0.9	102.2±50.3	13.4±2.9
S0484b	BB	B	173.4±5.0	29.4±0.9	118.5±11.8	10.9±2.5

4.3 Modeling Results

4.3.1 Detectability of Candidate Phases

In this section, we used the AXISEM synthetic waveforms computed from EH45TcoldCrust1 model to determine the detectability of MTZ sensitive phases that we subsequently search for in the InSight seismograms. For our analysis, we used the VBB noise level described in Section 4.2.1.2 to calculate the minimum magnitude thresholds and frequency bands required for detections. This analysis indicated which candidate phases are predicted to fall above the martian nighttime noise. Our analysis also indicated where potential interfering phases might be confused with the MTZ interacting phases.

4.3.1.1 P and S Triplications

We computed travel-time curves of P- and S- waves from the InSight blind test models (Clinton et al., 2017) to determine the relationship between the depths of 1,000-km discontinuity and the epicentral distances of the triplications. The travel-times of P and S waves (Figure 4.7a, 4.7b) are shown in reduced times ($T-X/V_{P,S}$) to highlight the "bow-tie" shapes of triplications. Figure 4.7 shows that despite different upper mantle velocity structures and depths of 1,000-km discontinuity, the epicentral distances of P and S triplications vary by only 8 degrees, in the range of 60-85 degrees. However, the travel-times of P and S triplications display variations up to 20-s and 40-s respectively owing to the differences in crust and upper mantle velocities between the models. In models with an 800-km discontinuity associated with the Opx to HP-Cpx phase transition, more than one triplication occurs in the travel-time curves. We highlight the convergence points of triplications to represent their average distances. Figure 4.7c illustrates that the distance of triplication is linearly correlated with the depth of 1,000-km discontinuity for both P (R^2=0.87) and S waves (R^2=0.74). The travel time analysis demonstrates that the depth of olivine-wadsleyite phase transition can be constrained where distance of the triplication arrivals is established to within 5 degrees, which is reliant upon an accurate velocity model of the martian interior to properly establish distance.

Travel times alone are not enough to identify the triplication arrivals; we used synthetic waveforms of P triplications, shown in Figure 4.8a to investigate the energy partitioning at triplication distances. Two triplications patterns are evident in the modeled waveforms, with arrival times consistent with the predicted travel-time curves

from TauP (Crotwell et al., 1999). The earliest triplication matches the ray-theory predictions for the structure associated with the 800-km discontinuity, whereas the later one is from the 1,000-km discontinuity. In both cases, the synthetics show that the amplitudes of the triplicated arrivals are comparable or even larger than that of the first P arrivals. For the P-triplications, the travel-times of the prograde and retrograde branches are only ~5 seconds later than first P arrivals. Our synthetics reveal that high frequency waves (1 Hz in Figure 4.8a) are required to distinguish each branch, at lower frequencies the triplication is expressed as a broadening of the P-waveform at the triplication distance. Furthermore, the modeling reveals that the triplications are followed by crustal reverberations such as Pv85pP which can interfere with the triplication waveforms. The depth phase of P (pP) would also interfere with the triplications, further complicating the waveform. However, we note that the slowness of crustal reverberations and depth phases are distinct from triplications, which can be used to distinguish them.

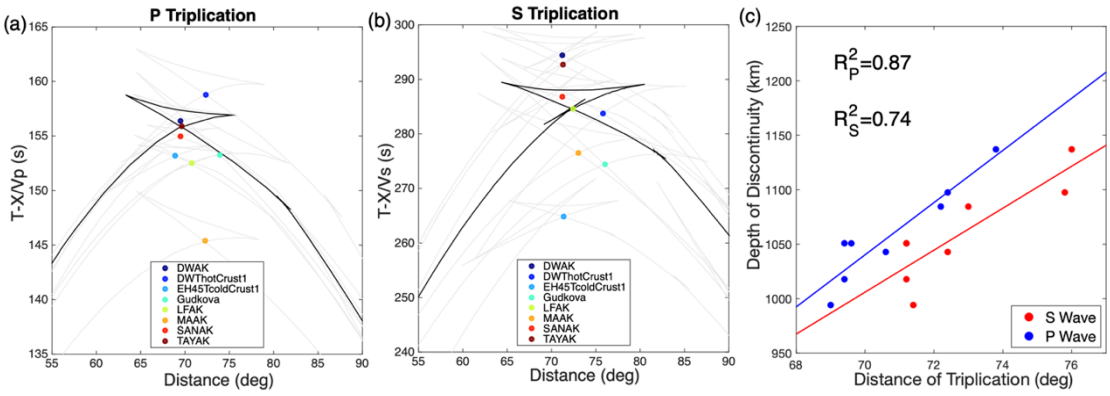

Figure 4.7 Reduced travel-time curves for (a) P and (b) S triplications computed from InSight blind test models (Clinton et al., 2017). The reduced velocities are Vp=12.0 km/s and Vs=6.5 km/s, and X represents the distance. The TAYAK and LFAK models are highlighted in black curves for P and S waves respectively, while other models are in gray colors. The convergence points of the triplications are highlighted in colored circles. (c) The depth of 1,000-km discontinuity vs. the distances of triplications. The depth and distance are linearly correlated, which suggests the depth of olivine-to-wadsleyite phase transition can be deduced from triplication distance.

To determine the detectability of triplications for marsquakes, we cut a 15-s time window centered around the triplication at 72 degrees and calculated the amplitude spectrum for comparisons with the VBB BHZ noise level (Figure 4.8b). The magnitude thresholds are defined as the minimum magnitudes of events when the signals are ~10dB above the noise level. The magnitude thresholds required for detections are Mw 2.5 and Mw 3.5 respectively using the night and day noise levels, which are comparable to the sizes of marsquakes (Mw 2.5-4.0) observed by SEIS (Banerdt et al., 2020; Giardini et al., 2020). We computed the SNR of P waves across different distances and frequencies from the difference between the amplitude spectra and BHZ night noise level (Figure 4.8c). As the magnitude increases, the SNR will similarly increase and also result in a broader bandwidth above the noise (>10dB to be detectable). The period range for the detection of P triplications is between 1-15s, and distance range is between 60-75 degrees.

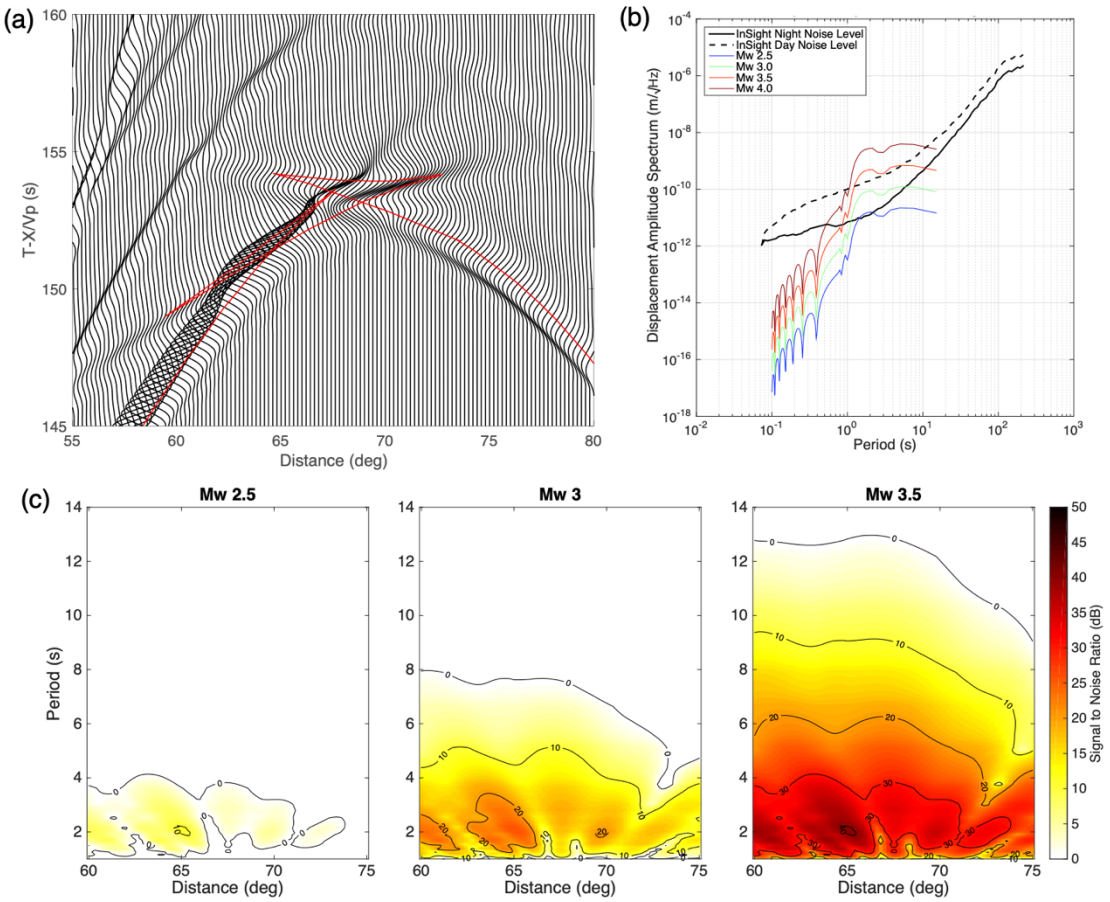

Figure 4.8 (a) Synthetic waveforms of P triplications on vertical component using EH45TcoldCrust1 model. The red lines are the predicted travel-time curves from TauP (Crotwell et al., 1999). The synthetics are bandpass filtered between 1-100 s. (b) The amplitude spectra of P triplications for different magnitudes of events. The amplitude spectra are computed from a 15-s time window centered around the triplication at 72 degrees. The VBB BHZ noise levels are in black curves. (c) The SNR of P triplications for different magnitudes of events. The magnitude threshold is Mw 2.5. The period range is 1-15 s, and the distance range is 60-75 degrees to detect the P triplications.

The synthetic waveforms of S triplications are more complicated with two triplications more closely intersecting with each other (Figure 4.9a). The travel-times of S triplications are 10-15s later than the first S waves, allowing them to be separable even in lower-frequency records. This will increase the chance of detecting the triplication since many high-quality events from InSight are low-frequency events (Giardini et al., 2020). The S triplications are also followed by crustal reverberations and depth phases, which can be distinguished from their slowness. Similar to P waves,

we cut a 50-s time window centered around the triplication at 70 degrees to calculate the amplitude spectra (Figure 4.9b). The magnitude thresholds required for detections are Mw 3.5 and Mw 4.0 respectively using BHE/BHN night and day noise level. The thresholds are larger than P waves because the horizontal component are noisier and S wave radiation is weaker from the source. Nonetheless, the magnitude thresholds are still comparable to the event sizes observed by SEIS (Mw 2.5-4.0). Figure 4.9c illustrates the SNR of S triplications for different magnitudes of events. The period range for detection is between 1-25s and distance range is between 60-85 degrees.

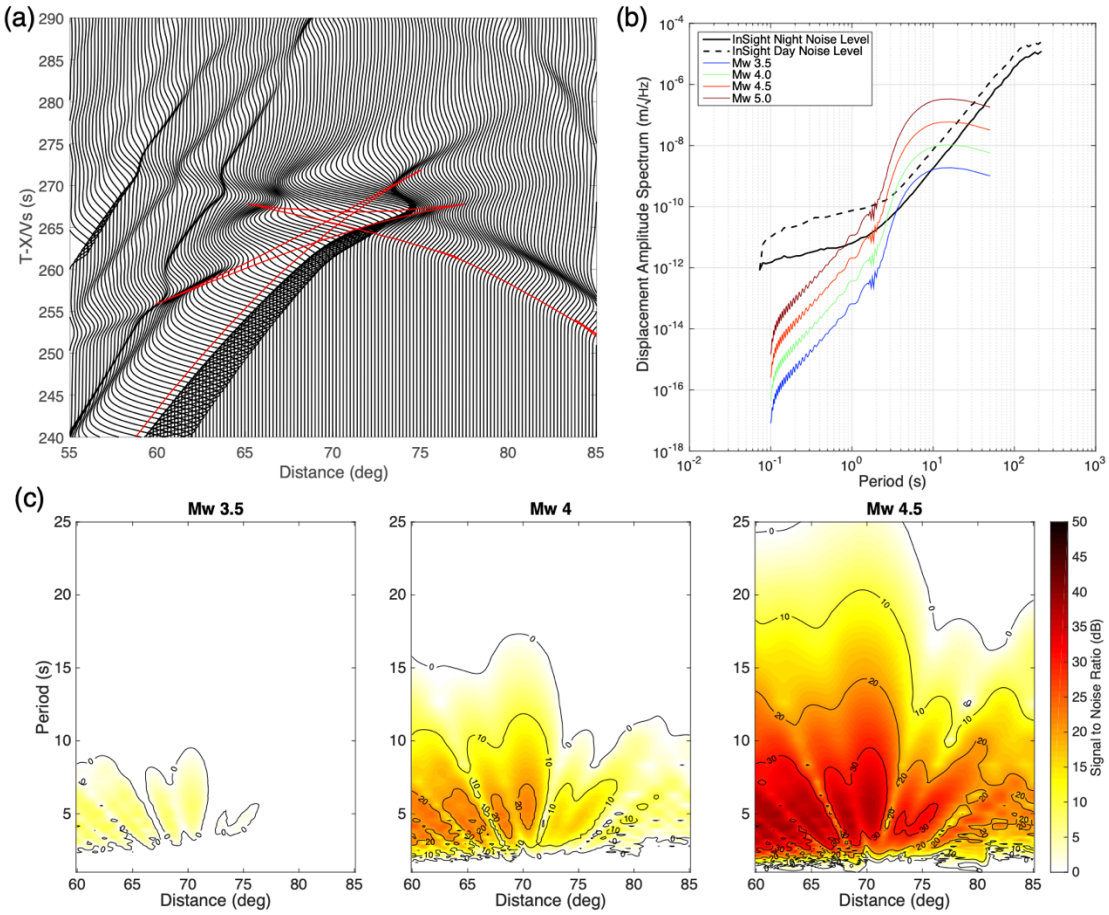

Figure 4.9 Same as Figure 4.8 but for S triplications. (a) The synthetic waveforms of S triplications on transverse component using EH45TcoldCrust1 model. The synthetics are bandpass filtered between 1-100 s. (b) The amplitude spectra of S triplications for different magnitudes of events. The amplitude spectra are computed from a 50-s time window centered around the triplication at 70 degrees. The average noise level of VBB BHE and BHN are shown in black curves. (c) The SNR of S triplications for different magnitudes of events. The magnitude threshold is Mw 3.5. The period range is 1-25 s, and the distance range is 60-85 degrees to detect the S triplications.

4.3.1.2 ScS Precursors

The ScS precursors are the seismic waves reflected from the topside of the mantle discontinuities. Figure 4.10a shows the transverse wavefield including the ScS precursors and surface waves. We observe two reflections in the synthetic waveforms: Sv800S and Sv1000S. Sv800S has larger amplitude even if the impedance contrast is smaller at 800-km compared to 1,000-km depth. The ScS precursors are followed by

the crustal phases (e.g., Sv85sSv1000S) which have opposite polarities. The crustal phases do not interfere with the ScS precursors in this model, but they could if the crust were thicker or 1,000-km discontinuity were shallower. The ScS precursors arrive right after the surface waves so the epicentral distances are only limited to 0-12 degrees. They are likely to be contaminated by the coda of surface waves due to crustal scattering or guided waves trapped in the regolith layer. We cut a time window including both Sv800S and Sv1000S and computed the power spectra to compare with the VBB BHE/BHN noise level (Figure 4.10b). The magnitude thresholds are Mw 5.0 and Mw 5.5 using the night and day noise level respectively, which are significantly larger than those of triplications. We also compute the SNR of ScS precursors at different distances and frequencies (Figure 4.10c). The SNR increases as the magnitude increases, and the period range for detection is between 2-25 seconds.

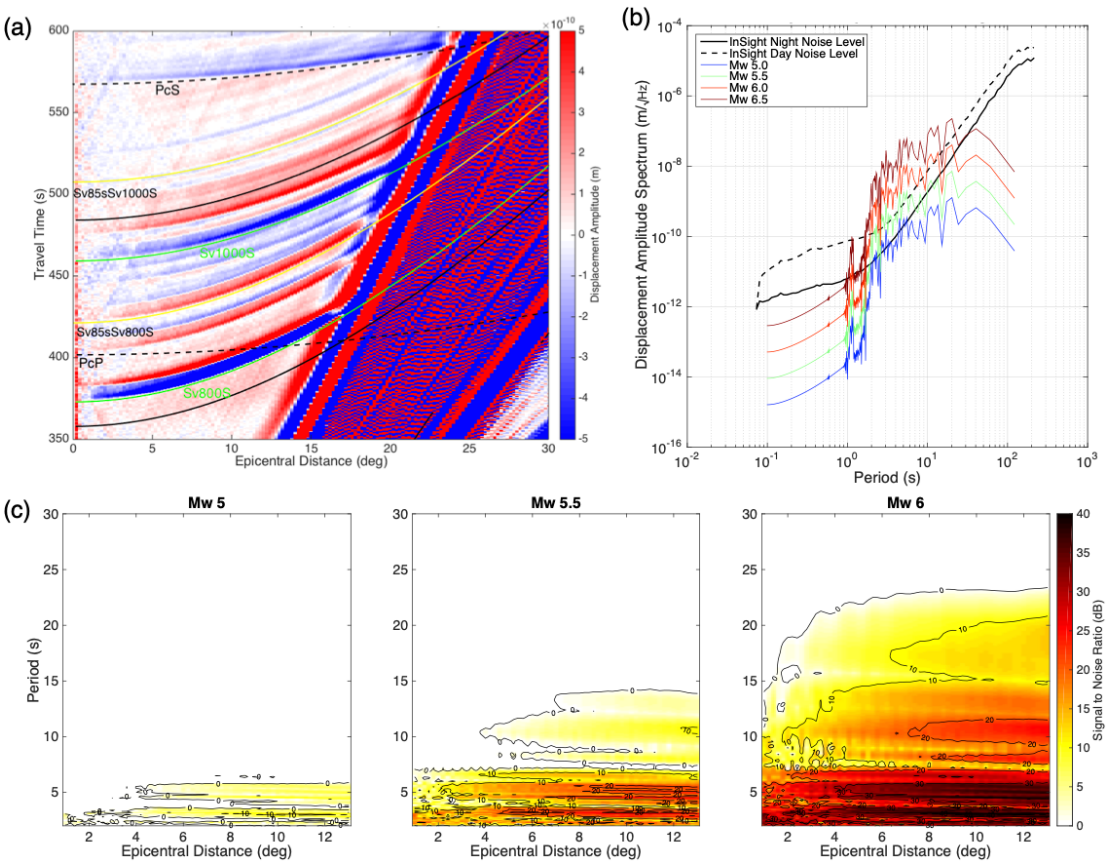

Figure 4.10 (a) Synthetic wavefield of ScS precursors on the transverse component. The size of event is Mw 5 and the synthetics are bandpass filtered between 2-50 s. The travel-time curves of ScS precursors (Sv800S and Sv1000S) are shown in green curves. The crustal reverberations are shown in yellow lines (Sv85sSv1000S and Sv85sSv1000S). The black lines highlight the time window used for the calculation of amplitude spectra. (b) The amplitude spectra of ScS precursors at 10 degree. The average noise levels of VBB BHE and BHN are shown in black curves. (c) The SNR of ScS precursors for different magnitudes of events. The magnitude threshold is Mw 5.0 using the martian night noise level. The period range is 2-25 s, and the distance range is 0-12 degrees for detections.

4.3.1.3 PP Precursors

PP precursors are underside reflections and arrive between Pdiff and PP (Figure 4.11a). The P1000P can be observed on the vertical wavefield, whereas P800P is too small to be seen. The PP precursors have a relatively clean time window for detections. The only interfering phase is the major-arc phase of Pdiff between 170-180 degrees. The crustal phases of Pdiff (e.g., Pv85pPdiff) arrive ~50s earlier than P1000P with opposite polarities. Unlike the ScS precursors, Pdiff and PP precursors lack high

frequency energy due to attenuation, so they are less likely to be affected by Pdiff coda. We also cut a time window to include both P800P and P1000P and calculated the amplitude spectra at 150 degrees. The magnitude thresholds are Mw 5.5 and Mw 6.0 using night and day noise levels. Similar to the ScS precursors, the magnitude thresholds are significantly larger than the observed event sizes on Mars. Although stacking multiple events can lower the thresholds, the retrieval of PP precursors typically requires tens of large events on Earth (e.g., Flanagan and Shearer, 1999), which can take years to be observed by InSight. Figure 4.11c illustrates the SNR of PP precursors at different distances and frequencies. The period range and distance range for detections are 1-30s and 140-165 degrees respectively.

The detectability of three types of candidate phases are summarized in Table 4.3. The candidate phases cover the entire epicentral distance range from near-field (ScS precursor), intermediate-field (triplications), and far-field (PP precursors). The magnitude thresholds for triplications are significantly lower than ScS and PP precursors, indicating that triplicated waves are more likely to be detected from the InSight data even though multiple events are required to figure out their travel-time curves.

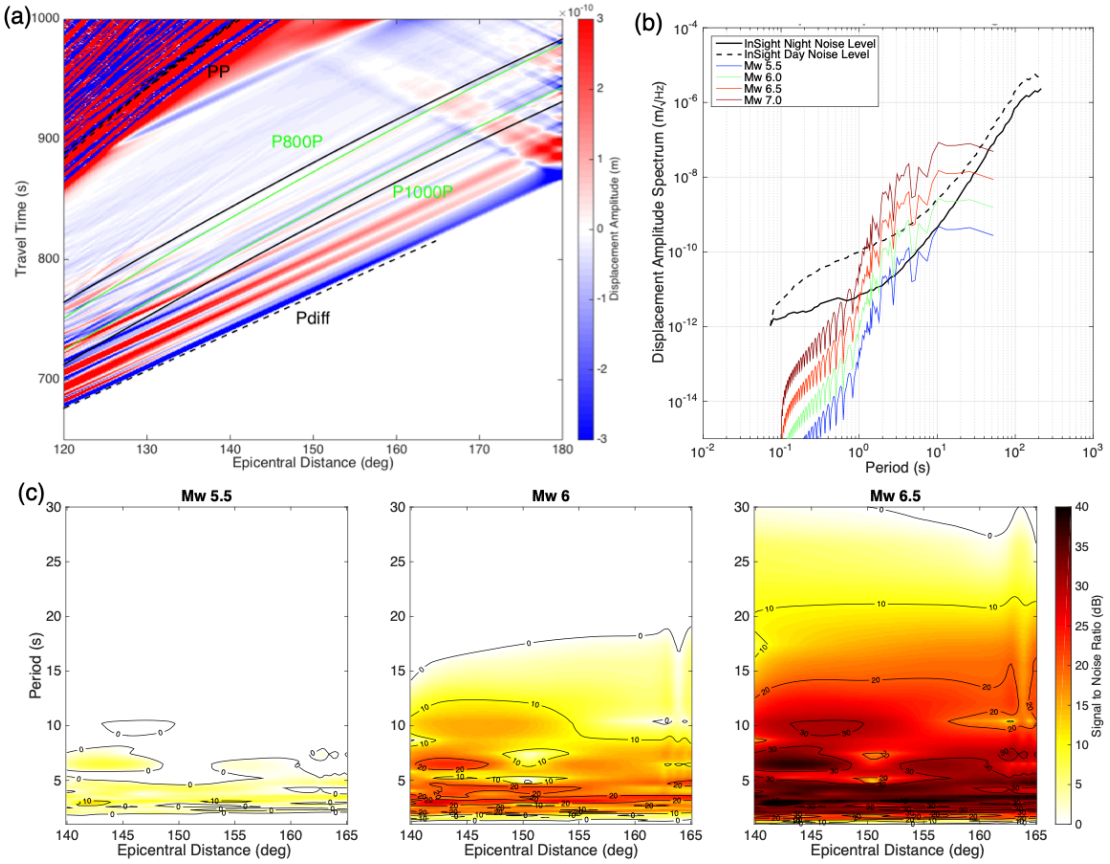

Figure 4.11 (a) Synthetic wavefield of PP precursors on the vertical component. The size of event is Mw 5 and the synthetics are bandpass filtered between 1-50s. The green lines represent the predicted travel-times of PP precursors (P800P and P1000P). The black lines highlight the time window used for the calculation of amplitude spectra. (b) The amplitude spectra of PP precursors at 150 degree. The VBB BHZ noise levels are shown in black curves. (c) The SNR of PP precursors for different magnitudes of events. The magnitude threshold is Mw 5.5, which is slightly larger than the ScS precursors. The frequency range is 1-30 s, and the distance range is 140-165 degrees to detect the PP precursors.

Table 4.3 Detectability of candidate body waves for martian MTZ.

	Magnitude (Mw)	**Period (s)**	**Distance (deg)**	**Noise Level**
P triplication	2.5	1-15	60-75	BHZ night
S triplication	3.5	1-25	60-85	BHN/BHE night
ScS Precursor	5.0	2-25	0-12	BHN/BHE night
PP Precursor	5.5	1-30	140-165	BHZ night

4.3.2 Effects of Regolith Layer

The pre-landing remote sensing data (Golombek et al., 2017, 2018) and post-landing observations (Golombek et al., 2020) reveal that the InSight landing site is coved by a ~3-m thick fragmented regolith layer overlying unconsolidated basalt flows. In terms of seismology, the martian regolith layer manifests as a low velocity layer near the surface. Here, we chose a pre-landing model EH45TcoldCrust1rq (Daubar et al., 2018) to simulate the effect of regolith layer on the waveforms of candidate phases. This model has an 80-m thick regolith layer, which is significantly thicker than that of InSight landing site, overlying on a 1-km fractured bedrock layer (Figure 4.12). The Vs and Vp of the regolith layer are only 150-300 m/s and 265-600 m/s respectively. The low velocity layer will lead to very small mesh grids near surface when computing synthetic waveforms, thus increase the computational costs significantly. Therefore, we ran the synthetics at lower frequency (3s) to compensate the expensive simulations of regolith layer. Figure 4.12 illustrates the comparisons of three models: EH45TcoldCrust1, EH45TcoldCrust1b and EH45TcoldCrust1rq. EH45TcoldCrust1 is the benchmark model we used for previous detectability studies, which does not have any regolith layer but a consistent velocity layer as the upper crust. EH45TcoldCrust1b is an intermediate model only with a 1-km fractured bedrock layer but lacking a regolith layer. All these three models have the same structures below 1-km depth. We use the same earthquake source (Figure 4.4) at two different depths: 0 and 40-km. The goal is to understand the role of source depth when a regolith layer is present.

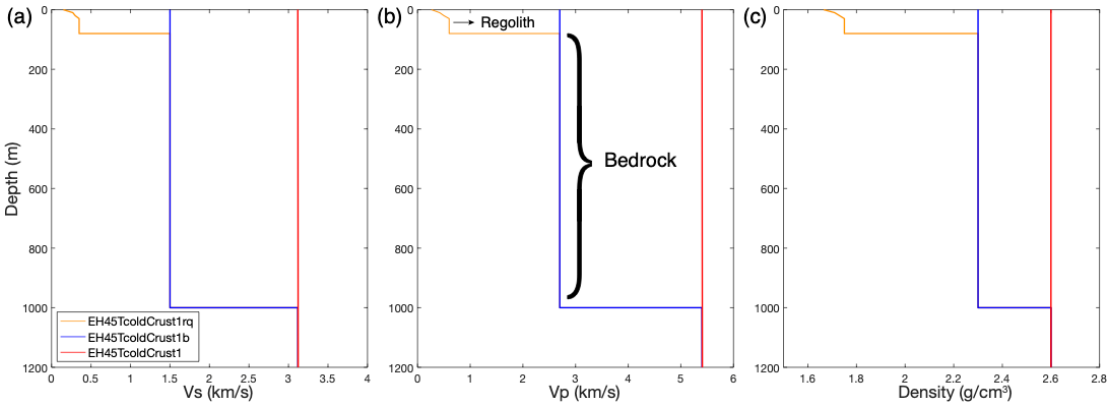

Figure 4.12 Comparisons of velocity models with and without a regolith layer. The near-surface profiles of (a) Vs, (b) Vp and (c) density for EH45TcoldCrust1, EH45TcoldCrust1b and EH45TcoldCrust1rq models (Daubar et al., 2018). EH45TcoldCrust1rq has an 80-m regolith layer on top of a bedrock layer. EH45TcoldCrust1b only has a 1-km bedrock layer without any regolith layer. EH45TcoldCrust1 does not have any regolith layer but has a faster bedrock layer.

A regolith layer with very low velocity can amplify seismic waves near the surface (Daubar et al., 2018). This low velocity layer can also generate surface waves and trap body waves as reverberations within the layer like a wave guide. We observe that these guided waves arrive after the surface waves, and strongly interfere with the wavefield of ScS precursors (Figure 4.13a). Luckily, the reverberations within the regolith layer are dominated with relatively high frequency content (> 0.1 Hz) which can be removed by a band-pass filter. We first use a 5-50 s band-pass filter which could only remove the trapped waves within 5 degrees range (Figure 4.13a). This only gives a very narrow epicentral distance range to observe the ScS precursors. Then, we push the filter to lower frequency corners at 10-50s, which completely remove the trapped waves (Figure 4.13b). However, the high frequency content of ScS precursors are also lost with the trapped waves due to the band-pass filter. We compute the SNR of ScS precursors after using the 10-50s filter (Figure 4.13c). Since the noise level is higher in lower frequency (Figure 4.3b), the magnitude threshold increases from Mw 5.0 to Mw 5.5 due to the loss of high frequency energy (Figure 4.13c). The fact that a regolith

layer exists beneath the InSight lander makes it more difficult to detect the ScS precursors, requiring larger events to be visible above the background noise. Note that the structures of regolith layer on Mars are likely heterogeneous (e.g., different thickness and scattering), so the constructive interreference of these trapped waves would likely be weaker than predicted by the homogeneous regolith structures implemented in the 1-D model. The 80-m regolith thickness in the model is much larger than the actual measurement of 3-m thickness beneath InSight (Golombek et al., 2020). A thinner regolith layer can further constrain the frequency content of trapped waves to even higher frequency, thus improve the detectability of ScS precursors.

Source depth plays a key role in the generation of guided waves in the regolith layer. A deep source can limit the ray angles entering the regolith layer, thus negate the guided waves. To test this hypothesis, we move the source depth to 40-km and compute the synthetics using the same model. As shown in Figure 4.14a, most of the reverberations are removed by 2-50 s band-pass filter, with only some residual signals contaminating the ScS precursors. A 5-50 s band-pass filter can completely remove the reverberations (Figure 4.14b), whereas only the close-by reverberations (<5 degrees) are removed for a 0-km depth source (Figure 4.13a). Even if the synthetics are filtered to higher frequency, the magnitude threshold still remains the same (Mw 5.5) as the 0-km depth model (Figure 4.14c). This test demonstrates that the guided waves can be suppressed when the source depth is deeper in the crust, but the detectability will not change as a function of depth.

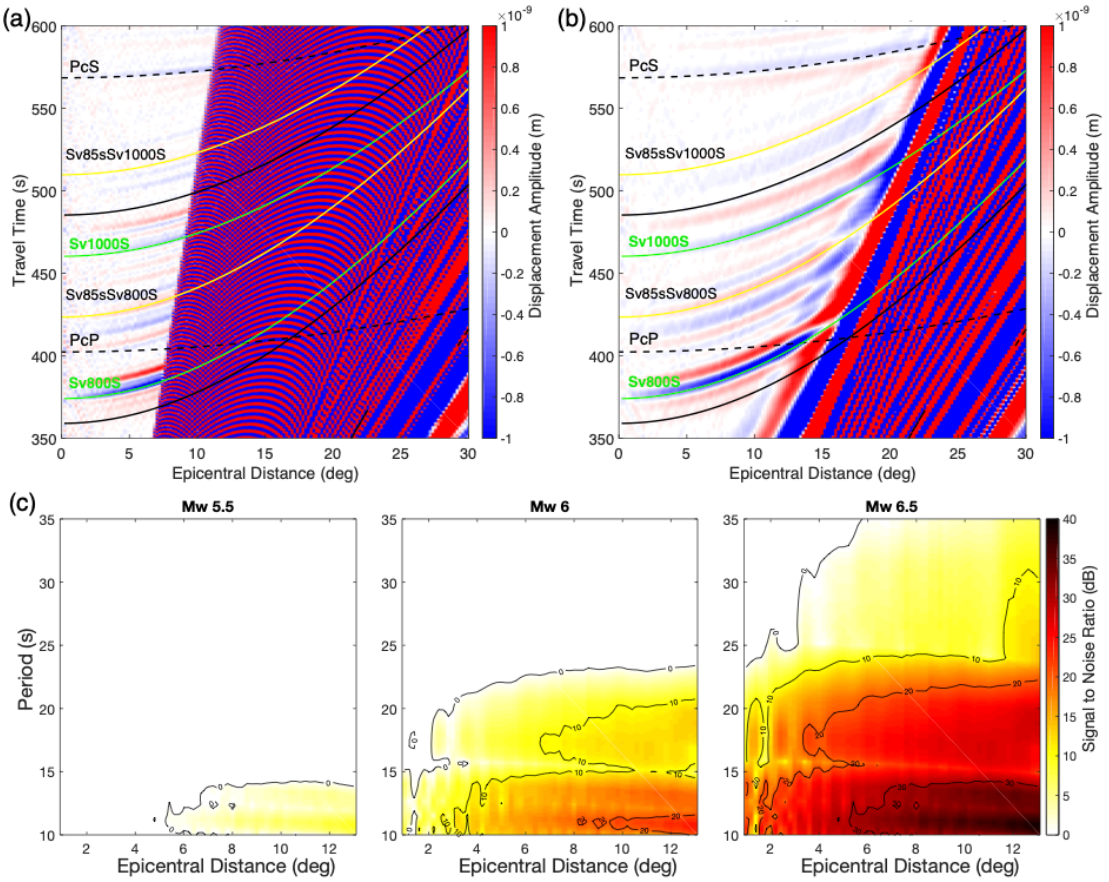

Figure 4.13 Synthetic wavefield of ScS precursors on the transverse component using EH45TcoldCrust1rq model (Daubar et al., 2018). The source depth is at 0 km. (a) The synthetics are bandpass filtered between 5-50 s. (b) The synthetics are bandpass filtered between 10-50 s. (c) The SNR of ScS precursors for different sizes of events using the 10-50s bandpass filter. The magnitude threshold is increased to Mw 5.5 due to the regolith layer.

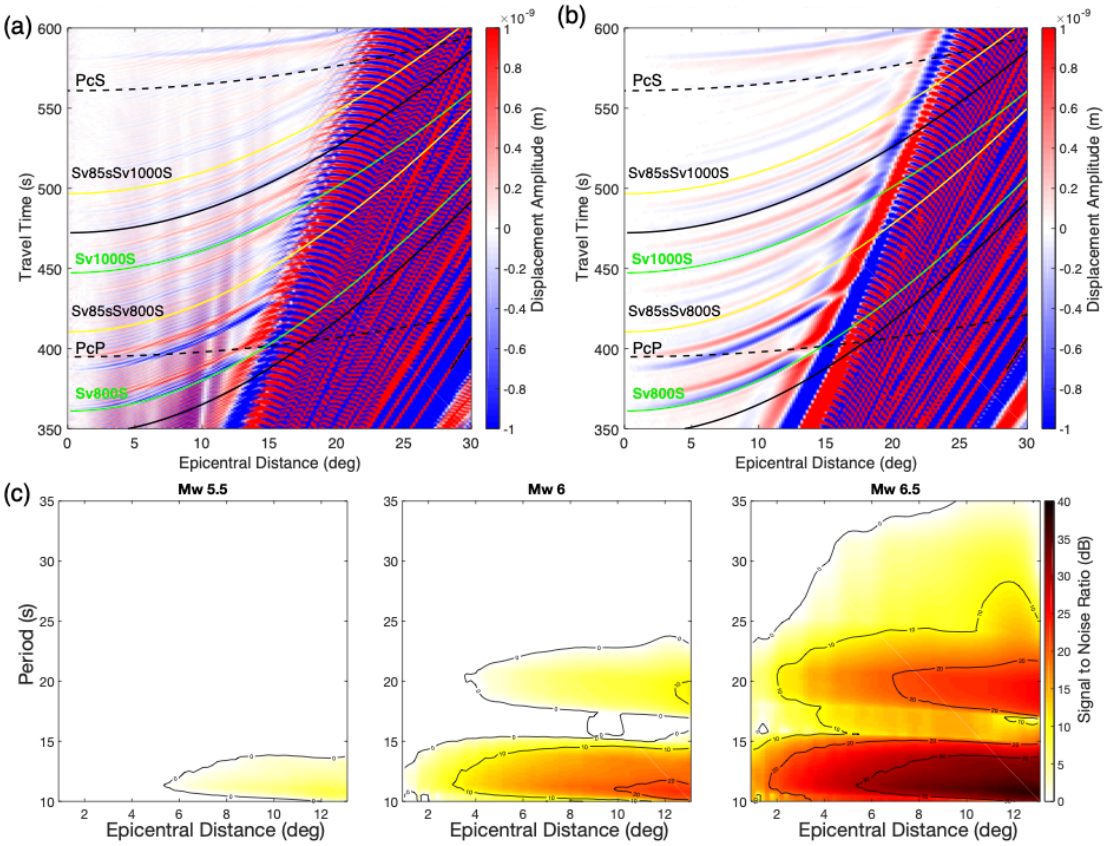

Figure 4.14 Same as Figure 4.13 except for that the source depth is at 40 km. (a) The synthetics are bandpass filtered between 2-50 s. (b) The synthetics are bandpass filtered between 5-50 s. (c) The SNR of ScS precursors for different sizes of events using the 5-50s bandpass filter. The magnitude threshold remains as Mw 5.5 compared to the 0-km depth source.

We also examined the wavefields of P and S triplications, and PP precursors. We find that the regolith layer has negligible effects on the waveforms of these teleseismic candidate phases. The high frequency content is lost due to attenuation in the crust and mantle after traveling more than 60 degrees. Therefore, the low frequency teleseismic waves are not sensitive to an 80-m regolith layer so they will not excite guided waves. In summary, a regolith layer could reduce the detectability of ScS precursors but has limited effect on the teleseismic waves such as triplications and PP precursors.

4.3.3 Effects of 3-D Scattering

We constructed two end-member scattering models (weak vs. strong) based on the impact crater distributions on Mars, assuming that the crustal scatterers were formed during the impact processes. (Schmerr et al., 2019). The parameters for weak and strong scattering models are: (1) dVp=dVs=-30%, dRho=-6%, R=2.5 km, L=50 km, N=1; (2) dVp=dVs=-30%, dRho=-6%, R=5.0 km, L=10 km, N=3 respectively (see Figure 4.5). The weak scattering model only has one layer of small scatterers near the surface, whereas the entire crust is filled with large and compact scatterers in the strong scattering model. The 3-D scattering synthetics are even more expensive than the modeling of regolith layers, so we increase the dominant frequency to 5 s. The goal is to understand how scattering plays a role in the detectability of candidate phases.

Figure 4.15 displays the comparisons of wavefield without scattering and the two scenarios described above. Strong surface wave codas are generated in both scattering models (Figure 4.15 b, c), and the codas are larger and last longer as scattering becomes stronger. However, the surface waves still exist in the wavefield instead of scattering away, which cannot explain the non-detection of surface waves in the InSight data (Lognonné et al, 2020). The ScS precursors are severely contaminated by the surface wave codas. Unlike the reverberations in regolith layer, the surface wave codas also exist in the low-frequency range, making it impossible to be separated from the ScS precursors. However, no surface waves have been detected yet on Mars, so this coda effect will likely be less problematic in the InSight data. The PP precursors are not affected by crustal scattering because the high frequency content of Pdiff is lost due to attenuation in the mantle, thus not sensitive to small scatterers. In the strong

scattering scenario (Figure 4.15c), PKP waves are followed by robust codas in all three components, which might have implications for core phase detections.

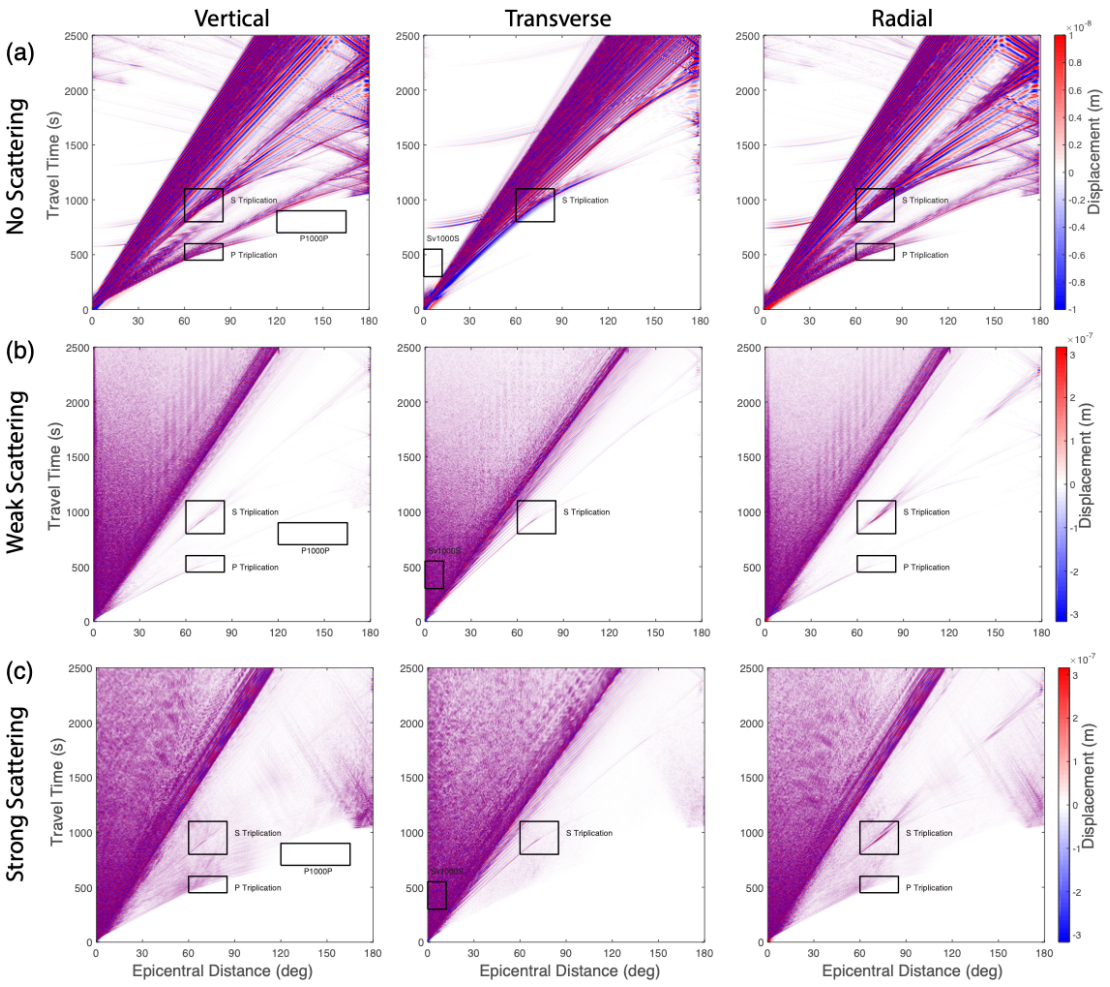

Figure 4.15 3-D scattering effects on candidate phases. The synthetic wavefield of (a) no-scattering, (b) weak scattering, and (c) strong scattering models. The candidate phases are highlighted in the black boxes on their corresponding components. The synthetics are filtered between 2-100 s. Note that the no-scattering model has a different amplitude scale to enhance the body waves.

Next, we zoom in on the wavefield of P and S triplications to examine the scattering effects (Figure 4.16). In weak scattering model (Figure 4.16a), P triplication can still be clearly observed even if coda arrive after P wave. However, P triplication is interfered by the strongly scattered waves (Figure 4.16c), and the triplication travel-time curves is no longer observable. On the contrary, S triplications remain observable

in both weak and strong scattering models (Figure 4.16 b, d). The codas are less excited in the transverse component, so S triplication is very robust even when scattering is strong in the crust (Figure 4.16d). This indicates that S triplication is expected to be more detectable than P triplication given that strong scattering exists on Mars. Moreover, the time separation between S triplication and first S wave arrival is larger than P wave, making it easier to detect in low-frequency events.

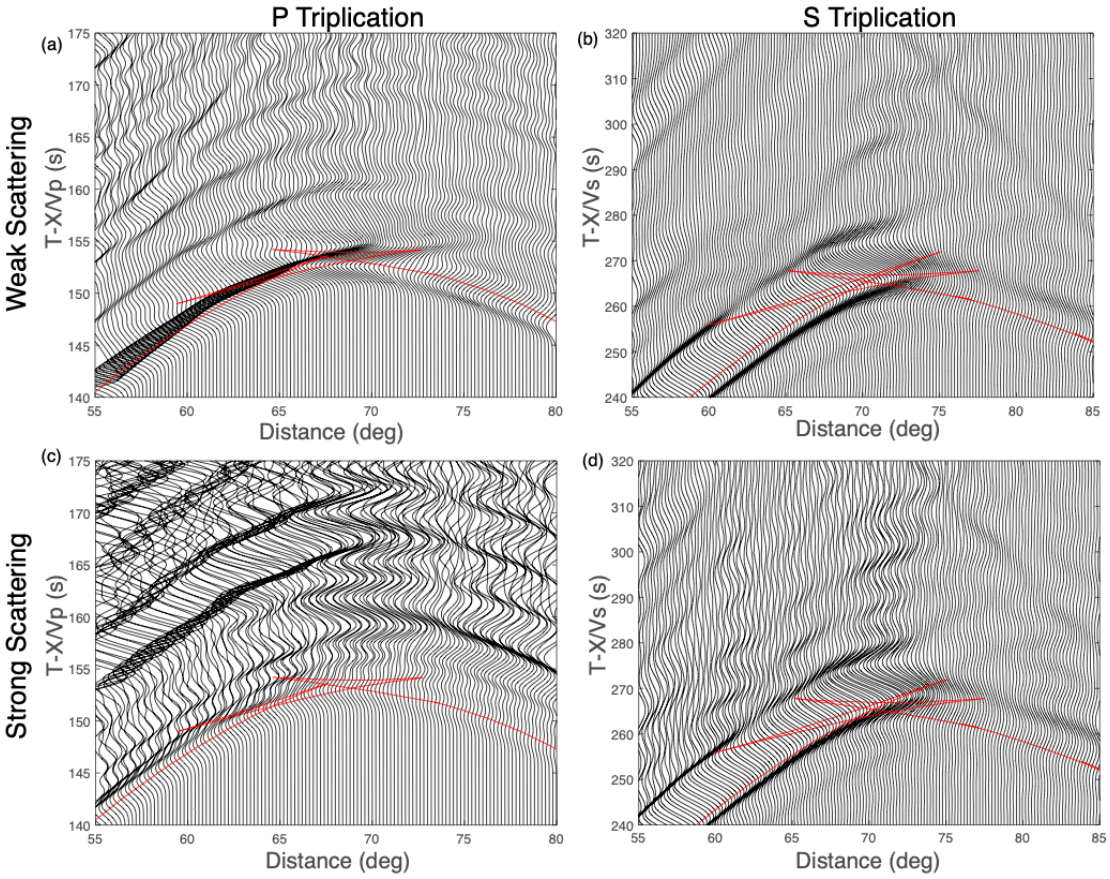

Figure 4.16 3-D scattering effects on P and S triplications. The top row shows the wavefield of (a) P and (b) S triplications in the weak scattering model. The bottom row displays the strong scattering model for (c) P and (d) S triplications. The synthetics are bandpass filtered between 1-100 s. The red lines denote the predicted travel-time curves.

4.4 Analysis of InSight Data

We first examined the alignment of high-quality LF and BB events (Quality A and B) to identify the multiple reflected phases (e.g., PP and SS). We used a vespagram approach to stack the envelopes of these events to quantify the slowness and arrival times of multiple reflected waves. Then, we investigated the low-quality LF events (Quality C and D) and HF events to search for P and S triplications bottoming at the martian MTZ. Our goal is to use multiple reflected waves to constrain crust and upper mantle velocity of Mars, as well as determine the depth of olivine-to-wadsleyite phase transition from triplications.

4.4.1 Multiple Reflected Waves

An event distance alignment was made based upon our picks for the main P- and S-arrivals, and the polarization filtered waveforms and envelopes are ordered by S-P time (Figure 4.17). The advantage of using S-P time, which is proportional to epicentral distance, is to avoid assumptions of Mars velocity models for distance calculations. The predicted travel-times of body waves are derived from vespagram analysis (see next section) to guide our picks on secondary body waves (Figure 4.17). We highlight the known instrument glitches identified by MQS (Scholz et al., 2020) in Figure 4.17 to avoid misidentifications of body waves. The glitches are usually stronger on the horizontal components, so the S waves can be more strongly contaminated. For example, the S-arrival pick of S0395a event is close to a glitch which increases the uncertainty of S-P time to this event (Figure 4.17b). A few P-arrival picks are also overlapping with glitches (e.g., S0409d) but those glitches are negligible on vertical component (Figure 4.17a).

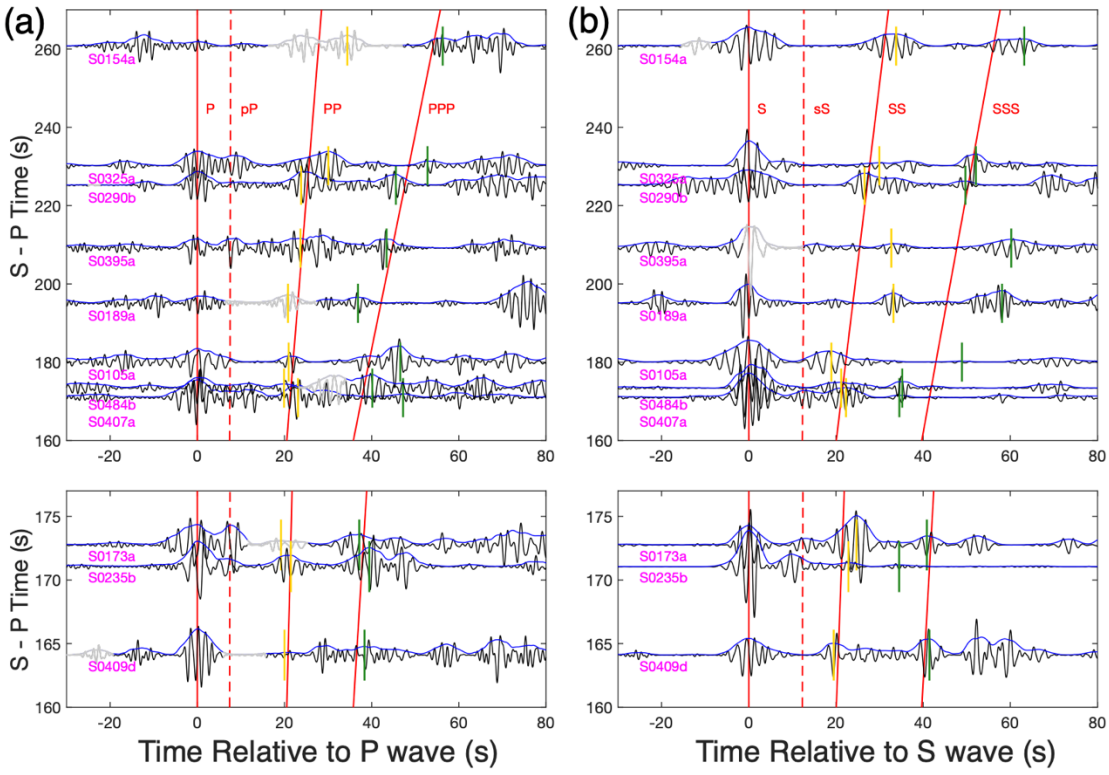

Figure 4.17 Alignment of polarization filtered waveforms and envelopes of low-frequency (LF) and broadband (BB) events. (a) P-wave alignment on the vertical component (BHZ). (b) S-wave alignment on the transverse component (BHT). The time-series waveforms are in black color and the envelopes are in blue color. The red solid lines represent predicted travel-times of multiple reflected phases (PP, SS, PPP and SSS) from vespagram analysis. The red dashed line denotes the predicted travel-time of depth phases (pP and sS) at 30 km depth using a reference model (Khan et al., 2020). The yellow and green lines highlight the PP/SS and PPP/SSS travel-time picks respectively. The grey shaded regions are the glitches identified by MQS (Scholz et al., 2020).

In Figure 4.17a, we observe a phase arrive immediately after P waves in some events such as S0173a and S0235b. We interpret this phase as the depth phase pP. We observe similar phases after S waves that are interpreted as sS (Figure 4.17b). These depth phases can constrain the source depth of the event. Our preliminary depth estimates for S0173a and S0235b are between 30-50 km. However, depth phases are absent in other events (e.g., S0105a), which suggests either the source depths are shallow, or the depth phases are below noise level. The phases after the depth phases are identified as multiple reflected waves from the free surface. For example, PP and

SS phases are the body waves reflecting beneath the free surface in the middle of raypath between source and receiver. These phases can be clearly observed on Earth, but they are difficult to identify on Mars due to crustal scattering and small event size. Polarization filter is an efficient technique to enhance these multiple reflected phases. We discover PP and SS phases with consistent moveouts compared to the predictions although the exact timings are different. The PPP and SSS phases are more ambiguous because multiple wave packets arrive near the predicted travel-times.

4.4.2 Vespagram Analysis

To detect seismic phases that may arrive coherently after the direct P- and S-waves, we applied a velocity spectral analysis (vespagram) approach to stack the envelopes across a range of slowness for common body waves. The vespagram approach was used to identify multiple reflected phases (e.g., SS and PP) and core phases (e.g., ScS and PcP) on Earth using seismic arrays (e.g., Davies et al., 1971; Rost and Thomas, 2009) and has often been used to study low amplitude phases that arrive near a larger amplitude parent, (e.g., the SS and PP precursors, Schmerr et al., 2013). The vespagram approach improves the SNR of coherent phases with similar move-outs and also distinguishes phases with distinct slowness (e.g., core phases). Here, we adapted the vespagram approach to a source array configuration on Mars, in which we leverage the relative timings of seismic waves arriving from a range of epicentral distances at a single station, in lieu of the more traditional station array method. The epicentral distance of each event was derived from the S-P time based on a reference Mars model (Khan et al., 2020), and the average distance was then used as the reference distance for vespagram analysis. Glitches were removed by zeroing the amplitudes in

the time windows of glitch arrivals. We selected 11 events located between 28-45 degrees for vespagram analysis (S0133a, S0183a, and S0185a events were not used). We created vespagrams for the polarization filtered LF and BB envelopes on three components: (1) BHZ component aligned on the P-wave arrival; (2) BHT and BHR components aligned on the S-wave arrival. The goal is to identify coherent body waves that come in with consistent timing and slowness after the initial P- and S-wave.

BHZ component vespagram (Figure 4.18a) reveals focused P-wave energy at zero relative slowness and a subsequent packet of coherent energy with slightly larger relative slowness. We interpret this second arrival as the seismic phase PP. A third more ambiguous arrival is tentatively interpreted as the PPP phase, although there are a series of arrivals near PPP, which could result from structural complexity near the bounce point. We observe a cluster of S wave energy between 200-300s near 5 s/degree on BHZ component. The three beams of S waves coincide with the predicted arrival times of S, SS and SSS although the slowness resolutions are vague. The S waves sometimes are suppressed by polarization filter on the vertical component because the horizontal components have stronger polarizations. This can explain the lack of coherence of S waves on BHZ component. The core phases such as ScP show coherent signals close to the predicted slowness but they are likely to be energy leaked from the S waves. The surface waves are also overshadowed by the S waves even though coherent energy exist near the predicted slowness.

BHT component vespagram displays a much cleaner result (Figure 4.18b). The vespagram has low energy at the expected arrival times of P-wave energy, suggesting that the back-azimuths used to rotate the records were appropriate (Figure 4.18b). The

BHT component vespagrams are aligned on the S- arrival, so the S-wave energy focuses at zero slowness and time. A subsequent packet of energy at larger slowness is interpreted as the SS phase. There is a series of more complex packets of energy following the SS phase, which we interpret as the SSS phase. We find an intriguing phase arriving at ~200s, close to the timing of surface wave. However, the slowness is much smaller compared to the surface wave with group velocity of 3.0 km/s. The ScS phase is expected to appear on the BHT component but we only observe very faint energy near the prediction of ScS. The BHR component vespagram (Figure 4.18c) is noisier compared to the other two components due to the P-to-S conversions. The P and S waves are not even coherent on the radial component. The S-to-P converted phases such as SP or ScP are not found neither. Surprisingly, the ScS phase shows very strong energy but the amplitude is much larger than the expected value. In summary, we do not have definitive evidence for core phases and surface waves from the vespagram analysis.

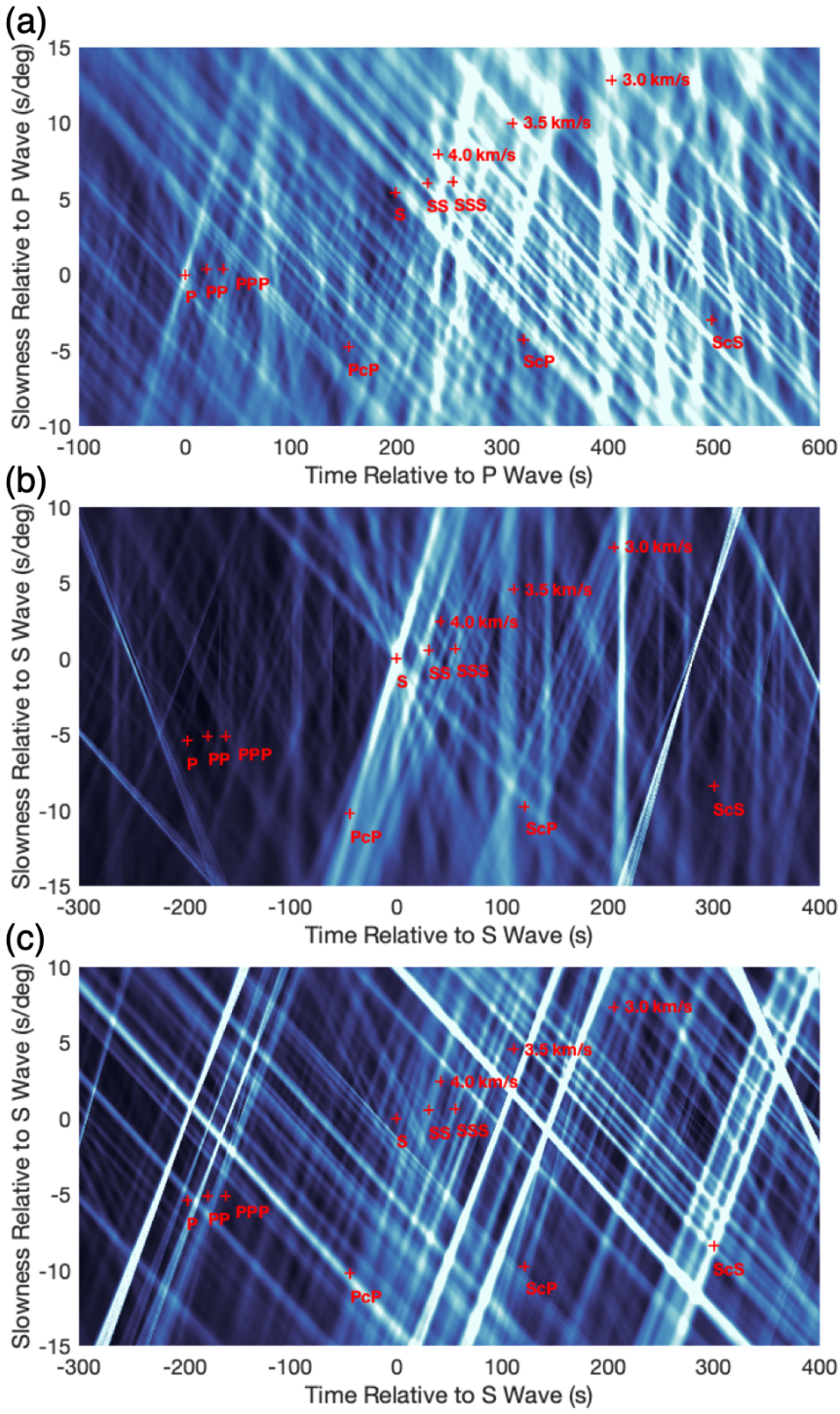

Figure 4.18 Vespagrams of polarization filtered LF and BB event envelopes on (a) vertical (BHZ), (b) transverse (BHT) and (c) radial (BHR) components. The predicted slowness and arrival times of body waves and surface waves are highlighted in red crosses. These predictions are calculated using a reference model (Khan et al., 2020) at the reference distance (33.4 degrees). The body waves include multiple reflected waves (PP/SS, PPP/SSS) and core phases (PcP, ScP and ScS). The surface waves are shown at the group velocities of 3.0, 3.5 and 4.0 km/s.

Next, we zoom in two regions of interest on vespagrams: (1) PP an PPP on BHZ; (2) SS and SSS on BHT (Figure 4.19) to quantify the arrival-times and slowness of these phases. We measured the arrival-times and slowness of these phases from the largest amplitudes on the stacked envelopes. The measured slowness of PP is 0.4±0.2 s/degree, consistent with the model prediction, whereas the arrival-time (23±5 s) is 3s later than the prediction (Figure 4.19a). The slowness of PPP is 1.0±0.3 s/degree which is larger than the prediction. Figure 4.19b illustrates the stacked envelopes of S waves on BHT component. The slowness of SS phase is 0.6±0.1 s/degree, also consistent with the model prediction. However, the arrival time of SS (24±5 s) is ~6 s earlier than the prediction. The similarity of PP and SS arrival times indicates a much smaller Vp/Vs ratio compared to the value in this model (Vp/Vs=1.7). The SSS phase is less coherent and has a slowness of 0.9±0.3 s/deg.

We used our vespagram results to guide the identification of PP and SS arrivals in the individual polarization-filtered event waveforms, as well as PPP and SSS arrivals. The observed slowness of each phase from the vespagram and reference distance (33.4 degrees) was used to compute the predicted arrival time of PP and SS, as well as PPP and SSS for individual events (Figure 4.17). The predicted arrival times then guided picks on the individual body waves in each event, with selection based upon the most coherent and high amplitude peak within ±10 s of the vespagram-derived predicted travel-times. These picked times are summarized in Table 4.4. The travel-times of multiple reflected waves will be used for the inversion of crust and upper mantle structures.

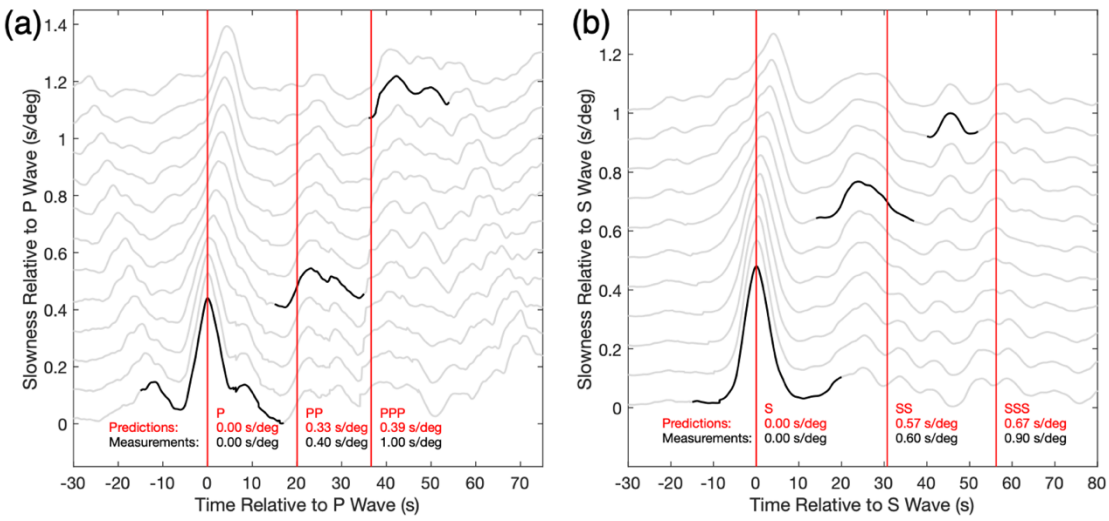

Figure 4.19 Stacked envelopes of (a) P waves on vertical component and (b) S waves on transverse component. The gray curves are the stacked envelopes at different slowness. The black curves highlight the envelopes of multiple reflected waves at the corresponding measured slowness. The red lines denote the predicted travel-times at the reference distance (33.4 degrees) using a reference model (Khan et al., 2020).

Table 4.4 Summary of body wave picks. Travel-times are relative to P arrivals.

Events	PP (s)	PPP (s)	S (s)	SS (s)	SSS (s)
S0105a	21.0±5.0	46.6±5.0	180.1±2.5	199.0±5.0	229.0±5.0
S0133a	29.3±5.0	65.2±5.0	195.5±2.5	227.4±5.0	239.8±5.0
S0154a	34.4±5.0	56.3±5.0	260.8±2.5	294.6±5.0	324.0±5.0
S0167b	52.5±5.0	78.1±5.0	414.9±2.5	465.4±5.0	492.6±5.0
S0173a	19.2±5.0	37.2±5.0	172.8±2.5	197.5±5.0	213.6±5.0
S0183a	42.5±5.0	85.9±5.0	305.6±2.5	332.3±5.0	360.1±5.0
S0185a	53.1±5.0	94.5±5.0	354.1±2.5	402.2±5.0	433.1±5.0
S0189a	20.8±5.0	36.9±5.0	195.1±2.5	228.3±5.0	253.2±5.0
S0235b	21.5±5.0	39.5±5.0	171.1±2.5	193.9±5.0	205.6±5.0
S0290b	23.8±5.0	45.6±5.0	225.2±2.5	251.8±5.0	274.9±5.0
S0325a	30.1±5.0	52.8±5.0	230.2±2.5	260.2±5.0	282.3±5.0
S0395a	23.7±5.0	43.4±5.0	209.2±2.5	241.9±5.0	269.4±5.0
S0407a	23.1±5.0	47.2±5.0	171.0±2.5	193.3±5.0	205.5±5.0
S0409d	20.0±5.0	38.4±5.0	164.1±2.5	183.6±5.0	205.6±5.0
S0484b	19.9±5.0	40.2±5.0	173.4±2.5	194.6±5.0	208.6±5.0

4.4.3 Candidate Events for Triplicated Waves

Most high-quality LF events are located 25-40 degrees away from InSight lander except S0185a event. However, based on our modeling of phases sensitive to the martian MTZ, the target distance to observe triplicated waves is between 60-85 degrees. Therefore, we opened our search across events to include the low-quality (C or D) LF events and HF events that may contain triplication arrivals. The P and S waves of these low-quality events are more difficult to identify, especially P waves, even after applying the polarization filter. Despite these difficulties, we still find 12 candidate events located in the target distance range (5 LF + 7 HF events) that have measurable P and S arrivals and are unassociated with glitches.

S0185a is the one of the best-quality events (Quality B) among these candidate events. Here, we use S0185a event as an example to illustrate the characteristics of teleseismic events on Mars (Figure 4.20). The amplitudes of P and S waves are much smaller than S0235a event, especially the P wave which is just above the instrument noise level (Figure 4.20a). Our modeling demonstrates that the polarization filter would suppress coda and noise after P and S waves (Figure 4.20b). On the spectrogram (Figure 4.20c), the energy content of S0185a is more constrained to a narrow band (0.3-1 Hz) lacking high-frequency energy like S0235b. The onsets of P and S can still be recognized on the spectrogram and guide the P and S wave picks. A glitch occurs ~50s after P arrival and manifests as strong low-frequency energy (< 0.3 Hz) on the spectrogram. The back-azimuth (Figure 4.20d) and incidence angle (Figure 4.20e) both display large uncertainties since P wave amplitude is small and is likely contaminated

by noise. We performed the polarization analysis of P- and S- waves for 12 triplication events and summarize their distances, back-azimuths and incidence angles in Table 4.5.

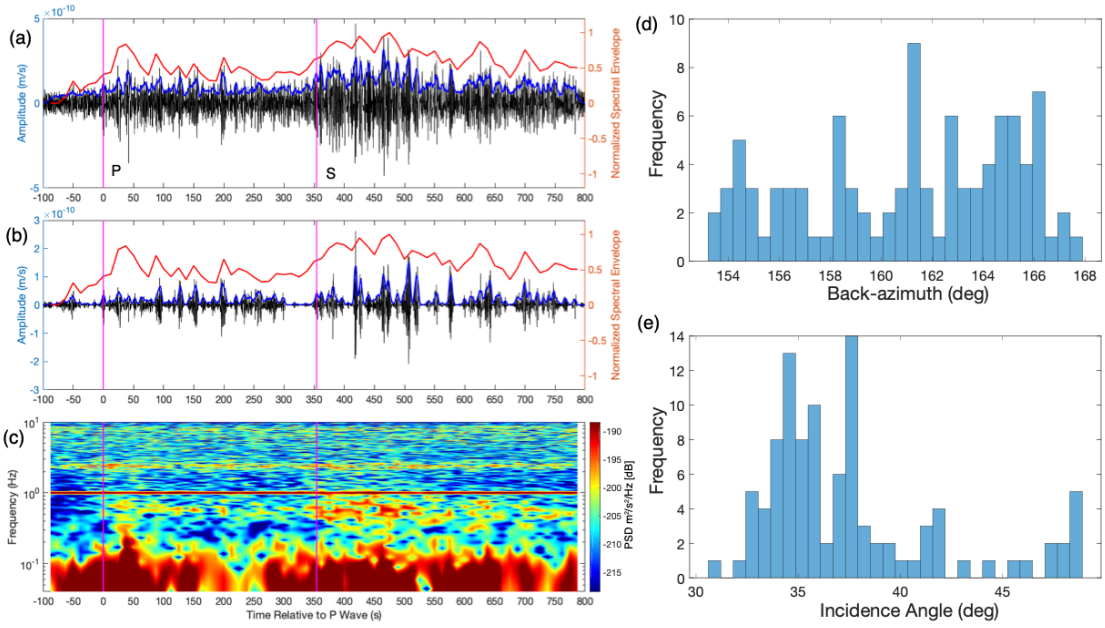

Figure 4.20 Data analysis of S0185a event based on polarization filtering. (a) The band-pass filtered waveform between 0.3-0.9 Hz. (b) The polarization filtered waveform. (c) The spectrogram of S0185a event. The legends are the same as Figure 4.6. The histograms of (d) back-azimuth and (e) incidence angle of S0185a event from polarization analysis of the P wave.

Table 4.5 Summary of the distances, back-azimuths and incidence angles of triplication events.

Event	Type	Quality	S-P time (s)	Distance (degree)	Back-azimuth (degree)	Incidence Angle (degree)
S0132a	BB	D	407.2±10.0	70.5±1.8	214.1±5.4	20.5±4.7
S0167a	LF	C	378.5±10.0	66.1±1.8	231.7±13.4	25.6±2.2
S0167b	LF	C	414.5±10.0	71.7±1.8	44.6±5.7	13.5±0.5
S0185a	LF	B	360.4±5.0	63.1±0.9	161.0±4.1	37.6±4.5
S0234c	LF	D	394.9±10.0	68.7±1.8	276.0±41.0	19.5±9.6
S0213a	HF	C	333.0±10.0	58.2±1.8	209.2±14.4	25.7±9.6
S0218a	VHF	B	343.8±5.0	60.2±0.9	143.9±13.0	9.7±1.6
S0264e	VHF	B	377.4±5.0	65.9±0.9	228.8±8.0	17.5±3.3
S0292a	HF	C	329.5±10.0	57.6±1.8	104.3±9.2	12.7±2.9
S0306a	HF	C	350.3±10.0	61.3±1.8	38.0±12.5	15.4±4.7
S0387a	VHF	B	336.2±5.0	58.8±0.9	43.8±22.0	8.4±1.3
S0421a	VHF	B	389.4±5.0	67.8±0.9	206.3±14.1	30.9±3.3

Similar to the high-quality events, we align the triplication events on P and S waves and order them by S-P time. We first examine the LF candidate events. Figure 4.21a displays the alignment of P waves on BHZ component. We plot the predicted travel-time curves of P triplications using EH45TcoldCrust1 model. The P-waveforms of four events (S0132a, S0234c, S0167a and S0185b) show double peaks and the second arrival is consistent with the predicted travel-times of P triplication. To further validate the second arrival, we compare the synthetic waveforms of P waves (EH45TcoldCrust1 model) at the same S-P time as the data (Figure 4.21c). We normalized the amplitudes of synthetics and adjusted the polarities of P-waves to account for different focal mechanisms of these events. Then, we cross-correlated the synthetic waveforms with the data to align them properly. The P-waveforms match the

synthetics almost wiggle-by-wiggle except where noise is present. The waveform matching indicates that these phases are P triplications from the martian MTZ.

We picked the S-arrival on radial or transverse components depending upon the SNR of S waves. After the event alignment on S-arrivals, we observe a secondary phase in S0167b, S0234c and S0167a events, and their move-out is consistent with the predicted travel-time curves of S triplications (Figure 4.21b). However, the S wave of S0132a event is followed by a glitch, potentially contaminating any secondary arrivals. We also performed waveform matching using the EH45TcoldCrust1 synthetics (Figure 4.21d). Due to the large uncertainties of back-azimuths, we used the synthetics on both radial and transverse components to match the S-waveforms and chose the one that fitted the data better. The S-waveforms of S0234c and S0167a events, including the secondary phases, match the synthetics very well. The other three events can only match part of the waveforms, but the S-waveforms are likely contaminated by S-to-P conversions especially on radial components. The center of the triplication coincides with the S-P time of S0132a, which can explain the absence of secondary phase here. The waveform and travel-time matching also suggests that these secondary phases are S triplications.

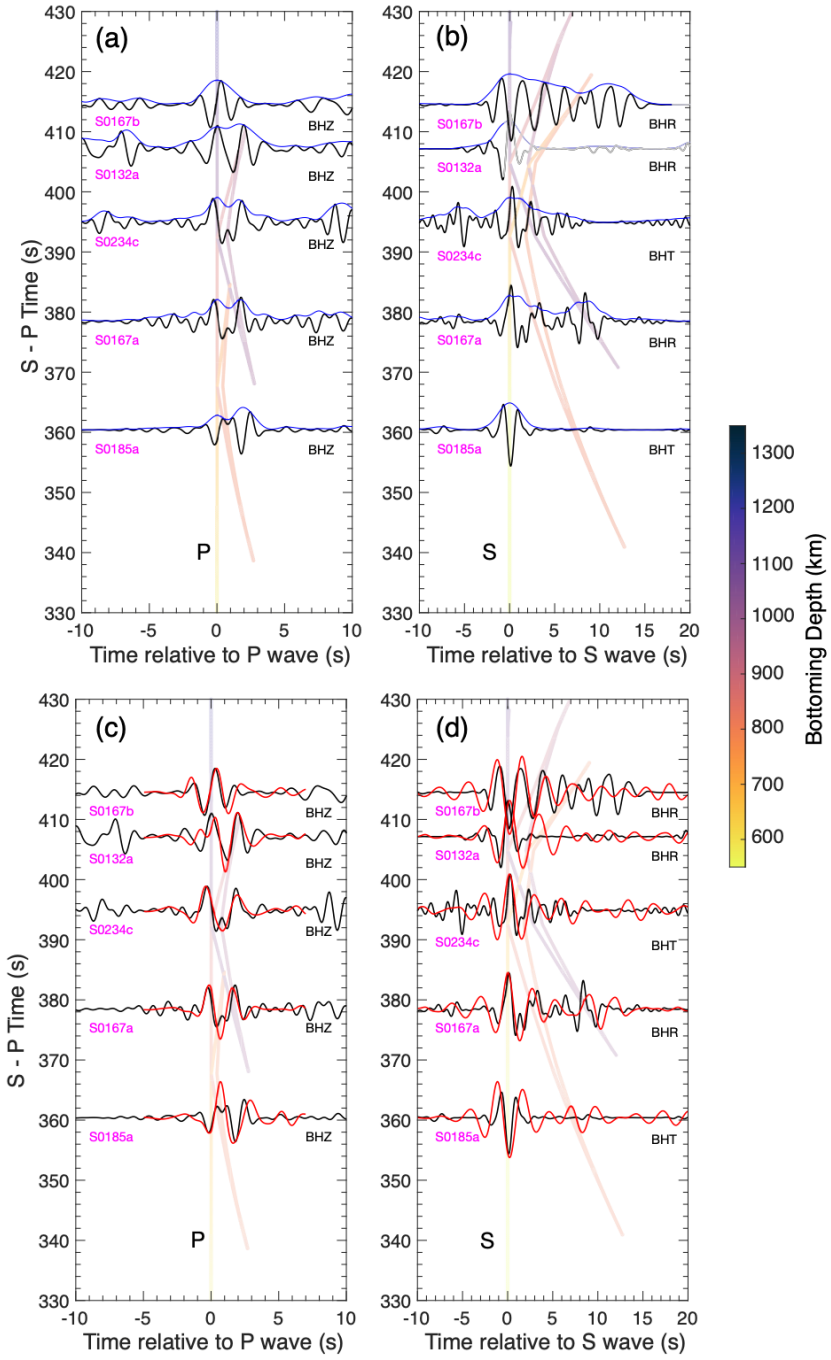

Figure 4.21 Alignment of LF triplication events based on the polarization filter. The data are bandpass filtered between 0.3-0.9 Hz. (a) P wave alignment on BHZ component. (b) S wave alignment on BHR or BHT components. The black lines are the time-series data and blue lines are their envelopes. The background curves are predicted travel-times using EH45TcoldCrust1 model (Rivoldini et al., 2011) and color coded by the bottoming depths of triplications. Note that two triplications are predicted for P and S waves, one from 800-km and the other from 1,000-km discontinuity. The grey shaded regions are known glitches identified by MQS (Scholz et al., 2020). Synthetic waveform matching for (c) P triplication and (d) S triplication. The red lines denote the synthetic waveforms computed from EH45TcoldCrust1 model.

We also aligned the HF candidate events in the same way as LF events (Figure 4.22). We can observe secondary phases after P-arrivals, but their arrival times do not agree with the predicted travel-times of P triplications (Figure 4.22a). The HF events only contain energy above 2 Hz, but we cannot compute global synthetics at such high frequency due to the expensive computational costs. Therefore, we cannot perform the synthetic waveform matching for HF events. The S-waveforms of S0421a and S0164e events also display secondary arrivals, and their moveout is consistent with the predicted S-triplication from the 800-km discontinuity (Figure 4.22b). However, we cannot rule out that these phases are crustal reverberations or depth phases. Giardini et al. (2020) interpreted HF events as shallow events occurred in the martian crust, and they are predominantly crustal guided waves. It is unclear whether these HF events can travel through the mantle to generate triplications, which would require the mantle to have weak attenuation. Therefore, we will only focus on the LF events to determine the depth of olivine-to-wadsleyite phase transition.

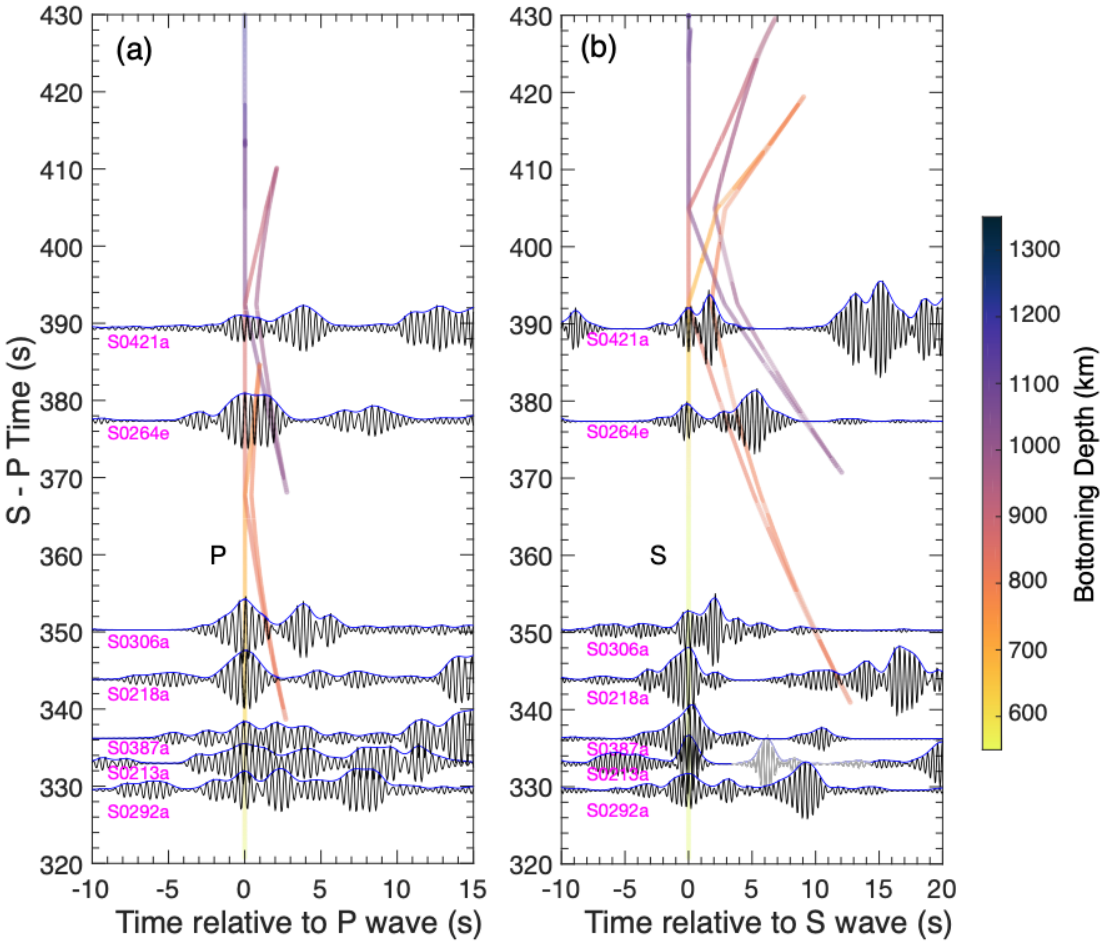

Figure 4.22 Alignment of HF triplication events based on the polarization filter. (a) P wave alignment on BHZ component. (b) S wave alignment on BHR or BHT components. The data are bandpass filtered between 2-3 Hz. The legends are the same as Figure 4.21.

4.5 Discussion

4.5.1 Instrument Glitches

SEIS is deployed on the surface of Mars where harsh environment inevitably causes artefacts in the data. Although SEIS is protected under the wind and thermal shield, the daily internal temperature variations can still reach up to 15 K. The thermal variations lead to one type of instrument self-noise manifested as large amplitude deviations over a short time period, hereafter referred to as a "glitch". A typical SEIS

glitch appears as a large one-sided pulse accompanied by high-frequency spikes near the onset (Scholz et al., 2020). Glitches often contaminate the seismic signals so deglitching (or removal of the glitches) is key for ensuring a robust phase identification. Four groups of scientists from: (1) University of California, Los Angeles (UCLA), (2) Max-Planck-Institute for Solar System Research (MPS), (3) Institut Supérieur de l'Aéronautique et de l'Espace SUPAERO (ISAE), (4) Université de Paris, Institut de physique du globe de Paris (IPGP) have created algorithms for automatically detecting and removing glitches from InSight data (Scholz et al., 2020). Here, we compare the four deglitched datasets to raw datasets and investigate how glitches affect our phase identifications and uncertainty estimates.

We first examine the time windows around P multiple reflected waves where multiple glitches are present (Figure 4.23). Overall, the differences between deglitched datasets and raw dataset are very small, and negligible for some events. UCLA group detect more smaller glitches because their detection threshold is set lower (Figure 4.23b). On the contrary, MPS group only remove those large glitches so no difference is observed when compared to raw data (Figure 4.23c). A few P wave picks are overlapping with glitches such as S0105a, S0409d and S0484b events. The peak of P wave envelope in S0105a event only shifts by a few seconds in the deglitched datasets, whereas S0409d and S0484b events remain the same. The PP phase in S0154a event is also overlapping with a glitch. After deglitching, the PP envelopes only change in the UCLA (Figure 4.23b) and IPGP datasets (Figure 4.23e). The IPGP dataset completely remove our PP pick whereas UCLA dataset agree with our PP pick and only remove the glitch before it. Note that IPGP group use a quite different approach from other

three groups which is based on 2 Hz raw data. Therefore, we only focus on the other three deglitched datasets.

The time windows around S multiple reflected waves only has one glitch near the S wave of S0395a event (Figure 4.24). The deglitched datasets only change the amplitude this S wave but still keep this phase except that IPGP group shift the peak of envelope. We also examine the glitches in triplication events where the S wave of S0132a event is contaminated by a glitch (Figure 4.21b). Similar to S wave here, the triplication events do not display any major difference to change the timing of our phase picks. In summary, the deglitched datasets can contribute to the uncertainties of our phase picks (e.g., P and PP) but do not change our interpretations of the dataset.

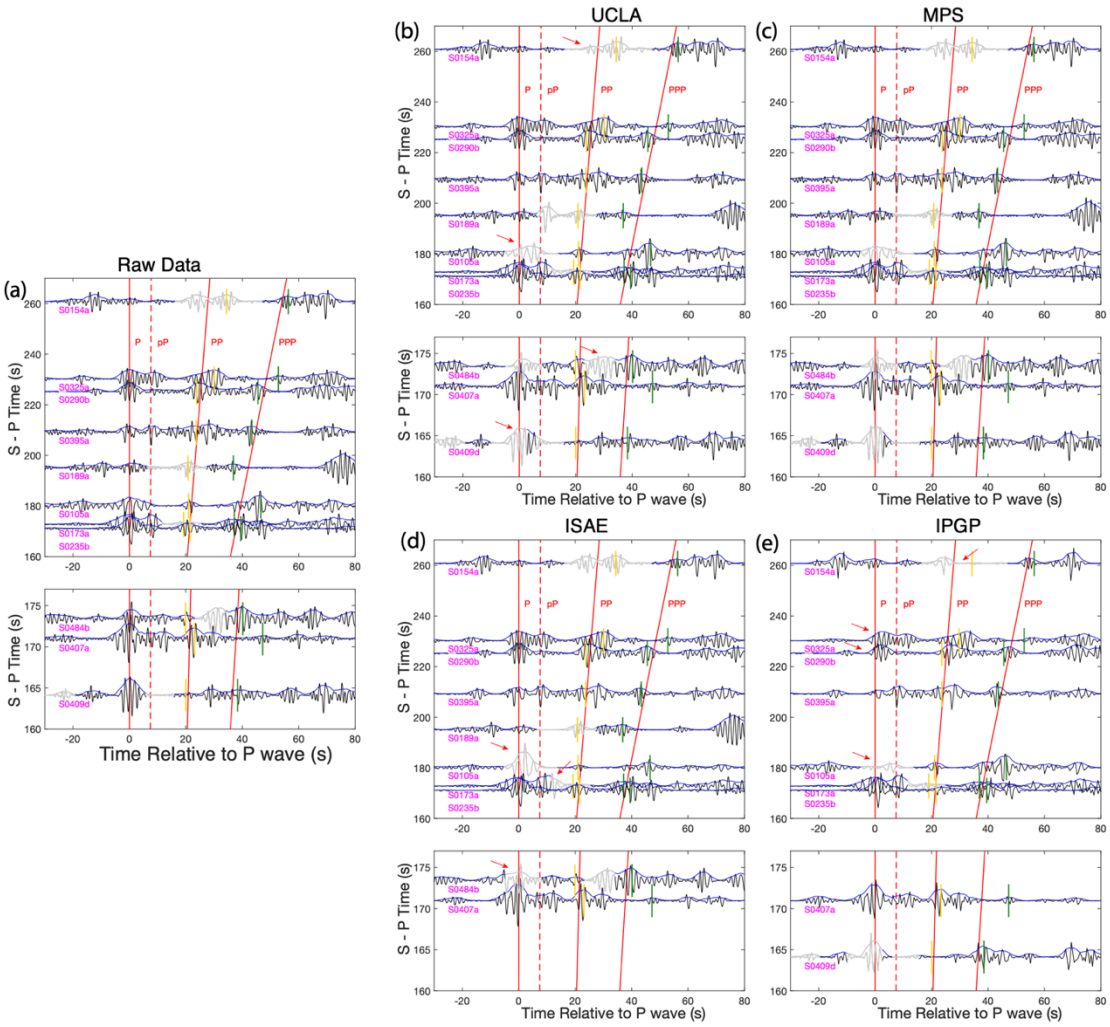

Figure 4.23 Comparison of four deglitched datasets and raw dataset for P waves. (a) The raw dataset for P wave alignment on BHZ component. The deglitched datasets from (b) UCLA, (c) MPS, (d) ISAE and (e) IPGP for P wave alignments on BHZ components. The legends are the same as Figure 4.17. The differences between deglitched datasets and raw dataset are highlighted by red arrows.

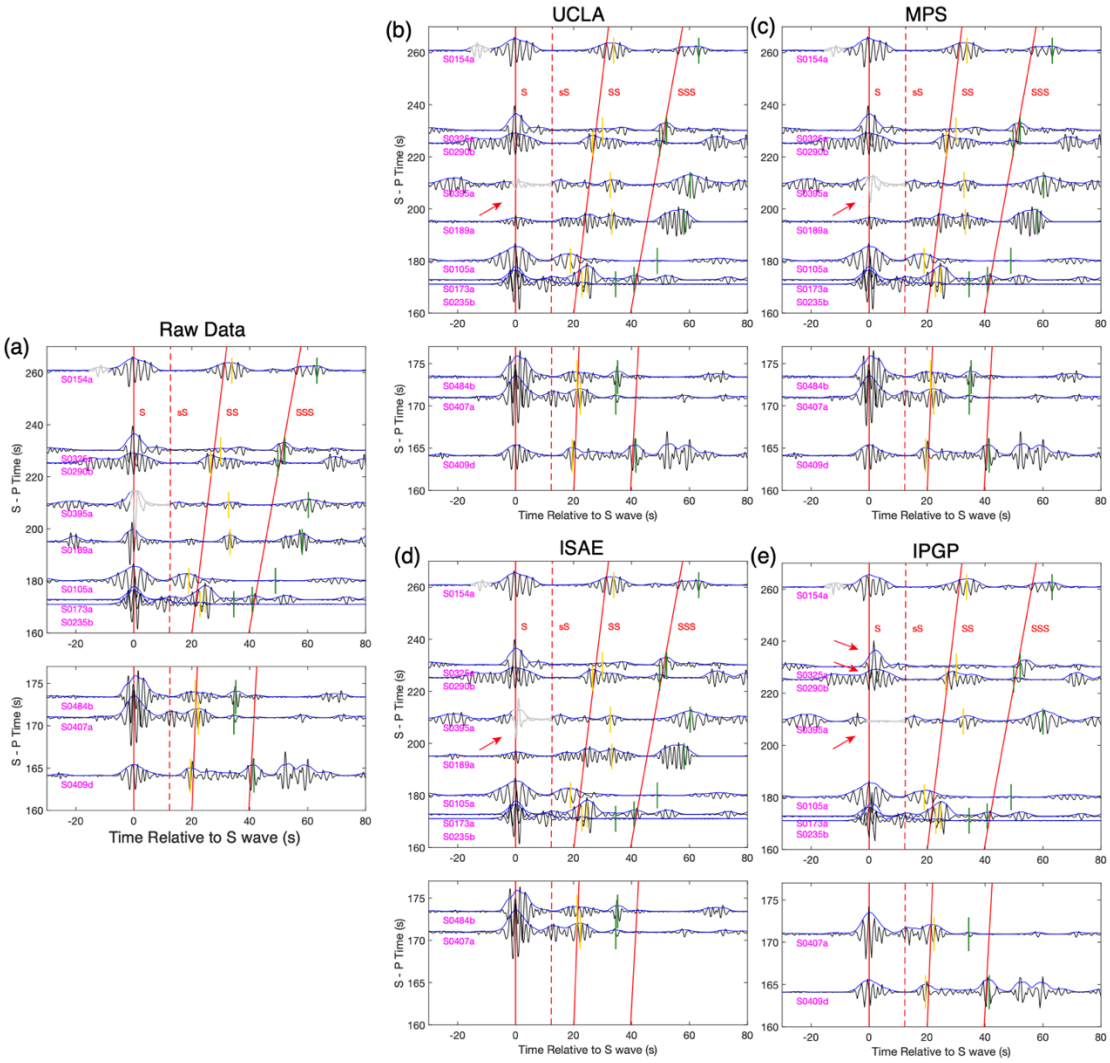

Figure 4.24 Comparison of four deglitched datasets and raw dataset for S waves. (a) The raw dataset for S wave alignment on BHT component. The deglitched datasets from (b) UCLA, (c) MPS, (d) ISAE and (e) IPGP for S wave alignments on BHT components. The legends are the same as Figure 4.17. The differences between deglitched datasets and raw dataset are highlighted by red arrows.

4.5.2 Crust and Upper Mantle Structure of Mars

Based upon our travel-time measurements of multiple reflected waves, we used a mineral physics approach to invert the velocity and density structures of martian crust and upper mantle. We assumed a mantle composition of Mars using the Taylor (2013) model and computed the velocity models that satisfy the minimization of Gibbs free energy as a function of temperature and pressure (Khan et al., 2018). We utilized a

Bayesian approach to search for the models that fit the data within uncertainty ranges, yielding 20,000 models out of 100,000 in total. We find two families of models that can equally explain the observations: red and blue models. Figure 4.25 displays a representative model from each family. The main differences between the two sets of models are due to lithospheric thickness (Z_{lit}) and thermal gradients (ΔT): (1) Z_{lit} is between 400-500 km in blue models, and 500-600 km in red models; (2) $\Delta T > 2.8$ K/m in blue models, $\Delta T < 2.8$ K/m in red models.

Our models have resolutions up to 600-km depth, while the rest of the models are based on mineral physics modeling. The depths of crust-mantle boundaries are 31-km and 43-km in blue and red models respectively, consistent with the receiver function estimates using the InSight data (Lognonné et al, 2020). A negative velocity gradient exists between 200-400 km depth in the Vs profile (Figure 4.25a), indicating the existence of a low velocity zone (LVZ) in the martian mantle, whereas it is weaker in the Vp profile (Figure 4.25b). LVZ is more prominent in the blue model compared to the red model due to its larger thermal gradient. The existence of LVZ agrees well with the seismological predictions based on the assumption of a stagnant conductive lithosphere overlying a convective upper mantle in Mars (e.g, Zheng et al., 2015). Constraints on the crust and upper mantle structures pave the road to the measurement of the olivine-to-wadsleyite phase transition depth.

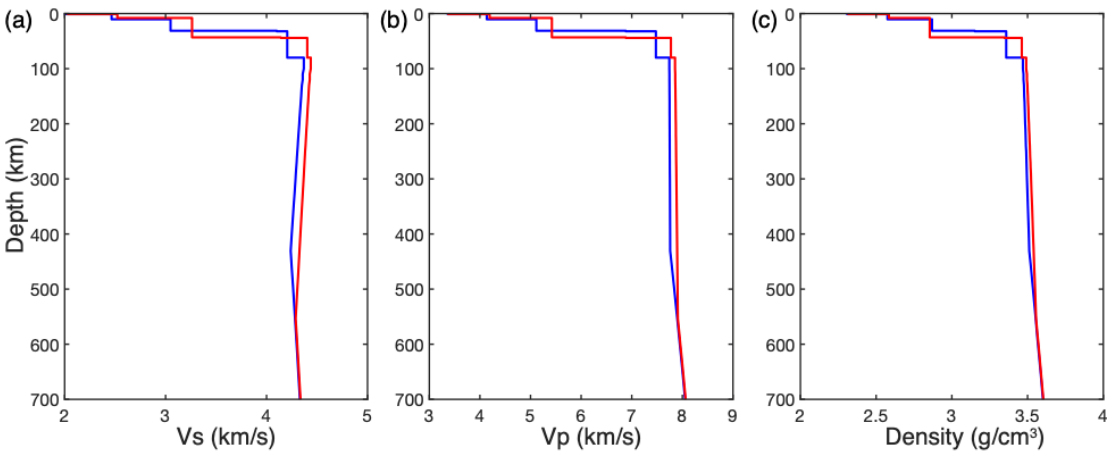

Figure 4.25 Crust and upper mantle structure of Mars inverted from the travel-times of multiple reflected waves. Vertical profiles of (a) Vs, (b) Vp and (c) density between 0-700 km depth. Red model has a lithospheric thickness (Z_{lit}) between 500-600 km, and thermal gradient ΔT < 2.8 K/m. Blue model has a Z_{lit} between 400-500 km and ΔT > 2.8 K/m.

4.5.3 Depth of Olivine-to-Wadsleyite Phase Transition

The depth of olivine-to-wadsleyite phase transition is a function of the composition and temperature of martian mantle (e.g., Xu et al., 2008). We used the thermodynamic codes PerpleX (Connolly, 2005) and BurnMan (Cottaar et al., 2014) to compute 1-D seismic profiles of Mars based on different mantle compositions and areotherms. We selected four composition models: (1) Drebus and Wänke (1985), (2) Lodders & Fegley (1997), (3) Khan and Konnoly (2008) and (4) Yoshizaki & McDonough (2020); three mantle potential temperatures (T_p): 1400K, 1500 K and 1600 K. We fixed the crustal thickness at 40-km and varied the core sizes and thermal gradients of mantle adiabat to obtain 48 models (Figure 4.26). All the models are within 2% mass of the planet and 1% moment of inertia from Konopliv et al. (2016). The depth of 1,000-km discontinuity increases with the mantle potential temperature due to the positive Clapeyron slope of olivine-to-wadsleyite phase change (Ita & Stixtrude,

1992; Katsura & Ito, 1989). The Vp and Vs values are generally greater than the Khan et al. (2020) models due to the colder areotherms used in these models.

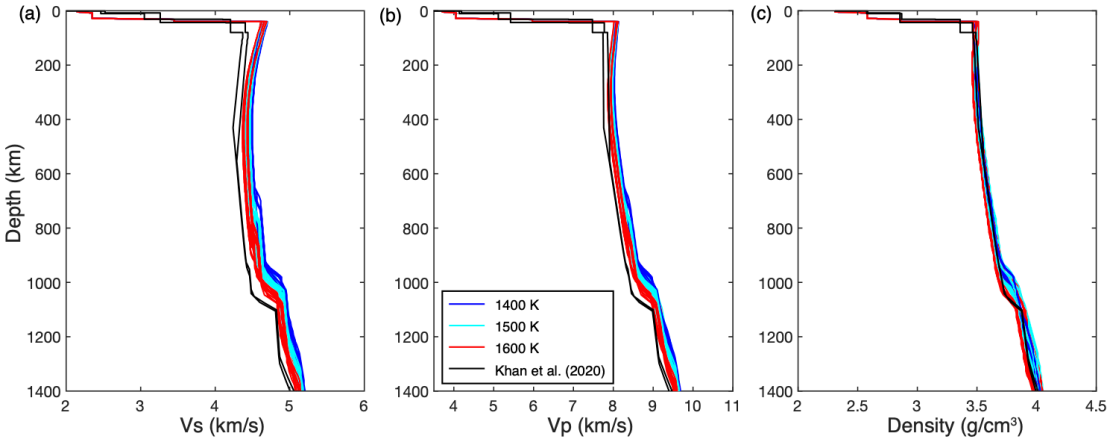

Figure 4.26 Vertical profiles of (a) Vs, (b) Vp and (c) density of martian mantle based on different mantle composition models and areotherms. The four composition models include Drebus and Wänke (1985), Lodders & Fegley (1997), Khan and Konnoly (2008) and Yoshizaki & McDonough (2020). The velocity and density profiles are color coded by mantle potential temperature (T_p): 1400 K, 1500 K and 1600 K. The black lines represent the upper mantle models constrained from InSight data (Khan et al., 2020).

We can use these thermodynamic models to constrain the depth of olivine-to-wadsleyite phase change as well as the martian mantle temperature and composition. In our modeling results, we demonstrated that the distance of triplication is well correlated with the depth of 1,000-km discontinuity (Figure 4.7). Here, we use S-P time instead of epicentral distance for depth calculations since we can directly measure S-P time from the triplications. We computed the travel-times of P and S triplications based on these models and measured the S-P times at the center of the S triplications. The S-P time of S triplication is well correlated with the depth of discontinuity as well as the mantle potential temperature (Figure 4.27). We have observed both P and S triplications from LF events, and S0132a event appears to be at the center of S triplication. We simply project the S-P time of S0132a event (407.2±10.0 s) to the best-fitting model to calculate the depth and uncertainties. Therefore, the depth of

olivine-to-wadsleyite phase transition is 1,016 ± 32 km based on S triplication. This depth also indicates that the mantle potential temperature of Mars is 1,600 ± 100 K. All these four composition models can fit into the uncertainty range of the depth.

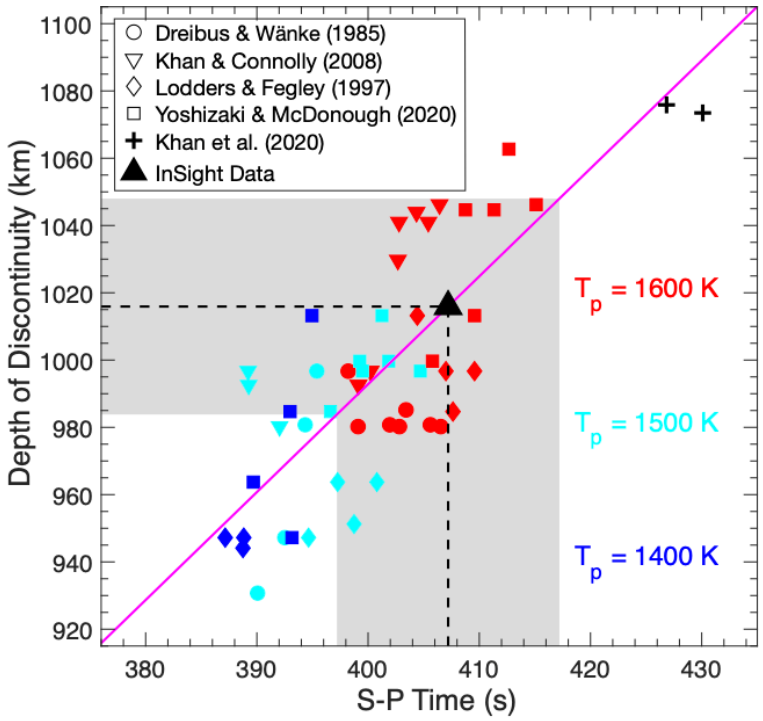

Figure 4.27 Depth of olivine-to-wadsleyite phase transition derived from S triplication and thermodynamic models. The magenta line represents the best-fitting model. The depth is calculated using the S-P time at the center of S triplication (S0132a event, black triangle). The gray shaded regions indicate the uncertainties of S-P times (±10 s) and 1,000-km discontinuity depths. We used a seismic source at 30-km depth when computing the travel-times of triplications.

4.6 Conclusions

We have performed synthetic waveform modeling and analyses of InSight data to detect the martian MTZ. We investigated the detectability of three candidate body waves through AxiSEM synthetics and SEIS VBB noise level. Our modeling results demonstrate that P and S triplications are the best candidate phases, only require ~Mw 3 events to be detectable. The magnitude thresholds to detect reflected waves such as

ScS precursors and PP precursors are larger than Mw 5. However, the largest event observed on Mars is close to Mw 4.0 after nearly two-year operation (Banerdt et al., 2020), suggesting it is less likely to detect these reflected phases within a few years. We also explored the effects of regolith layer and 3-D scattering on the detectability of candidate phases. The presence of regolith layer beneath InSight lander can generate high-frequency guided waves to contaminate ScS precursors, increasing the magnitude threshold to Mw 5.5, whereas the triplicated waves and PP precursors are not strongly influenced by the guided waves. A deep marsquake source (e.g., 40 km) and heterogeneities in regolith layer can negate the guided waves and increase detectability. 3-D scattering modeling confirms that P triplication is more likely to be interfered by the crustal scattered waves, and S triplication is more detectable, also considering its larger time delay can be more observable in low-frequency events.

We applied a polarization filter to identify body waves, including both multiple reflected waves and triplicated waves, from InSight data. We aligned high-quality LF and BB events based on S-P times and discovered multiple reflected waves (PP, PPP, SS and SSS) with consistent moveout compared to model predictions. Our measurements of the relative slowness of PP and SS phases are 0.4 ± 0.2 and 0.6 ± 0.1 s/degree respectively based on the vespagram analysis of the LF and BB event envelopes. PPP and SSS phases are more ambiguously detected on vespagrams. The slowness and arrival-time measurements from vespagram analysis guide our picks on the multiple reflected waves. The core phases and surface waves were not definitively observed on the vespagrams. We have identified 12 candidate events (5 LF + 7 HF events) in the target distance range of triplications from martian MTZ. In the LF events,

we observed both P and S triplications based on their waveform and travel-time matching with the synthetics. However, HF events did not show clear evidence for triplicated waves. Preliminary estimate on the depth of olivine-to-wadsleyite phase change is 1,016 $\pm$ 32 km based on the S triplication. This depth indicates a relatively cold martian mantle with mantle potential temperature of 1,600 $\pm$ 100 K.

Acknowledgements

The InSight SEIS data are available at IRIS-DMC (Incorporated Research Institutions for Seismology-Data Management Center) and NASA PDS (Planetary Data Service). We thank Marsquake Service (MQS) for providing catalogues of seismic events on Mars. We also thank the developers of AxiSEM and AxiSEM3D for distributing the codes freely online. QH, NS and RM were supported by NASA under grant number 80NSSC18K1628. This is InSight contribution number 203.

Chapter 5: Summary and Outlook

5.1 Summary of Conclusions

Structures of Earth's MTZ and Martian deep interior were investigated using multiple body wave approaches in my dissertation. On Earth, SS precursors were proposed as a novel approach to constrain seismic anisotropy in the MTZ. Global and regional observations indicate seismic anisotropy is weak in the MTZ but can be locally enhanced near subduction zones. 3-D synthetic modeling results demonstrate that SS precursors can resolve ≥3% azimuthal anisotropy, consistent with the observations in the subduction zones. On Mars, our detectability studies suggest that triplicated waves are the best candidate phases to detect the martian MTZ. I have found evidence for S and P triplications in the 5 candidate LF/BB events based on synthetic waveform modeling. Preliminary depth estimates suggest that the olivine-to-wadsleyite phase transition occurs shallower than those in the pre-landing models, indicating a colder Martian mantle.

Observational results of MTZ topography and anisotropy are the main topics in Chapter 2. A new MTZ topography model was proposed in this chapter. This model was derived from an up-to-date SS dataset and corrected for upper mantle and MTZ anisotropy. The MTZ is thickened beneath subduction zones and thinned beneath hotspots, consistent with previous MTZ topography models (e.g., Flanagan and Shearer, 1998), although discrepancies of small-scale structures still exist among these models. The anomalies of MTZ topography coincide with thermal heterogeneities in the mantle, suggesting that temperature is a key factor controlling the depths of MTZ discontinuities. However, compositional effects such as the enrichment of water

(Smyth and Frost, 2002; Litasov et al., 2005) or magnesium content (Fei and Bertka, 1999) can also affect the MTZ topography especially beneath subduction zones. Houser (2016) investigated the correlations between MTZ topography and shear velocity anomalies and concluded that the MTZ is globally dry with ~0.6 wt% water. Our new topography model generally agrees with the Houser (2016) model: we find the regions with thicker MTZ tend to have faster shear velocity near subduction zones. However, this does not indicate the MTZ is dry from our study because it is unclear whether temperature or water content is the dominant effect that controls shear velocity in the subduction zones. A large-scale hydration of the MTZ in the vicinity of slabs could potentially alter other properties of the mantle, in particular, it may change the slip system of wadsleyite, as has been observed for olivine (Karato et al., 2008), or increase the attenuation in the vicinity of the slab, as has been observed at shallower depths in the mantle wedge (e.g., Stachnik et al., 2004). These would be additional parameters that could inform on mantle hydration beyond velocity and discontinuity depth. I would recommend careful lab measurements of the slip systems of hydrated wadsleyite and ringwoodite to help determine if the mantle flow pattern can be affected by hydration of MTZ minerals or not.

Another key finding is that azimuthal anisotropy exists in the circum-pacific subduction zones with ~3% strength and a trench-perpendicular fast direction. The azimuthal anisotropy is interpreted as the LPO of wadsleyite in the MTZ induced by mantle flow near subduction zones. However, global azimuthal stacking results only revealed a nearly isotropic MTZ (<1%) suggesting that the LPO of wadsleyite is very weak in the ambient mantle without the alignment from mantle flow. Upper mantle

anisotropy was also discovered beneath the central Pacific region and subduction zones. The fast direction beneath the central Pacific region agrees well with the plate motion direction. This indicates that current mantle flow in the asthenosphere is passively driven by the motion of overlying Pacific lithosphere (e.g., Becker et al., 2014). The subduction zones show a trench-parallel fast direction in the upper mantle, perpendicular to that in the MTZ. The transition of fast directions indicates either the change in mantle flow direction with depths or a different slip system between olivine and wadsleyite. Mineral physics experiments show that the dominant slip system of wadsleyite is similar to B-type olivine (e.g., Kawazoe et al., 2013). Therefore, the flow direction in the MTZ is expected to be perpendicular to the fast direction. This indicates that the orientations of mantle flow around the subducting slabs remain trench-parallel from upper mantle to the MTZ. The trench-parallel flow is likely a large-scale flow pattern existing around the slab.

Chapter 3 focused on the synthetic tests of SS precursors to demonstrate their sensitivities to azimuthal anisotropy. One of the key findings is that SS precursors can distinguish multiple depths of anisotropy: shallow and deep upper mantle, and the MTZ, via the measurements of amplitudes and travel-times. This greatly improves the depth resolution compared to the traditional shear wave splitting measurements. SS precursors also have better horizontal resolution (~1,000 km in radius) compared to surface wave measurements (~6,500 km). Therefore, our new SS precursor method would provide a higher resolution of lateral changes in anisotropy than the surface wave methods. The modeling results also suggest that SS precursors can detect $\geq 3\%$ azimuthal anisotropy when azimuthal coverage is sufficient (NR>100 in each

azimuthal bin). Source and receiver geometry play a key role in the resolution since it directly determines the azimuthal coverage. In the future, the deployments of ocean bottom seismometers (e.g., Kawakatsu et al., 2009) can help increase the azimuthal coverage in subduction zones (e.g., Japan), making it feasible to measure anisotropy in those regions more precisely with SS precursors.

The sensitivity tests were applied to two densely sampled regions: central Pacific region near Hawaiian hotspots and Japan subduction zones. In the central Pacific region, sensitivity tests suggest at least 3% anisotropy can be resolved but the data failed to detect such a signal. Therefore, the azimuthal anisotropy is likely much smaller than 3% in this region, indicating that mantle plume does not produce strong azimuthal anisotropy in the MTZ. The morphology of Hawaiian plume conduit in the MTZ is debated among tomography models: French and Romanowicz (2015) reported that the conduit is deflected to the northwest at 410-km depth, whereas other models show a slightly tilted plume conduit (e.g., Li et al., 2008). Our results are more consistent with a nearly vertical plume conduit that mainly introduce vertical entrained flow into the MTZ (e.g., Steinberger & O'Connell, 1998), thereby not causing detectable azimuthal anisotropy.

In Japan subduction zone, a trench-perpendicular fast direction was discovered from the data, which agrees well with the results in Chapter 2 and other studies (e.g., Lynner and Long, 2015). However, the strength of anisotropy was not constrained from the data due to the poor azimuthal coverage in this region. The trench-perpendicular fast direction is interpreted as the LPO of wadsleyite caused by trench-parallel mantle flow based on the slip system of wadsleyite (e.g., Kawazoe et al, 2013). The mantle

flow remains consistently trench-parallel throughout the sub-slab upper mantle and MTZ. The trench-parallel flow agrees well with the toroidal flow near the slab induced by trench migration (Faccenda and Capitanio, 2012). Our observations support that 3-D toroidal flow is the dominant flow pattern that is associated with the trench migration and slab roll-back in the upper mantle and MTZ. The other predicted flow pattern is the entrained flow with the downgoing slab which is expected be trench-perpendicular (Faccenda, 2014). However, this component was not observed in our SS precursor measurements, indicating that the entrained flow is a relatively small-scale structure (i.e., a thin layer of anisotropy near the slab surface).

In Chapter 4, I investigated the detectability of Martian MTZ through synthetic modeling. The reflected waves and triplicated waves were proposed as candidate body waves. A key finding of this chapter is that P and S triplications only require ~Mw 3 events to be detectable, whereas the reflected waves require at least Mw 5 events. The magnitude thresholds for reflected waves are greater than the largest events recorded by InSight Mission so far (~Mw 4). Therefore, triplicated waves are identified as the best candidate phases to detect the Martian MTZ. I also tested the effects of regolith layer and 3-D scattering on the detectability of Martian MTZ. The regolith layer can reduce the detectability of ScS precursors due to the strong coda of surface waves trapped in the regolith layer. However, PP precursors and triplicated waves are not sensitive to a regolith layer due to the lack of high-frequency energy. The 3-D scattering can contaminate P triplication by introducing coda after first P-arrival, whereas S triplication is less affected by crustal scattering. S triplication also displays a larger time

delay after first S-arrival. Therefore, the modeling results suggest S triplication is more detectable than P triplication in the low frequency events.

The mantle structures of Mars were constrained from the analysis of InSight data in Chapter 4. I applied a joint approach with polarization filtering and vespagram analysis to identify body waves on Mars. The alignment of P and S waves in the LF and BB events revealed the existence of multiple reflected waves (e.g., PP and SS) on Mars. The vespagram analysis can further quantify the arrival-times and slowness of PP and SS phases, but PPP and SSS phases are more ambiguous due to the complexities of wave propagations in the Martian crust. The arrival-time picks of these multiple reflected waves were accomplished under the guidance of vespagram predictions. These travel-time measurements can be used for the inversions of crustal and upper mantle structures of Mars. Another important discovery is the detection of S and P triplication in the LF/BB events through synthetic waveform matching. The observations of triplicated waves prove that Mars has a mantle transition zone associated with the olivine-to-wadsleyite phase transition as predicted by the mineral physics models. The depth of olivine-to-wadsleyite phase transition is derived from the S-P time at the center of S triplication: 1,016 $\pm$ 32 km. The depth constraints suggest that mantle potential temperature of Mars is 1,600 $\pm$ 100 K.

The cold mantle temperature requires an effective cooling mechanism such as plate tectonics during the early thermal evolution of Mars. Sleep (1994) proposed that the northern lowlands of Mars is a thin crust produced by plate tectonics, more specifically sea floor spreading, during the Late Noachian and Early Hesperian time. An early episode of short-lived plate tectonics would cool down the planet quickly

because the cold lithosphere is constantly recycled into the hot mantle, thereby eliminating the heat in martian interior (Nimmo & Stevenson, 2000). This is more efficient than a stagnant lid model in which the temperature difference between the recycled materials and mantle is only a few hundred degrees, much smaller than the thousands of degrees difference in the plate tectonics regime. Therefore, our preliminary results are suggestive of a Mars that likely went through an early episode of plate tectonics and then transitioned into a single plate regime. Alternatively, the shallow depth of 1,000-km discontinuity can be explained by enrichment of water content in the MTZ (Smyth and Frost, 2002). The Earth's MTZ is proposed as a water reservoir in the mantle due to the large water solubility of wadsleyite and ringwoodite (Bercovici & Karato, 2003). Similar to Earth, the martian MTZ can potentially trap water within this layer when subduction was actively transporting water into the mantle during Noachian period or mantle plume is currently rising from the base of the mantle. Therefore, our observation is also consistent with a hydrated MTZ in martian interior.

5.2 Future Work

My PhD work only focused on the analysis of SS precursor travel-times in Chapter 2 and 3, but their amplitudes can also provide useful insights into the sharpness of MTZ discontinuities. The amplitudes of SS precursors are determined by the impedance contrasts across the MTZ discontinuities, although attenuation and geometrical spreading also play a role here. I followed the method by Shearer and Flanagan (1999) but used an up-to-date SS dataset to constrain the S impedance contrasts of 410-km and 660-km discontinuities (Figure A.1 and A.2). Preliminary results suggest that the S impedance contrasts in the 1-D reference models (PREM and

AK135) do not agree with our observations, especially the 660-km discontinuities (Figure A.3). The density contrasts in AK135 model are much larger than our observations for both 410-km and 660-km discontinuities, although the 410-km impedance contrast in PREM is close to our observation. Future 1-D reference models can take into account the amplitude constraints from SS and PP precursors to improve the accuracy of velocity and density jumps at the 410-km and 660-km discontinuities. Regional analysis of impedance contrasts can also shed light on the compositional, to a lesser extent thermal, heterogeneities in the MTZ (e.g., Yu et al., 2018). My future work can model the impedance contrasts through mineral physics approaches to constrain the temperature and composition of mantle (e.g., Xu et al., 2008).

SS precursors can also be applied to investigate seismic anisotropy near the shallow discontinuities such as lithosphere-asthenosphere boundary (LAB) and mid-lithospheric discontinuities (MLD). Seismic anisotropy appears stronger near these shallow discontinuities due to larger single-crystal anisotropy of olivine compared to wadsleyite. Amplitudes of SS precursors did not reveal useful information about MTZ anisotropy due to the large uncertainties. However, large anisotropy at shallower depths can potentially change the polarity of SS precursors as a function of azimuth, making it more applicable to detect anisotropy (e.g., Rychert et al., 2014). SS precursors have been successfully applied to constrain the depth of oceanic LAB (e.g., Schmerr, 2012). Future work can implement azimuthal stacking of amplitudes and travel-times in the analysis of shallower SS precursors, especially in the densely sampled regions such as central Pacific and northwestern Pacific regions. Constraints on shallow anisotropy can

provide useful insights into the patterns of current mantle flow in the asthenosphere or past tectonic activities associated with the "fossil anisotropy" in the lithosphere.

On Mars, multiple reflected waves such as PP and SS were identified from InSight data in Chapter 4. I measured the travel-times of these body waves based upon polarization filtering and vespagram analysis. However, the uncertainties of travel-times were not well constrained. The presence of glitches and frequency dependent waveforms can both contribute to the uncertainties. In my next steps, I will attempt to quantify the uncertainties by picking the body waves in the four deglitched datasets. The variations of picks in these datasets can be computed as part of the uncertainties. On the other hand, I only used a certain bandpass filter (0.3-0.9 Hz) when picking these body waves. Apparently, the waveforms of Marsquakes would change when using a different filter, thus affecting the travel-time picks. I combined polarization filtering with filter banks to investigate the variations of travel-time picks at different frequencies (Figure A.8-A.12). I will also pick these body waves using filter banks to better quantify the uncertainties. Using the robust travel-time picks and uncertainties of multiple reflected waves, one can invert the structures of martian crust and upper mantle based on a transdimensional Bayesian approach (e.g., Gao and Lekić, 2018). Future work can also include the body wave picks in the HF events (Figure A.13-A.15) to provide additional constraints on the crustal and upper mantle structures of Mars.

Preliminary depth estimates of olivine-to-wadsleyite phase transition on Mars were simply derived from the S-P times at the center of triplication. Next step is to use synthetic waveform modeling to search for the best-fitting model in our model space. Currently, I have 48 models with different compositions and thermal profiles, thereby

changing the depths of discontinuities. My goal is to compute AxiSEM synthetics using these models and determine the depth of discontinuity based on waveform matching. The source complexities (e.g., focal mechanism and source time function) and crustal scattering should also be considered for waveform modeling. The source depths can trade-off with the depth of discontinuity, but source depths are unknown for these candidate events. Therefore, the uncertainty estimates of discontinuity depth should take into account the model uncertainties as well as the S-P time and source depth uncertainties of the candidate events.

Appendices

Appendix A: Impedance Contrasts across 410-km and 660-km Discontinuities

We followed the method by Shearer and Flanagan (1999) to constrain the impedance contrasts of MTZ discontinuities from amplitudes of SS precursors. The amplitudes were measured from the stacking results of entire SS dataset by epicentral distance and corrected for attenuation and geometrical spreading using PREM (Yu et al., 2018). The Vs and density contrasts of 410-km and 660-km discontinuities were inverted from a grid-search method. The impedance contrasts from 1-D Earth models and body wave studies are summarized in Table A.1.

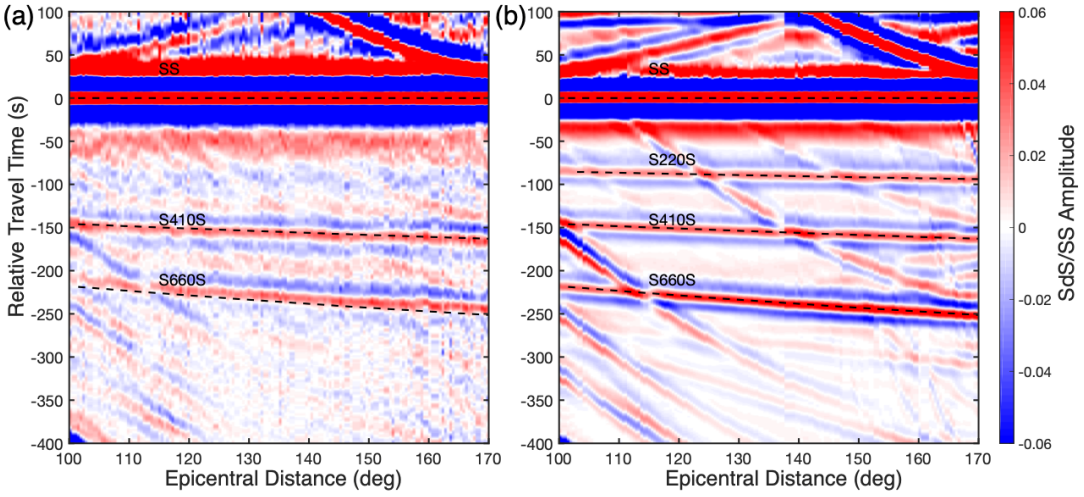

Figure A.1 Stacking results of the entire (a) SS dataset and (b) corresponding PREM synthetics by epicentral distance. The dashed lines are predicted travel-time curves for SS phase and the precursors based on PREM (Dziewonski and Anderson, 1981). The bin size is 0.5 degree.

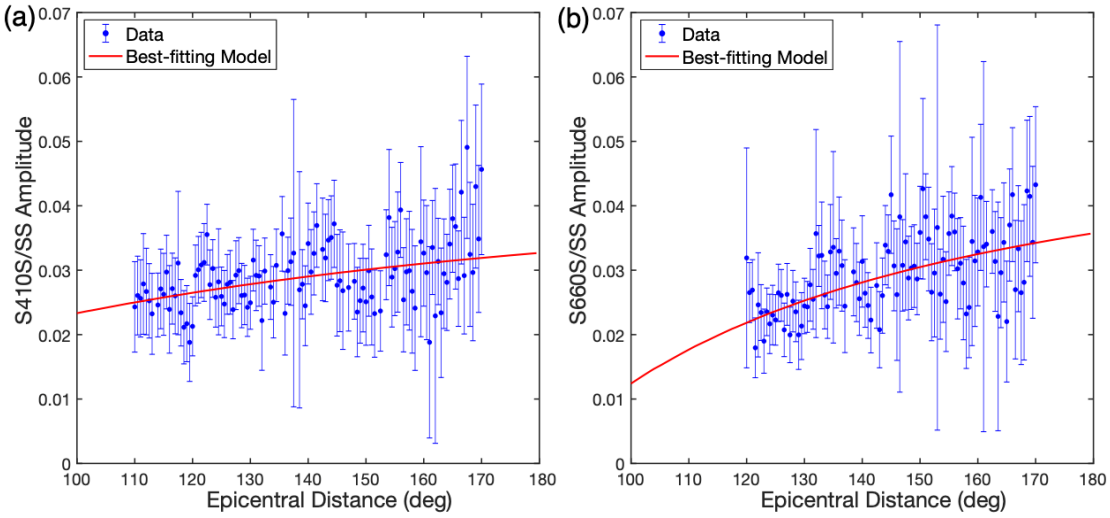

Figure A.2 Measurements of SS precursor amplitudes from the stacking results by epicentral distance. (a) S410S/SS amplitudes and (b) S660S/SS amplitudes as a function of epicentral distance. The amplitudes are corrected for attenuation and geometrical spreading (Yu et al., 2018). The error bars are 2σ uncertainties of amplitudes estimated from bootstrapping. The red lines indicate the best-fitting models from the grid-search of impedance contrasts at 410-km and 660-km discontinuities.

Table A.1 Summary of impedance contrast observations across 410-km and 660-km discontinuities. The uncertainties from this study are 1σ errors. 1-D Earth's models and other observations are included for comparisons: (1) PREM (Dziewonski and Anderson, 1981); (2) AK135 (Kennett et al., 1995); (3) SF99 (Shearer and Flanagan, 1999); (4) LS06 (Lawrence and Shearer, 2006b).

410-km Discontinuity					
	This Study	**PREM**	**AK135**	**SF99**	**LS06**
Density Contrast (%)	3.4±1.4	4.97	11.42	0.9	4.8
Vs Contrast (%)	4.0±2.4	3.35	4.23	9.7	5.1
Impedance Contrast (%)	7.4±1.0	8.32	15.65	10.6	9.9
660-km Discontinuity					
Density Contrast (%)	4.5±0.6	9.28	7.81	5.2	4.4
Vs Contrast (%)	4.1±1.7	6.51	6.05	4.8	4.2
Impedance Contrast (%)	8.6±1.2	15.79	13.86	10	8.6

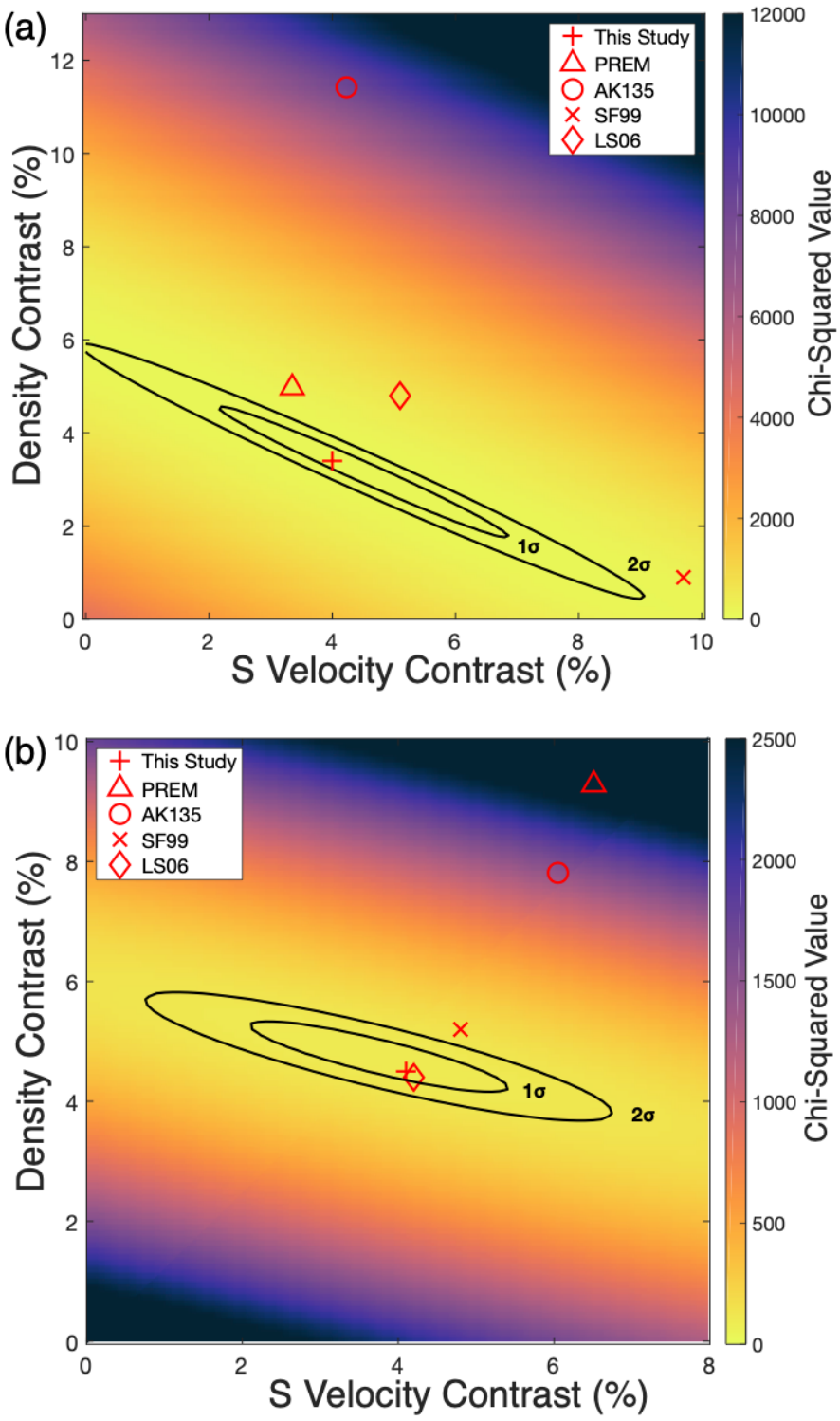

Figure A.3 Grid-search of the density and Vs contrasts across (a) 410-km and (b) 660-km discontinuities based on the amplitudes of SS precursors. The red crosses represent the best-fitting models. The black lines denote the 1σ and 2σ error ellipses. 1-D Earth's models and other observations are included for comparisons: (1) PREM (Dziewonski and Anderson, 1981); (2) AK135 (Kennett et al., 1995); (3) SF99 (Shearer and Flanagan, 1999); (4) LS06 (Lawrence and Shearer, 2006b).

Appendix B: Detectability of Martian Core

We investigated the detectability of martian core using synthetics computed from AxiSEM and SEIS-VBB noise levels. We identified core reflected waves (ScS, PcP and ScP) and core traversing phases (PKP and SKS) as candidate body waves to detect the martian core. The detectability of these body waves is summarized in Table A.2.

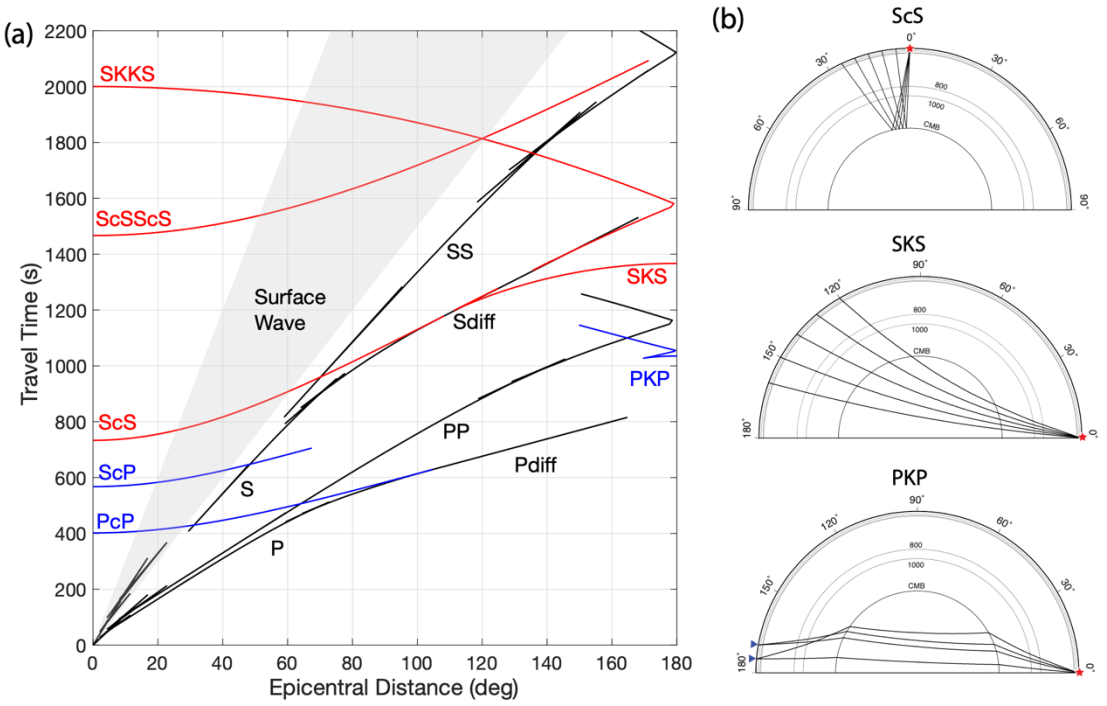

Figure A.4 (a) Predicted travel-time curves of core phases based on EH45TcoldCrust1 model (Rivoldini et al., 2011) using TauP. The black curves represent the main body waves. The blue and red curves are core related P and S waves respectively. The gray shaded region indicates the surface waves. (b) The raypaths of core phases including ScS, SKS and PKP phases.

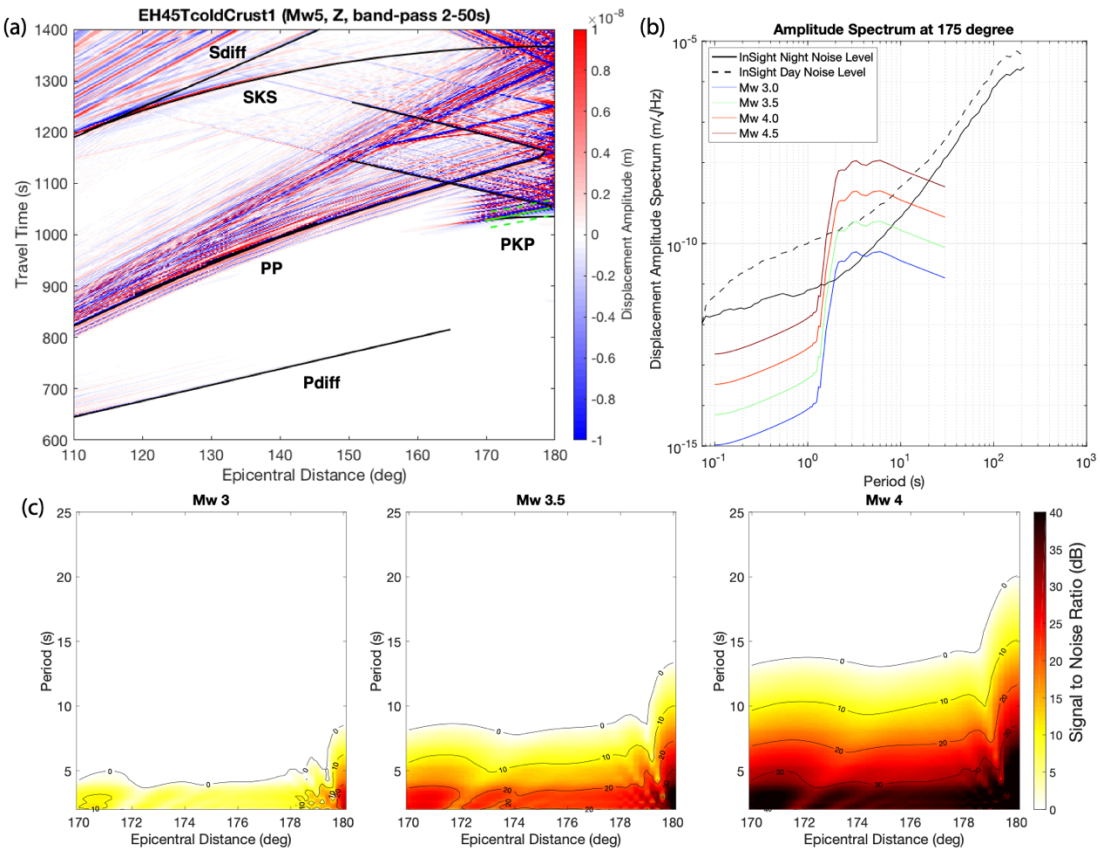

Figure A.5 (a) Synthetic wavefield of PKP on the vertical component. The size of event is Mw 5 and the filter is a 2s low-pass filter. The green lines represent the predicted travel-time of PKP and the time window used for the amplitude spectrum calculation. We focus on the minor-arc branch of PKP arrivals, which has the largest amplitude, to avoid interference with other phases. Pdiff has negligible amplitude between 160 and 180 degrees so PKP would be become the first arrival if it is detected by InSight. (b) Amplitude spectra of PKP phase in comparison with the noise model. The PKP phase requires at least Mw 3.0 event to be detected. Among all the core phases, PKP has the largest amplitude so it is more likely to be detected by InSight. (c) SNR of PKP for different magnitudes of events. The magnitude threshold is Mw 3.0 using the martian night noise level (BHZ). The frequency range is between 2-20 s and the distance range is between 160-180 degrees to detect PKP.

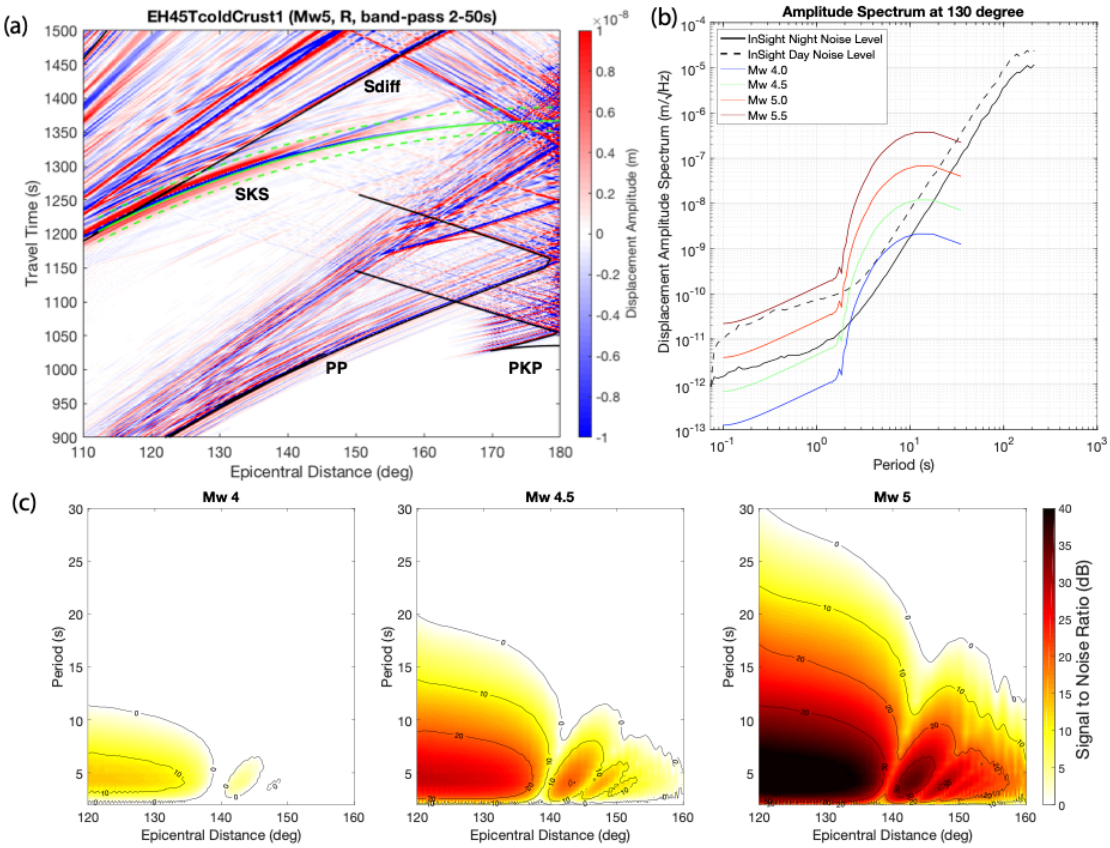

Figure A.6 Same as Figure A.5 but for SKS phase on the radial component. The magnitude threshold is Mw 4.0 using the martian night noise level on the horizontal components. The frequency range is between 2-30 s and the distance range is between 120-160 degrees to detect SKS.

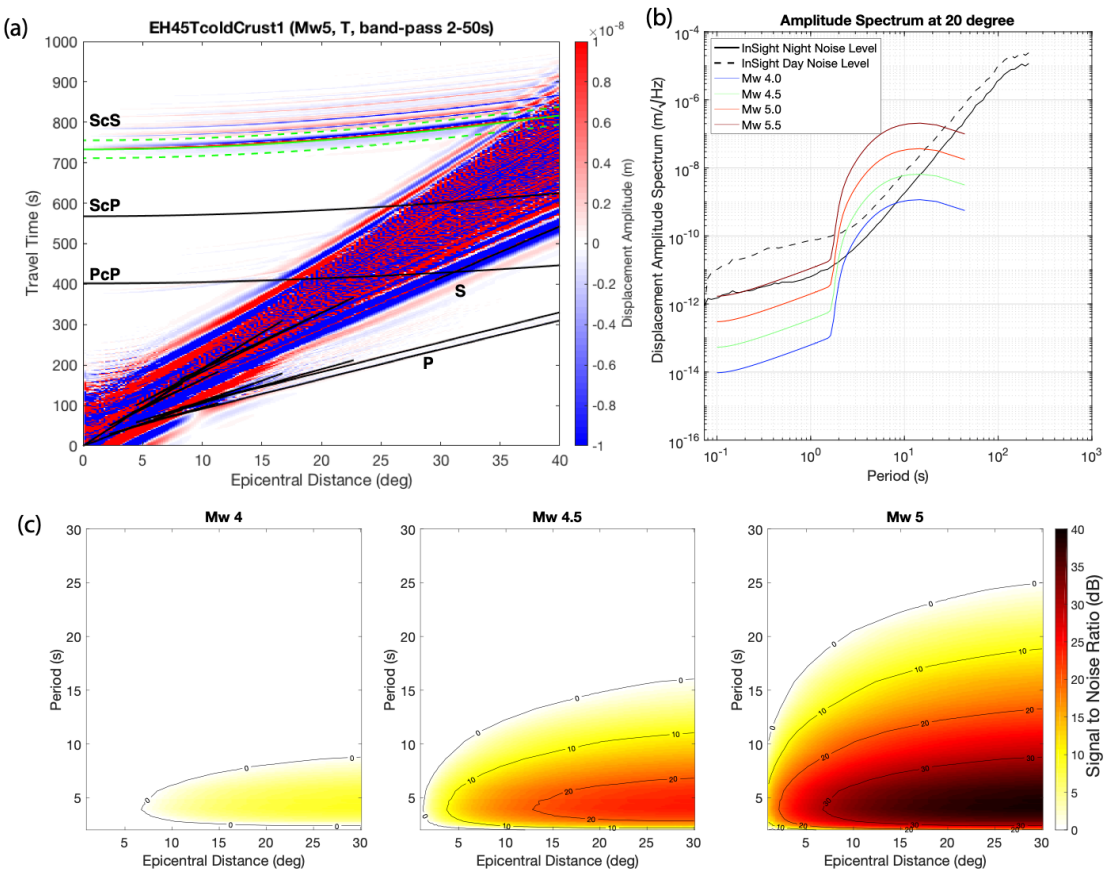

Figure A.7 Same as Figure A.5 but for ScS phase on the transverse component. The magnitude threshold is Mw 4.0 using the martian night noise level on the horizontal components. The frequency range is between 2-25 s and the distance range is between 0-40 degrees to detect ScS.

Table A.2 Detectability of core phases.

Core Phases	Magnitude Threshold (Mw)	Period (s)	Distance Range (degree)	Noise Model
ScS	4.0	2 - 25	0 - 30	BHE + BHN night
ScP	4.0	2 - 30	0 - 20	BHZ night
PcP	4.5	2 - 20	0 -10	BHZ night
PKP	3.0	2 - 20	170 -180	BHZ night
SKS	4.0	2 - 30	120 - 160	BHE + BHN night

Appendix C: Polarization Filtering Implemented with Filter Banks

We implemented the polarization filtering technique with filter banks to show the frequency dependent waveforms of Marsquakes. Here, we choose five high-quality events as examples: S0173a, S0235b, S0325a, S0407a and S0484b events. The uncertainties of these body wave picks can be quantified using filter banks. We also compare the picks made by ETH group with our own picks.

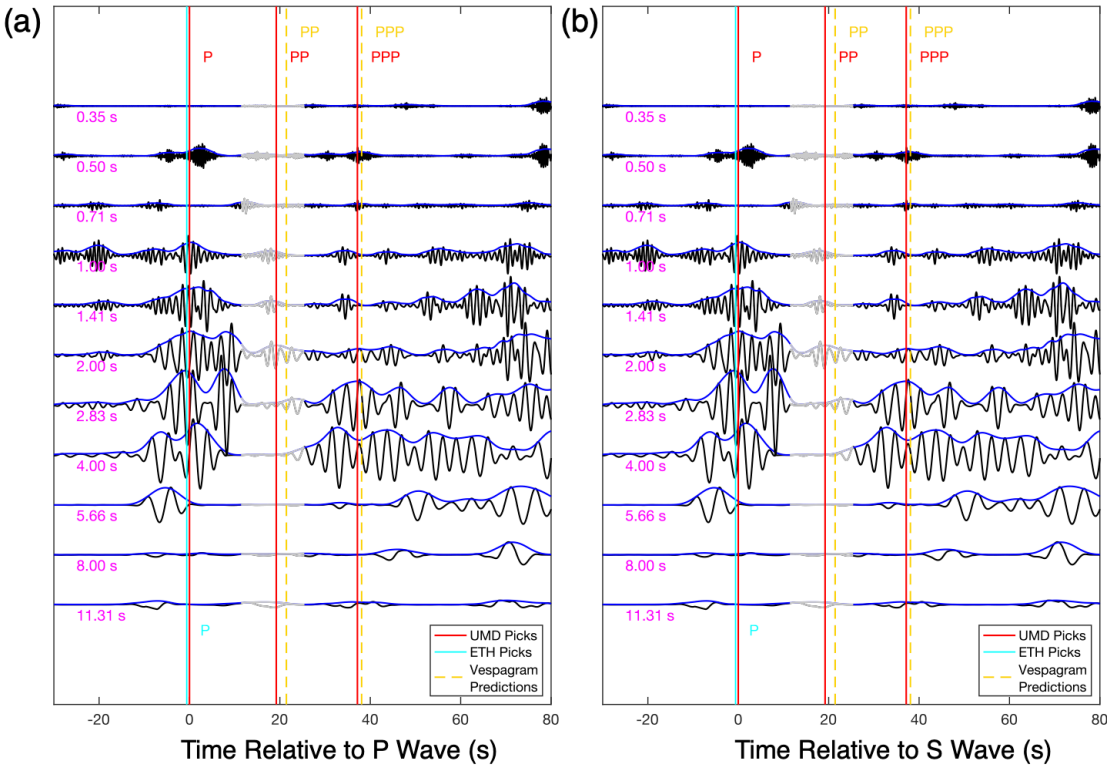

Figure A.8 Polarization filtered waveforms for S0173a event using filter banks. The center frequencies of filter banks are labelled in magenta color. The solid lines indicate the body wave picks made by the UMD group (red) and ETH group (cyan). The yellow dashed lines denote the predicted travel-times from vespagram analysis. The gray shaded regions are time windows for known glitches (Scholz et al., 2020).

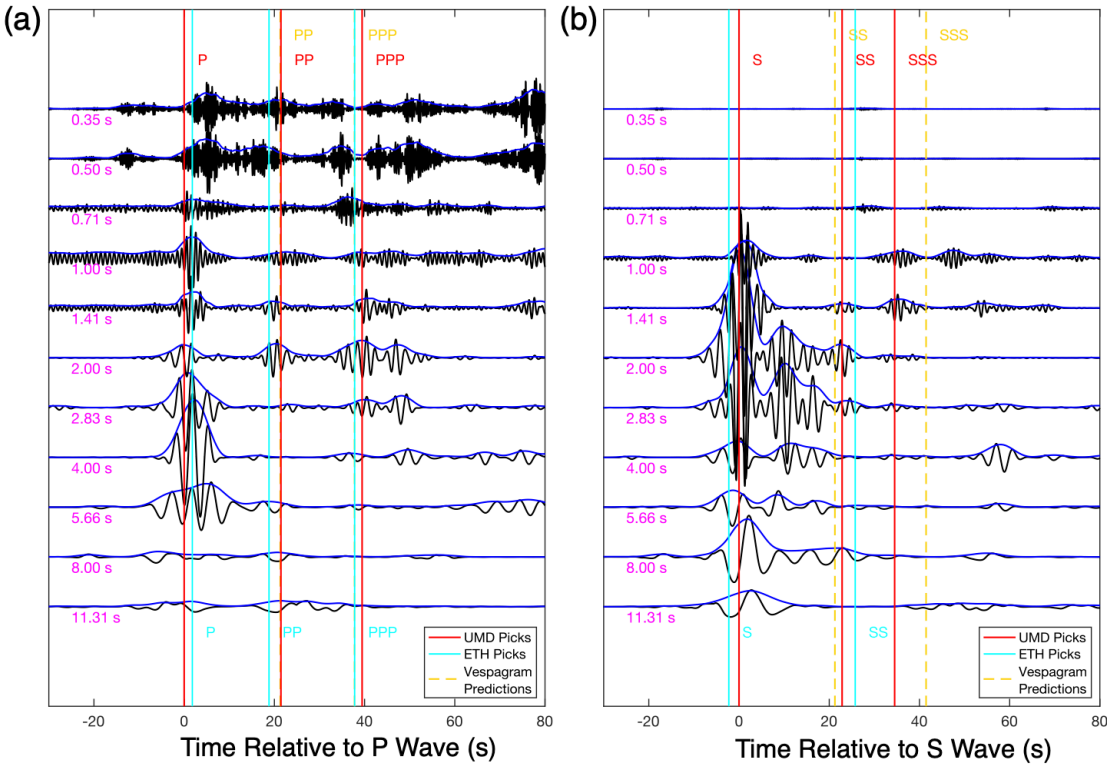

Figure A.9 Polarization filtered waveforms for S0235b event using filter banks. The legends are the same as Figure A.8.

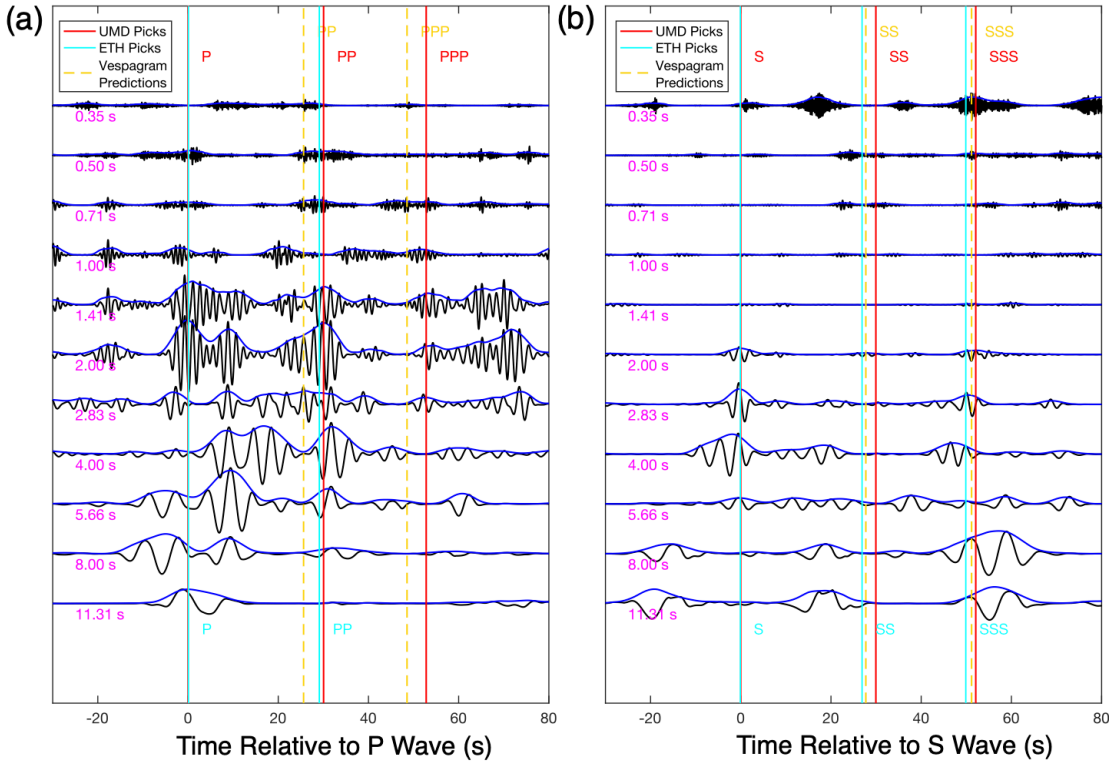

Figure A.10 Polarization filtered waveforms for S0325a event using filter banks. The legends are the same as Figure A.8.

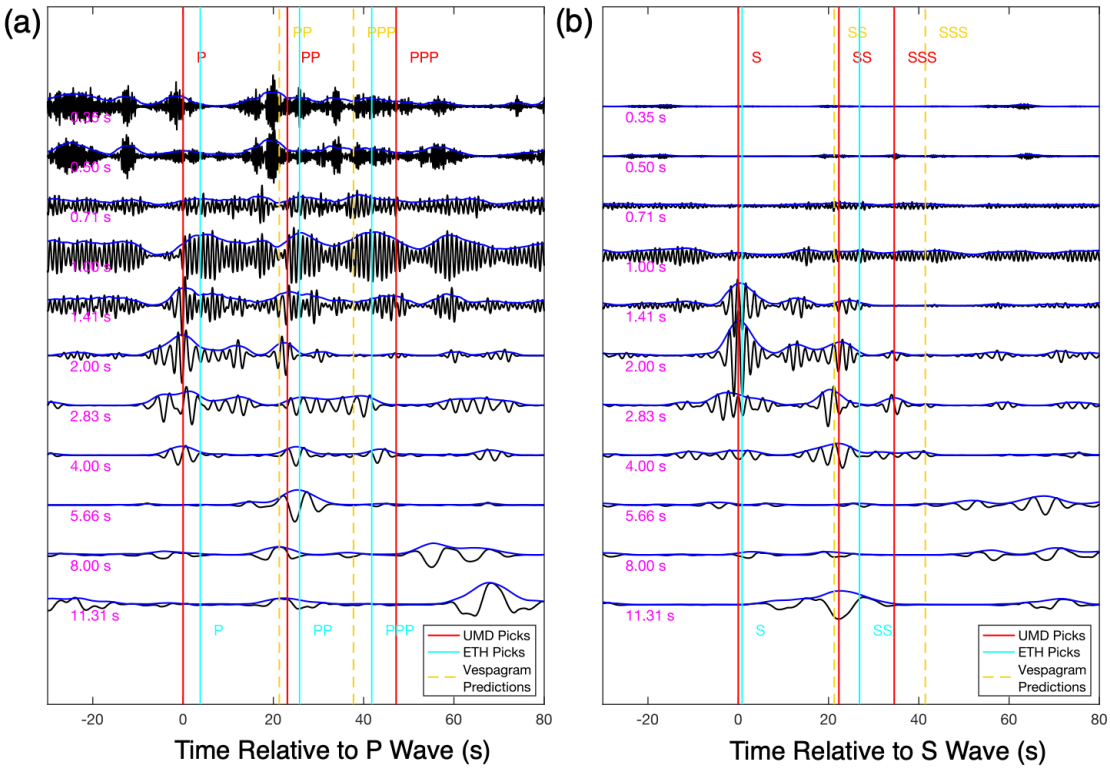

Figure A.11 Polarization filtered waveforms for S0407a event using filter banks. The legends are the same as Figure A.8.

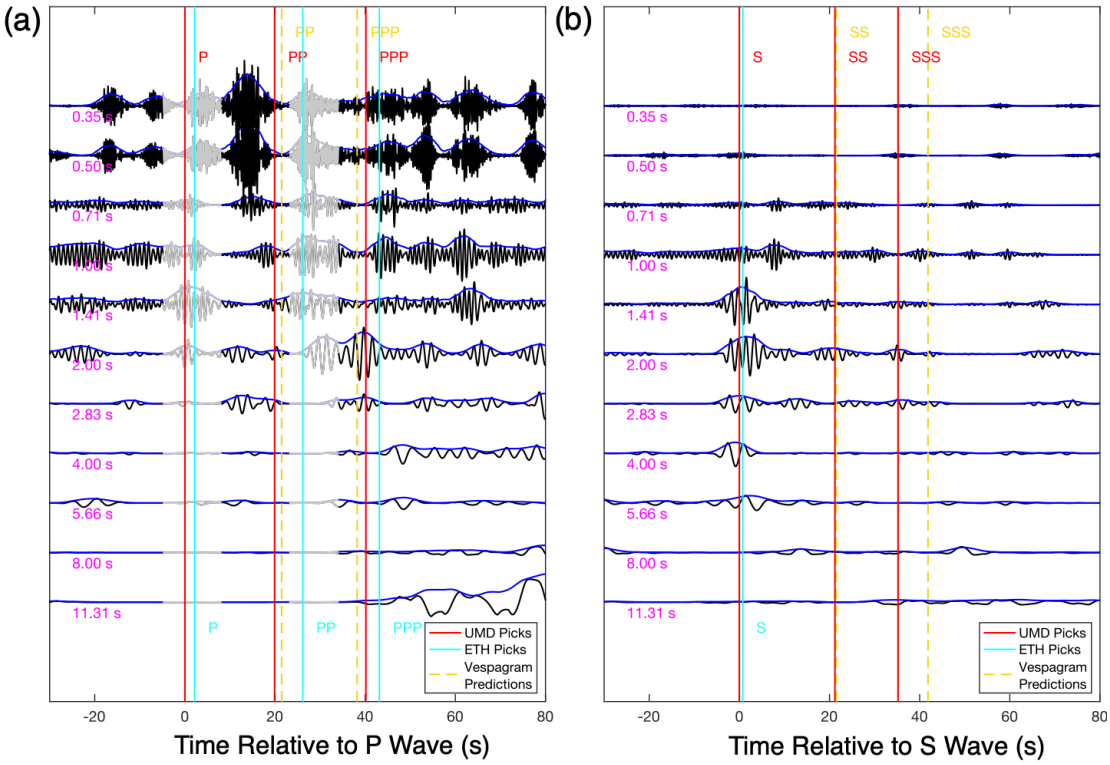

Figure A.12 Polarization filtered waveforms for S0484b event using filter banks. The legends are the same as Figure A.8.

Appendix D: Vespagram Analysis for HF Events

We aligned the spectral envelopes of HF events using an automatic sequencing approach (Kim et al., 2020). The HF events were divided into three groups based on the epicentral distances and stacked at different slowness to produce vespagrams.

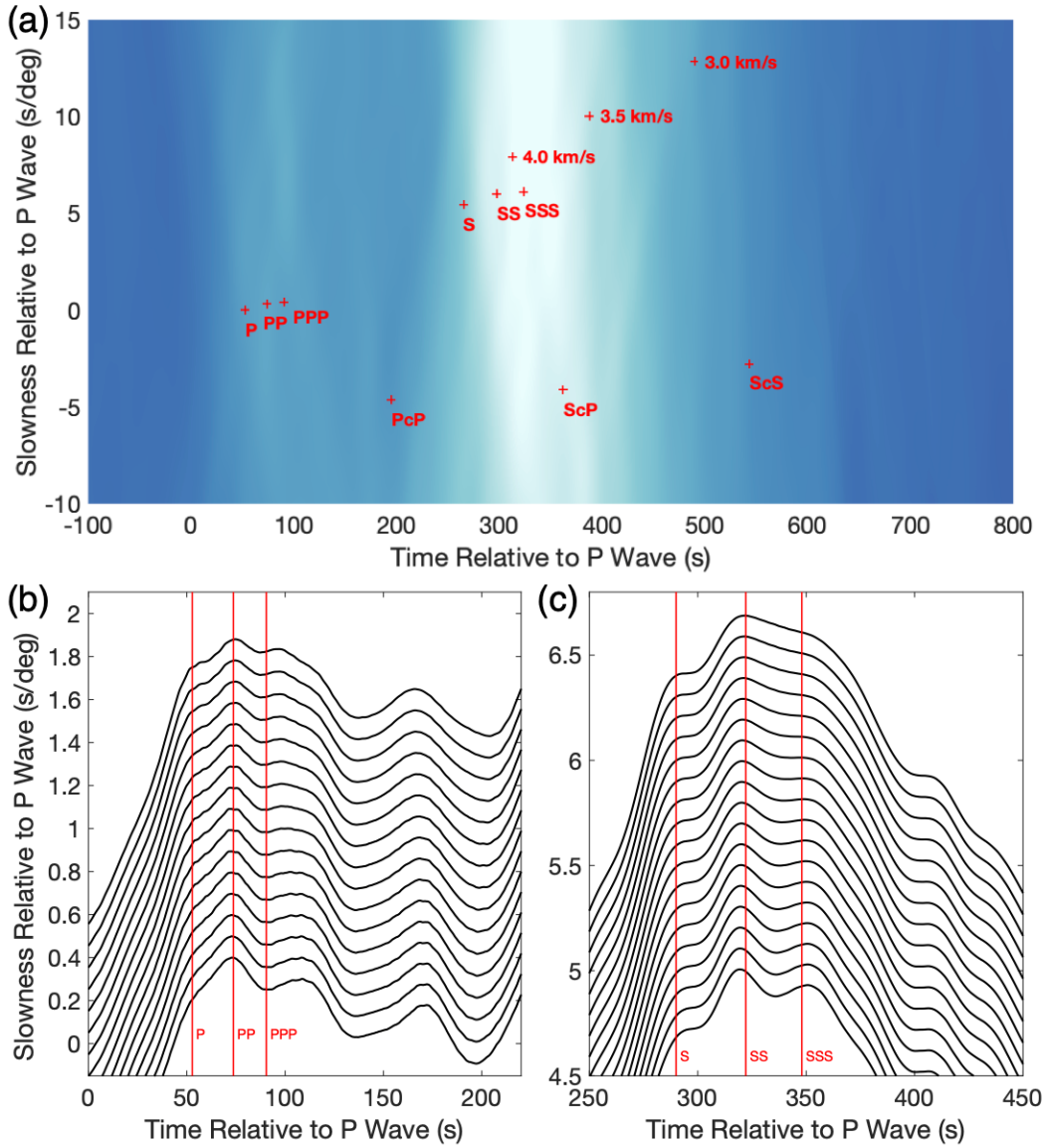

Figure A.13 Vespagram for HF events with distances between 31 and 39 degrees (Group 1). (a) Vespagram derived from the average spectral envelopes of HF events. The spectral envelopes were automatically aligned and ordered using a sequencing approach (Kim et al., 2020). Expanded views of (b) P multiple reflected waves and (c) S multiple reflected waves on the vespagram. The red crosses and red lines denote the predicted slowness and arrival-times of body waves and surface waves using a reference model (Khan et al., 2020).

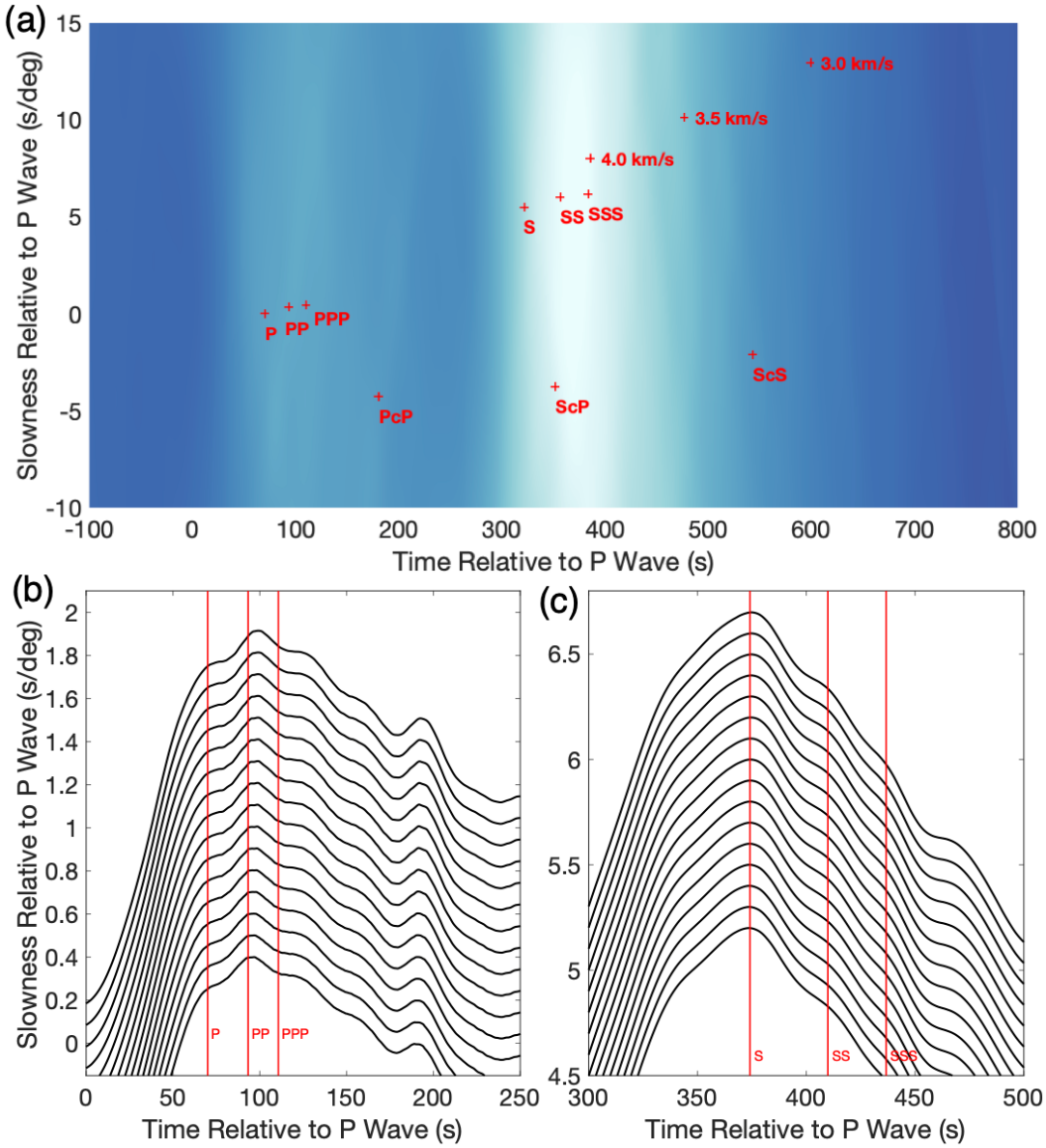

Figure A.14 Vespagram for HF events with distances between 39 and 47 degrees (Group 2). (a) Vespagram derived from the average spectral envelopes of HF events. Expanded views of (b) P multiple reflected waves and (c) S multiple reflected waves on the vespagram. Legends are the same as Figure A.13.

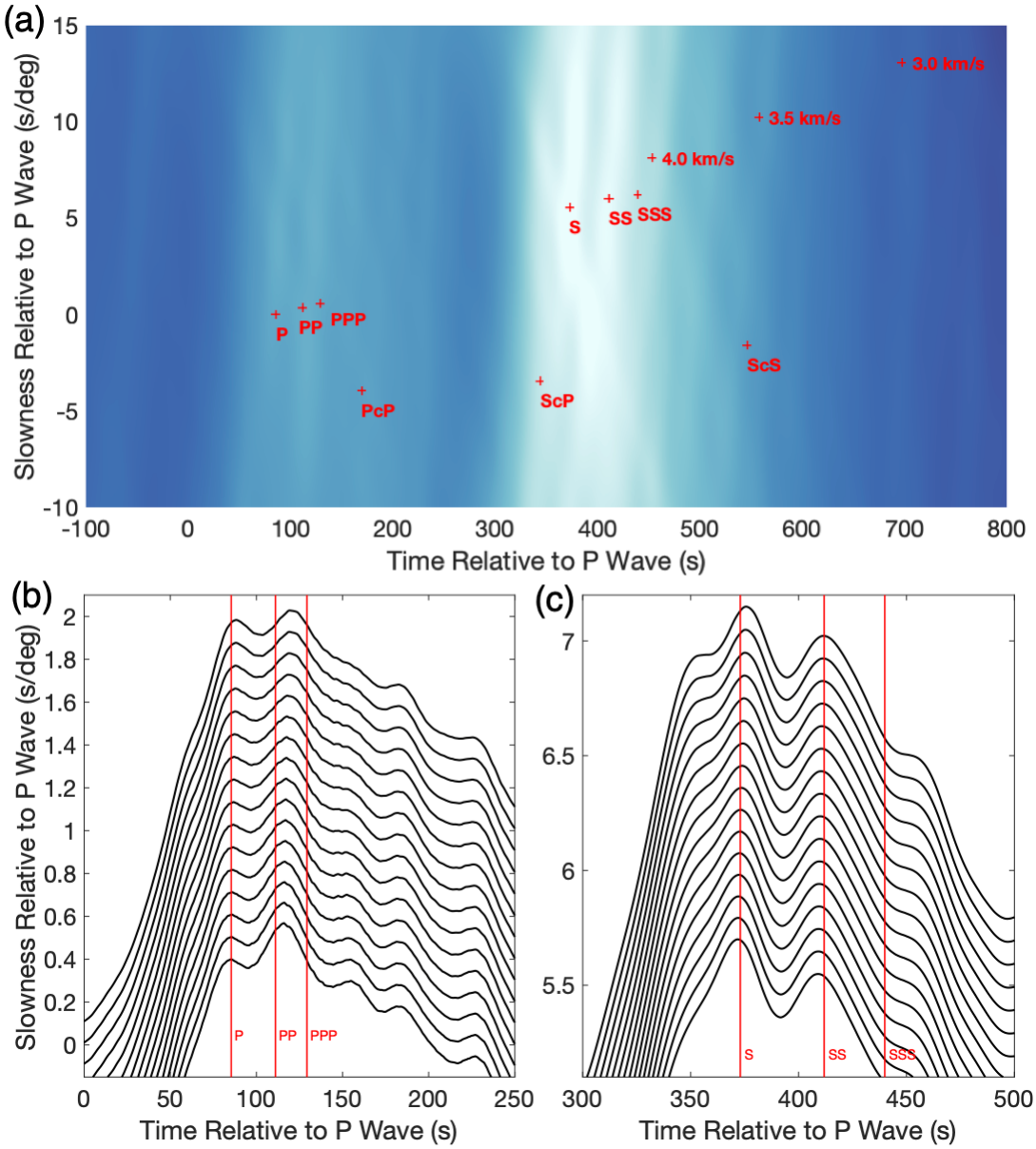

Figure A.15 Vespagram for HF events with distances between 47 and 56 degrees (Group 3). (a) Vespagram derived from the average spectral envelopes of HF events. Expanded views of (b) P multiple reflected waves and (c) S multiple reflected waves on the vespagram. Legends are the same as Figure A.13.

Bibliography

Akaogi, M., Ito, E., & Navrotsky, A. (1989). Olivine-modified spinel-spinel transitions in the system Mg2SiO4-Fe2SiO4: Calorimetric measurements, thermochemical calculation, and geophysical application. *Journal of Geophysical Research: Solid Earth*, *94*(B11), 15671–15685. http://doi.org/10.1029/JB094iB11p15671

Anderson, D. L. (1962). Love Wave Dispersion in Heterogeneous Anisotropic Media. *Geophysics*, *27*(4), 427–541. http://doi.org/https://doi.org/10.1190/1.1439042

Anderson, D. L., Duennebier, F. K., Latham, G. V., TOKSÖZ, M. F., KOVACH, R. L., KNIGHT, T. C. D., et al. (1976). The Viking Seismic Experiment. *Science*, *194*(4271), 1318–1321. http://doi.org/10.1126/science.194.4271.1318

Anderson, D. L., Miller, W. F., Latham, G. V., Nakamura, Y., Toksöz, M. N., Dainty, A. M., et al. (1977). Seismology on Mars. *Journal of Geophysical Research: Solid Earth*, *82*(28), 4524–4546. http://doi.org/10.1029/JS082i028p04524@10.1002/(ISSN)2156-2202.VIKPROJ1

Bai, L., Zhang, Y., & Ritsema, J. (2012). An analysis of SS precursors using spectral-element method seismograms. *Geophysical Journal International*, *188*(1), 293–300. http://doi.org/10.1111/j.1365-246X.2011.05256.x

Banerdt, W. B., Smrekar, S. E., Banfield, D., Giardini, D., Golombek, M., Johnson, C. L., et al. (2020). Initial results from the InSight mission on Mars. *Nature Geoscience*, *13*(3), 183–. http://doi.org/10.1038/s41561-020-0544-y

Bass, J. D., & Kanzaki, M. (1990). Elasticity of a majorite-pyrope solid solution. *Geophysical Research Letters*, *17*(11), 1989–1992. http://doi.org/10.1029/GL017i011p01989

Bassin, C., Laske, G., & Masters, G. (2000). The current limits of resolution for surface wave tomography in North America. *EOS Trans. AGU. 81 : Fall Meet. Suppl., Abstract*.

Becker, T. W., Chevrot, S., Pelkum, V. S., & Blackman, D. K. (2006). Statistical properties of seismic anisotropy predicted by upper mantle geodynamic models. *Journal of Geophysical Research: Solid Earth*, *111*(B8), 12253. http://doi.org/10.1029/2005JB004095

Becker, T. W., Conrad, C. P., Schaeffer, A. J., & Lebedev, S. (2014). Origin of azimuthal seismic anisotropy in oceanic plates and mantle. *Earth and Planetary Science Letters*, *401*, 236–250. http://doi.org/10.1016/j.epsl.2014.06.014

Becker, T. W., Lebedev, S., & Long, M. D. (2012). On the relationship between azimuthal anisotropy from shear wave splitting and surface wave tomography. *Journal of Geophysical Research: Solid Earth*, *117*(B1), B01306. http://doi.org/10.1029/2011JB008705

Becker, T. W., Schaeffer, A. J., Lebedev, S., & Conrad, C. P. (2015). Toward a generalized plate motion reference frame. *Geophysical Research Letters*, *42*(9), 3188–3196. http://doi.org/10.1002/2015GL063695

Beghein, C., & Trampert, J. (2003). Robust Normal Mode Constraints on Inner-Core Anisotropy from Model Space Search. *Science*, *299*(5606), 552–555. http://doi.org/10.1126/science.1078159

Beghein, C., & Trampert, J. (2004). Probability density functions for radial anisotropy: implications for the upper 1200 km of the mantle. *Earth and Planetary Science Letters*, *217*(1-2), 151–162. http://doi.org/10.1016/S0012-821X(03)00575-2

Beghein, C., Resovsky, J., & van der Hilst, R. D. (2008). The signal of mantle anisotropy in the coupling of normal modes. *Geophysical Journal International*, *175*(3), 1209–1234. http://doi.org/10.1111/j.1365-246X.2008.03970.x

Bellini, G., Ianni, A., Ludhova, L., Mantovani, F., & McDonough, W. F. (2013). Geo-neutrinos. *Progress in Particle and Nuclear Physics*, *73*, 1–34. http://doi.org/10.1016/j.ppnp.2013.07.001

Bercovici, D., & Karato, S.-I. (2003). Whole-mantle convection and the transition-zone water filter. *Nature*, *425*(6953), 39–44. http://doi.org/10.1038/nature01918

Bertka, C. M., & Fei, Y. (1997). Mineralogy of the Martian interior up to core-mantle boundary pressures. *Journal of Geophysical Research: Solid Earth*, *102*(B3), 5251–5264. http://doi.org/10.1029/96JB03270

Bertka, C. M., & Fei, Y. (1998). Density profile of an SNC model Martian interior and the moment-of-inertia factor of Mars. *Earth and Planetary Science Letters*, *157*(1-2), 79–88. http://doi.org/https://doi.org/10.1016/S0012-821X(98)00030-2

Billen, M. I. (2008). Modeling the dynamics of subducting slabs. *Annual Review of Earth and Planetary Sciences*, *36*(1), 325–356. http://doi.org/10.1146/annurev.earth.36.031207.124129

Billen, M. I. (2010). Slab dynamics in the transition zone. *Physics of the Earth and Planetary Interiors*, *183*(1-2), 296–308. http://doi.org/10.1016/j.pepi.2010.05.005

Bina, C. R., & Helffrich, G. (1994). Phase transition Clapeyron slopes and transition zone seismic discontinuity topography. *Journal of Geophysical Research: Solid Earth*, *99*(B8), 15853–15860. http://doi.org/10.1029/94JB00462

Birch, F. (1952). Elasticity and constitution of the Earth's interior. *Journal of Geophysical Research: Solid Earth*, *57*(2), 227–286. http://doi.org/10.1029/JZ057i002p00227

Birch, F. (1961). Composition of the Earths Mantle. *Geophysical Journal of the Royal Astronomical Society*, *4*(s0), 295–311. http://doi.org/https://doi.org/10.1111/j.1365-246X.1961.tb06821.x

Burbine, T. H., & O'Brien, K. M. (2004). Determining the possible building blocks of the Earth and Mars. *Meteoritics & Planetary Science*, *39*(5), 667–681. http://doi.org/10.1111/j.1945-5100.2004.tb00110.x

Cao, Q., Van der Hilst, R. D., De Hoop, M. V., & Shim, S. H. (2011). Seismic Imaging of Transition Zone Discontinuities Suggests Hot Mantle West of Hawaii. *Science*, *332*(6033), 1068–1071. http://doi.org/10.1126/science.1202731

Chaljub, E., & Tarantola, A. (1997). Sensitivity of SS precursors to topography on the upper-mantle 660-km discontinuity. *Geophysical Research Letters*, *24*(21), 2613–2616. http://doi.org/10.1029/97GL52693

Chambers, K., Deuss, A., & Woodhouse, J. H. (2005a). Reflectivity of the 410-km discontinuity from PP and SS precursors. *Journal of Geophysical Research: Solid Earth*, *110*(B2). http://doi.org/10.1029/2004JB003345

Chambers, K., Woodhouse, J. H., & Deuss, A. (2005b). Topography of the 410-km discontinuity from PP and SS precursors. *Earth and Planetary Science Letters*, *235*(3-4), 610–622. http://doi.org/10.1016/j.epsl.2005.05.014

Chang, S.-J., Ferreira, A. M. G., Ritsema, J., van Heijst, H. J., & Woodhouse, J. H. (2015). Joint inversion for global isotropic and radially anisotropic mantle structure including crustal thickness perturbations. *Journal of Geophysical Research: Solid Earth*, *120*(6), 4278–4300. http://doi.org/10.1002/2014JB011824

Chen, W. P., & Brudzinski, M. R. (2003). Seismic anisotropy in the mantle transition zone beneath Fiji-Tonga. *Geophysical Research Letters*, *30*(13). http://doi.org/10.1029/2002GL016330

Clinton, J. F., Ceylan, S., van Driel, M., & Giardini, D. (2020). The Marsquake Catalogue from InSight, Sols 0-478. http://doi.org/10.31219/osf.io/ws967

Clinton, J. F., Giardini, D., Lognonné, P., Banerdt, B., van Driel, M., Drilleau, M., et al. (2017). Preparing for InSight: An Invitation to Participate in a Blind Test for Martian Seismicity. *Seismological Research Letters*, *88*(5), 1290–1302. http://doi.org/10.1785/0220170094

Collins, J. A., Wolfe, C. J., & Laske, G. (2012). Shear wave splitting at the Hawaiian hot spot from the PLUME land and ocean bottom seismometer deployments. *Geochemistry, Geophysics, Geosystems*, *13*(2), n/a–n/a. http://doi.org/10.1029/2011GC003881

Connolly, J. A. D. (2005). Computation of phase equilibria by linear programming: A tool for geodynamic modeling and its application to subduction zone decarbonation. *Earth and Planetary Science Letters*, *236*(1-2), 524–541. http://doi.org/10.1016/j.epsl.2005.04.033

Cottaar, S., Heister, T., Rose, I., & Unterborn, C. (2014). BurnMan: A lower mantle mineral physics toolkit. *Geochemistry, Geophysics, Geosystems*, *15*(4), 1164–1179. http://doi.org/10.1002/2013GC005122

Courtier, A. M., Jackson, M. G., Lawrence, J. F., Wang, Z., Lee, C.-T. A., Halama, R., et al. (2007). Correlation of seismic and petrologic thermometers suggests deep thermal anomalies beneath hotspots. *Earth and Planetary Science Letters*, *264*(1-2), 308–316. http://doi.org/10.1016/j.epsl.2007.10.003

Courtillot, V., Davaille, A., Besse, J., & Stock, J. (2003). Three distinct types of hotspots in the Earth's mantle. *Earth and Planetary Science Letters*, *205*(3-4), 295–308. http://doi.org/10.1016/S0012-821X(02)01048-8

Crampin, S. (1984). An introduction to wave propagation in anisotropic media. *Geophysical Journal International*, *76*(1), 17–28. http://doi.org/10.1111/j.1365-246X.1984.tb05018.x

Crotwell, H. P., Owens, T. J., & Ritsema, J. (1999). The TauP Toolkit: Flexible Seismic Travel-time and Ray-path Utilities. *Seismological Research Letters*, *70*(2), 154–160. http://doi.org/10.1785/gssrl.70.2.154

Dahlen, F. A. (2005). Finite-frequency sensitivity kernels for boundary topography perturbations. *Geophysical Journal International*, *162*(2), 525–540. http://doi.org/10.1111/j.1365-246X.2005.02682.x

Daubar, I. J., Lognonné, P., Teanby, N. A., Collins, G. S., InSight Marsquake Service, Stahler, S., et al. (2020). A New Crater Near InSight: Implications for

Seismic Impact Detectability on Mars. *Journal of Geophysical Research: Planets*, *125*(8), 133. http://doi.org/10.1029/2020JE006382
Daubar, I., Lognonne, P., Teanby, N. A., Miljkovic, K., Stevanovic, J., Vaubaillon, J., et al. (2018). Impact-Seismic Investigations of the InSight Mission. *Space Science Reviews*, *214*(8). http://doi.org/10.1007/s11214-018-0562-x
Davies, D., Kelly, E. J., & Filson, J. R. (1971). Vespa Process for Analysis of Seismic Signals. *Nature-Physical Science*, *232*(27), 8–&.
Debayle, E., Dubuffet, F., & Durand, S. (2016). An automatically updated S-wave model of the upper mantle and the depth extent of azimuthal anisotropy. *Geophysical Research Letters*, *43*(2), 674–682. http://doi.org/10.1002/2015GL067329
DeMets, C., Gordon, R. G., Argus, D. F., & Stein, S. (1990). Current Plate Motions. *Geophysical Journal International*, *101*(2), 425–478. http://doi.org/10.1111/j.1365-246X.1990.tb06579.x
Demouchy, S., Mainprice, D., Tommasi, A., Couvy, H., Barou, F., Frost, D. J., & Cordier, P. (2011). Forsterite to wadsleyite phase transformation under shear stress and consequences for the Earth's mantle transition zone. *Physics of the Earth and Planetary Interiors*, *184*(1-2), 91–104. http://doi.org/10.1016/j.pepi.2010.11.001
Deuss, A. (2009). Global Observations of Mantle Discontinuities Using SS and PP Precursors. *Surveys in Geophysics*, *30*(4-5), 301–326. http://doi.org/10.1007/s10712-009-9078-y
Deuss, A., & Woodhouse, J. H. (2002). A systematic search for mantle discontinuities using SS-precursors. *Geophysical Research Letters*, *29*(8), 90–1–90–4. http://doi.org/10.1029/2002GL014768
Di Leo, J. F., Wookey, J., Hammond, J. O. S., Kendall, J. M., Kaneshima, S., Inoue, H., et al. (2012). Mantle flow in regions of complex tectonics: Insights from Indonesia. *Geochemistry, Geophysics, Geosystems*, *13*(12), 253. http://doi.org/10.1029/2012GC004417
Dreibus, G., & Wänke, H. (1985). Mars, a Volatile-Rich Planet. *Meteoritics*, *20*, 367–381. Retrieved from http://adsabs.harvard.edu/full/1985Metic..20..367D
Dziewonski, A. M., & Anderson, D. L. (1981). Preliminary reference Earth model. *Physics of the Earth and Planetary Interiors*, *25*(4), 297–356. http://doi.org/10.1016/0031-9201(81)90046-7
Efron, B., & Tibshirani, R. (1986). Bootstrap methods for standard errors, confidence intervals, and other measures of statistical accuracy. *Statistical Science*. http://doi.org/10.2307/2245500
Faccenda, M. (2014). Mid mantle seismic anisotropy around subduction zones. *Physics of the Earth and Planetary Interiors*, *227*, 1–19. http://doi.org/10.1016/j.pepi.2013.11.015
Faccenda, M., & Capitanio, F. A. (2012). Development of mantle seismic anisotropy during subduction-induced 3-D flow. *Geophysical Research Letters*, *39*(11), n/a–n/a. http://doi.org/10.1029/2012GL051988
Faccenda, M., Ferreira, A. M. G., Tisato, N., Bertelloni, C. L., Stixrude, L., & Pennacchioni, G. (2019). Extrinsic Elastic Anisotropy in a Compositionally

Heterogeneous Earth's Mantle. *Journal of Geophysical Research: Solid Earth*, *124*(2), 1671–1687. http://doi.org/10.1029/2018JB016482

Fei, Y., & Bertka, C. (2005). The Interior of Mars. *Science*, *308*(5725), 1120–1121. http://doi.org/10.1126/science.1110531

Fei, Y., & Bertka, C. M. (1999). Phase transitions in the Earth's mantle and mantle mineralogy (pp. 189–207). In Mantle Petrology: Field Observations and High-Pressure Experimentation: A Tribute to F. R. Boyd.

Ferreira, A. M. G., Faccenda, M., Sturgeon, W., Chang, S.-J., & Schardong, L. (2019). Ubiquitous lower-mantle anisotropy beneath subduction zones. *Nature Geoscience*, *12*(4), 301–306. http://doi.org/10.1038/s41561-019-0325-7

Flanagan, M. P., & Shearer, P. M. (1998). Global mapping of topography on transition zone velocity discontinuities by stacking SS precursors. *Journal of Geophysical Research: Solid Earth*, *103*(B2), 2673–2692. http://doi.org/10.1029/97JB03212

Flanagan, M. P., & Shearer, P. M. (1999). A map of topography on the 410-km discontinuity from PP precursors. *Geophysical Research Letters*, *26*(5), 549–552. http://doi.org/10.1029/1999GL900036

Foley, B. J., & Long, M. D. (2011). Upper and mid-mantle anisotropy beneath the Tonga slab. *Geophysical Research Letters*, *38*(2), L02303. http://doi.org/10.1029/2010GL046021

Folkner, W. M., Dehant, V., Le Maistre, S., Yseboodt, M., Rivoldini, A., Van Hoolst, T., et al. (2018). The Rotation and Interior Structure Experiment on the InSight Mission to Mars. *Space Science Reviews*, *214*(5), 1–16. http://doi.org/10.1007/s11214-018-0530-5

Fouch, M. J., & Fischer, K. M. (1996). Mantle anisotropy beneath northwest Pacific subduction zones. *Journal of Geophysical Research: Solid Earth*, *101*(B7), 15987–16002. http://doi.org/10.1029/96JB00881

French, S. W., & Romanowicz, B. (2015). Broad plumes rooted at the base of the Earth's mantle beneath major hotspots. *Nature*, *525*(7567), 95–99. http://doi.org/10.1038/nature14876

French, S. W., & Romanowicz, B. A. (2014). Whole-mantle radially anisotropic shear velocity structure from spectral-element waveform tomography. *Geophysical Journal International*, *199*(3), 1303–1327. http://doi.org/10.1093/gji/ggu334

Friederich, W., & Dalkolmo, J. (1995). Complete synthetic seismograms for a spherically symmetric earth by a numerical computation of the Green's function in the frequency domain. *Geophysical Journal International*, *122*(2), 537–550. http://doi.org/10.1111/j.1365-246X.1995.tb07012.x

Friedrich, A., Krüger, F., & Klinge, K. (1998). Ocean-generated microseismic noise located with the Gräfenberg array. *Journal of Seismology*, *2*(1), 47–64. http://doi.org/10.1023/A:1009788904007

Fukao, Y., & Obayashi, M. (2013). Subducted slabs stagnant above, penetrating through, and trapped below the 660 km discontinuity. *Journal of Geophysical Research: Solid Earth*, *118*(11), 5920–5938. http://doi.org/10.1002/2013JB010466

Fukao, Y., Widiyantoro, S., & Obayashi, M. (2001). Stagnant slabs in the upper and lower mantle transition region. *Reviews of Geophysics*, *39*(3), 291–323. http://doi.org/10.1029/1999RG000068

Gagnepain-Beyneix, J., Lognonne, P., Chenet, H., Lombardi, D., & Spohn, T. (2006). A seismic model of the lunar mantle and constraints on temperature and mineralogy. *Physics of the Earth and Planetary Interiors*, *159*(3-4), 140–166. http://doi.org/10.1016/j.pepi.2006.05.009

Gao, C., & Lekic, V. (2018). Consequences of parameterization choices in surface wave inversion: Insights from transdimensional Bayesian methods. *Geophysical Journal International*. http://doi.org/10.1093/gji/ggy310

Garcia, R. F., Gagnepain-Beyneix, J., Chevrot, S., & Lognonne, P. (2011). Very preliminary reference Moon model. *Physics of the Earth and Planetary Interiors*, *188*(1-2), 96–113. http://doi.org/10.1016/j.pepi.2011.06.015

Genova, A., Goossens, S., Lemoine, F. G., Mazarico, E., Neumann, G. A., Smith, D. E., & Zuber, M. T. (2016). Seasonal and static gravity field of Mars from MGS, Mars Odyssey and MRO radio science. *Icarus*, *272*, 228–245. http://doi.org/10.1016/j.icarus.2016.02.050

Giardini, D., Lognonné, P., Banerdt, W. B., Pike, W. T., Christensen, U., Ceylan, S., et al. (2020). The seismicity of Mars. *Nature Geoscience*, *13*(3), 205–. http://doi.org/10.1038/s41561-020-0539-8

Golombek, M., Grott, M., Kargl, G., Andrade, J., Marshall, J., Warner, N., et al. (2018). Geology and Physical Properties Investigations by the InSight Lander. *Space Science Reviews*, *214*(5), 1–52. http://doi.org/10.1007/s11214-018-0512-7

Golombek, M., Kipp, D., Warner, N., Daubar, I. J., Fergason, R., Kirk, R. L., et al. (2017). Selection of the InSight Landing Site. *Space Science Reviews*, *211*(1), 5–95. http://doi.org/10.1007/s11214-016-0321-9

Golombek, M., Warner, N. H., Grant, J. A., Hauber, E., Ansan, V., Weitz, C. M., et al. (2020). Geology of the InSight landing site on Mars. *Nature Communications*, *11*(1), 1–11. http://doi.org/10.1038/s41467-020-14679-1

Goossens, S., Sabaka, T. J., Genova, A., Mazarico, E., Nicholas, J. B., & Neumann, G. A. (2017). Evidence for a low bulk crustal density for Mars from gravity and topography. *Geophysical Research Letters*, *44*(15), 7686–7694. http://doi.org/10.1002/2017GL074172

Grand, S. P., & Helmberger, D. V. (1984). Upper Mantle Shear Structure of North-America. *Geophysical Journal of the Royal Astronomical Society*, *76*(2), 399–438. http://doi.org/10.1111/j.1365-246X.1984.tb05053.x

Gu, Y. J., & Dziewonski, A. M. (2002). Global variability of transition zone thickness. *Journal of Geophysical Research: Solid Earth*, *107*(B7), ESE 2–1–ESE 2–17. http://doi.org/10.1029/2001JB000489

Gu, Y. J., Dziewonski, A. M., & Ekström, G. (2003). Simultaneous inversion for mantle shear velocity and topography of transition zone discontinuities. *Geophysical Journal International*, *154*(2), 559–583. http://doi.org/10.1046/j.1365-246X.2003.01967.x

Gu, Y., Dziewonski, A. M., & Agee, C. B. (1998). Global de-correlation of the topography of transition zone discontinuities. *Earth and Planetary Science Letters*, *157*(1-2), 57–67. http://doi.org/10.1016/S0012-821X(98)00027-2

Gung, Y., Panning, M., & Romanowicz, B. (2003). Global anisotropy and the thickness of continents. *Nature*, *422*(6933), 707–711. http://doi.org/10.1038/nature01559

Hayes, G. P., Wald, D. J., & Johnson, R. L. (2012). Slab1.0: A three-dimensional model of global subduction zone geometries. *Journal of Geophysical Research: Solid Earth*, *117*(B1), B01302. http://doi.org/10.1029/2011JB008524

Heit, B., Yuan, X., Bianchi, M., Kind, R., & Gossler, J. (2010). Study of the lithospheric and upper-mantle discontinuities beneath eastern Asia by SS precursors. *Geophysical Journal International*, *183*(1), 252–266. http://doi.org/10.1111/j.1365-246X.2010.04714.x

Helffrich, G. (2000). Topography of the transition zone seismic discontinuities. *Reviews of Geophysics*, *38*(1), 141–158. http://doi.org/10.1029/1999RG000060

Houser, C. (2016). Global seismic data reveal little water in the mantle transition zone. *Earth and Planetary Science Letters*, *448*, 94–101. http://doi.org/10.1016/j.epsl.2016.04.018

Houser, C., Masters, G., Flanagan, M., & Shearer, P. (2008). Determination and analysis of long-wavelength transition zone structure using SS precursors. *Geophysical Journal International*, *174*(1), 178–194. http://doi.org/10.1111/j.1365-246X.2008.03719.x

Huang, Q., Schmerr, N., Waszek, L., & Beghein, C. (2019). Constraints on Seismic Anisotropy in the Mantle Transition Zone From Long-Period SS Precursors. *Journal of Geophysical Research: Solid Earth*, *124*(7), 6779–6800. http://doi.org/10.1029/2019JB017307

Huang, X., Xu, Y., & Karato, S.-I. (2005). Water content in the transition zone from electrical conductivity of wadsleyite and ringwoodite. *Nature*, *434*(7034), 746–749. http://doi.org/10.1038/nature03426

Ita, J., & Stixrude, L. (1992). Petrology, elasticity, and composition of the mantle transition zone. *Journal of Geophysical Research: Solid Earth*, *97*(B5), 6849–6866. http://doi.org/10.1029/92JB00068

Ito, E., & Takahashi, E. (1989). Postspinel transformations in the system Mg2SiO4-Fe2SiO4 and some geophysical implications. *Journal of Geophysical Research: Solid Earth*, *94*(B8), 10637–10646. http://doi.org/10.1029/JB094iB08p10637

Jung, H., & Karato, S.-I. (2001). Water-Induced Fabric Transitions in Olivine. *Science*, *293*(5534), 1460–1463. http://doi.org/10.1126/science.1062235

Karato, S. (1988). The Role of Recrystallization in the Preferred Orientation of Olivine. *Physics of the Earth and Planetary Interiors*, *51*(1-3), 107–122. http://doi.org/10.1016/0031-9201(88)90029-5

Karato, S.-I. (2008). Insights into the nature of plume–asthenosphere interaction from central Pacific geophysical anomalies. *Earth and Planetary Science Letters*, *274*(1-2), 234–240. http://doi.org/10.1016/j.epsl.2008.07.033

Karato, S.-I., Jung, H., Katayama, I., & Skemer, P. (2008). Geodynamic Significance of Seismic Anisotropy of the Upper Mantle: New Insights from Laboratory Studies. *Dx.Doi.org*, *36*(1), 59–95. http://doi.org/10.1146/annurev.earth.36.031207.124120

Katsura, T., & Ito, E. (1989). The system Mg2SiO4-Fe2SiO4 at high pressures and temperatures: Precise determination of stabilities of olivine, modified spinel, and

spinel. *Journal of Geophysical Research: Solid Earth*, *94*(B11), 15663–15670. http://doi.org/10.1029/JB094iB11p15663

Kawakatsu, H., Kumar, P., Takei, Y., Shinohara, M., Kanazawa, T., Araki, E., & Suyehiro, K. (2009). Seismic Evidence for Sharp Lithosphere-Asthenosphere Boundaries of Oceanic Plates. *Science*, *324*(5926), 499–502. http://doi.org/10.1126/science.1169499

Kawazoe, T., Ohuchi, T., Nishihara, Y., Nishiyama, N., Fujino, K., & Irifune, T. (2013). Seismic anisotropy in the mantle transition zone induced by shear deformation of wadsleyite. *Physics of the Earth and Planetary Interiors*, *216*, 91–98. http://doi.org/10.1016/j.pepi.2012.12.005

Kennett, B. L. N., Engdahl, E. R., & Buland, R. (1995). Constraints on seismic velocities in the Earth from traveltimes. *Geophysical Journal International*, *122*(1), 108–124. http://doi.org/10.1111/j.1365-246X.1995.tb03540.x

Khan, A., & Connolly, J. A. D. (2008). Constraining the composition and thermal state of Mars from inversion of geophysical data. *Journal of Geophysical Research: Planets*, *113*(E7). http://doi.org/10.1029/2007JE002996

Khan, A., Liebske, C., Rozel, A., Rivoldini, A., Nimmo, F., Connolly, J. A. D., et al. (2018). A Geophysical Perspective on the Bulk Composition of Mars. *Journal of Geophysical Research: Planets*, *123*(2), 575–611. http://doi.org/10.1002/2017JE005371

Khan, A., Mosegaard, K., & Rasmussen, K. L. (2000). A new seismic velocity model for the Moon from a Monte Carlo inversion of the Apollo lunar seismic data. *Geophysical Research Letters*, *27*(11), 1591–1594. http://doi.org/10.1029/1999GL008452

Khan, A., Mosegaard, K., Williams, J. G., & Lognonné, P. (2004). Does the Moon possess a molten core? Probing the deep lunar interior using results from LLR and Lunar Prospector. *Journal of Geophysical Research: Solid Earth*, *109*(E9), 80. http://doi.org/10.1029/2004JE002294

Khan, A., van Driel, M., Böse, M., Giardini, D., Ceylan, S., Yan, J., et al. (2016). Single-station and single-event marsquake location and inversion for structure using synthetic Martian waveforms. *Physics of the Earth and Planetary Interiors*, *258*, 28–42. http://doi.org/10.1016/j.pepi.2016.05.017

Kiefer, B., Stixrude, L., & Wentzcovitch, R. M. (1997). Calculated elastic constants and anisotropy of Mg2SiO4 spinel at high pressure. *Geophysical Research Letters*, *24*(22), 2841–2844. http://doi.org/10.1029/97GL02975

Kim, D., Lekić, V., Ménard, B., Baron, D., & Taghizadeh-Popp, M. (2020). Sequencing seismograms: A panoptic view of scattering in the core-mantle boundary region. *Science*, *368*(6496), 1223–1228. http://doi.org/10.1126/science.aba8972

Komatitsch, D., & Tromp, J. (2002a). Spectral-element simulations of global seismic wave propagation-II. Three-dimensional models, oceans, rotation and self-gravitation. *Geophysical Journal International*, *150*(1), 303–318. http://doi.org/10.1046/j.1365-246X.2002.01716.x

Komatitsch, D., & Tromp, J. (2002b). Spectral-element simulations of global seismic wave propagation—I. Validation. *Geophysical Journal International*, *149*(2), 390–412. http://doi.org/doi.org/10.1046/j.1365-246X.2002.01653.x

Konopliv, A. S., Park, R. S., & Folkner, W. M. (2016). An improved JPL Mars gravity field and orientation from Mars orbiter and lander tracking data. *Icarus*, *274*, 253–260. http://doi.org/10.1016/j.icarus.2016.02.052

Koroni, M., & Trampert, J. (2016). The effect of topography of upper-mantle discontinuities on SS precursors. *Geophysical Journal International*, *204*(1), 667–681. http://doi.org/10.1093/gji/ggv471

Koroni, M., Bozdag, E., Paulssen, H., & Trampert, J. (2017). Sensitivity analysis of seismic waveforms to upper-mantle discontinuities using the adjoint method. *Geophysical Journal International*, *210*(3), 1965–1980. http://doi.org/10.1093/gji/ggx286

Lammlein, D. R., Latham, G. V., Dorman, J., Nakamura, Y., & Ewing, M. (1974). Lunar Seismicity, Structure, and Tectonics. *Reviews of Geophysics*, *12*(1), 1–21. http://doi.org/10.1029/RG012i001p00001

Latham, G. V., Ewing, M., Press, F., Sutton, G., Dorman, J., Nakamura, Y., et al. (1970). Passive Seismic Experiment. *Science*, *167*(3918), 455–457. http://doi.org/10.1126/science.167.3918.455

Latham, G., Ewing, M., Press, F., & Sutton, G. (1969). The Apollo Passive Seismic Experiment. *Science*, *165*(3890), 241–250. http://doi.org/10.1126/science.165.3890.241

Lawrence, J. F., & Shearer, P. M. (2006a). A global study of transition zone thickness using receiver functions. *Journal of Geophysical Research: Solid Earth*, *111*(B6), n/a–n/a. http://doi.org/10.1029/2005JB003973

Lawrence, J. F., & Shearer, P. M. (2006b). Constraining seismic velocity and density for the mantle transition zone with reflected and transmitted waveforms. *Geochemistry, Geophysics, Geosystems*, *7*(10), Q10012. http://doi.org/10.1029/2006GC001339

Lawrence, J. F., & Shearer, P. M. (2008). Imaging mantle transition zone thickness with SdS-SS finite-frequency sensitivity kernels. *Geophysical Journal International*, *174*(1), 143–158. http://doi.org/10.1111/j.1365-246X.2007.03673.x

Lazarewicz, A. R., Anderson, D. L., Anderson, K., & Daonty, A. M. (1981). The Viking seismometry. *NASA Document*.

Lekić, V., & Romanowicz, B. (2011). Inferring upper-mantle structure by full waveform tomography with the spectral element method. *Geophysical Journal International*, *185*(2), 799–831. http://doi.org/10.1111/j.1365-246X.2011.04969.x

Leng, K., Nissen-Meyer, T., & van Driel, M. (2016). Efficient global wave propagation adapted to 3-D structural complexity: a pseudospectral/spectral-element approach. *Geophysical Journal International*, *207*(3), 1700–1721. http://doi.org/10.1093/gji/ggw363

Leng, K., Nissen-Meyer, T., van Driel, M., Hosseini, K., & Al-Attar, D. (2019). AxiSEM3D: broad-band seismic wavefields in 3-D global earth models with undulating discontinuities. *Geophysical Journal International*, *217*(3), 2125–2146. http://doi.org/10.1093/gji/ggz092

Lessing, S., Thomas, C., Rost, S., Cobden, L., & Dobson, D. P. (2014). Mantle transition zone structure beneath India and Western China from migration of PP and SS precursors. *Geophysical Journal International*, *197*(1), 396–413. http://doi.org/10.1093/gji/ggt511

Lessing, S., Thomas, C., Saki, M., Schmerr, N., & Vanacore, E. (2015). On the difficulties of detecting PP precursors. *Geophysical Journal International*, *201*(3), 1666–1681. http://doi.org/10.1093/gji/ggv105

Li, Chang, van der Hilst, R. D., Engdahl, E. R., & Burdick, S. (2008). A new global model for P wave speed variations in Earth's mantle. *Geochemistry, Geophysics, Geosystems*, *9*(5), n/a–n/a. http://doi.org/10.1029/2007GC001806

Li, Jiaxuan, Zheng, Y., Thomsen, L., Lapen, T. J., & Fang, X. (2018). Deep earthquakes in subducting slabs hosted in highly anisotropic rock fabric. *Nature Geoscience*, *11*(9), 696–700. http://doi.org/10.1038/s41561-018-0188-3

Li, Li, Weidner, D. J., Brodholt, J., Alfè, D., & Price, G. D. (2006). Elasticity of Mg2SiO4 ringwoodite at mantle conditions. *Physics of the Earth and Planetary Interiors*, *157*(3-4), 181–187. http://doi.org/10.1016/j.pepi.2006.04.002

Litasov, K., Ohtani, E., Sano, A., Suzuki, A., & Funakoshi, K. (2005). In situ X-ray diffraction study of post-spinel transformation in a peridotite mantle: Implication for the 660-km discontinuity. *Earth and Planetary Science Letters*, *238*(3-4), 311–328. http://doi.org/10.1016/j.epsl.2005.08.001

Lodders, K., & Fegley, B., Jr. (1997). An Oxygen Isotope Model for the Composition of Mars. *Icarus*, *126*(2), 373–394. http://doi.org/10.1006/icar.1996.5653

Lognonné, P., & Mosser, B. (1993). Planetary seismology. *Surveys in Geophysics*, *14*(3), 239–302. http://doi.org/10.1007/BF00690946

Lognonné, P., Gagnepain-Beyneix, J., & Chenet, H. (2003). A new seismic model of the Moon: implications for structure, thermal evolution and formation of the Moon. *Earth and Planetary Science Letters*, *211*(1-2), 27–44. http://doi.org/10.1016/S0012-821X(03)00172-9

Lognonné, P. (2005). Planetary seismology. *Annual Review of Earth and Planetary Sciences*, *33*(1), 571–604. http://doi.org/10.1146/annurev.earth.33.092203.122604

Lognonné, P., Banerdt, W. B., Giardini, D., Pike, W. T., Christensen, U., Laudet, P., et al. (2019). SEIS: Insight's Seismic Experiment for Internal Structure of Mars. *Space Science Reviews*, *215*(1). http://doi.org/10.1007/s11214-018-0574-6

Lognonné, P., Banerdt, W. B., Pike, W. T., Giardini, D., Christensen, U., Garcia, R. F., et al. (2020). Constraints on the shallow elastic and anelastic structure of Mars from InSight seismic data. *Nature Geoscience*, *13*(3), 213–. http://doi.org/10.1038/s41561-020-0536-y

Long, M. D. (2013). Constraints on subduction geodynamics from seismic anisotropy. *Reviews of Geophysics*, *51*(1), 76–112. http://doi.org/10.1002/rog.20008

Long, M. D., & Becker, T. W. (2010). Mantle dynamics and seismic anisotropy. *Earth and Planetary Science Letters*, *297*(3-4), 341–354. http://doi.org/10.1016/j.epsl.2010.06.036

Long, M. D., & Silver, P. G. (2008). The Subduction Zone Flow Field from Seismic Anisotropy: A Global View. *Science*, *319*(5861), 315–318. http://doi.org/10.1126/science.1150809

Long, M. D., & Silver, P. G. (2009). Mantle flow in subduction systems: The subslab flow field and implications for mantle dynamics. *Journal of Geophysical Research: Solid Earth*, *114*(B10), Q05S15. http://doi.org/10.1029/2008JB006200

Long, M. D., & Van Der Hilst, R. D. (2005). Upper mantle anisotropy beneath Japan from shear wave splitting. *Physics of the Earth and Planetary Interiors*, *151*(3-4), 206–222. http://doi.org/10.1016/j.pepi.2005.03.003

Long, M. D., & Wirth, E. A. (2013). Mantle flow in subduction systems: The mantle wedge flow field and implications for wedge processes. *Journal of Geophysical Research: Solid Earth*, *118*(2), 583–606. http://doi.org/10.1002/jgrb.50063

Longhi, J., Knittle, E., Holloway, J. R., & Waenke, H. (1992). The bulk composition, mineralogy and internal structure of Mars. *Mars*, 184–208.

Lynner, C., & Long, M. D. (2015). Heterogeneous seismic anisotropy in the transition zone and uppermost lower mantle: evidence from South America, Izu-Bonin and Japan. *Geophysical Journal International*, *201*(3), 1545–1552. http://doi.org/10.1093/gji/ggv099

Maguire, R., Ritsema, J., & Goes, S. (2018). Evidence of Subduction-Related Thermal and Compositional Heterogeneity Below the United States From Transition Zone Receiver Functions. *Geophysical Research Letters*, *45*(17), 8913–8922. http://doi.org/10.1029/2018GL078378

Mainprice, D. (2007). Seismic anisotropy of the deep Earth from a mineral and rock physics perspective. Treatise in Geophysics Volume 2 pp437-492.

Mainprice, D., Tommasi, A., Couvy, H., Cordier, P., & Frost, D. J. (2005). Pressure sensitivity of olivine slip systems and seismic anisotropy of Earth's upper mantle. *Nature*, *433*(7027), 731–733. http://doi.org/10.1038/nature03266

Mainprice, D., Tommasi, A., Ferré, D., Carrez, P., & Cordier, P. (2008). Predicted glide systems and crystal preferred orientations of polycrystalline silicate Mg-Perovskite at high pressure: Implications for the seismic anisotropy in the lower mantle. *Earth and Planetary Science Letters*, *271*(1-4), 135–144. http://doi.org/10.1016/j.epsl.2008.03.058

Marone, F., & Romanowicz, B. (2007). The depth distribution of azimuthal anisotropy in the continental upper mantle. *Nature*, *447*(7141), 198–U4. http://doi.org/10.1038/nature05742

Marusiak, A. G., Schmerr, N. C., Banks, M. E., & Daubar, I. J. (2020). Terrestrial single-station analog for constraining the martian core and deep interior: Implications for InSight. *Icarus*, *335*, 113396. http://doi.org/10.1016/j.icarus.2019.113396

McDonough, W. F., & Sun, S. S. (1995). The composition of the Earth. *Chemical Geology*, *120*(3-4), 223–253. http://doi.org/10.1016/0009-2541(94)00140-4

Mimoun, D., Murdoch, N., Lognonne, P., Hurst, K., Pike, W. T., Hurley, J., et al. (2017). The Noise Model of the SEIS Seismometer of the InSight Mission to Mars. *Space Science Reviews*, *211*(1-4), 383–428. http://doi.org/10.1007/s11214-017-0409-x

Mohapatra, R. K., & Murty, S. (2003). Precursors of Mars: Constraints from nitrogen and oxygen isotopic compositions of martian meteorites. *Meteoritics & Planetary Science*, *38*(2), 225–241. http://doi.org/10.1111/j.1945-5100.2003.tb00261.x

Mohiuddin, A., Long, M. D., & Lynner, C. (2015). Mid-mantle seismic anisotropy beneath southwestern Pacific subduction systems and implications for mid-mantle deformation. *Physics of the Earth and Planetary Interiors*, *245*, 1–14. http://doi.org/10.1016/j.pepi.2015.05.003

Mondal, P., & Long, M. D. (2020). Strong seismic anisotropy in the deep upper mantle beneath the Cascadia backarc: Constraints from probabilistic finite-frequency SKS splitting intensity tomography. *Earth and Planetary Science Letters*, *539*, 116172. http://doi.org/10.1016/j.epsl.2020.116172

Montagner, J. P. (2002). Upper mantle low anisotropy channels below the Pacific Plate. *Earth and Planetary Science Letters*, *202*(2), 263–274. http://doi.org/10.1016/S0012-821X(02)00791-4

Montagner, J.-P., & Nataf, H. C. (1986). A simple method for inverting the azimuthal anisotropy of surface waves. *Journal of Geophysical Research: Solid Earth*, *91*(B1), 511–520. http://doi.org/10.1029/JB091iB01p00511

Montagner, J.-P., Griot Pommera, D. A., & Lavé, J. (2000). How to relate body wave and surface wave anisotropy? *Journal of Geophysical Research: Solid Earth*, *105*(B8), 19015–19027. http://doi.org/10.1029/2000JB900015

Montalbetti, J. F., & Kanasewich, E. R. (1970). Enhancement of Teleseismic Body Phases with a Polarization Filter. *Geophysical Journal International*, *21*(2), 119–129. http://doi.org/10.1111/j.1365-246X.1970.tb01771.x

Morgan, J. P., & Shearer, P. M. (1993). Seismic constraints on mantle flow and topography of the 660-km discontinuity: evidence for whole-mantle convection. *Nature*, *365*(6446), 506–511. http://doi.org/10.1038/365506a0

Morgan, J. W., & Anders, E. (1979). Chemical composition of Mars. *Geochimica Et Cosmochimica Acta*, *43*(10), 1601–1610. http://doi.org/10.1016/0016-7037(79)90180-7

Morgan, W. J. (1971). Convection Plumes in the Lower Mantle. *Nature*, *230*(5288), 42–43. http://doi.org/10.1038/230042a0

Moulik, P., & Ekström, G. (2014). An anisotropic shear velocity model of the Earth's mantle using normal modes, body waves, surface waves and long-period waveforms. *Geophysical Journal International*, *199*(3), 1713–1738. http://doi.org/10.1093/gji/ggu356

Muir, J. B., & Tkalčić, H. (2015). A method of spherical harmonic analysis in the geosciences via hierarchical Bayesian inference. *Geophysical Journal International*, *203*(2), 1164–1171. http://doi.org/https://doi.org/10.1093/gji/ggv361

Murdoch, N., Mimoun, D., Garcia, R. F., Rapin, W., Kawamura, T., Lognonne, P., et al. (2017). Evaluating the Wind-Induced Mechanical Noise on the InSight Seismometers. *Space Science Reviews*, *211*(1), 429–455. http://doi.org/10.1007/s11214-016-0311-y

Nakamura, Y. (1983). Seismic velocity structure of the lunar mantle. *Journal of Geophysical Research*, *88*(B1), 677–686. http://doi.org/10.1029/JB088iB01p00677

Nakamura, Y. (2005). Farside deep moonquakes and deep interior of the Moon. *Journal of Geophysical Research: Planets*, *110*(E1). http://doi.org/10.1029/2004JE002332

Nakamura, Y., Latham, G. V., & Dorman, H. J. (1982). Apollo Lunar Seismic Experiment—Final summary. *Journal of Geophysical Research: Planets*, *87*(S01), A117–A123. http://doi.org/10.1029/JB087iS01p0A117@10.1002/(ISSN)2169-9356.LPSC13

Neal, C. R., Weber, R. C., Banerdt, W. B., Beghein, C., Chi, P. J., Currie, D. G., et al. (n.d.). The Lunar Geophysical Network Mission. *Agufm*, *2019*, P33D–05. http://doi.org/10.1002/essoar.10502158.1

Nettles, M., & Dziewonski, A. M. (2008). Radially anisotropic shear velocity structure of the upper mantle globally and beneath North America. *Journal of Geophysical Research: Solid Earth*, *113*(B2), 219. http://doi.org/10.1029/2006JB004819

Neumann, G. A., Zuber, M. T., Wieczorek, M. A., McGovern, P. J., Lemoine, F. G., & Smith, D. E. (2004). Crustal structure of Mars from gravity and topography. *Journal of Geophysical Research: Planets*, *109*(E8). http://doi.org/10.1029/2004JE002262

Nimmo, F., & Stevenson, D. J. (2000). Influence of early plate tectonics on the thermal evolution and magnetic field of Mars. *Journal of Geophysical Research: Planets*, *105*(E5), 11969–11979. http://doi.org/10.1029/1999JE001216

Nishimura, C. E., & Forsyth, D. W. (1989). The anisotropic structure of the upper mantle in the Pacific. *Geophysical Journal International*, *96*(2), 203–229. http://doi.org/10.1111/j.1365-246X.1989.tb04446.x

Nissen-Meyer, T., Driel, M. V., Stahler, S., Hosseini, K., Hempel, S., Auer, L., et al. (2014). AxiSEM: broadband 3-D seismic wavefields in axisymmetric media. *Solid Earth*, *5*(1), 425–445. http://doi.org/10.5194/se-5-425-2014

Nowacki, A., Kendall, J. M., Wookey, J., & Pemberton, A. (2015). Mid-mantle anisotropy in subduction zones and deep water transport. *Geochemistry, Geophysics, Geosystems*, *16*(3), 764–784. http://doi.org/10.1002/2014GC005667

Ohuchi, T., Fujino, K., Kawazoe, T., & Irifune, T. (2014). Crystallographic preferred orientation of wadsleyite and ringwoodite: Effects of phase transformation and water on seismic anisotropy in the mantle transition zone. *Earth and Planetary Science Letters*, *397*, 133–144. http://doi.org/10.1016/j.epsl.2014.03.066

Pamato, M. G., Kurnosov, A., Boffa Ballaran, T., Frost, D. J., Ziberna, L., Giannini, M., et al. (2016). Single crystal elasticity of majoritic garnets: Stagnant slabs and thermal anomalies at the base of the transition zone. *Earth and Planetary Science Letters*, *451*, 114–124. http://doi.org/10.1016/j.epsl.2016.07.019

Panero, W. R., Thomas, C., Myhill, R., Pigott, J. S., Raepsaet, C., & Bureau, H. (2020). Dehydration Melting Below the Undersaturated Transition Zone. *Geochemistry, Geophysics, Geosystems*, *21*(2), 1666. http://doi.org/10.1029/2019GC008712

Panning, M. P., Lognonne, P., Banerdt, W. B., Garcia, R., Golombek, M., Kedar, S., et al. (2016). Planned Products of the Mars Structure Service for the InSight Mission to Mars. *Space Science Reviews*, *211*(1-4), 611–650. http://doi.org/10.1007/s11214-016-0317-5

Panning, M. P., Pike, W. T., Lognonné, P., Banerdt, W. B., Murdoch, N., Banfield, D., et al. (2020). On-Deck Seismology: Lessons from InSight for Future Planetary Seismology. *Journal of Geophysical Research: Planets*, *125*(4), 1363. http://doi.org/10.1029/2019JE006353

Pearson, D. G., Brenker, F. E., Nestola, F., McNeill, J., Nasdala, L., Hutchison, M. T., et al. (2014). Hydrous mantle transition zone indicated by ringwoodite

included within diamond. *Nature*, *507*(7491), 221–224. http://doi.org/10.1038/nature13080
Peterson, J. R. (1993). Observations and modeling of seismic background noise. *Open-File Report*, (93-322). http://doi.org/10.3133/ofr93322
Plesa, A. C., Grott, M., Tosi, N., Breuer, D., Spohn, T., & Wieczorek, M. A. (2016). How large are present-day heat flux variations across the surface of Mars? *Journal of Geophysical Research: Planets*, *121*(12), 2386–2403. http://doi.org/10.1002/2016JE005126
Reasenberg, R. D. (1977). The moment of inertia and isostasy of Mars. *Journal of Geophysical Research: Solid Earth*, *82*(2), 369–375. http://doi.org/10.1029/JB082i002p00369
Revenaugh, J. S., & Jordan, T. H. (1991). Mantle layering from ScS reverberation, 2, The transition zone. *Journal of Geophysical Research*, *103*, 2673–2692. http://doi.org/https://doi.org/10.1029/91JB01486
Ringwood, A. E. (1970). Phase transformations and the constitution of the mantle. *Physics of the Earth and Planetary Interiors*, *3*, 109–155. http://doi.org/10.1016/0031-9201(70)90047-6
Ringwood, A. E. (1975). Composition and petrology of the earth's mantle. McGraw-Hill, New York.
Ritsema, J., Deuss, A., van Heijst, H. J., & Woodhouse, J. H. (2011). S40RTS: a degree-40 shear-velocity model for the mantle from new Rayleigh wave dispersion, teleseismic traveltime and normal-mode splitting function measurements. *Geophysical Journal International*, *184*(3), 1223–1236. http://doi.org/10.1111/j.1365-246X.2010.04884.x
Rivoldini, A., Van Hoolst, T., Verhoeven, O., Mocquet, A., & Dehant, V. (2011). Geodesy constraints on the interior structure and composition of Mars. *Icarus*, *213*(2), 451–472. http://doi.org/10.1016/j.icarus.2011.03.024
Rost, S., & Thomas, C. (2009). Improving Seismic Resolution Through Array Processing Techniques. *Surveys in Geophysics*, *30*(4-5), 271–299. http://doi.org/10.1007/s10712-009-9070-6
Rost, S., & Weber, M. (2002). The upper mantle transition zone discontinuities in the Pacific as determined by short-period array data. *Earth and Planetary Science Letters*, *204*(3-4), 347–361. http://doi.org/10.1016/S0012-821X(02)00999-8
Rychert, C. A., Harmon, N., & Schmerr, N. (2014). Synthetic waveform modelling of SS precursors from anisotropic upper-mantle discontinuities. *Geophysical Journal International*, *196*(3), 1694–1705. http://doi.org/10.1093/gji/ggt474
Rychert, C. A., Schmerr, N., & Harmon, N. (2012). The Pacific lithosphere-asthenosphere boundary: Seismic imaging and anisotropic constraints from SS waveforms. *Geochemistry, Geophysics, Geosystems*, *13*(9), 83. http://doi.org/10.1029/2012GC004194
Saki, M., Thomas, C., Merkel, S., & Wookey, J. (2018). Detecting seismic anisotropy above the 410 km discontinuity using reflection coefficients of underside reflections. *Physics of the Earth and Planetary Interiors*, *274*, 170–183. http://doi.org/10.1016/j.pepi.2017.12.001

Sang, L., & Bass, J. D. (2014). Single-crystal elasticity of diopside to 14 GPa by Brillouin scattering. *Physics of the Earth and Planetary Interiors*, *228*, 75–79. http://doi.org/10.1016/j.pepi.2013.12.011

Sanloup, C., Jambon, A., & Gillet, P. (1999). A simple chondritic model of Mars. *Physics of the Earth and Planetary Interiors*, *112*(1-2), 43–54. http://doi.org/10.1016/S0031-9201(98)00175-7

Sawamoto, H., Weidner, D. J., Sasaki, S., & Kumazawa, M. (1984). Single-crystal elastic properties of the modified spinal (beta) phase of magnesium orthosilicate. *Science*, *224*(4650), 749–752. http://doi.org/10.1126/science.224.4650.749

Schaeffer, A. J., Lebedev, S., & Becker, T. W. (2016). Azimuthal seismic anisotropy in the Earth's upper mantle and the thickness of tectonic plates. *Geophysical Journal International*, *207*(2), 901–933. http://doi.org/10.1093/gji/ggw309

Schmandt, B., Jacobsen, S. D., Becker, T. W., Liu, Z., & Dueker, K. G. (2014). Dehydration melting at the top of the lower mantle. *Science*, *344*(6189), 1265–1268. http://doi.org/10.1126/science.1253358

Schmerr, N. (2012). The Gutenberg Discontinuity: Melt at the Lithosphere-Asthenosphere Boundary. *Science*, *335*(6075), 1480–1483. http://doi.org/10.1126/science.1215433

Schmerr, N. C., Banks, M., & Daubar, I. (2019). The Seismic Signatures of Recently Formed Impact Craters on Mars. *Journal of Geophysical Research: Planets*, 2019JE006044. http://doi.org/10.1029/2019JE006044

Schmerr, N. C., Kelly, B. M., & Thorne, M. S. (2013). Broadband array observations of the 300 km seismic discontinuity. *Geophysical Research Letters*, *40*(5), 841–846. http://doi.org/10.1002/grl.50257

Schmerr, N., & Garnero, E. (2006). Investigation of upper mantle discontinuity structure beneath the central Pacific using SS precursors. *Journal of Geophysical Research: Solid Earth*, *111*(B8), B08305. http://doi.org/10.1029/2005JB004197

Schmerr, N., & Garnero, E. J. (2007). Upper Mantle Discontinuity Topography from Thermal and Chemical Heterogeneity. *Science*, *318*(5850), 623–626. http://doi.org/10.1126/science.1145962

Schmerr, N., Garnero, E., & McNamara, A. (2010). Deep mantle plumes and convective upwelling beneath the Pacific Ocean. *Earth and Planetary Science Letters*, *294*(1-2), 143–151. http://doi.org/10.1016/j.epsl.2010.03.014

Scholz, J.-R., Schnidrig, R. W., Davis, P., Lognonne, P., Pinot, B., Garcia, R. F., et al. (2020). Detection, Analysis, and Removal of Glitches From InSight's Seismic Data From Mars. *Earth and Space Science*, *7*(11), 215. http://doi.org/10.1029/2020EA001317

Sharp, T. G., Bussod, G. Y. A., & Katsura, T. (1994). Microstructures in β-Mg1.8Fe0.2SiO4 experimentally deformed at transition-zone conditions. *Physics of the Earth and Planetary Interiors*, *86*(1-3), 69–83. http://doi.org/10.1016/0031-9201(94)05062-7

Shearer, P. M. (1991). Constraints on upper mantle discontinuities from observations of long-period reflected and converted phases. *Journal of Geophysical Research: Solid Earth*, *96*(B11), 18147–18182. http://doi.org/10.1029/91JB01592

Shearer, P. M. (1993). Global mapping of upper mantle reflectors from long-period SS precursors. *Geophysical Journal International*, *115*(3), 878–904. http://doi.org/10.1111/j.1365-246X.1993.tb01499.x

Shearer, P. M., & Buehler, J. (2019). Imaging Upper-Mantle Structure Under USArray Using Long-Period Reflection Seismology. *Journal of Geophysical Research: Solid Earth*, *124*(9), 9638–9652. http://doi.org/10.1029/2019JB017326

Shearer, P. M., & Flanagan, M. P. (1999). Seismic Velocity and Density Jumps Across the 410- and 660-Kilometer Discontinuities. *Science*, *285*(5433), 1545–1548. http://doi.org/10.1126/science.285.5433.1545

Silver, P. G. (1996). SEISMIC ANISOTROPY BENEATH THE CONTINENTS: Probing the Depths of Geology. *Annual Review of Earth and Planetary Sciences*, *24*(1), 385–432. http://doi.org/10.1146/annurev.earth.24.1.385

Silver, P. G., & Chan, W. W. (1988). Implications for continental structure and evolution from seismic anisotropy. *Nature*, *335*(6185), 34–39. http://doi.org/10.1038/335034a0

Silver, P. G., & Chan, W. W. (1991). Shear wave splitting and subcontinental mantle deformation. *Journal of Geophysical Research: Solid Earth*, *96*(B10), 16429–16454. http://doi.org/10.1029/91JB00899

Sinogeikin, S. V., Bass, J. D., & Katsura, T. (2003). Single-crystal elasticity of ringwoodite to high pressures and high temperatures: implications for 520 km seismic discontinuity. *Physics of the Earth and Planetary Interiors*, *136*(1-2), 41–66. http://doi.org/10.1016/S0031-9201(03)00022-0

Sinogeikin, S. V., Katsura, T., & Bass, J. D. (1998). Sound velocities and elastic properties of Fe-bearing wadsleyite and ringwoodite. *Journal of Geophysical Research: Solid Earth*, *103*(B9), 20819–20825. http://doi.org/10.1029/98JB01819

Sleep, N. H. (1994). Martian plate tectonics. *Journal of Geophysical Research: Planets*, *99*(E3), 5639–5655. http://doi.org/10.1029/94JE00216

Smith, D. E. (1999). The global topography of Mars and Implications for surface evolution (vol 284, pg 1495, 1999). *Science*, *284*(5422), 1932–1932.

Smrekar, S. E., Lognonne, P., Spohn, T., Banerdt, W. B., Breuer, D., Christensen, U., et al. (2019). Pre-mission InSights on the Interior of Mars. *Space Science Reviews*, *215*(1). http://doi.org/10.1007/s11214-018-0563-9

Smyth, J. R., & Frost, D. J. (2002). The effect of water on the 410-km discontinuity: An experimental study. *Geophysical Research Letters*, *29*(10), 123–1–123–4. http://doi.org/10.1029/2001GL014418

Sohl, F., & Spohn, T. (1997). The interior structure of Mars: Implications from SNC meteorites. *Journal of Geophysical Research: Planets*, *102*(E1), 1613–1635. http://doi.org/10.1029/96JE03419

Song, T.-R. A., Helmberger, D. V., & Grand, S. P. (2004). Low-velocity zone atop the 410-km seismic discontinuity in the northwestern United States. *Nature*, *427*(6974), 530–533. http://doi.org/10.1038/nature02231

Spohn, T., Grott, M., Smrekar, S. E., Knollenberg, J., Hudson, T. L., Krause, C., et al. (2018). The Heat Flow and Physical Properties Package (HP 3) for the InSight Mission. *Space Science Reviews*, *214*(5), 1–33. http://doi.org/10.1007/s11214-018-0531-4

Stähler, S. C., Sigloch, K., & Nissen-Meyer, T. (2012). Triplicated P-wave measurements for waveform tomography of the mantle transition zone. *Solid Earth*, *3*(2), 339–354. http://doi.org/10.3929/ethz-b-000067293

Stachnik, J. C., Abers, G. A., & Christensen, D. H. (2004). Seismic attenuation and mantle wedge temperatures in the Alaska subduction zone. *Journal of Geophysical Research: Planets*, *109*(B10), 24,015. http://doi.org/10.1029/2004JB003018

Steinberger, B., & O'Connell, R. J. (1998). Advection of plumes in mantle flow: implications for hotspot motion, mantle viscosity and plume distribution. *Geophysical Journal International*, *132*(2), 412–434. http://doi.org/10.1046/j.1365-246x.1998.00447.x

Stixrude, L. (1997). Structure and sharpness of phase transitions and mantle discontinuities. *Journal of Geophysical Research: Solid Earth*, *102*(B7), 14835–14852. http://doi.org/10.1029/97JB00550

Sturgeon, W., Ferreira, A. M. G., Faccenda, M., Chang, S.-J., & Schardong, L. (2019). On the Origin of Radial Anisotropy Near Subducted Slabs in the Midmantle. *Geochemistry, Geophysics, Geosystems*, *464*(11), 10. http://doi.org/10.1029/2019GC008462

Tajima, F., & Grand, S. P. (1998). Variation of transition zone high-velocity anomalies and depression of 660 km discontinuity associated with subduction zones from the southern Kuriles to Izu-Bonin and Ryukyu. *Journal of Geophysical Research: Solid Earth*, *103*(B7), 15015–15036. http://doi.org/10.1029/98JB00752

Taylor, G. J. (2013). The bulk composition of Mars. *Geochemistry*, *73*(4), 401–420. http://doi.org/10.1016/j.chemer.2013.09.006

Thomas, C., & Billen, M. I. (2009). Mantle transition zone structure along a profile in the SW Pacific: Thermal and compositional variations. *Geophysical Journal International*, *176*(1), 113–125. http://doi.org/10.1111/j.1365-246X.2008.03934.x

Thurel, E., Cordier, P., Frost, D., & Karato, S. I. (2003). Plastic deformation of wadsleyite: II. High-pressure deformation in shear. *Physics and Chemistry of Minerals*, *30*(5), 267–270. http://doi.org/10.1007/s00269-003-0313-7

Tommasi, A., Mainprice, D., Cordier, P., Thoraval, C., & Couvy, H. (2004). Strain-induced seismic anisotropy of wadsleyite polycrystals and flow patterns in the mantle transition zone. *Journal of Geophysical Research: Solid Earth*, *109*(B12). http://doi.org/10.1029/2004JB003158

Tong, C., Gudmundsson, O., & Kennett, B. L. N. (1994). Shear wave splitting in refracted waves returned from the upper mantle transition zone beneath northern Australia. *Journal of Geophysical Research: Solid Earth*, *99*(B8), 15783–15797. http://doi.org/10.1029/94JB00460

Trampert, J., & van Heijst, H. J. (2002). Global Azimuthal Anisotropy in the Transition Zone. *Science*, *296*(5571), 1297–1299. http://doi.org/10.1126/science.1070264

Tsujino, N., Nishihara, Y., Yamazaki, D., Seto, Y., Higo, Y., & Takahashi, E. (2016). Mantle dynamics inferred from the crystallographic preferred orientation of bridgmanite. *Nature*, *539*(7627), 81–84. http://doi.org/10.1038/nature19777

Van Hoolst, T., Dehant, V., Roosbeek, F., & Lognonné, P. (2003). Tidally induced surface displacements, external potential variations, and gravity variations on Mars. *Icarus*, *161*(2), 281–296. http://doi.org/10.1016/S0019-1035(02)00045-3

van Keken, P. E., Hacker, B. R., Syracuse, E. M., & Abers, G. A. (2011). Subduction factory: 4. Depth-dependent flux of H2O from subducting slabs worldwide. *Journal of Geophysical Research: Solid Earth*, *116*(B1), B01401. http://doi.org/10.1029/2010JB007922

Verhoeven, O., Rivoldini, A., Vacher, P., Mocquet, A., Choblet, G., Menvielle, M., et al. (2005). Interior structure of terrestrial planets: Modeling Mars' mantle and its electromagnetic, geodetic, and seismic properties. *Journal of Geophysical Research: Solid Earth*, *110*(E4), 790. http://doi.org/10.1029/2004JE002271

Vinnik, L., Chenet, H., Beyneix, J. G., & Lognonne, P. (2001). First seismic receiver functions on the Moon. *Geophysical Research Letters*, *28*(15), 3031–3034. http://doi.org/10.1029/2001GL012859

Visser, K., Trampert, J., & Kennett, B. L. N. (2008). Global anisotropic phase velocity maps for higher mode Love and Rayleigh waves. *Geophysical Journal International*, *172*(3), 1016–1032. http://doi.org/10.1111/j.1365-246X.2007.03685.x

Walck, M. C. (1984). The P-Wave Upper Mantle Structure Beneath an Active Spreading Center - the Gulf of California. *Geophysical Journal of the Royal Astronomical Society*, *76*(3), 697–723. http://doi.org/10.1111/j.1365-246X.1984.tb01918.x

Warren, P. H. (2011). Stable-isotopic anomalies and the accretionary assemblage of the Earth and Mars: A subordinate role for carbonaceous chondrites. *Earth and Planetary Science Letters*, *311*(1-2), 93–100. http://doi.org/10.1016/j.epsl.2011.08.047

Waszek, L., Schmerr, N. C., & Ballmer, M. D. (2018). Global observations of reflectors in the mid-mantle with implications for mantle structure and dynamics. *Nature Communications*, *9*(1), 385. http://doi.org/10.1038/s41467-017-02709-4

Webb, S. L. (1989). The elasticity of the upper mantle orthosilicates olivine and garnet to 3 GPa. *Physics and Chemistry of Minerals*, *16*(7), 684–692. http://doi.org/10.1007/BF00223318

Weber, R. C., Lin, P.-Y., Garnero, E. J., Williams, Q., & Lognonne, P. (2011). Seismic Detection of the Lunar Core. *Science*, *331*(6015), 309–312. http://doi.org/10.1126/science.1199375

Weidner, D. J., Sawamoto, H., Sasaki, S., & Kumazawa, M. (1984). Single-crystal elastic properties of the spinel phase of Mg2SiO4. *Journal of Geophysical Research: Solid Earth*, *89*(B9), 7852–7860. http://doi.org/10.1029/JB089iB09p07852

Wieczorek, M. A., & Zuber, M. T. (2004). Thickness of the Martian crust: Improved constraints from geoid-to-topography ratios. *Journal of Geophysical Research: Planets*, *109*(E1). http://doi.org/10.1029/2003JE002153

Wirth, E. A., & Long, M. D. (2014). A contrast in anisotropy across mid-lithospheric discontinuities beneath the central United States—A relic of craton formation. *Geology*, *42*(10), 851–854. http://doi.org/10.1130/G35804.1

Wolfe, C. J., & Silver, P. G. (1998). Seismic anisotropy of oceanic upper mantle: Shear wave splitting methodologies and observations. *Journal of Geophysical Research: Solid Earth*, *103*(B1), 749–771. http://doi.org/10.1029/97JB02023

Wookey, J., Kendall, J. M., & Barruol, G. (2002). Mid-mantle deformation inferred from seismic anisotropy. *Nature*, *415*(6873), 777–780. http://doi.org/10.1038/415777a

Wu, W., Ni, S., & Irving, J. C. E. (2019). Inferring Earth's discontinuous chemical layering from the 660-kilometer boundary topography. *Science*, *363*(6428), 736–740. http://doi.org/10.1126/science.aav0822

Xu, W., Lithgow Bertelloni, C., Stixrude, L., & Ritsema, J. (2008). The effect of bulk composition and temperature on mantle seismic structure. *Earth and Planetary Science Letters*, *275*(1-2), 70–79. http://doi.org/10.1016/j.epsl.2008.08.012

Yang, J., Mao, Z., Lin, J.-F., & Prakapenka, V. B. (2014). Single-crystal elasticity of the deep-mantle magnesite at high pressure and temperature. *Earth and Planetary Science Letters*, *392*, 292–299. http://doi.org/10.1016/j.epsl.2014.01.027

Ye, L., Li, J., Tseng, T.-L., & Yao, Z. (2011). A stagnant slab in a water-bearing mantle transition zone beneath northeast China: implications from regional SH waveform modelling. *Geophysical Journal International*, *186*(2), 706–710. http://doi.org/10.1111/j.1365-246X.2011.05063.x

Yoder, C. F., Konopliv, A. S., Yuan, D. N., Standish, E. M., & Folkner, W. M. (2003). Fluid Core Size of Mars from Detection of the Solar Tide. *Science*, *300*(5617), 299–303. http://doi.org/10.1126/science.1079645

Yoshino, T., Manthilake, G., Matsuzaki, T., & Katsura, T. (2008). Dry mantle transition zone inferred from the conductivity of wadsleyite and ringwoodite. *Nature*, *451*(7176), 326–329. http://doi.org/10.1038/nature06427

Yoshizaki, T., & McDonough, W. F. (2020). The composition of Mars. *Geochimica Et Cosmochimica Acta*, *273*, 137–162. http://doi.org/10.1016/j.gca.2020.01.011

Yu, C., Day, E. A., de Hoop, M. V., Campillo, M., & van der Hilst, R. D. (2017). Mapping Mantle Transition Zone Discontinuities Beneath the Central Pacific With Array Processing of SS Precursors. *Journal of Geophysical Research: Solid Earth*, *122*(12), 10,364–10,378. http://doi.org/10.1002/2017JB014327

Yu, C., Day, E. A., de Hoop, M. V., Campillo, M., Goes, S., Blythe, R. A., & van der Hilst, R. D. (2018). Compositional heterogeneity near the base of the mantle transition zone beneath Hawaii. *Nature Communications*, *9*(1), 1266. http://doi.org/10.1038/s41467-018-03654-6

Yuan, K., & Beghein, C. (2013). Seismic anisotropy changes across upper mantle phase transitions. *Earth and Planetary Science Letters*, *374*, 132–144. http://doi.org/10.1016/j.epsl.2013.05.031

Yuan, K., & Beghein, C. (2014). Three-dimensional variations in Love and Rayleigh wave azimuthal anisotropy for the upper 800 km of the mantle. *Journal of Geophysical Research: Solid Earth*, *119*(4), 3232–3255. http://doi.org/10.1002/2013JB010853

Yuan, K., & Beghein, C. (2018). A Bayesian method to quantify azimuthal anisotropy model uncertainties: application to global azimuthal anisotropy in the upper mantle and transition zone. *Geophysical Journal International*, *213*(1), 603–622. http://doi.org/10.1093/gji/ggy004

Zha, C. S., Duffy, T. S., Mao, H. K., Downs, R. T., Hemley, R. J., & Weidner, D. J. (1997). Single-crystal elasticity of β-Mg2SiO4 to the pressure of the 410 km seismic discontinuity in the Earth's mantle. *Earth and Planetary Science Letters*, *147*(1-4), E9–E15. http://doi.org/10.1016/S0012-821X(97)00010-1

Zhang, J. S., Bass, J. D., & Schmandt, B. (2018). The Elastic Anisotropy Change Near the 410-km Discontinuity: Predictions From Single-Crystal Elasticity Measurements of Olivine and Wadsleyite. *Journal of Geophysical Research: Solid Earth*, *123*(4), 2674–2684. http://doi.org/10.1002/2017JB015339

Zhao, L., & Chevrot, S. (2003). SS-wave sensitivity to upper mantle structure: Implications for the mapping of transition zone discontinuity topographies. *Geophysical Research Letters*, *30*(11), 1590. http://doi.org/10.1029/2003GL017223

Zharkov, V. N., & Gudkova, T. V. (2005). Construction of Martian Interior Model. *Solar System Research*, *39*(5), 343–373. http://doi.org/10.1007/s11208-005-0049-7

Zheng, Y., Nimmo, F., & Lay, T. (2015). Seismological implications of a lithospheric low seismic velocity zone in Mars. *Physics of the Earth and Planetary Interiors*, *240*, 132–141. http://doi.org/10.1016/j.pepi.2014.10.004

Zuber, M. T., Smith, D. E., Solomon, S. C., MUHLEMAN, D. O., HEAD, J. W., GARVIN, J. B., et al. (1992). The Mars-Observer Laser Altimeter Investigation. *Journal of Geophysical Research*, *97*(E5), 7781–7797. http://doi.org/10.1029/92JE00341